

NATIONAL AERONAUTICS AND SPACE ADMINISTRATION

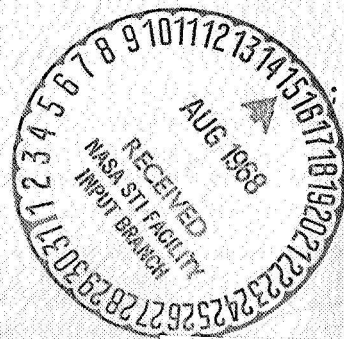
*Technical Report 32-883*

*Mariner Mars 1964 Project Report:  
Scientific Experiments*

*R. K. Sloan*

FACILITY FORM 602

<b>N 68-30303</b>	
(ACCESSION NUMBER)	(THRU)
<u>180</u>	<u>1</u>
(PAGES)	(CODE)
<u>CR-95876</u>	<u>30</u>
(NASA CR OR TMX OR AD NUMBER)	(CATEGORY)



JET PROPULSION LABORATORY  
CALIFORNIA INSTITUTE OF TECHNOLOGY  
PASADENA, CALIFORNIA

July 15, 1968

GPO PRICE \$ \_\_\_\_\_

CSFTI PRICE(S) \$ \_\_\_\_\_

Hard copy (HC) \_\_\_\_\_

Microfiche (MF) \_\_\_\_\_

NATIONAL AERONAUTICS AND SPACE ADMINISTRATION

*Technical Report 32-883*

*Mariner Mars 1964 Project Report:  
Scientific Experiments*

*R. K. Sloan*

JET PROPULSION LABORATORY  
CALIFORNIA INSTITUTE OF TECHNOLOGY  
PASADENA, CALIFORNIA

July 15, 1968



***TECHNICAL REPORT 32-883***

Copyright © 1968  
Jet Propulsion Laboratory  
California Institute of Technology  
Prepared Under Contract No. NAS 7-100  
National Aeronautics & Space Administration

## Preface

On November 28, 1964, *Mariner IV* was successfully launched on a trajectory that would take it within 150,000 miles of Mars. On December 5, 1964, the spacecraft performed a successful midcourse maneuver, altering its flight path so that it would pass within 6118 miles of the planet. The flight took approximately  $7\frac{1}{2}$  months, during which time a great deal of scientific information was gathered concerning the environment of both near-earth and interplanetary space. On July 14, 1965, *Mariner IV* photographed the surface of Mars and telemetered to earth the most advanced scientific and technical data regarding the planet yet recorded.

The *Mariner* Mars 1964 Project has been documented in a series of reports (see next page). The present report provides the results of the *Mariner IV* scientific experiments, exclusive of the television experiment. Each experiment presentation includes a brief description of the operation and calibration of the experimental instrumentation.

It is believed that the techniques, procedures and results documented herein are important contributions to the exploration of space and the advancement of science.



W. H. Pickering, Director  
Jet Propulsion Laboratory



J. A. James, Deputy Assistant Laboratory  
Director for Flight Projects



D. Schneiderman, Project Manager  
*Mariner Mars 1964*

## **Elements of the *Mariner Mars 1964* Project Report**

The *Mariner Mars 1964* Project Report consists of the following volumes:

*Mariner Mars 1964* Project Report: Mission and Spacecraft Development,  
Volume I. From Project Inception Through Midcourse Maneuver (TR 32-  
740, Vol. I)

*Mariner Mars 1964* Project Report: Mission and Spacecraft Development,  
Volume II. Appendixes (TR 32-740, Vol. II)

*Mariner Mars 1964* Project Report: Mission Operations (TR 32-881)

*Mariner Mars 1964* Project Report: Spacecraft Performance and Analysis  
(TR 32-882)

*Mariner Mars 1964* Project Report: Scientific Experiments (TR 32-883)

*Mariner Mars 1964* Project Report: Television Experiment, Part I. Investigators'  
Report (TR 32-884, Part I)

*Mariner Mars 1964* Project Report: Television Experiment, Part II. Picture  
Element Matrices (TR 32-884, Part II)

Tracking and Data Acquisition Support for *Mariner Mars 1964*, Volume II.  
Cruise to Post-Encounter Phase (TM 33-239, Vol. II)

## **Acknowledgment**

The author wishes to acknowledge the considerable assistance and advice of the scientific investigator and experiment support personnel during the preparation of this report. These people are mentioned separately in each appropriate section of the report. Special acknowledgment should be accorded to V. G. Annigian and S. T. Murakami of the JPL Technical Information and Documentation Division for creative and editorial assistance.





PRECEDING PAGE BLANK NOT FILMED.

## Contents

<b>I. Introduction</b>	<b>1</b>
<b>II. Science Subsystem</b>	<b>3</b>
A. Introduction	3
B. Data Automation Subsystem	7
1. Functional description of real-time DAS	7
2. Functional description of NRT DAS	12
3. Physical description	15
4. Design evolution	15
<b>References</b>	<b>16</b>
<b>III. Trapped Radiation Detector</b>	<b>17</b>
A. Introduction	17
B. Purpose	18
C. Instrument	18
1. Electronics	19
2. Detectors	22
D. Results	22
1. Absence of 40-keV electrons at 3300 earth radii	24
2. Impulsive emission of $\sim 40$ -keV electrons from the sun	24
3. Observation of $\sim 500$ -keV protons	27
4. Martian encounter	30
5. Implications of the absence of radiation belts	32
E. Sources	34
<b>References</b>	<b>34</b>
<b>Bibliography</b>	<b>35</b>
<b>IV. Cosmic Dust Detector</b>	<b>37</b>
A. Introduction	37
B. Experiment Objectives	37
C. Instrumentation	38
D. Instrument Calibration	41

## Contents (contd)

E. Trajectory . . . . .	42
1. Spacecraft position in space/time . . . . .	42
2. Cosmic dust sensor attitude in space . . . . .	44
F. Data from the Experiment . . . . .	51
G. Sources . . . . .	57
<b>References . . . . .</b>	<b>58</b>
 <b>V. Ionization Chamber . . . . .</b>	 <b>59</b>
A. Introduction . . . . .	59
B. Instrument . . . . .	59
1. Measurements . . . . .	59
2. Description . . . . .	60
3. Absolute calibration of ion chamber . . . . .	61
4. Absolute calibration of Geiger-Mueller tube . . . . .	62
5. Construction . . . . .	64
6. Response to environment . . . . .	65
C. Results . . . . .	67
1. Galactic cosmic rays . . . . .	67
2. Solar protons . . . . .	68
3. Trapped particles at earth . . . . .	68
4. Failure of G-M tube and ion chamber . . . . .	68
<b>References . . . . .</b>	<b>71</b>
<b>Bibliography . . . . .</b>	<b>71</b>
 <b>VI. Cosmic Ray Telescope . . . . .</b>	 <b>73</b>
A. Introduction . . . . .	73
B. Objectives . . . . .	74
C. Instrument . . . . .	74
1. Accumulation, readout, and format of data . . . . .	76
2. Calibration and checkout procedures . . . . .	77
3. Stability and degradation modes . . . . .	78
4. Leading particulars . . . . .	78
D. Results . . . . .	79
<b>References . . . . .</b>	<b>84</b>

## Contents (contd)

<b>VII. Helium Magnetometer</b>	85
A. Introduction	85
B. Purpose	85
C. Instrument	86
D. Results	89
1. The near-earth measurements	89
2. Interplanetary magnetic field measurements	100
3. Measurements near Mars	119
<b>References</b>	123
<b>Bibliography</b>	125
 <b>VIII. Solar Plasma Probe</b>	 127
A. Introduction	127
B. Purpose	127
C. Instrument	128
1. Circuits	128
2. Digital programmer	133
3. Standard signal self-check	133
4. High-voltage self-check	134
5. Temperature and marker check	134
6. Power supply	134
D. Results	134
1. Interplanetary data	134
2. Results near Mars and near the earth	135
3. High-voltage supply failure	139
<b>References</b>	140
<b>Bibliography</b>	140
 <b>IX. Occultation Experiment</b>	 141
A. Introduction and Purpose	141
B. Instrumentation	143
C. Data Analysis	144
1. Audio recorded data	146
2. Phase-lock data	147

## Contents (contd)

D. Results . . . . .	149
1. Lower atmosphere . . . . .	150
2. Radius measurement . . . . .	156
3. Ionosphere and upper atmosphere . . . . .	158
<b>References</b> . . . . .	162
<b>Appendix.</b> Abbreviations . . . . .	164

## Tables

II-1. <i>Mariner</i> Mars 1964 instruments and ancillaries . . . . .	5
II-2. RT DAS words and events . . . . .	11
III-1. Characteristics of trapped radiation detectors . . . . .	19
III-2. Proton events observed with <i>Mariner IV</i> , Nov. 28, 1964–Oct. 1, 1965 . . . . .	29
IV-1. Threshold levels in terms of momentum of particles for different PHA levels . . . . .	42
IV-2. Data from CDD experiment by time, event No., and PHA level . . . . .	54
IV-3. Cumulative flux-mass distribution for various heliocentric distances . . . . .	57
V-1. Critical specifications of environmental test . . . . .	65
V-2. Response of ion chamber to environment . . . . .	66
V-3. Response of G–M tubes to environment . . . . .	66
IX-1. Summary of preliminary results for the lower atmosphere of Mars . . . . .	153
IX-2. Parameters of theoretical model atmospheres . . . . .	155
IX-3. Comparison of atmospheric quantities computed from occultation immersion and emersion data . . . . .	156
IX-4. Computations of the radius of Mars . . . . .	157

## Figures

II-1. Science subsystem and interfaces, functional block diagram . . . . .	4
II-2. Data automation subsystem subassemblies . . . . .	7
II-3. Real-time DAS functional block diagram . . . . .	8
II-4. RT DAS word format . . . . .	9

## Contents (contd)

### Figures (contd)

II-5. Non-real-time DAS functional block diagram . . . . .	13
II-6. NRT DAS word format . . . . .	14
III-1. TRD, top and bottom views . . . . .	18
III-2. TRD, functional block diagram . . . . .	20
III-3. <i>Mariner IV</i> through the magnetosphere on Nov. 28–29, 1964 . . . . .	21
III-4. <i>Mariner IV</i> near-earth trajectory . . . . .	22
III-5. Counting rates of detectors A, B, and C on <i>Mariner IV</i> during outward traversal of the earth magnetosphere (Nov. 28–29, 1964) . . . . .	23
III-6. Comprehensive plot of data from all detectors for the major part of the May 25–28, 1965 solar electron event . . . . .	25
III-7. An expanded plot of the early part of the May 25–28 event . . . . .	26
III-8. An alternative plot of the early part of the May 25–28 event, showing net counting rates due to solar electrons . . . . .	27
III-9. Daily averages of the counting rates of channels $D_1$ and $D_2$ during 10 mo of interplanetary flight . . . . .	28
III-10. A comprehensive plot of the counting rates of detectors A, C, B, $D_1$ and $D_2$ before, during, and after the encounter with Mars on July 14–15, 1965 . . . . .	31
III-11. An analytical diagram used for inferring an upper limit to the ratio of the magnetic dipole moment of Mars to that of earth . . . . .	33
IV-1. Cosmic dust detector . . . . .	39
IV-2. Cosmic dust detector, functional block diagram . . . . .	40
IV-3. <i>Mariner IV</i> heliocentric longitude vs spacecraft distance above ecliptic plane . . . . .	42
IV-4. Polar plot of spacecraft flight path with sun at origin . . . . .	43
IV-5. <i>Mariner IV</i> heliocentric range and longitude vs time . . . . .	45
IV-6. View of the CDD impact plate as <i>Mariner IV</i> approaches Mars . . . . .	46
IV-7. Geometrical illustration of the relationships of the plate-normal $\hat{n}$ and the heliocentric velocity vector $\vec{V}_s$ in the heliocentric ecliptic system . . . . .	47
IV-8. $\chi_n$ and $\psi_s$ vs time from injection . . . . .	47
IV-9. <i>Mariner IV</i> scalar heliocentric velocity vs time . . . . .	47
IV-10. Spherical geometry used to describe particle path relative to the sensor impact plate . . . . .	48
IV-11. Contour of accessibility-to-measurement of the forward-looking plate surface, <i>Mariner IV</i> CDD . . . . .	49
IV-12. Projection of the rear-looking contour of accessibility of the plane of impact plate . . . . .	50



## Contents (contd)

### Figures (contd)

IV-13. <i>Mariner IV</i> CDD, solar simulator data, August 26, 1964 . . . . .	52
IV-14. <i>Mariner IV</i> CDD, estimated launch-temperature history . . . . .	52
IV-15. <i>Mariner IV</i> CDD, estimated flight temperatures . . . . .	53
V-1. Ionization chamber, <i>Mariner Mars 1964</i> . . . . .	60
V-2. Block diagram of ionization chamber . . . . .	61
V-3. Proton response of G-M tube . . . . .	63
V-4. Response of ion chamber and G-M tube to electrons . . . . .	63
V-5. Cross-sectional view of ion chamber . . . . .	64
V-6. Cross-sectional view of G-M counter tube . . . . .	65
V-7. True counting rates vs observed rate of an ion chamber . . . . .	66
V-8. True counting rates vs observed rate of G-M counter . . . . .	66
V-9. Averages (6-h) of ionization rate and G-M tube counting rate for the first portion of the <i>Mariner IV</i> mission . . . . .	67
V-10. Averages (20-min) of ionization rate, true G-M tube counting rate, and average specific ionization for the period following solar flare of February 5, 1965 . . . . .	68
V-11. Ionization rate, true G-M tube counting rate, and average specific ionization in the earth's Van Allen radiation belts . . . . .	69
VI-1. Cosmic ray telescope . . . . .	73
VI-2. Cross section of telescope showing sensors . . . . .	74
VI-3. Energy loss of particles in D <sub>1</sub> and D <sub>3</sub> detectors vs incident particle energy . . . . .	75
VI-4. CRT block diagram showing logical functions . . . . .	76
VI-5. Typical pulse-height spectrum produced in D <sub>1</sub> by inertial <sup>241</sup> Am source with instrument in calibrate mode . . . . .	77
VI-6. Solar flare protons E > MeV, 5 February 1965 . . . . .	80
VI-7. Integrated pulse-height distribution for protons 15–70 Mev . . . . .	81
VI-8. Onset phase of solar proton event, 5 February 1965 . . . . .	81
VI-9. Decay of intensity of solar event, 5 February 1965 . . . . .	82
VI-10. Continuous time-intensity profile for successive solar rotations Nos. 1804–1808, <i>Mariner IV</i> and IMP-3 . . . . .	83
VI-11. <i>Mariner IV</i> trajectory and idealized interplanetary magnetic field configuration . . . . .	83
VII-1. <i>Mariner IV</i> vector helium magnetometer, simplified functional block diagram . . . . .	86

## Contents (contd)

### Figures (contd)

VII-2. <i>Mariner IV</i> magnetometer . . . . .	87
VII-3. <i>Mariner IV</i> magnetometer, simplified schematic . . . . .	88
VII-4. <i>Mariner IV</i> magnetometer data acquired near earth . . . . .	90
VII-5. <i>Mariner IV</i> near-earth trajectory . . . . .	91
VII-6. <i>Mariner IV</i> magnetometer data showing multiple passages of shock front . . . . .	92
VII-7. Five-minute averages and standard deviations of absolute field magnitude in magnetosheath . . . . .	94
VII-8. Five-minute averages of field direction angles in solar ecliptic coordinates . . . . .	95
VII-9. Power spectra of $B$ . . . . .	96
VII-10. Power spectrum of $B$ . . . . .	96
VII-11. Smoothed $B_{  }$ . . . . .	97
VII-12. Smoothed $B_{\perp}$ . . . . .	97
VII-13. Absolute magnitude of magnetic field . . . . .	98
VII-14. A plane, torsional oscillation projected onto XY and XZ planes . . . . .	99
VII-15. Directional distributions of normals to planar variations . . . . .	100
VII-16. <i>Mariner IV</i> distributions of component magnitudes . . . . .	102
VII-17. Spiral field component, preferred values . . . . .	103
VII-18. Polarity distribution of interplanetary field during solar rotations 1797–1808 as derived from Fig. VII-17 . . . . .	104
VII-19. Trajectory of <i>Mariner IV</i> in geocentric coordinate system . . . . .	105
VII-20. Distribution of $K_p$ for period from November 29, 1964 to March 12, 1965 . . . . .	106
VII-21. Plots of $\overline{\sigma B_{T, N}}$ , a function of transverse oscillation in interplanetary field and $K_p$ . . . . .	107
VII-22. Relationship between values of $\overline{\sigma B_{T, N}}$ and $\overline{K_p}$ . . . . .	108
VII-23. Simultaneous measurements of interplanetary magnetic field direction $\phi$ . . . . .	110
VII-24. Simultaneous measurements of interplanetary field magnitude $B_{\perp}$ . . . . .	110
VII-25. Range parameters of trajectory of <i>Mariner IV</i> as functions of time . . . . .	111
VII-26. Solar-equatorial system parameters of trajectory of <i>Mariner IV</i> as functions of time . . . . .	111
VII-27. Mean values of magnitudes of various components of interplanetary magnetic field versus time, heliocentric range, and latitude . . . . .	112

## Contents (contd)

### Figures (contd)

VII-28. Standard deviations of various components of interplanetary magnetic field versus time, heliocentric range, and latitude . . . . .	113
VII-29. Power spectra of field obtained for three days near beginning of flight . . . . .	115
VII-30. Power spectra of field obtained for three days near end of high data rate interval . . . . .	116
VII-31. Examples of discontinuities in interplanetary magnetic field . . . . .	117
VII-32. Directional distribution of current sheet normals . . . . .	118
VII-33. Illustrating north-south orientation of radially convected ( <i>ab</i> ) current-sheet normal due to negative latitudinal solar-wind shear . . . . .	119
VII-34. <i>Mariner IV</i> encounter, shock front locations . . . . .	120
VII-35. Three components of measured magnetic field and total magnitude <i>B</i> from magnetometer data during encounter . . . . .	122
VIII-1. Solar plasma probe . . . . .	128
VIII-2. Plasma detector cup . . . . .	129
VIII-3. Sequence of energy measurements . . . . .	130
VIII-4. Solar plasma probe functional block diagram . . . . .	131
VIII-5. EOGO and SPP high-voltage rectifier chains and high-voltage monitor. . . . .	132
VIII-6. Days 3–29, 3-h averages . . . . .	135
VIII-7. Days 29–55, 3-h averages . . . . .	136
VIII-8. Days 55–81, 3-h averages . . . . .	137
VIII-9. Spectra, days 333 and 334, current vs voltage . . . . .	138
VIII-10. Individual spectra taken during Mars encounter, and sun–Mars–probe plane . . . . .	139
IX-1. Geometry of occultation . . . . .	142
IX-2. DSIF instrumentation for the occultation experiment . . . . .	144
IX-3. Power spectrum of signal at the time of switching from one-way to two-way frequency . . . . .	145
IX-4. Data obtained during occultation experiment . . . . .	146
IX-5. Occultation-exit audio doppler residuals, DSSs 11 and 12 . . . . .	147
IX-6. Difference, observed data minus computed data, in cycles . . . . .	149
IX-7. Range-rate doppler residuals from DSSs 11, 12, and 42 . . . . .	150
IX-8. Phase difference (residual sum) — DSS 11 data . . . . .	151
IX-9. Phase change due only to atmosphere . . . . .	152

## Contents (contd)

### Figures (contd)

IX-10. Maximum changes in doppler, phase, and amplitude as functions of surface refractivity and scale height . . . . .	152
IX-11. Atmospheric mass density vs altitude above Electris at the time of entry into occultation. . . . .	153
IX-12. Comparison of occultation-entry and -exit residuals . . . . .	154
IX-13. Occultation-exit residuals with theoretical models . . . . .	155
IX-14. Occultation-exit residual sums with theoretical models . . . . .	155
IX-15. Ionospheric phase change vs time, during occultation entry . . . . .	158
IX-16. Electron-number density vs altitude above Electris at the time and location corresponding to entry into occultation . . . . .	159
IX-17. Number density vs altitude for three different atmospheric models . . . . .	160
IX-18. Temperature vs altitude for three different atmospheric models . . . . .	160
IX-19. Two-way ionospheric phase path vs altitude above the limb . . . . .	161

## Abstract

Discussions are presented for each of the six instruments and the measurements obtained from the fields and particles experiments of the *Mariner* Mars 1964 mission. The majority of the instruments performed well and all provided useful measurements enhancing the information on interplanetary space and on the near-earth and near-Mars environments. Specifically, the six instruments on the *Mariner IV* spacecraft measured:

- (1) Trapped radiation detector – electron and proton radiation belts at earth and Mars and particle phenomena in interplanetary space.
- (2) Cosmic dust detector – mass and flux distribution of interplanetary dust particles.
- (3) Ionization chamber – average total ionization of high-energy particle radiation.
- (4) Cosmic ray telescope – spectral energy analysis of high-energy cosmic and solar protons and  $\alpha$  particles including directional variations.
- (5) Helium magnetometer – magnitude and direction of planetary and interplanetary magnetic fields.
- (6) Plasma probe – density, velocity, and direction of charged particles making up the solar wind.

Also included is the radio frequency occultation experiment using the spacecraft radio signal passage through the Martian atmosphere to determine characteristics of its atmosphere, specifically the density and intensity of the ionosphere, surface pressure, and scale height of the lower atmosphere.



## I. Introduction

This report presents a compilation of the significant results of the scientific experiments performed by the *Mariner IV* mission. An attempt has been made to make the discussion as comprehensive as possible so that the interested space scientist will find included herein all of the pertinent information about the spacecraft and mission. However, the reader should be cautioned to return to the original publications of the various scientific experimenters, which have been extensively referenced, for a presentation of detailed points.

The primary objective of the *Mariner Mars 1964* mission was to conduct close-up scientific observations of the planet Mars and to transmit the results of these observations back to earth. Secondary objectives were to perform certain field and particle measurements in interplanetary space and in the vicinity of Mars, and to provide experience and knowledge about the performance of the basic engineering equipment of an altitude stabilized spacecraft during a long-duration interplanetary flight farther from the sun than earth's orbit.

The *Mariner IV* spacecraft successfully transported its carefully selected complement of scientific instruments to its target, which was 134 million miles from the

earth at the time of encounter, and flew them past the planet at an accurately known distance and with accurately known orientations. The experiments were designed "to provide maximum information about Mars" within the weight limitations imposed by a 575-lb spacecraft. The payload had to be sharply reduced when the *Atlas/Centaur* launch vehicle had to be replaced by an *Atlas/Agena* vehicle, which had only about a third of the weight-lifting capacity for interplanetary missions.

Five of the instruments placed aboard *Mariner IV* sampled the magnetic field and energetic particles in the region between the earth and Mars, as *Mariner II* had previously sampled fields and particles between the earth and Venus. A sixth instrument measured the impact of micrometeorites during the voyage. At Mars, the magnetic-field and radiation instruments also searched for the planet's magnetic field and determined whether or not Mars was circled by radiation belts similar to the earth's Van Allen belts. In addition, the trajectory of *Mariner IV* was selected to carry the spacecraft behind Mars so that radio transmission from the craft to the earth was interrupted for a short period. During this occultation experiment, as it was called, the radio signals passing between *Mariner IV* and the earth grazed the edge of the planet, passing through its atmosphere as

the craft disappeared behind Mars and again as it reappeared. By measuring how the signal was distorted during this experiment it was possible to infer important properties of the Martian atmosphere.

The responsibility for the scientific aspects of the mission was spread widely among investigators in government and academic institutions (see Table II-1 of Section II of this report).

## II. Science Subsystem

### A. Introduction

The *Mariner* Mars 1964 science subsystem consisted of instruments designed to yield data for scientific experiments, ancillaries designed to perform specified functions, and the television experiment. All instruments, except the television camera (covered in a separate report in this series, Ref. 1), were designed to operate and collect scientific data in interplanetary space as well as in the vicinity of Mars. The instruments and experiments comprising the science subsystem consisted of the following:

- (1) Cosmic ray telescope.
- (2) Cosmic dust detector.
- (3) Trapped radiation detector.
- (4) Ionization chamber.
- (5) Solar plasma probe.
- (6) Helium magnetometer.
- (7) Occultation (used ground instrumentation).
- (8) Television camera.

The ancillaries consisted of the data automation subsystem (DAS), the planetary scan subsystem, and the narrow-angle Mars gate (NAMG). The instruments and ancillaries with interfaces between units are shown in Fig. II-1.

The DAS comprised two functionally independent sections: the real-time (RT) subsystem and the non-real-time (NRT) subsystem. The former operated throughout the mission and performed all of the functions necessary for the proper collection and sequencing of data from the cruise instruments and formatting the data. The latter operated in the vicinity of Mars to control the planetary scan and television camera and to provide for the transfer of television picture data to the spacecraft recorder.

The planetary scan subsystem was equipped with a wide-angle optical sensing device mounted on a movable platform, and was designed to search for, acquire, and track the planet so that the television camera would be correctly oriented toward the desired portions of the planet surface. The narrow-angle Mars gate provided a

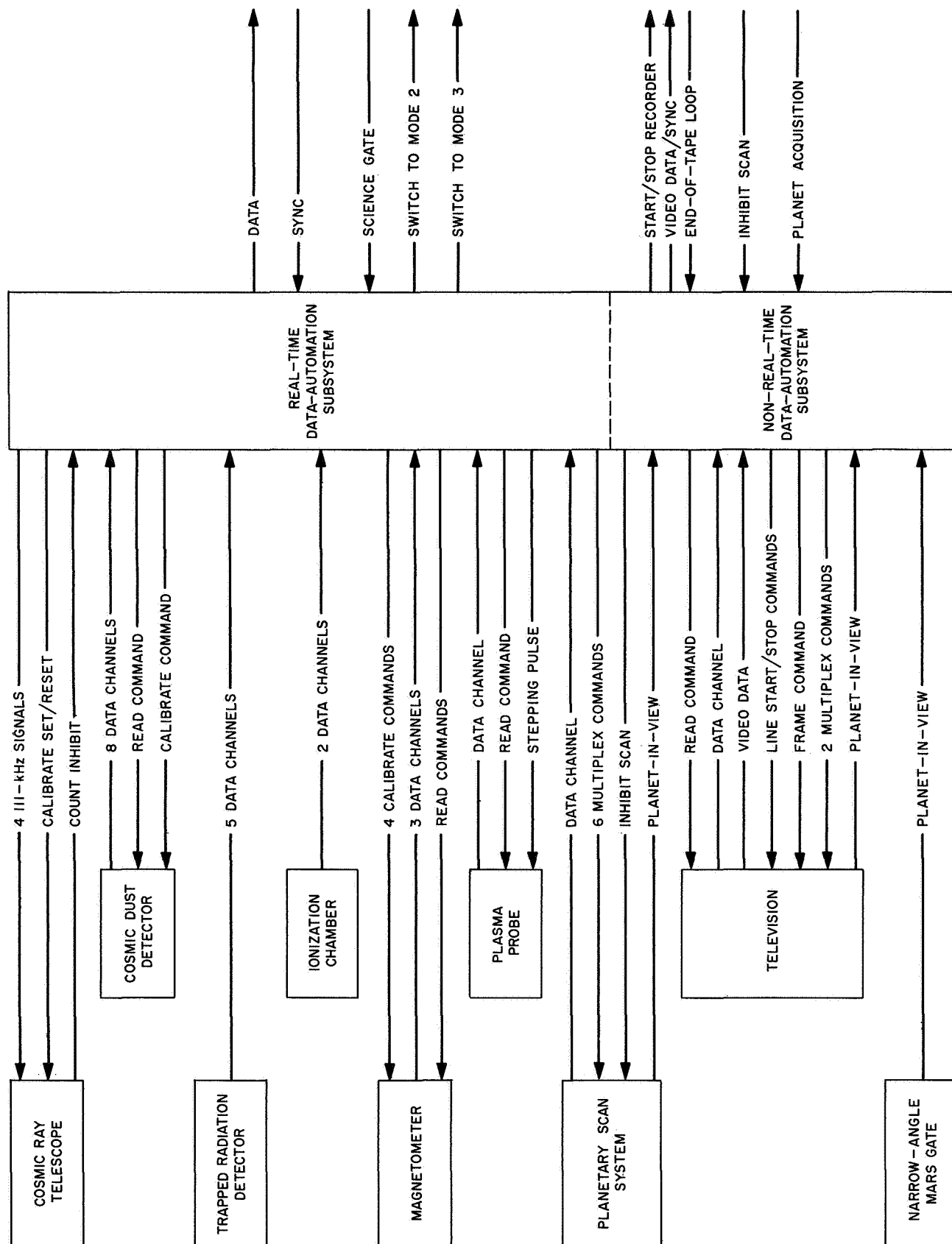


Fig. II-1. Science subsystem and interfaces, functional block diagram

signal that caused the DAS to inhibit the scan-platform motion and to initiate the picture-recording sequence just before the near limb of the planet entered the television camera field of view. Complete descriptions of the planetary scan subsystem and NAMG are provided in Ref. 2.

Table II-1 summarizes some of the important characteristics of each instrument and its purposes, and lists the investigating teams. Since the occultation experiment

did not involve instruments of the science subsystem, only the investigators are included in this table.

Although the science subsystem weighed only 51.25 lb (less than 10% of the total spacecraft weight) it contained half of the 34,000 electronic components in the spacecraft. During interplanetary cruise, the science instruments consumed 21.56 W of power; during planet encounter, the instruments consumed 37.02 W.

**Table II-1. Mariner Mars 1964 instruments and ancillaries**

Name (Unit No.)	Weight, lb (Power, W)	Look angle	Purpose	Number of sensors (Output data)	Investigator/affiliation (* = principal)
<b>Instrument</b>					
Cosmic ray telescope (21)	2.58 (0.598)	30-deg ½-angle cone along Z axis	To detect and measure trapped corpuscular radiation in vicinity of Mars; to measure flux and energy of alpha particles and protons as a function of position and time in interplanetary space	1 sensor, 3 detectors in telescope  (Digital—4)	*Dr. J. A. Simpson, Univ. of Chicago  Mr. J. O'Gallagher, Univ. of Chicago
Cosmic dust detector (24)	2.10 (0.201)	Into plane of ecliptic in direct and retrograde motion	To make direct measurements of dust particle momentum and mass distribution in the earth-moon, Mars-Deimos-Phobos, and interplanetary regions	2 sensors  (Digital—1)	*Mr. W. M. Alexander, NASA GSFC  Mr. O. E. Berg, GSFC Dr. J. L. Bohn, Temple Univ. Mr. C. W. McCracken, GSFC Mr. L. Secrestan, GSFC
Trapped radiation detectors (25)	2.20 (0.350)	3 sensors, 70 deg to probe-sun line, 30-deg ½-angle cone  1 sensor, 135 deg to probe-sun line, —30- deg ½-angle cone	To search for magnetically trapped particles in vicinity of Mars and, if found, make a preliminary estimate of their distribution, energy spectra, and identify; to monitor solar cosmic rays and energetic electrons in interplanetary space, to determine their angular distribution, energy spectra, and time history	4 sensors  (Digital—5)	*Dr. J. A. Van Allen, State Univ. of Iowa  Dr. L. A. Frank, SUI Mr. S. M. Krimigis, SUI
Ionization chamber (26)	2.71 (0.460)	Omni- directional	To detect and measure average omnidirectional flux of corpuscular radiation in regions between the earth and Mars. To measure the average specific ionization attributable to this flux. To measure the omnidirectional flux and specific ionization of charged particles that may be trapped in vicinity of Mars	2 sensors  (Digital—2)	*Dr. H. V. Neher, CIT  Dr. H. R. Anderson, JPL
Solar plasma probe (32)	6.41 (2.65 av, 2.90 peak)	30-deg ½-angle cone, 10 deg from probe- sun line	To measure spectral distribution, flux density, and time history of positively charged solar plasma traveling outward from sun and to correlate their measurements with those from magnetometer	1 sensor, 3 sections  (Pulse width—1)	*Dr. H. S. Bridge, MIT  Dr. A. Lazarus, MIT Dr. C. W. Snyder, JPL



Table II-1 (contd)

Name (Unit No.)	Weight, lb (Power, W)	Look angle	Purpose	Number of sensors (Output data)	Investigator/affiliation (* = principal)
Helium magnetometer  (33)	7.50  (7.30)	1 sensor along Z axis, 1 sensor along Y axis, 1 sensor along X axis	To investigate existence of a Martian planetary field and determine its characteristics as function of direction, magnitude, multipolarity, and orientation with respect to planetary rotational axis; to investigate interaction between planetary and interplanetary magnetic fields; to measure magnitude and direction of steady and slowly varying components of interplanetary magnetic field and to determine its variation with heliographic latitude and longitude	3 sensors  (Pulse width—3)	*Dr. E. J. Smith, JPL  Mr. P. J. Coleman, Jr., UCLA Dr. L. Davis, Jr., CIT Dr. D. E. Jones, BYU
Television  (36)	11.28  (8.0)	1.05 × 1.05 deg	To make preliminary topographic reconnaissance of portions of surface of Mars; to attain an improved knowledge of areas of possible living matter; to obtain additional data on Martian surface reflectivities so that design of future systems will be enhanced	1 sensor, 2 alternate color filters  (Digital—3, pulse width—1 sequenced)	*Dr. R. B. Leighton, CIT  Dr. B. C. Murray, CIT Dr. R. P. Sharp, CIT Mr. R. K. Sloan, JPL Mr. J. D. Allen, JPL
Occultation					*Dr. A. J. Kliore, JPL Dr. Von R. Eshleman, Stanford Mr. D. L. Cain, JPL Dr. G. S. Levy, JPL Dr. F. D. Drake, Cornell Dr. Gunnar Fjeldbo, Stanford
Ancillary					
Data automation subsystem  (20)	11.91  (6.5 av. during cruise, 5.6 av. during encounter, 8.0 peak during encounter)	Not applicable	Provided sequencing, processing, storage, buffering, and encoding necessary to realize optimum scientific value of each instrument; performed certain engineering measurements in addition to those made by spacecraft data encoder	None  (Non-video RT digital data- to-data en- coder; bit sync and RZ video data to video storage)	
Planetary scan subsystem  (31)	5.65  (4.65 at 2400 Hz, 2.81 at 400 Hz)	25-deg ½-angle cone	Used to point television camera at a planet point that depends on bisector of radiation and trajectory of spacecraft	1 sensor  (Pulse width—1)	
Narrow-angle Mars gate  (7MG1)	0.20  (Part of DAS power req.)	2.5 × 1.5 deg	Served to trigger DAS into initiating television picture recording mode, serving as a backup to TV.	1 sensor  (No output data)	

Since the nominal lifetime of the mission was approximately 6000 h, all science equipment underwent hundreds of hours of pre-launch testing (Ref. 3). This testing included an electronic-component-part screening program for each instrument and ancillary. This program assured that every part installed in each instrument was tested well beyond the normal failure region, prevented catastrophic in-flight failures, and reduced costly delays resulting from failures during the instrument and spacecraft test phases. The screening program was also designed to reveal parts or processes inadequacies that otherwise would not be immediately apparent.

## B. Data Automation Subsystem

The data automation subsystem was the nerve center of the science subsystem. It had to supply the synchronizing, controlling, sampling, formatting, converting, buffering, and encoding of data from the science instruments or their ancillaries. In addition, it provided a central terminal for the issuance and receipt of commands to or from other spacecraft subsystems.

The DAS was divided into two functionally and physically separate units: the real-time DAS and the non-real-time DAS. The entire DAS subsystem (Fig. II-2) consisted of:

- (1) The RT DAS, packaged in two  $1\frac{1}{2} \times 6 \times 7$ -in. chassis.
- (2) The NRT DAS, packaged in one  $2 \times 6 \times 7$ -in. chassis.
- (3) Two identical 1320-bit core buffer memories, which are used in conjunction with the NRT DAS and are housed in one  $1 \times 6 \times 6$ -in. chassis.
- (4) Two electrically separate ac-to-dc power converters (one for the RT DAS and one for the buffers and NRT DAS) both of which are packaged in one  $1\frac{1}{2} \times 6 \times 6$ -in. chassis.

**1. Functional description of real-time DAS.** A functional block diagram of the RT DAS is shown in Fig. II-3. Its primary purpose was to gather data samples from the science instruments and to arrange them in a format suitable for real-time transmission by the telemetry link. The RT DAS performed the basic functions of analog-to-digital conversion, pulse-rate conversions, event timing, and digital data transfers.

The real-time DAS had three basic modes of operation: cruise, cruise-calibrate, and encounter. During the cruise mode of operation, the real-time DAS shared the telemetry channel, and was synchronized with the engineering data by a science gate signal from the data encoder at the start of each data frame. In this mode, 280 bits out of the 420-bit RT DAS frame were used by the data encoder for science. The remaining 140 bits were commutated by the data encoder through 100 engineering measurements.

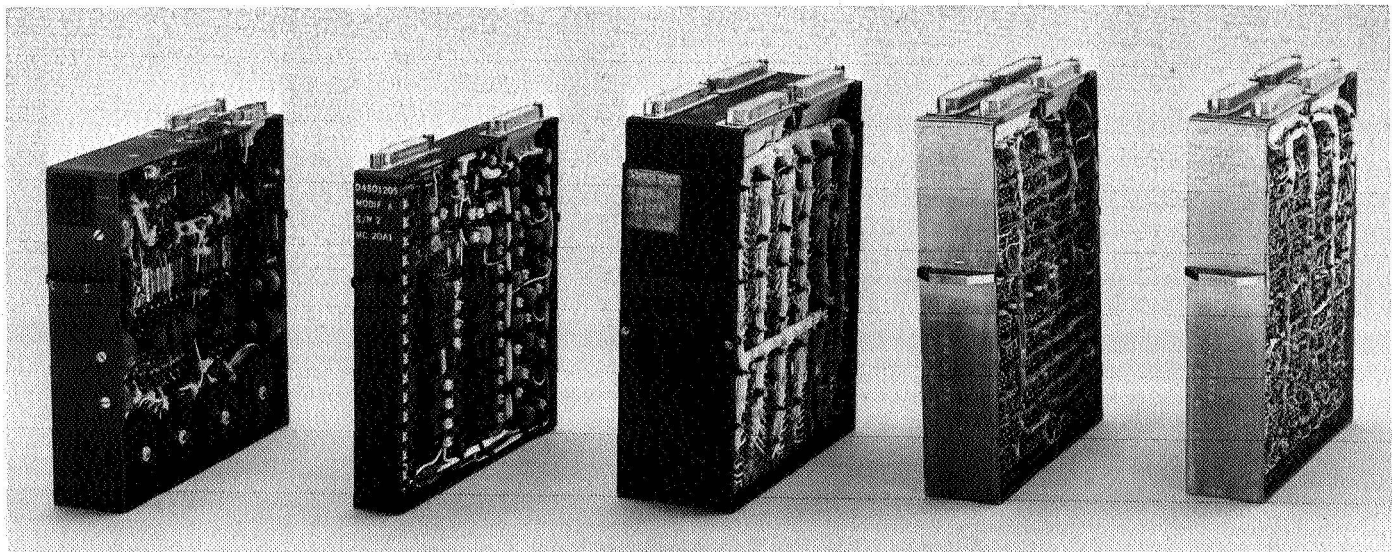


Fig. II-2. Data automation subsystem subassemblies

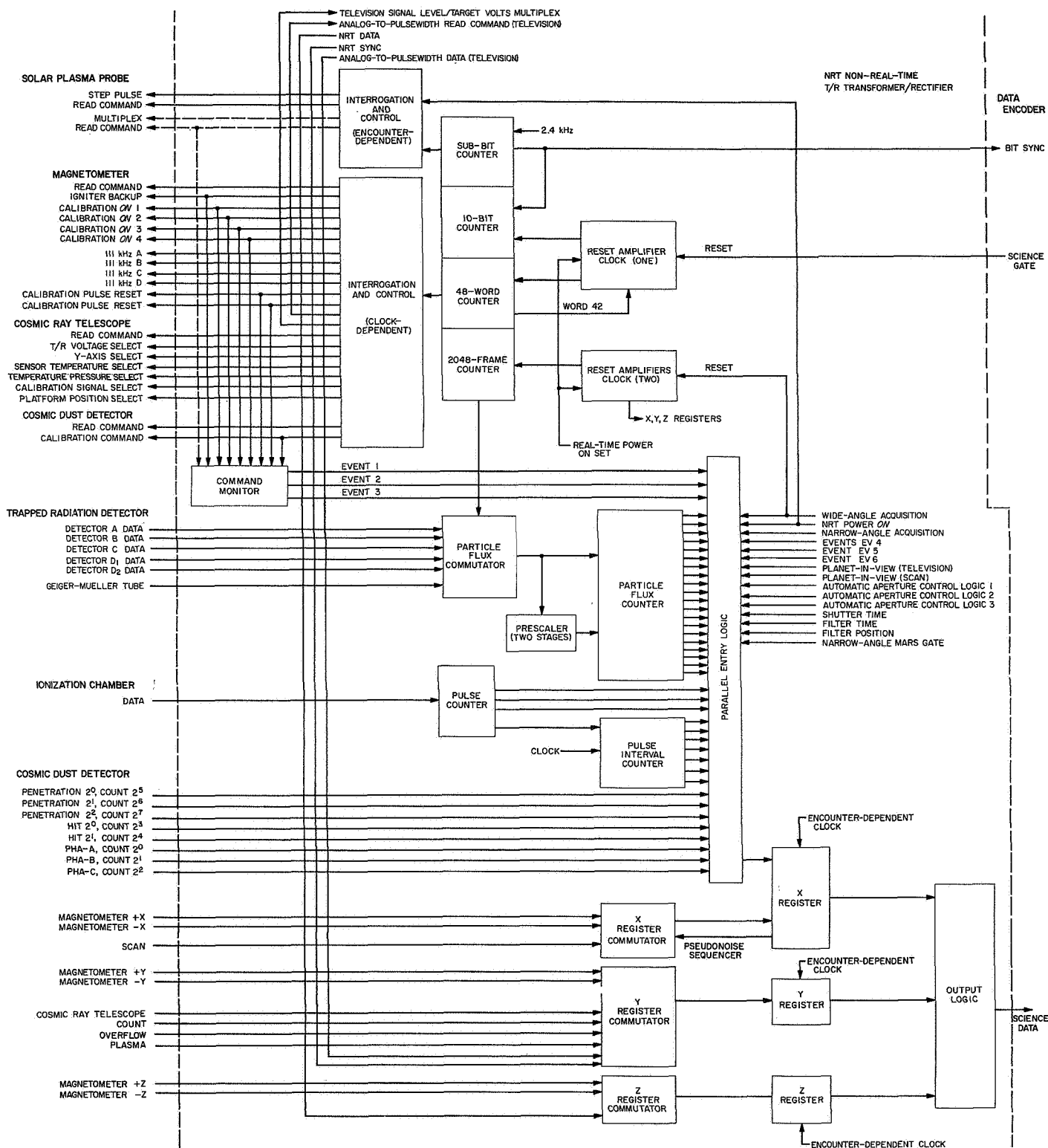


Fig. II-3. Real-time DAS functional block diagram

The calibrate mode exercised the inflight calibration circuits in some of the instruments. This mode was activated at 7.17- or 28.67-h intervals, depending upon the spacecraft bit rate. The format did not change during this mode of operation. The cosmic ray telescope calibrate mode consisted of a 128-frame sequence. During the 24-frame magnetometer calibrate mode, a sequence of four commands was generated by the RT DAS. A single start command was used to calibrate the cosmic dust detector.

The encounter mode, enabled through the initiation of Data Mode 3, added the 140 bits normally used by the data encoder from engineering measurements to the RT DAS output.

*a. Format.* The data format of the real-time system is shown in Fig. II-4. Although the science data words were of various fixed lengths (from 1 to 20 bits), the DAS word length was 10 bits. There were 28 words (280 bits) in the Data Mode 2 (cruise) format and 42 words in the Data Mode 3 (encounter) format of which 10 were encounter-oriented. The RT DAS was mechanized in such a fashion that it always operated as though it were in Data Mode 3. Dormant encounter instruments were sampled through Data Mode 2 even though the telemetry data encoder did not accept these 14 words. In this manner, the DAS format was not changed for Data Mode 3; it was merely expanded by appending the 14 encounter-oriented words. During Data Mode 2, the DAS format contained 39 measurements; in Data Mode 3, 61 measurements were made.

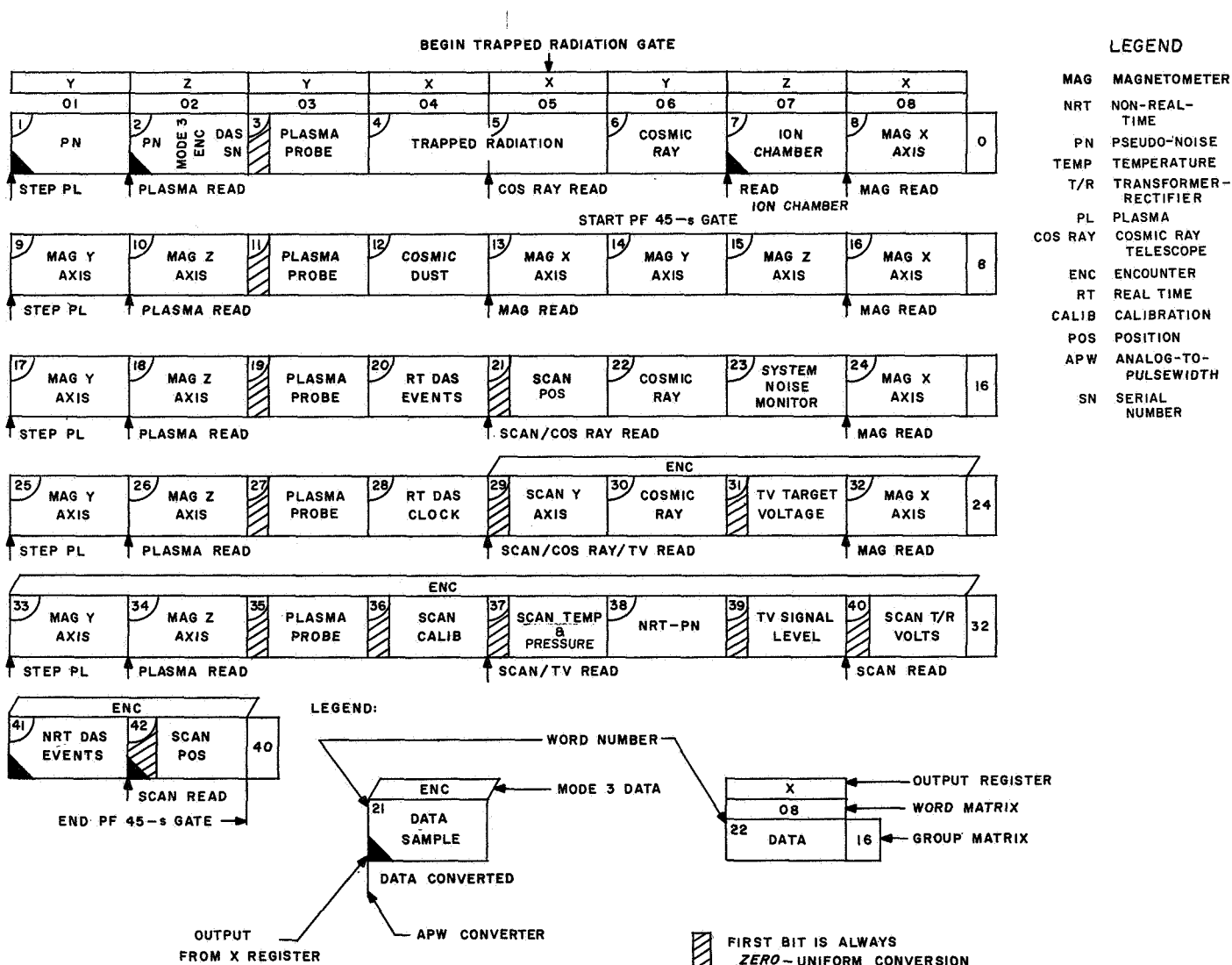


Fig. II-4. RT DAS word format

The RT DAS contained three output-counter shift registers (X, Y, and Z). These registers and their operation during each data frame are shown at the top of the data-word column of Fig. II-4. They enabled the DAS to make analog conversions of the three axes in the magnetometer simultaneously, thereby eliminating the correlation ambiguities inherent in making successive samples of the three axes.

Since the RT DAS was synchronized to the telemetry bit rate, a change in the bit rate only compressed or expanded the time scale of the DAS format. Every word and bit that could otherwise be spared was used (as indicated in Table II-2) to give as much information about the status of the science subsystem as possible. Each frame of RT science data contained approximately 42 bits that were known or were predictable *a priori* in Data Mode 2; an additional 27 bits were added in Data Mode 3. The known bits include:

- (1) 15 bits of pseudo-noise sequence for the identification of science data.
- (2) 3 bits of DAS serial number to preclude any ambiguity if more than one spacecraft is being tracked, and to furnish each system with a distinguishable mark for the purpose of test history.
- (3) 11 bits of frame number to identify each frame uniquely for recurring periods of  $28\frac{2}{3}$  h.
- (4) 13 sign bits that are always *zero* because of unipolar analog conversions.
- (5) 43 bits for continually monitoring the internal status of DAS functions and events, and for measuring predictable events in science instruments.

*b. Data handling.* The data handling accomplished by the RT DAS consisted of complementary count conversions, interval and pulse counting, parallel data acquisition, and analog-to-digital conversions.

*Complementary count.* In an instrument containing its own count accumulator (the cosmic ray telescope), the complement of the binary number in the accumulator was read out by the DAS. This readout was done in a manner similar to the way the DAS handles analog signals through the analog-to-pulse-width converters. The DAS sent a burst of 111-kHz pulses to the instrument for a maximum interval of 11.5 ms. These pulses entered the instrument count accumulator in parallel with the data input and were simultaneously counted by the DAS. When the counter in the instrument overflowed, an

inhibit signal was sent to the DAS; the DAS, in turn, stopped counting and sending pulses to the instrument. The binary number in the DAS register was *one* plus the *one's* complement of the original number in the instrument accumulator.

*Count rates.* If an instrument having one or more random count-rate outputs did not have its own count accumulators, this function was performed by the DAS. There were six such inputs to the *Mariner IV* DAS. These count-rate inputs from the energetic particle detectors were commutated so that four inputs were read once every eight frames and two inputs were read once every four frames. The inputs were sampled for approximately 45 s at  $8\frac{1}{3}$  bits/s, and for one-fourth of this period at the  $33\frac{1}{3}$ -bits/s telemetry rate. A single, 20-stage counter was available for these inputs. When a *one* appeared in the twentieth stage, two stages of prescaling were added to the count; however, these stages were not read out since their use was indicated by the twentieth bit. Twenty bits were read out each frame for the count-rate data inputs.

*Interval and pulse counting.* The ionization chamber data were encoded in a different manner from the data of any other instrument; the ionization chamber pulses were counted continuously by the DAS and were encoded in two different ways. At a fixed point in each frame, the 10-stage ion-pulse interval counter was reset and six stages of the counter began counting pulses having a 1.2-s period (at the  $33\frac{1}{3}$ -bits/s telemetry rate, the time interval was 0.3 s). When the first ion pulse occurred, it inhibited the 6-bit time count for the remainder of that frame; it was also counted in a three-stage counter, thereby giving the time from the last reset to the first pulse and the total number of pulses in that frame. When 7 pulses were received in one frame, the 6-bit time portion of the register was reset to zero. When 8 pulses were received, the tenth stage was set to indicate that the remaining 9 bits then represented a straight binary count of accumulated pulses; the tenth stage remained a *one* for the remainder of the frame. The register overflowed after the receipt of 511 pulses.

*Parallel data.* When it was not required that registers in an instrument be cleared upon readout, or when only a few bits were to be read, the DAS performed a parallel bit transfer. This transfer was done for the cosmic dust detector and the television subsystems. The cosmic dust detector had two 8-bit registers that were sampled during alternate frames. The TV subsystem had 5 bits of

Table II-2. RT DAS words and events

Word No.	Bits	Events	Word No.	Bits	Events
1	1-10	PN (pseudo-noise) sequence	23	1-10	Readout of Z register is normally zero, but will indicate presence of noise
2	1-5	PN sequence	24	1-10	Same as Word 8, except conversion time is during Word 24
	6 <sup>a</sup>	Wide-angle acquisition	25	1-10	Same as Word 9, except conversion time is during Word 24
	7 <sup>a</sup>	Narrow-angle acquisition	26	1-10	Same as Word 10, except conversion time is during Word 24
	8-10	DAS serial number readout	27	1-10	Same as Word 3, except conversion time is during Word 26
3	1-10	Plasma probe data (bit 1 = 0)	28	1-10	Readout of RT DAS clock (C11-C20)
4, 5	1-20	TRD count rate	29	1-10	Unipolar A/D conversion on scan Y-axis signal
6	1-10	10-bit complement of content of a 10-bit register in the CRT experiment	30	1-10	Same as Word 6, except conversion time is during Word 29
7	1-10	Ion chamber data readout	31	1-10	Unipolar A/D conversion on TV target voltage signal
8	1-10	Bipolar A/D conversion of magnetometer X-axis data	32	1-10	Same as Word 8, except conversion time is during Word 32
9	1-10	Bipolar A/D conversion of magnetometer Y-axis data	33	1-10	Same as Word 9, except conversion time is during Word 32
10	1-10	Bipolar A/D conversion of magnetometer Z-axis data	34	1-10	Same as Word 10, except conversion time is during Word 32
11	1-10	Same as Word 3, except that conversion time is during Word 10	35	1-10	Same as Word 11, except conversion time is during Word 34
12	1-8	Readout of 8 cosmic dust outputs	36	1-10	Unipolar A/D conversion on scan calibrate signal
	9	Readout of calibrate control CC, in RT DAS	37	1-10	Even subframes: unipolar A/D conversion on scan temperature signal; Odd subframes: unipolar A/D conversion on scan bearing pressure signal
	10	Readout of last stage of calibrate counter	38	1-10	10-bit sample of NRT output data to tape machine
13	1-10	Same as Word 8, except conversion time is during Word 13	39	1-10	Unipolar A/D conversion on TV signal level signal
14	1-10	Same as Word 9, except conversion time is during Word 13	40	1-10	Unipolar A/D conversion of the scan transformer-rectifier voltage
15	1-10	Same as Word 10, except conversion time is during Word 13	41	1	TV shutter time
16	1-10	Same as Word 8, except that conversion time is during Word 16	2		TV AAC (automatic aperture control) 3
17	1-10	Same as Word 9, except that conversion time is during Word 16	3		TV AAC 2
18	1-10	Same as Word 10, except that conversion time is during Word 16	4		TV AAC 1
19	1-10	Same as Word 3, except that conversion time is during Word 18	5		TV planet in view <sup>b</sup>
20	1-4	Magnetometer calibrate signals readout numbers 4, 3, 2, and 1, respectively	6		TV filter position
	5 <sup>a, b</sup>	NAMG readout	7		Inhibit scan <sup>b</sup>
	6 <sup>a, b</sup>	Scan planet in view readout	8		Shutter/end of loop
	7	NRT power on readout	9		Start-stop tape
	8	CRT calibrate readout	10		CDD readout (same as bit 10 of Word 20 during NRT power off)
	9	CDD calibrate/magnetometer ignition readout	42	1-10	Same as Word 21, except conversion time is during Word 42
	10	CDD readout			
21	1-10	Unipolar A/D conversion of scan platform position signal			
22	1-10	Same as Word 6			

<sup>a</sup>Always "1" if NRT power is off.  
<sup>b</sup>Indicates that "0" equals occurrence of event.

status information (shutter time, filter position, planet-in-view, and automatic aperture control 1, 2, and 3) which was read once each frame during Data Mode 3.

*Analog-to-digital conversions.* The use of an analog-to-pulse-width converter can improve analog-to-digital conversions in systems in which physical separation of the analog source and the digital converter is a necessity. In such systems, the transmission of analog signals from one part of the system to the other may result in errors in measurement due to noise interference.

When a measurement was made, a read command was initiated by the DAS and sent to the instrument. An analog-voltage-to-pulse-width converter in the instrument generated a rectangle whose length was proportional to the magnitude of the voltage being measured. The trailing edge of the rectangle was shaped and sent to the DAS.

Coincident with the generation of the read command, a gate was opened allowing a known clock frequency to be counted in a DAS register. When the delayed signal was returned by the instrument, the gate was closed and the state of the counter represented the analog voltage.

**2. Functional description of NRT DAS.** The primary functions performed by the NRT DAS (Fig. II-5) were:

- (1) Provide logical control of the encounter sequence.
- (2) Control the television and video storage subsystem operation during encounter.
- (3) Format, identify, and buffer the television data before transferring it to the video storage subsystem.
- (4) Provide logical control of real-time data transferred from the RT DAS to the tape recorder.

The NRT DAS had three basic operational modes: reset, cycle, and record.

*a. Reset mode.* The reset mode, although listed among the operating modes, represented an essentially nonoperative condition of the NRT DAS. The reset mode was in effect until the dc supply voltages stabilized at their proper levels after the application of 2.4-kHz power to the power supply unit. The 2.4-kHz power was switched to the DAS by the CC&S or by ground command. During the application of power, critical control functions had to be maintained in an *off* condition.

*b. Cycle mode.* During the cycle mode, which became effective when dc voltages were developed, the NRT system performed all of its normal data sampling functions. The TV pictures were commanded and data samples were taken and stored in the core buffers. During this time, however, tape start commands were not generated, and data were not recorded on magnetic tape.

The cycle mode was a system requirement, since the television subsystem required certain control signals from the DAS to synchronize its logic. The scan subsystem detected the planet during the cycle mode and produced the wide-angle acquisition signal. The wide-angle acquisition signal was routed to the data encoder and to the RT DAS to initiate Data Mode 3. The NRT system re-entered the cycle mode at the end of the record mode and remained in this condition until power was removed from the system.

*c. Record mode.* The record mode was enabled when the planet came into the field-of-view of either the TV vidicon or the narrow-angle Mars sensor. The record mode could also be enabled by ground command DC-16. During the record mode, data were acquired as shown in Fig. II-6, which is a gross timing diagram of the NRT encounter data frame. During the 144-s encounter data frame, two TV pictures were taken and recorded during subframes zero and two. A TV picture contained a  $200 \times 200$  element matrix of discrete points, and 24.12 s were required to read, identify, and record the data. An additional TV picture, indicated by the dotted line, was shuttered but not recorded. The phase of the sub-frame counter, which was cycling continuously during the cycle mode, was an additional condition for the entry of the system into the record mode. The record mode, therefore, was entered in such a way that only complete encounter data frames were recorded on tape.

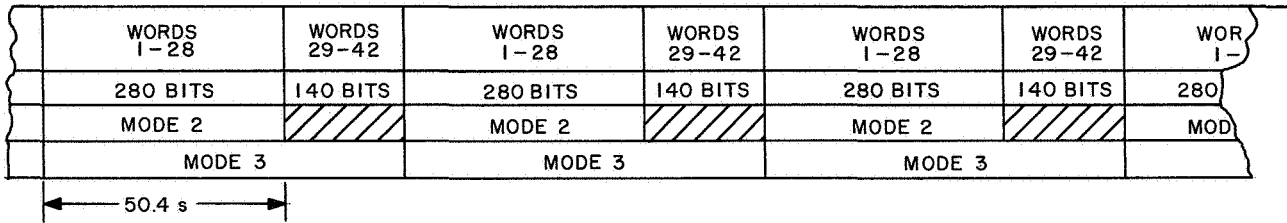
An encounter data frame produced 401 data blocks of approximately 1280 bits (one line) each. The number of spare bits in each data block was a function of the stability of the 10.7-kHz oscillator. During subframes zero and two, the TV and real-time data were multiplexed between the two buffers. One block of data was generated every 120 ms (the TV line rate and the encounter real-time telemetry rate).

The NRT system was capable of handling 1200 bits of TV information, and of making one analog-to-digital conversion of 10 bits and a number of parallel digital transfers in the 120-ms line interval.

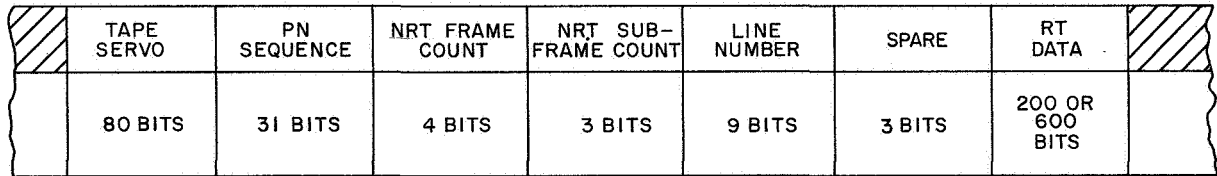




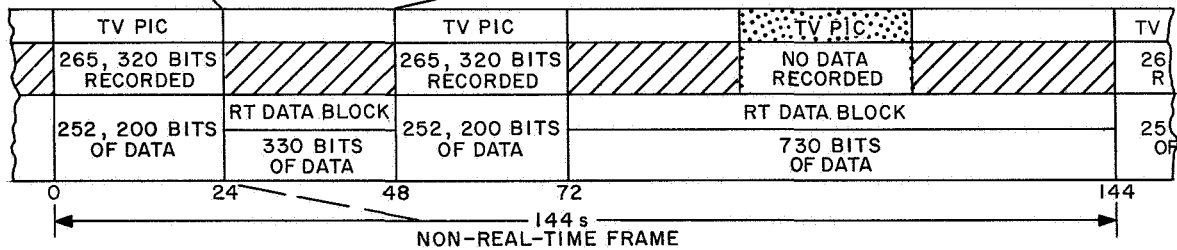
# REAL-TIME DATA FRAME



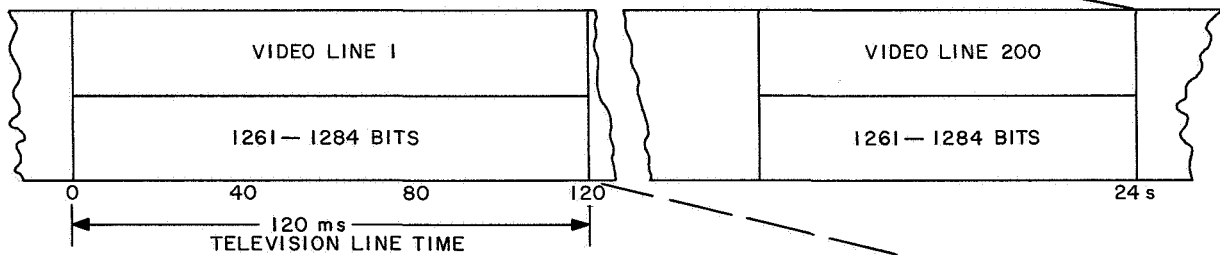
## REAL-TIME (RT) DATA ACCUMULATED IN BUFFERS DURING PICTURE SEQUENCE



## NON-REAL-TIME (NRT) DATA FRAME



## TELEVISION DATA BLOCK



## TELEVISION LINE FORMAT

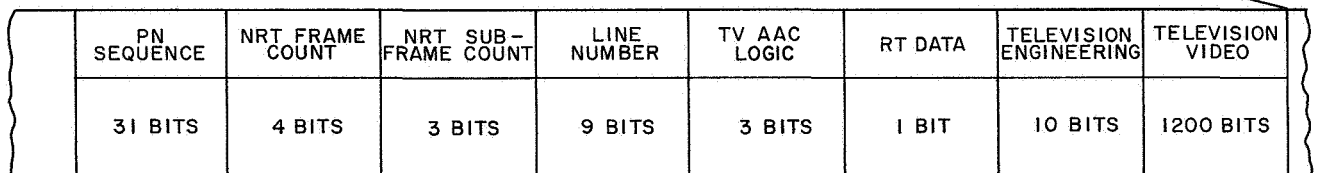


Fig. II-6. NRT DAS word format

The record mode is terminated when the second end-of-tape loop signal occurs in the tape recorder. A backup signal from the DAS can also terminate the record mode when 22 TV pictures have been commanded.

**3. Physical description.** The flight configuration of the DAS (excepting the interconnect harness) is shown in Fig. II-2. The system was composed of these five subassemblies plus nine ancillary analog-to-pulse-width converters, which were located in the science instruments.

Subassembly 20A1, the NRT DAS buffers, contained two physically and electrically identical 1320-bit-serial, sequentially-addressed core memories or buffers. The average weight of these subassemblies was 1.25 lb.

The non-real-time subsystem was packaged on one subassembly, which contained 52 welded cordwood modules and weighed approximately 3.25 lb.

The real-time subsystem was packaged in two subassemblies, and was composed of 86 pellet-component modules, 11 transformer modules, and 1 crystal module. The two subassemblies weighed approximately 2.8 lb and 2.6 lb each.

One subassembly contained two independent power supplies: one for the NRT DAS subassembly and buffers, and one for the two RT DAS subassemblies. The complete power supply weighed 2 lb. When energized, the NRT DAS drew 5.6 W of 2.4-kHz, 50-V-rms power. The RT DAS used 6.5 W of 2.4-kHz, 50-V-rms power. The DAS contained 11,130 components, including 961 transistors, 3520 diodes, and 2640 cores (for the buffer storage).

**4. Design evolution.** The initial design envisioned a science subsystem that relied upon synchronization and interrogation signals from the data encoder, and upon switching and control functions from the central computer and sequencer. The data conditioning required for each instrument was to be accomplished in the instrument.

It soon became apparent that the functions necessary to properly operate the science instruments could not be supplied from either the data encoder or the central computer and sequencer. In addition, it was decided that the handling of the digital output of the TV data would be done by a science data automation subsystem, but that the video data would be digitized within the TV subsystem.

As the number of instruments increased from five to nine, the complexity of the DAS increased from simple data conditioning to that of data sequencing, buffering, converting, and controlling. With a growth in the requirements placed upon it by the instruments and the spacecraft, the DAS design had to be modified in the following manner:

- (1) The tape recorder was made into a separate subsystem (video storage subsystem).
- (2) The DAS was split into two separate sections:  
(a) the NRT DAS, comprising the control logic for the encounter instruments and the buffers; and  
(b) the RT DAS, comprising the real-time control logic.
- (3) The power supply was split into two completely separate parts, one for the RT DAS and one for the NRT DAS. The NRT DAS power supply was energized only during the period that the encounter instruments were operating.
- (4) The DAS format was changed to incorporate new instruments, which necessitated changes in both the design and the interfaces of the DAS.

In March 1963, a NASA Headquarters review resulted in another modification to the science subsystem; some instruments were removed and new ones were added. These changes forced another redesign of the RT DAS, which occurred after the DAS design was to have been frozen; as a result, the actual design freeze could not be made until May 15, 1963.

After the first PTM spacecraft system test, a number of modifications were made to the DAS to enhance the performance of the science subsystem and the spacecraft. These were:

- (1) Isolation of bit synchronization between RT and NRT DAS to prevent one from interfering with the other.
- (2) Increase of DAS output pulse margins to the instruments.
- (3) Modification of event registers to use NRT power-on as the set function.
- (4) Improvement of narrow-angle-acquisition interface isolation with the RT DAS, through the use of an isolation amplifier, to prevent a false indication of planet acquisition.

- (5) Modification of the logic to prevent spurious pulse output at NRT power-on and power-off.
- (6) Modification of NAMG interface circuits to prevent shorted or open connections between the NAMG and the DAS from causing false planet acquisition.
- (7) Reduction of high-speed flip-flop loading.
- (8) Increase of high-speed flip-flop margins.
- (9) Elimination of four high-speed flip-flops.
- (10) Modification of the output of the DAS to be "data" instead of "not data."
- (11) Decrease of capacitive loading and isolation of some RT DAS functions from those in the NRT DAS.
- (12) Addition of event register outputs to the OSE.
- (13) A decision to revert the NRT DAS to welded cordwood construction rather than pellet construction.

The removal of the ultraviolet photometer in July 1964 resulted in elimination of the encounter-dependent function of the RT DAS format. This removal was accomplished by shifting a few wires in the gating circuits, and was considered to be only a minor change.

## References

1. *Mariner Mars 1964 Project Report: Television Experiment*, Technical Report 32-884. Jet Propulsion Laboratory, Pasadena, Calif., Dec. 15, 1967.
2. *Mariner Mars 1964 Project Report: Mission and Spacecraft Development*, Technical Report 32-740. Jet Propulsion Laboratory, Pasadena, Calif., Mar. 1, 1965.
3. Schutz, F. L., et al., *Mariner-Mars Science Subsystem*, Technical Report 32-813. Jet Propulsion Laboratory, Pasadena, Calif., Aug. 15, 1966.

### III. Trapped Radiation Detector

#### A. Introduction

The trapped radiation detector (TRD) experiment was developed at SUI, with James A. Van Allen as principal investigator, and L. A. Frank and S. M. Krimigis as co-investigators. The experiment consisted of an array of particle detectors designed to search for and measure any belts of trapped radiation possessed by Mars and to measure interplanetary cosmic rays while en route to Mars. These measurements included flux, energy, directional characteristics, and identity of the particles.

Data obtained during the approach and encounter with Mars contrast sharply with those obtained in the vicinity of the earth just after launch. The same sensitive particle detectors, which were able to indicate the presence of electrons of energy less than 40 keV out to a radial distance of 165,000 km in the morning fringe of the earth's magnetosphere, failed to detect any such electrons during the close encounter with Mars at the time when the minimum areocentric (with Mars as center) radial distance was 13,200 km. This result indicates that the ratio of the magnetic dipole moment of Mars and the earth  $M_m/M_e$  is surely less than  $10^{-3}$  and probably less

than  $5 \times 10^{-4}$ . Corresponding upper limits on the equatorial magnetic field at the surface of Mars are 200 and 100  $\gamma$ , respectively, as contrasted with a field of about 50,000  $\gamma$  at the earth surface. On the basis of this finding, it appears possible that the solar wind interacts directly with the Martian atmosphere.

Since reestablishment of intermittent telemetry contact with *Mariner IV* on May 3, 1966 with the JPL/NASA Goldstone 210-ft facility, it has been found that the SUI experiment is continuing to operate properly up to and including the latest available data of Jan. 15, 1967, after over 25½ mo. of interplanetary flight. Despite the inevitably high bit-error rate in the telecommunications link, the experimenters have succeeded in obtaining valid data on a series of solar cosmic ray events which have also been observed by satellite near the earth. The combination of these two bodies of simultaneous data at such widely different regions of the solar system is unique in the history of space experimentation. The implications of these results on the mechanism of the diffusion of solar cosmic rays in the interplanetary medium are under study.

## B. Purpose

The TRD experiment was of interest in connection with several scientific problems, including:

- (1) The magnitude and orientation of the magnetic moment of Mars.
- (2) The radial extent of the atmosphere of Mars.
- (3) Delineation of the possibilities for aurorae and magnetic storms on Mars.
- (4) The interaction of the solar plasma with the magnetosphere, if any, on Mars.
- (5) The relationship between solar phenomena and the emission of energetic particles.
- (6) The propagation of charged particles in interplanetary space.
- (7) The relationship of the occurrence of energetic particles in interplanetary space to solar and geophysical effects.

The data from a previous, similar but simpler, experiment flown on *Mariner II* revealed the presence of many significant increases in the counting rates of Geiger-Mueller tubes which were interpreted on the detection of beams of low energy protons and electrons from the sun. The unit used for *Mariner IV* permitted the separation of protons from electrons. If similar events occurred during the flight of *Mariner IV*, it could prove possible to determine the identity of the particles causing the increases in counting rate. The identification capability was also of direct interest in connection with the belts of trapped radiation, if any, surrounding Mars. The Van Allen belts around the earth are observed to consist of complex distributions of protons and electrons. This differentiation into particle types becomes more difficult at low energies. The presence of such a differentiation around Mars could suggest conclusions concerning the nature of the processes by which particles are trapped into the planetary magnetic field.

The purpose of the TRD was to search for magnetically trapped charged particles in the vicinity of Mars. If any were found, the experiment would make a preliminary determination of their distribution in space, their energy spectra, and their identities. The experiment was also designed to monitor the occurrence of solar cosmic rays and energetic electrons in interplanetary space. The unit allowed their angular distributions, energy spectra, and time histories to be studied.

## C. Instrument

The TRD comprised three end-window (Fig. III-1) Geiger-Mueller detectors, designated A, B, and C; and, one 35- $\mu$  surface-barrier solid-state detector having two discrimination levels, designated  $D_1$  and  $D_2$ . Each of the four detectors has a conical collimator with a full vertex

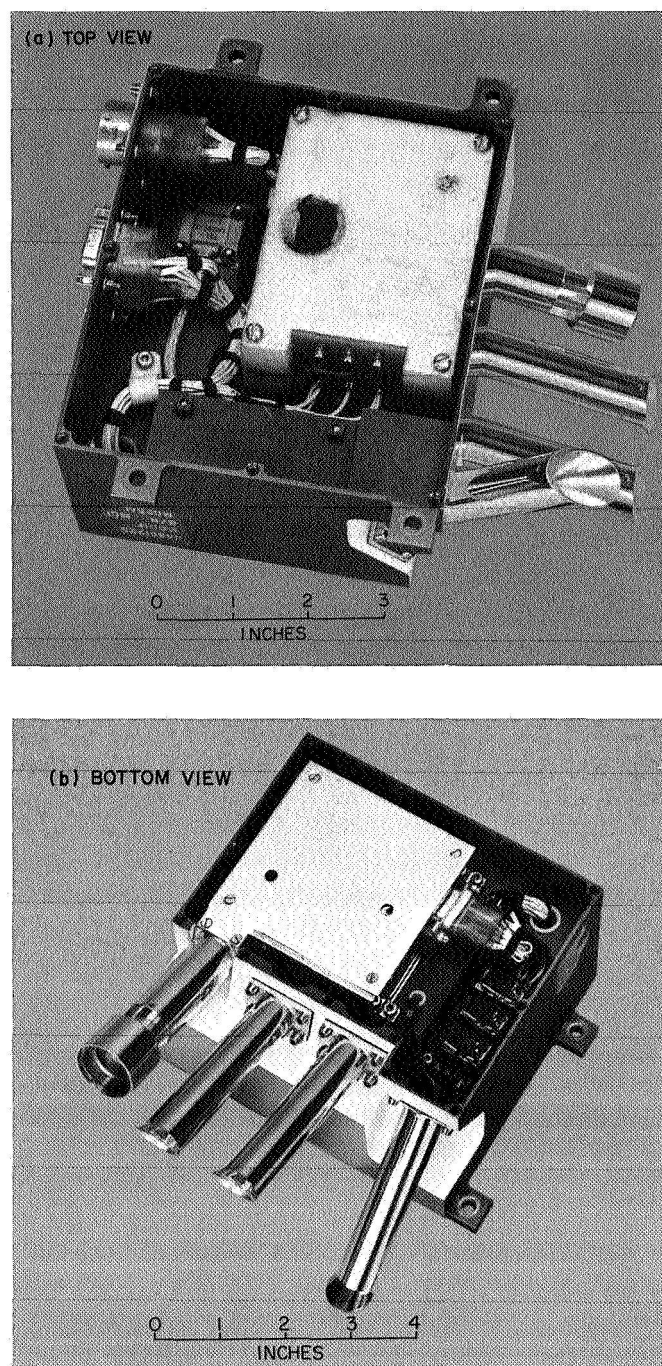


Fig. III-1. TRD, top and bottom views

angle of 60 deg (nominal). The axis of the collimators of B, C, and D were parallel to each other and at an angle of 70 deg to the roll axis of the spacecraft. The axis of the collimator of A was at an angle of 135 deg. The roll axis of the spacecraft was directed continuously at the sun with an error of less than 1 deg. Rotation of the spacecraft about this axis was controlled in such a way as to point the axis of a spacecraft-fixed, directional antenna approximately toward the earth. Thus, detectors B, C, and D received particles moving generally outward from the sun and at angles to the sun-to-probe vector of  $70 \pm 30$  deg. The detectors themselves and the complete inner walls of their collimators were shielded from the direct light and X rays of the sun. Detector A received particles moving generally inward toward the sun at angles to the sun-probe vector of  $135 \pm 30$  deg.

The sidewall shielding of all detectors had a minimum thickness corresponding to the range of  $\sim 50$ -MeV protons. Both discrimination levels of the solid-state detector,  $D_1$  and  $D_2$ , were insensitive to electrons of any energy in the intensities found in the current series of experiments. This insensitivity was designed into the system (thin detector, high-bias level, and 200-ns delay-line pulse-clipping) and was demonstrated through thorough preflight testing. It was further confirmed during traversal of the magnetosphere in the early phase of the

flight of *Mariner IV*. Detector channels  $D_1$  and  $D_2$  were also insensitive to galactic cosmic rays. In order to have direct observational knowledge of the proper operation of these channels during interplanetary flight, the solid-state detector was equipped with an  $^{95}\text{Am}^{241}$  source of  $\sim 5.5$ -MeV  $\alpha$  particles which provided in-flight counting rates of 0.071 and 0.059/s on  $D_1$  and  $D_2$ , respectively—rates which are accurately identical to their prelaunch values.

The counting rate of each of the three Geiger-Mueller tubes was the sum of the rates due to galactic cosmic rays (about 0.6 counts/s); to electrons, X rays, protons, alpha particles, etc., which passed through their collimators; and, in some cases, to sidewall penetrations. Table III-1 lists details concerning the characteristics of the detectors.

The instrument weighed approximately 2.6 lb and occupied a volume of 82.5 in.<sup>3</sup>. The 630 mW of 2.4-kHz square-wave power was converted to the necessary 500, 75, and 8 Vdc to supply the components.

**1. Electronics.** The output pulses from each of the Geiger-Mueller counters are sent to one of the amplifiers. Each amplifier is a complementary NPN-PNP saturating device which shapes and conditions the pulses

**Table III-1. Characteristics of trapped radiation detectors**

Detector	Output	Geometric factors		Sensitivity to charged particles detected	Angle between each acceptance cone and sun-probe vector, deg	Dynamic range
		Unidirectional, cm <sup>2</sup> sr	Omnidirectional, cm <sup>2</sup>			
6213 G-M counter	A	0.044 ± 0.005	~0.15	Electrons: $E_e \geq 45$ keV Protons: $E_p > 670 \pm 30$ keV	135	From galactic cosmic ray rate of 0.6 counts/s to 10 <sup>7</sup> counts/s
6213 G-M counter	B	0.055 ± 0.005	~0.15	Electrons: $E_e \geq 40$ keV Protons: $E_p > 550 \pm 20$ keV	70	
6213 G-M counter	C	0.050 ± 0.005	~0.15	Electrons: $E_e \geq 150$ keV Protons: $E_p > 3.1$ MeV		
Lower discriminator of pn junction	D <sub>1</sub>	0.065 ± 0.003	—	Electrons: None Protons: $0.50 \leq E_p \leq 11.0$ MeV		From in-flight source rate to 10 <sup>6</sup> counts/s
Upper discriminator of pn junction	D <sub>2</sub>	0.065 ± 0.003	—	Electrons: None Protons: $0.88 \leq E_p \leq 4.0$ MeV		

to meet the requirements of the data automation subsystem (DAS) interface. The amplifiers were designed, fabricated, and tested by the University of Iowa. The overall operation of the detector may be understood by referring to Fig. III-2.

A charged particle entering the solid-state detector will release a number of electrons proportional to the energy of the particle which is lost in the detector. The charge resulting from the released electrons together with the detector capacitance determines the

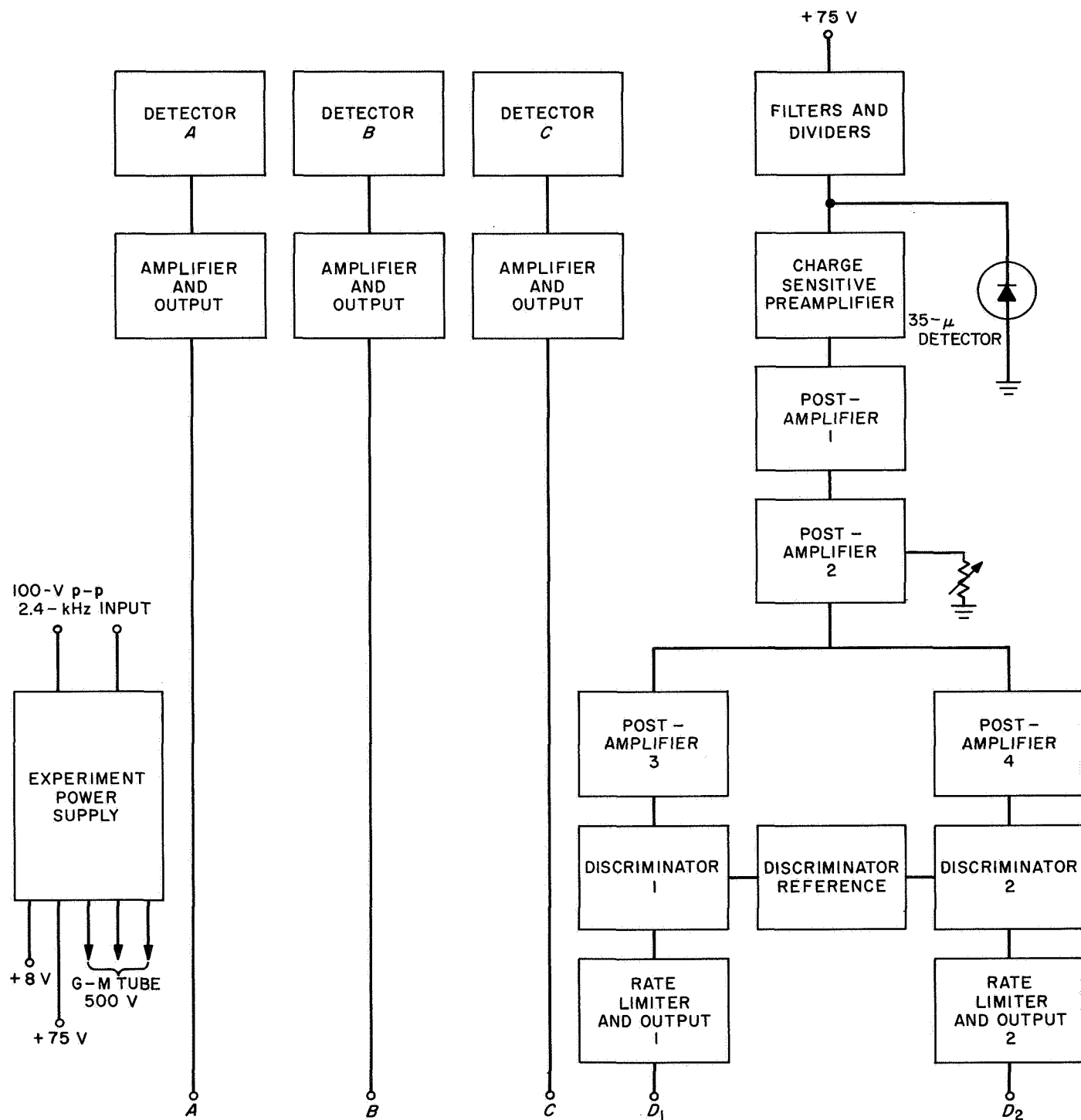


Fig. III-2. TRD, functional block diagram

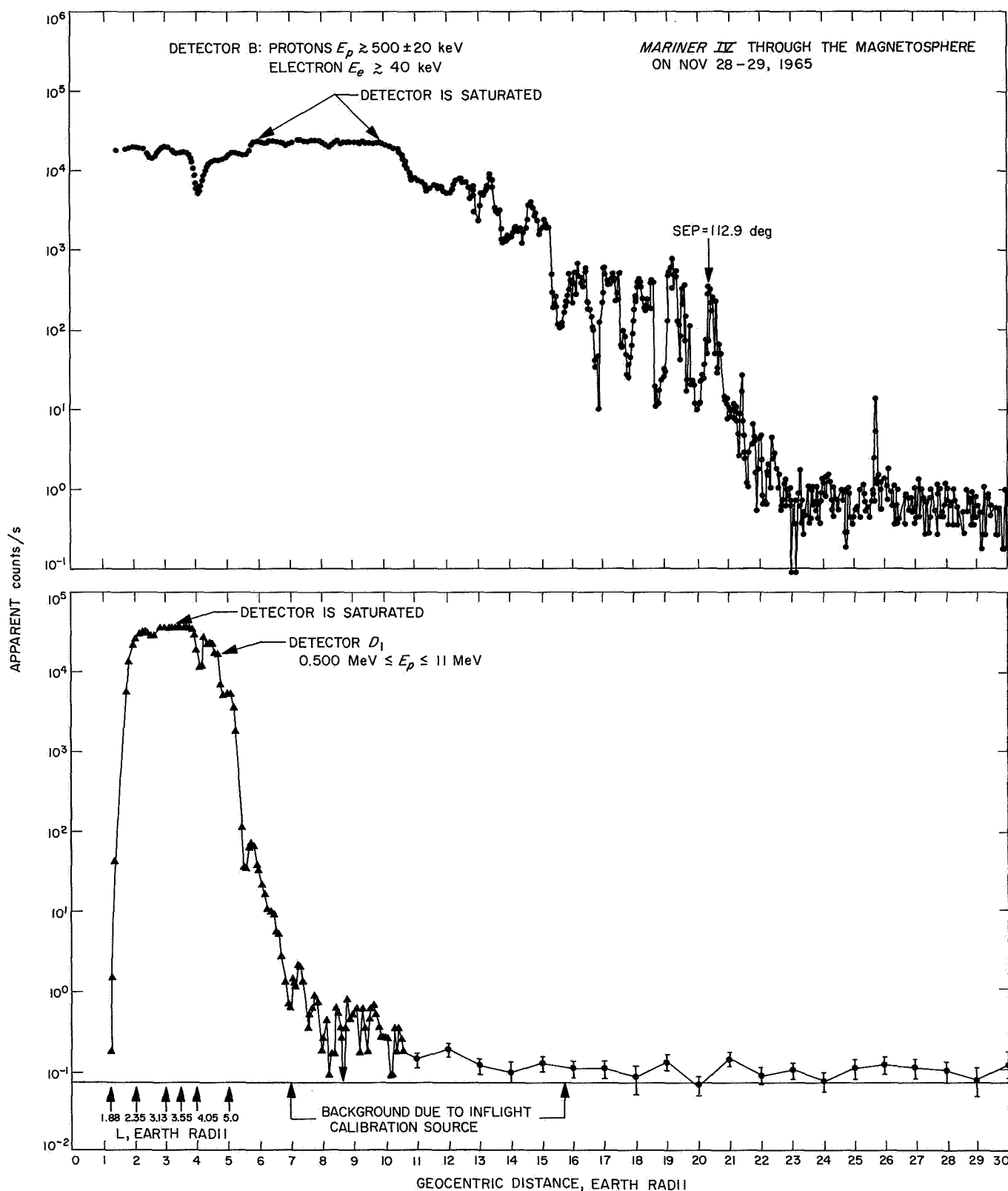


Fig. III-3. Mariner IV through the magnetosphere on Nov. 28-29, 1964



magnitude of the output voltage pulse. The capacitance of a solid-state detector varies when the detector pulse varies; however, charge released by the particle does not change with capacitance. This makes the charge-sensitive amplifier a great deal more desirable than a voltage amplifier.

The post amplifiers of this instrument are highly stable negative-feedback voltage amplifiers. They receive pulses from the preamplifiers, amplify them, and send them to the discriminators. The overall gain of each string of post amplifiers is adjusted so as to give voltage pulses at the discriminators of levels corresponding to the particles detected. The discriminators accept voltages above a preset level ( $>1.4$  V) and reject all pulses under this value. The output and rate limiter circuit is based on a monostable multivibrator. It receives the data from the discriminators and serves to limit the maximum counting rates to 50,000 counts/s. The circuits generate standard pulses to meet the DAS interface requirements.

**2. Detectors.** A striking illustration of the electron insensitivity of the detector (in addition to preflight testing) is shown in Fig. III-3, where detector *B* (looking in the same direction as *D*<sub>1</sub>) has been plotted on the same scale as *D*<sub>1</sub>. It is seen that while *B* is saturated at 10 *R*<sub>e</sub> (earth radii) due to the 40-keV electrons flux, *D*<sub>1</sub> is counting at about 3 times background. The corresponding fluxes of particles seen by *B* and *D*<sub>1</sub> are about  $2 \times 10^7$  (cm<sup>2</sup> s)<sup>-1</sup> and 2 (cm<sup>2</sup> s sr)<sup>-1</sup>, respectively. The electron counting efficiency is therefore  $<10^{-7}$ .

The physical configuration of the detector is such that it has a conical collimator with a full vertex angle of 60 deg. The sidewall shielding of the detector has a minimum thickness corresponding to the range of  $\sim 50$ -MeV protons. In order to shield against sunlight, a nickel foil, whose thickness of 0.22 mg/cm<sup>2</sup> of air equivalent for  $\alpha$  particles, was placed in front of the detector. The effect of the foil is properly taken into account when the discrimination levels are set. Knowledge of the proper operation of the instrument is assured through an inflight <sup>95</sup>Am<sup>241</sup> source of 5.477-MeV  $\alpha$  particles, which was gold-plated in order to obtain a falling spectrum between 500 and 880 keV. Thus, any change in the detector characteristics and/or drift in the discrimination levels would have been immediately noticeable; a preliminary inspection of the data has shown no such change over the 10-mo period of operation of the instrument. Because the thin detector collects only a few tens of keV from a minimum ionizing particle, the con-

tribution of cosmic rays to the background counting rate for particles coming in through the collimator is negligible. The contribution to the background counting rates for particles coming in through the shielding and crossing the detector sideways is about 3 orders of magnitude less than the background counting rate due to the in-flight source.

## D. Results

The outward traversal of the earth magnetosphere by *Mariner IV* provided a basic calibration of the capabilities of the system and the direct foundation for the interpretation of the observations during the Martian encounter. Figure III-4 illustrates the spacecraft trajectory through the magnetosphere. Figure III-5 shows plots of the responses of detectors A, B, and C during the traversal of the morning fringe of the earth's magnetosphere. The sun-earth-probe (SEP) angle at which the spacecraft crossed the magnetospheric boundary (at 23 *R*<sub>e</sub>) was 112.4 deg, on the dawn side of the magnetosphere. After launch, the orbit of the spacecraft rapidly approached the geomagnetic equatorial plane, and beyond  $\sim 3$  *R*<sub>e</sub> stayed continuously on this plane.

The unidirectional geometric factors of detectors A and B are over 20 times as great as those of similar low-energy electron detectors used on *Explorer XIV* (Ref. 1) and *OGO-I* and by Van Allen et al., Ref. 2, in *IMPs 1, 2, and 3*. Their omnidirectional factors are, however, about the same. Hence the detectors on *Mariner*

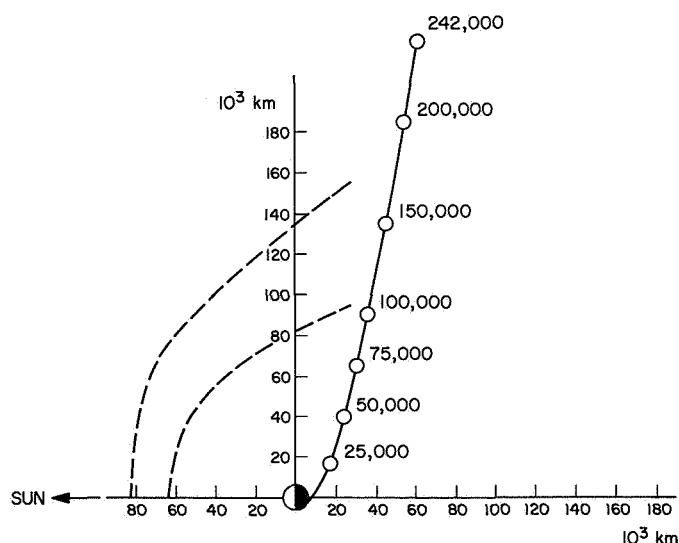
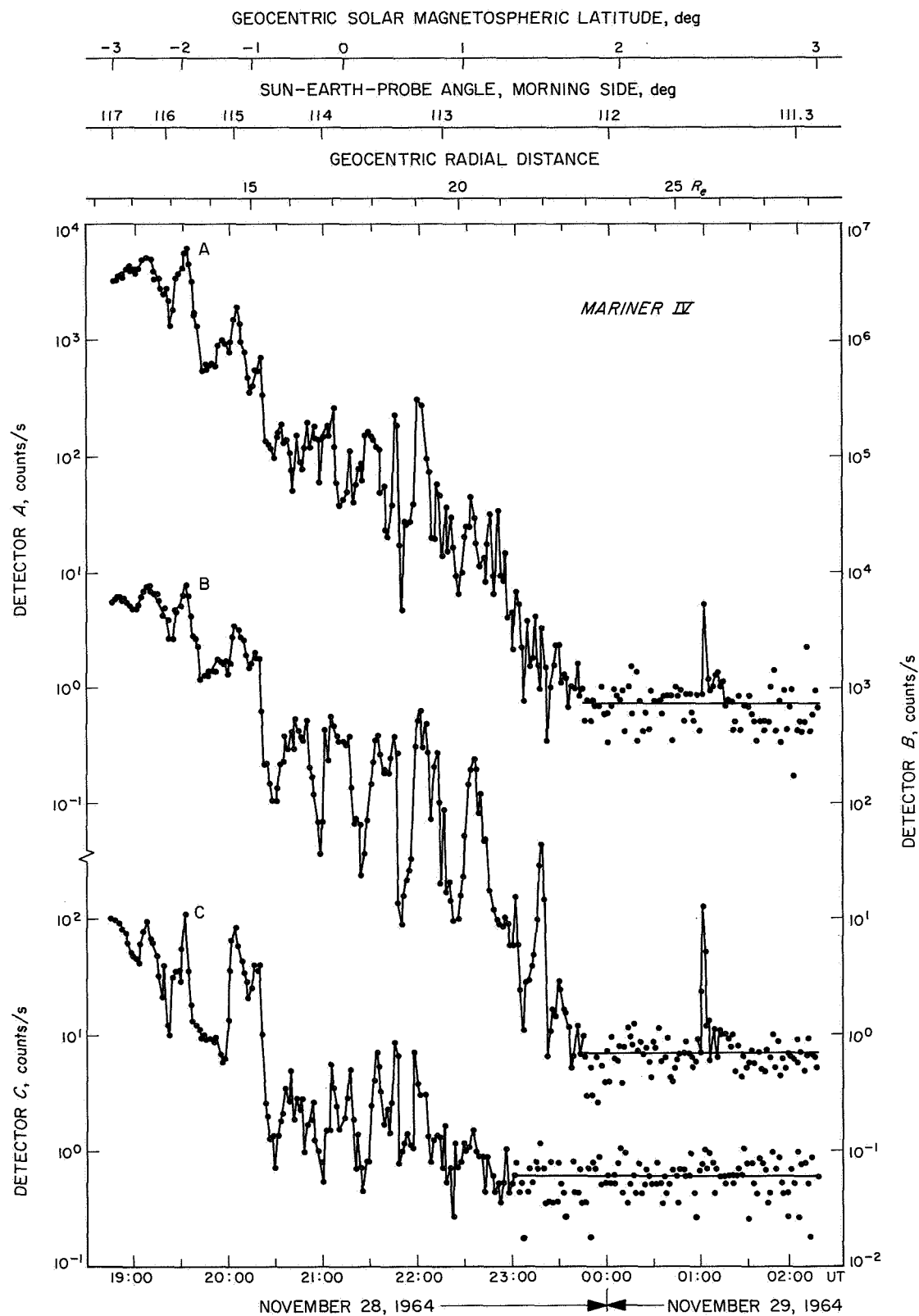


Fig. III-4. *Mariner IV* near-earth trajectory



**Fig. III-5. Counting rates of detectors A, B, and C on Mariner IV during outward traversal of the earth magnetosphere (Nov. 28–29, 1964)**

have a 20-fold increase in signal-to-noise ratio for the detection of electrons having energies of the order of some tens of keV. It is noted that the outermost detectable limit of the earth's magnetosphere (25.7  $R_e$  at SEP of 112 deg) as shown by detectors A and B is nearly the same as that reported by Ness et al., Ref. 3, using a sensitive magnetometer on *IMP-1*.

**1. Absence of 40-keV electrons at 3300 earth radii.** During late Jan. and early Feb., *Mariner IV* drifted westward through the presumed region of an extended magnetospheric tail of the earth at a geocentric radial distance of 3300  $R_e$ . A pair of thin-window Geiger tubes (A and B), with their wide-angle collimators, had shown the presence of electrons  $E_e > 40$  keV out to 23  $R_e$  in the morning fringe of the magnetospheric tail during the early phase of flight; this pair had failed to detect any effects of a magnetospheric tail during 7 days of flight within a geocentric angle between 1 and 5 deg from its presumed center line.

Of the four detectors in the equipment, the low-energy electron detectors A and B are the most sensitive for the detection of a magnetospheric tail. A specific demonstration is provided by the data from *Mariner IV* itself during its outbound traversal of the morning fringe of the magnetosphere on November 28–29, 1964; see Fig. III-5. If electrons in the magnetospheric tail are streaming outward from the earth at angles less than 40 deg or inward at angles greater than 165 deg to the sun-probe line, they will not enter the collimators of A or B. These possibilities constitute a qualification to the failure to observe an effect, but such neat directionality seems quite unlikely, in view of the *roughness* in direction and magnitude of the B vector, as reported by the magnetometer measurements on *Mariner IV* during the same period (Ref. 4).

Since *Mariner IV* made only a single pass along a somewhat off-center line through the presumed region of the magnetospheric tail, it may be argued that the negative results do not establish the absence of a detectable tail at 3300  $R_e$ . But, since the spacecraft spends some 7 days within a geocentric angle between 1 and 5 deg of the presumed center line of the tail, it seems quite unlikely that the tail, if indeed significant at this distance, would not have *waggled* past the spacecraft close enough to produce an effect equivalent to an average intensity  $j \geq 2$  ( $\text{cm}^2 \text{ s sr}^{-1}$ ) for 4 h.

The magnetospheric tail of the earth becomes unobservable by the means used in this investigation between

32 and 3300  $R_e$  (at least during conditions of mild geomagnetic activity). In view of the great interplanetary melee of lower-energy particles and turbulent magnetic fields, this conclusion seems acceptable. The corresponding failure of the magnetometer on *Mariner IV* to detect a magnetospheric tail at  $\sim 3300 R_e$  has been reported in a preliminary way by Coleman et al., Ref. 4.

**2. Impulsive emission of  $\sim 40$ -keV electrons from the sun.** The interplanetary particle events observed on May 25–28, June 5–7, and June 13–14, 1965 are identified conclusively as electrons of energy  $E_e \gtrsim 40$  keV with steeply falling energy spectrums and with approximately isotropic angular distributions. The maximum unidirectional intensities are 80, 58, and 5 ( $\text{cm}^2 \text{ s sr}^{-1}$ ), respectively. The time profiles of intensity exhibit abrupt onsets, increases to maximum values in times of the order of several hours, and gradual declines over periods of the order of a day. It appears that these bursts of interplanetary electrons are emitted impulsively from the sun at approximately the same time as bursts of radio noise and X rays observed by others with terrestrial equipment. It is estimated that about  $10^{34}$  electrons  $E_e > 40$  keV were emitted on May 25 and on June 5 and about  $10^{33}$  on June 13. The solar emission of non-thermal electrons has been suggested previously but not observed so clearly. Such electrons constitute a new tool for study of the structure of the interplanetary magnetic field and for discussion of the physics of solar flares.

*a. Solar electron event of May 25–28, 1965.* The observed counting rates of detectors C, A, B,  $D_1$ , and  $D_2$  are shown in Fig. III-6 as a function of earth time for the period 22:00 UT May 25 to 12:00 UT May 28. Enlarged plots of the counting rates of A and B during the early part of the event are given in Figs. III-7 and III-8. The *apparent* onset time is 23:20 ( $\pm 5$  min) UT on May 25. From this time to about 07:30 UT on May 26 the observed particle beam consists exclusively of electrons having  $40 \leq E_e \leq 150$  keV. This conclusive identification proceeds as follows:

- (1) There is a major effect detected by A and B, but no comparable effect is observed by C,  $D_1$ , and  $D_2$ , all of which have geometric factors similar to those of A and B. Also B, C, and  $D_1$  and  $D_2$  receive particles from the same directions in space.
- (2) The absence of an effect in C means that the particles received by B (and very likely by A also) must be either electrons  $40 \leq E_e \leq 150$  keV or protons  $0.55 \leq E_p \leq 3.1$  MeV.

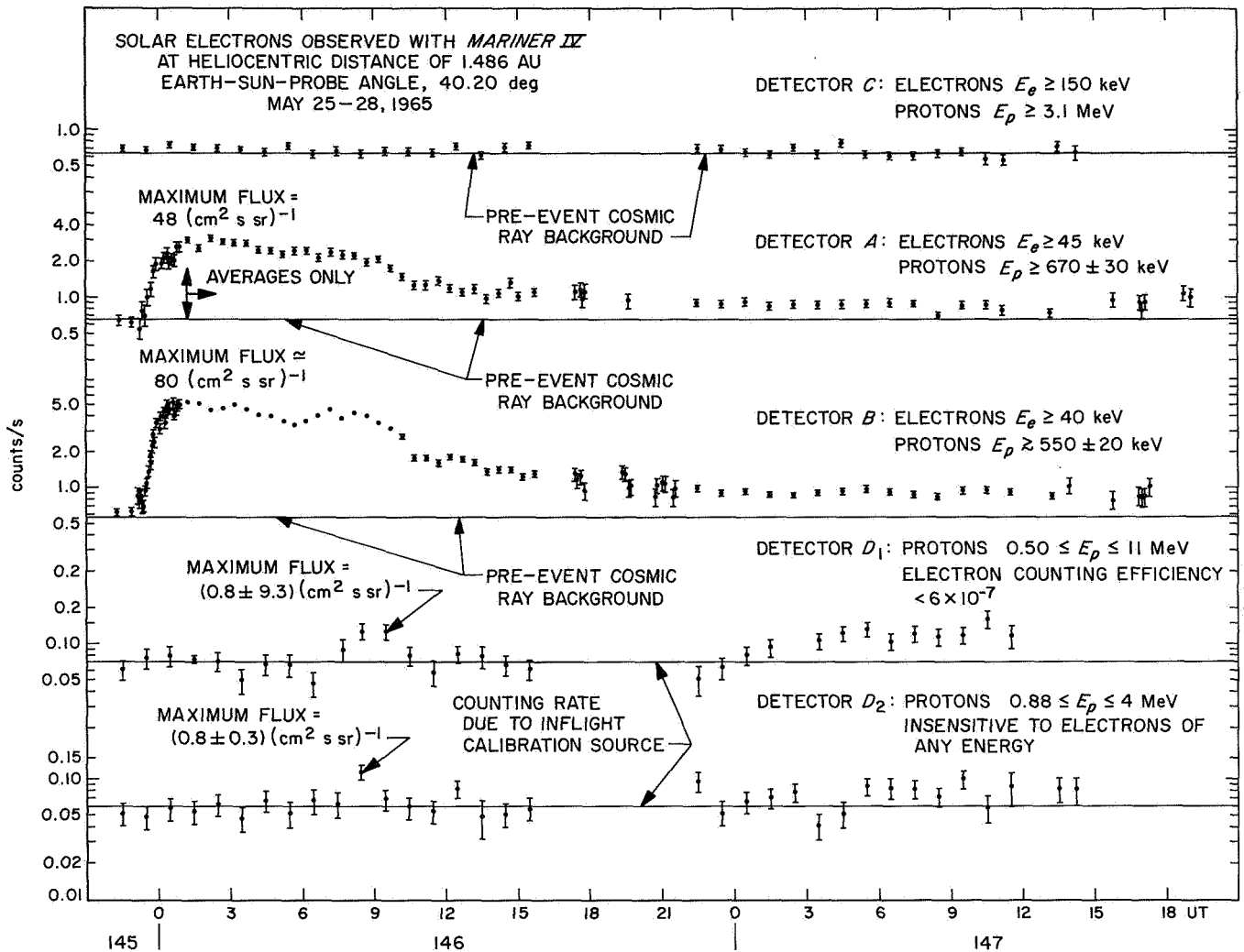


Fig. III-6. Comprehensive plot of data from all detectors for the major part of the May 25-28, 1965 solar electron event

- (3) The absence of an effect in  $D_1$  means that the intensity of protons  $0.50 \leq E_p \leq 11$  MeV [an energy range that completely encompasses that of the  $B$ - $C$  difference of (2)] is negligible, by at least a factor of 200.
- (4) Hence the particles received by  $B$  must be electrons  $40 \leq E_e \leq 150$  keV.
- (5) Even though  $A$  receives particles from different directions in space and has a slightly higher threshold than  $B$ , it is supposed henceforward that the foregoing identification is applicable to its output also, on the primary ground that the time histories of the counting dates of  $A$  and  $B$  are quite similar.
- (6) It may be noted that the  $\alpha$ -particle sensitivities of the several detectors are as follows:  $A$ ,  $E_a > 2.20$  MeV;  $B$ ,  $E_a > 1.90$  MeV;  $C$ ,  $E_a > 12.4$  MeV;  $D_1$ ,  $0.8 \leq E_a \leq 120$  MeV; and  $D_2$ ,  $1.15 \leq E_a \leq 50$  MeV. Hence an argument similar to that just given also conclusively eliminates  $\alpha$  particles (as well as heavier nuclear particles) on the basis of direct experimental knowledge.
- (7)  $D_1$  has a detection efficiency of less than  $6 \times 10^{-7}$  for  $\sim 40$ -keV electrons.
- (8) Neither direct X rays nor light from the sun can illuminate any part of the inner collimators or the windows of detectors  $A$  and  $B$ . Also, no part of the spacecraft lies within the field of view of the collimators. Scattering of such electromagnetic radiations from interplanetary gas, from interplanetary dust, and from planets is easily demonstrated to reduce their intensity by many orders

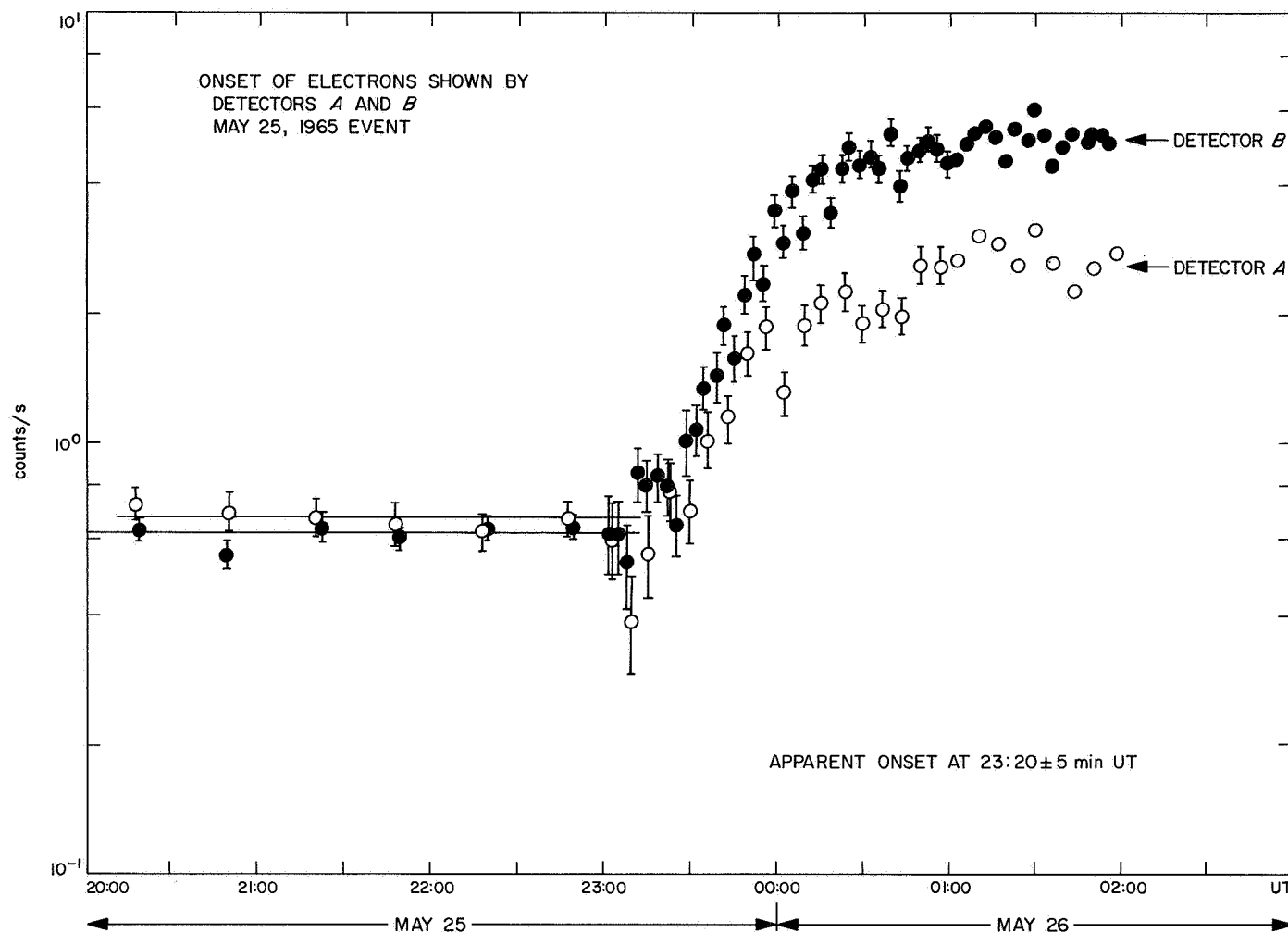


Fig. III-7. An expanded plot of the early part of the May 25-28 event

of magnitude below that inferred from observations with similar detectors pointed directly at the sun (Ref. 5). Also the time profile of X-ray flares is quite different from that of the events reported herein. JPL data on the alignment of the axis of the spacecraft with the probe-sun line assure that the nominal orientation of the detectors is maintained during the flight periods of interest. Thus, there appears to be no possibility that the responses of A and B can be attributed to solar X rays or ultraviolet light.

Later in the event, 07:30 to 11:00 UT May 26, a relatively small intensity of protons appears clearly on  $D_1$  and less clearly on  $D_2$ , and corresponding enhancements of the rates of B and A are observed. There is no effect on C. Hence, these protons are in the energy range 0.5 to 11 MeV and mainly toward the lower end of this

range. A subsequent, gradual reappearance of such protons begins about 00:00 UT on May 27, and they continue to be present for at least a day. A detectable intensity of electrons  $E_e > 40$  keV persisted to  $\sim 18:00$  UT May 28.

*b. Solar electron event of June 5-7, 1965.* The general run of data during the period 18:00 UT June 5 to 06:00 UT June 7 is similar to that of the May 25-28 event. Again, the response of B is attributed conclusively to electrons  $40 \leq E_e \leq 150$  keV. As before, it is supposed that the same identification argument is applicable to A. There is no evidence for protons  $E_p > 0.5$  MeV at any stage of the June 5-7 event.

*c. Solar electron event of June 13-14, 1965.* The apparent onset time for the third interplanetary electron

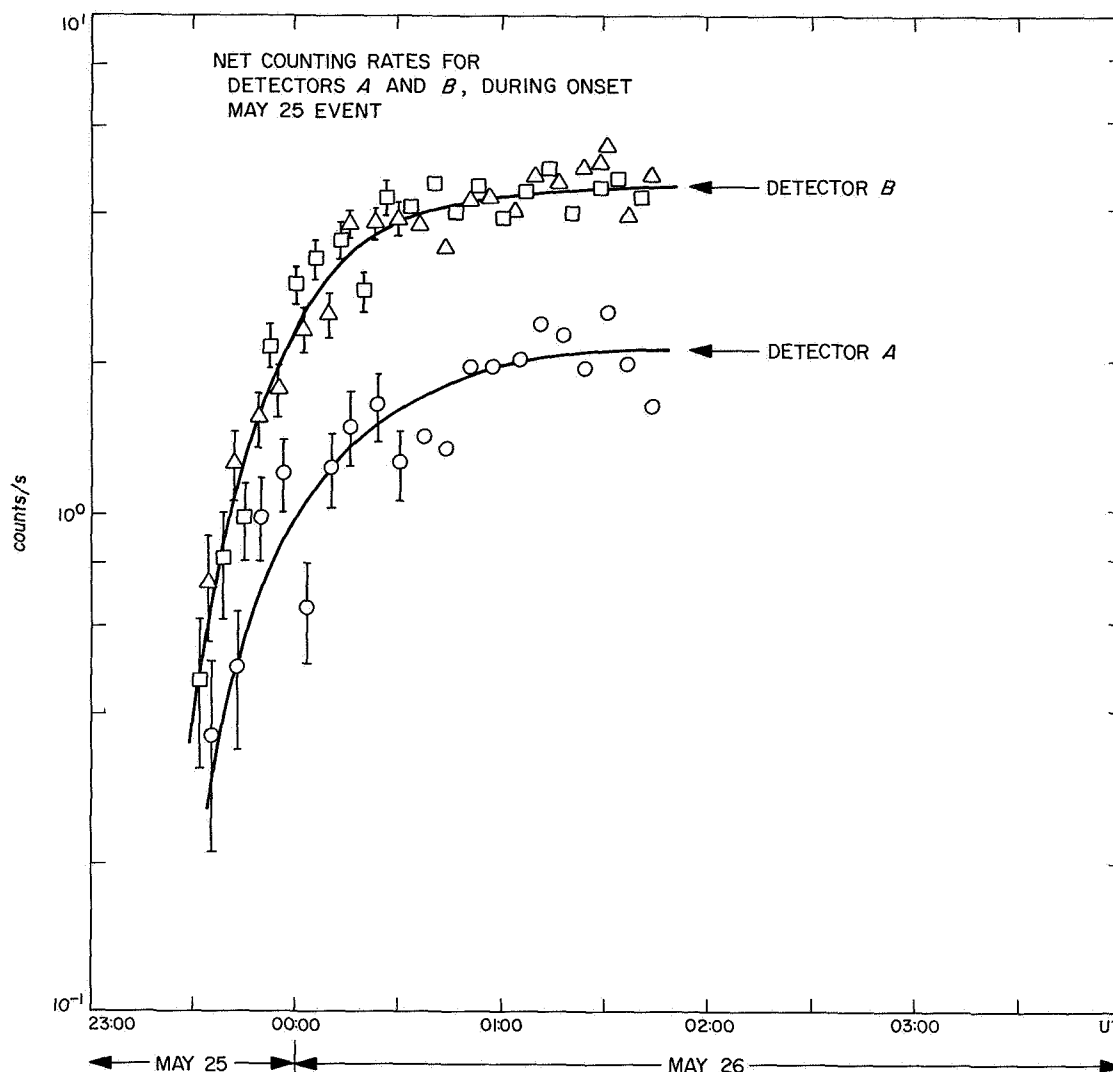
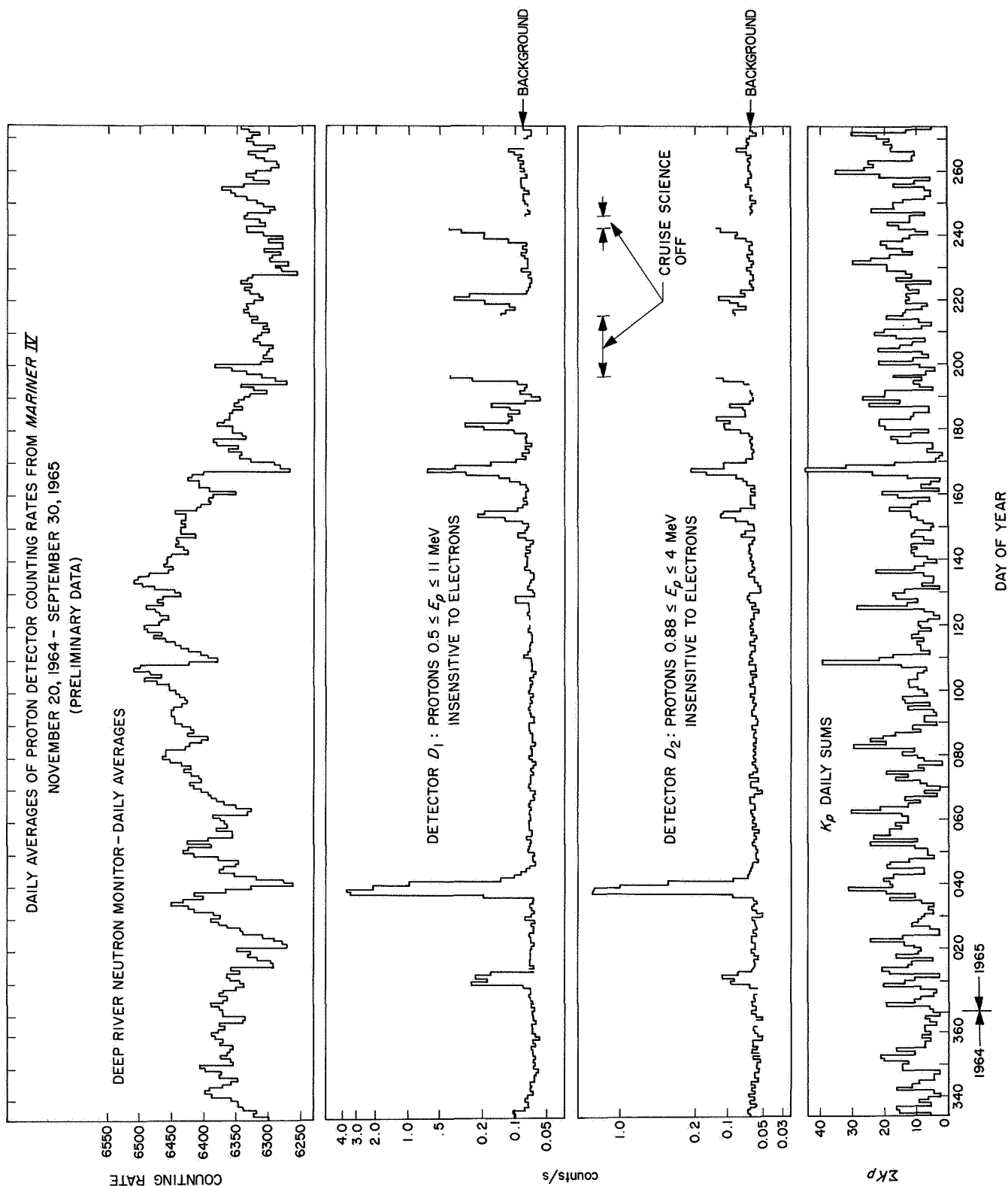


Fig. III-8. An alternative plot of the early part of the May 25–28 event, showing net counting rates due to solar electrons

event is 05:20 UT on June 13; the maximum unidirectional intensity of electrons, at about 14:00 UT on June 13, is  $j(E_e > 40 \text{ keV}) = 5.4 \text{ (cm}^2 \text{ s sr)}^{-1}$ . The electron event is superimposed on a proton event that begins at  $\sim 10:00$  UT on June 12, reaches a maximum in midday on June 16, and declines into the background on June 19. The electron and proton events appear to be unrelated.

**3. Observation of  $\sim 500\text{-keV}$  protons.** The daily averages of the counting rates of channels  $D_1$  and  $D_2$  during ten months of interplanetary flight are shown in Fig. III-9. Simultaneous data from the three Geiger-Mueller counters assure that all protons reported herein in fact entered

the solid-state detector through its collimator and *not* through the protective shield. Cruise science was commanded *off* for days 197–214 and days 243–245 of 1965 in order to use the spacecraft for other purposes and was finally commanded *off* on day 274 for an indefinite period, thus terminating the present series of observations. The daily average of the counting rate of the Deep River neutron monitor (courtesy H. Carmichael) is also plotted in Fig. III-9, as is the daily sum of the 3-h geomagnetic disturbance indices  $K_p$ . These auxiliary data provide direct measures of the galactic cosmic ray intensity at the earth and of geomagnetic activity and thus, inferentially, a measure of the state of the interplanetary medium.



**Fig. III-9. Daily averages of the counting rates of channels  $D_1$  and  $D_2$  during 10 mo of interplanetary flight**

The observational duty cycle of each channel  $D_1$  and  $D_2$  is 11.161%. During a solid day of observations 9643 s of data were obtained from each channel. Hence, the statistical standard deviation  $\sigma$  of the daily average background rates of  $D_1$  (0.069 count/s) and  $D_2$  (0.057 count/s) is 0.0025 count/s. A  $3\text{-}\sigma$  departure from the daily mean corresponds to a detection sensitivity for interplanetary protons having a unidirectional intensity  $j$  of  $0.12 \text{ (cm}^2 \text{ s sr)}^{-1}$  in the energy ranges quoted above.

Table III-2 lists 20 resolvable proton events having clear statistical significance. It is probable that further

analysis of the final data will reveal other events of lesser intensity. The following summary remarks result from a study of the data:

- (1) The counting rate of  $D_1$  is significantly above that due to the calibration source for 10% of the period of observation Nov. 29, 1964–Apr. 20, 1965, for 32% of the period of observation Apr. 21–Sept. 30, 1965, and for 24% of the entire period.
- (2) There is a striking general negative correlation between interplanetary proton activity and the intensity of galactic cosmic rays as measured by the

**Table III-2. Proton events observed with Mariner IV, Nov. 28, 1964–Oct. 1, 1965**

Dates 1965, inclusive	Days 1965, inclusive	Heliocentric radial distance of spacecraft, AU	Difference in helio- centric ecliptic longi- tudes of spacecraft and earth, deg <sup>a, b</sup>	Maximum unidirec- tional intensity, $j^c$ $0.50 \leq E_p \leq 11 \text{ MeV}$ $(\text{cm}^2 \text{ s sr})^{-1}$	Possibly pertinent solar activity as seen from the earth <sup>d</sup>
Jan. 8–12	8–12	1.06	+1.7	$4.3 \pm 0.3$	IMP 2 flare, Jan. 6, 08:10 UT
Feb. 5–13	36–44 <sup>e, f</sup>	1.15	–1.9	140	IMP 2 <sup>+</sup> flare, Feb. 5, 17:50 UT
April 20	110 <sup>e, f</sup>	1.39	–24.5	$0.4 \pm 0.1$	IMP 2 flare, Apr. 15, 09:15 UT
May 7–8	127–128	1.44	–32.0	$0.8 \pm 0.2$	—
May 26	146	1.48	–40.3	$0.9 \pm 0.3$	—
May 27	147	1.48	–40.8	$1.1 \pm 0.3$	—
June 1–5	152–156 <sup>e</sup>	1.50	–44.2	$3.0 \pm 0.2$	IMP 2 flare, May 28, 09:16 UT
June 12–19	163–170 <sup>e, f</sup>	1.52	–50.4	$1.7 \pm 0.5$	IMP 3 flare, June 9, 05:59 UT
June 21	172	1.53	–53.2	$0.6 \pm 0.2$	—
June 28–July 1	179–182	1.54	–57.0	$4.2 \pm 0.2$	IMP 2 <sup>+</sup> flare, June 28, 10:20 UT
July 2–3	183–184	1.54	–58.4	$1.1 \pm 0.2$	—
July 4–6	185–187 <sup>e</sup>	1.55	–59.7	$2.1 \pm 0.2$	—
July 10	191 <sup>e</sup>	1.55	–62.2	$0.4 \pm 0.1$	—
July 13–15	194–196 <sup>f</sup>	1.55	–64.3	$6.4 \pm 0.3$	—
No Observations July 16–Aug. 2	197–214	—	—	—	—
Aug. 3–4	215–216	1.57	–74.4	$1.4 \pm 0.2$	—
Aug. 6–9	218–221	1.57	–76.4	$6.6 \pm 0.3$	—
Aug. 17	229 <sup>e, f</sup>	1.57	–81.0	$0.4 \pm 0.1$	IMP 2 flare, Aug. 15, 06:15 UT
Aug. 26–30	238–242	1.57	–86.9	$6.0 \pm 0.3$	—
No Observations Aug. 31–Sept. 2	243–245	—	—	—	—
Sept. 22–24	265–267	1.56	–100.0	$0.8 \pm 0.2$	—
Sept. 25–26	268–269	1.56	–101.6	$0.5 \pm 0.1$	—

<sup>a</sup>Heliocentric ecliptic longitude is measured counterclockwise as viewed from the north ecliptic pole.

<sup>b</sup>Positional coordinates are from the JPL ephemeris IBSYS-JPTAJ-SFPRO 111464 of Dec. 15, 1964.

<sup>c</sup>Maximum intensity is derived from the highest 4-h average counting rate during the event.

<sup>d</sup>Extracted from the monthly "Compilations of Solar-Geophysical Data" of the U. S. Department of Commerce NBS/CRPL, Boulder, Colorado.

<sup>e</sup>A magnetic sudden commencement.

<sup>f</sup>A clear Forbush decrease in galactic cosmic ray intensity observed approximately simultaneously at the earth.



Deep River neutron monitor; see Fig. III-9. It is tempting to regard this negative correlation as physically significant and to suggest further that May 1965 is the *bottom* of the solar activity cycle.

- (3) The most intense event of the series is that of Feb. 5-13, 1965. Of the 20 events it is the only one which is convincingly associated with a specific solar flare. In addition to the low energy protons shown in Fig. III-9, it contains a maximum omnidirectional intensity  $I_0 \sim 80 \text{ (cm}^2 \text{ s)}^{-1}$  of protons  $E_p > \text{MeV}$  as measured with the shielded Geiger tube. The energy spectrum of the particles in this event is distinctly flatter than that of any of the other 10 events for which a significant spectral determination is feasible. The time profile of the intensity of the hard component in the Feb. 5-13 event is reasonably well understood on the basis of free diffusion in the interplanetary medium. But the time profile of the intensity of the soft component shown in Fig. III-9 is not so explicable.
- (4) The time-intensity profiles of most of the other 19 events reported here are roughly symmetrical and have widths in the range of one to several days.
- (5) Also, in most of the other 19 events, the ratio of the counting rate of  $D_1$  to that of  $D_2$  is roughly constant throughout each event for which the  $D_2$  rate is adequate for a significant determination. The differential energy spectra corresponding to these ratios can be represented by  $dj/dE \approx \exp(-E/E_0)$  with  $E_0$  in the range of 200 to 600 keV or by  $dj/dE \approx E^{-\gamma}$  with  $\gamma$  in the range of 2 to 4.
- (6) Despite paragraph (2), in only 5 cases is there a convincing association between the occurrence of low-energy protons at the spacecraft and a specific Forbush decrease at earth; and in only 7 cases is there an associated geomagnetic sudden commencement at the earth; see Table III-2. It appears that these associations weaken as the difference in heliocentric longitude of the spacecraft and the earth increases.
- (7) The occurrence of successive events, with the exception of the first two, has no simple relationship to the period of rotation of the sun, as seen from the spacecraft, though it is possible that rotational periodicity is masked by the combination of several active centers at different heliographic longitudes and latitudes. A similar situation prevailed in our earlier observations with *Mariner II* in late

1962. The simple periodicity noted by Bryant et al., Refs. 6 and 7, for protons in the higher energy range  $3 < E_p < 20 \text{ MeV}$  during a different time period may be attributable to differences in instrumental characteristics (i.e., considerably higher energy threshold and lower intensity threshold) or to the existence of a simpler activity pattern on the sun during their observations.

- (8) During no one of the proton events (except the Feb. 5-13 one) is there an intensity of associated electrons  $E_e > 40 \text{ keV}$  exceeding a unidirectional value comparable to that of protons  $E_p > 500 \text{ keV}$  (using data from the Geiger tubes, not shown herein).

There is little doubt that the observed low-energy protons owe their existence to the sun, either (1) by direct emission at essentially the energy observed or (2) by generation in turbulent regions of the solar wind in interplanetary space. It is concluded that both alternatives (1) and (2) and perhaps some combination of them survive a qualitative discussion, but (1) is still favored as a working hypothesis.

**4. Martian encounter.** The Martian encounter occurred on July 14-15, 1965 after 228 days of interplanetary flight during which the apparatus operated properly and provided a large volume of data on solar proton and electron events. Every data point from each of the detectors A, B, C,  $D_1$ , and  $D_2$  is shown in Fig. III-10 for the time period 10:00 UT of July 14, 1965 to 11:54 UT of July 15, 1965, together with scales of areocentric latitude and areocentric radial distance  $R$ . Areocentric latitude is measured positive north and negative south from the equatorial plane of the planet (the plane through its center perpendicular to its axis of rotation). Closest approach of *Mariner IV* to the center of Mars, areocentric radial distance 13,200 km, occurred at 01:13 UT of July 15. During the period 02:31 to 03:25 UT of July 15 the spacecraft, as viewed from the earth, was occulted by Mars and no signals were received.

Prior to 15:20 UT of July 14 the counting rates of all detectors were indistinguishable from their long term interplanetary background values. At 15:20 ( $\pm 10 \text{ min}$ ) UT the rates of  $D_1$ ,  $D_2$ , and B began to depart from their background values and continued clearly above background until spacecraft *science* was turned off at 11:54 UT of July 15. The effect was weak or absent on detectors A and C. The particles responsible for the effect are identified conclusively as protons, or other

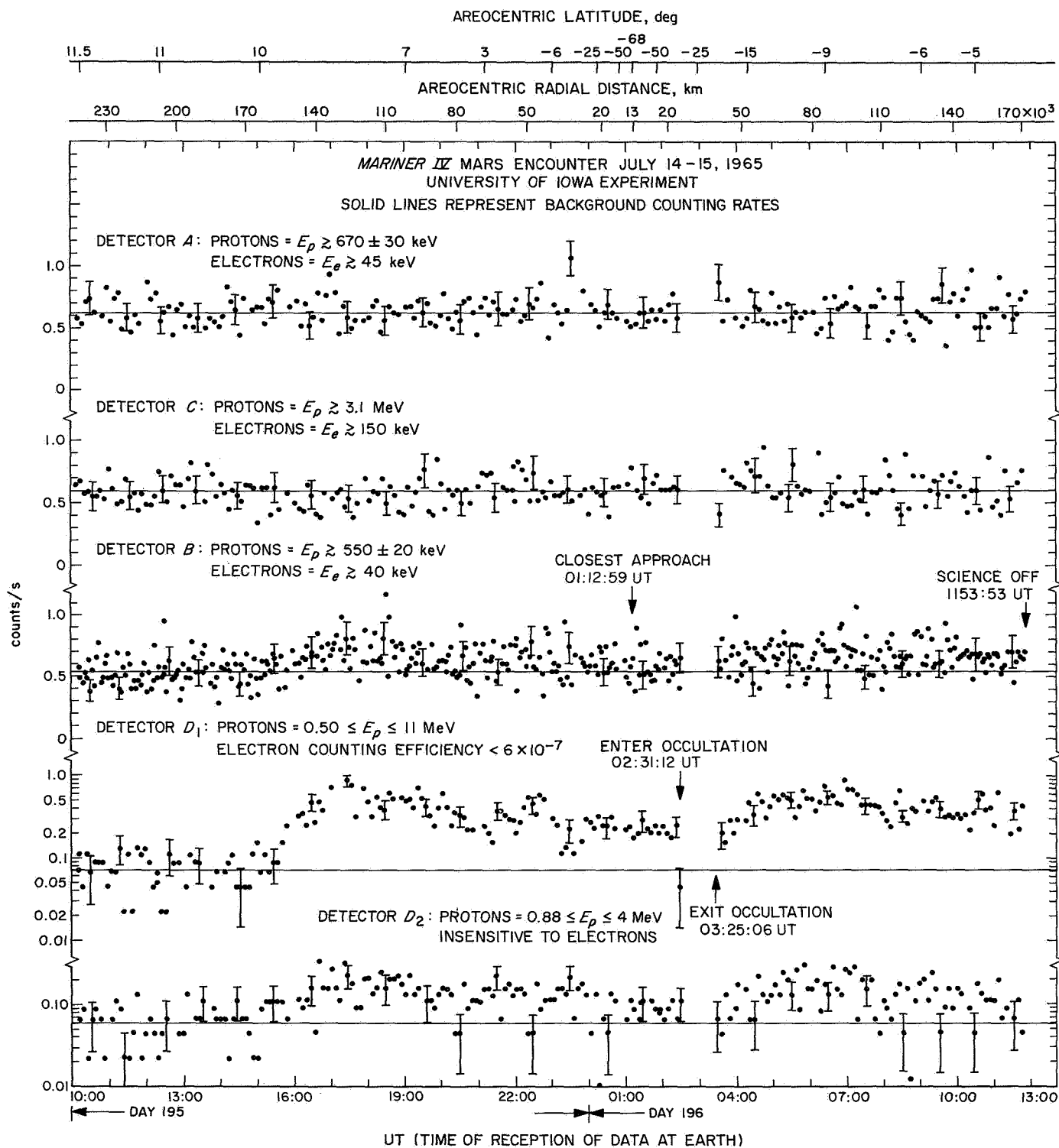


**Fig. III-10. A comprehensive plot of the counting rates of detectors A, C, B, D<sub>1</sub>, and D<sub>2</sub> before, during, and after the encounter with Mars on July 14-15, 1965**

heavy particles, with an energy spectrum which falls steeply between 0.5 and 0.9 MeV. At the time of onset of the effect the spacecraft was 162,000 km from the center of the planet at a sun-Mars-probe angle of 34 deg. It is concluded that the observed protons are not associated with Mars on the following grounds:

- (1) The time (and spatial) dependence of the intensity as measured along the trajectory of the spacecraft is quite different than that to be expected in a planetary radiation belt.
- (2) No such intensities of protons are found beyond about 65,000 km from the earth in any direction; and, as will be shown later, the particle populations much nearer to Mars are vastly less than those at similar distances from the earth.
- (3) Both observationally and theoretically the outer fringe of a planetary magnetosphere is characterized by energetic electrons not protons.
- (4) The time history, proton intensity, and proton spectrum observed on July 14-15 are all similar to those commonly observed in interplanetary space remote from any celestial body. Five events of this nature were observed during the 2 wk previous to the Martian encounter period.

For the above reasons, the observed protons on July 14-15 are identified as a *solar proton event* whose appearance during this period was coincidental with the Martian encounter.

Throughout the remainder of the encounter period, there was no further significant departure from background rates by any of the five detector channels. Detectors A and B were presumably the most sensitive to the fringe of a magnetosphere.

Thus, no particle effects whatever attributable to Mars were detected despite the close approach of the spacecraft.

More precisely, the unidirectional intensity of electrons  $E_e > 40$  keV did not exceed  $6 \text{ (cm}^2 \text{ s sr)}^{-1}$  over any 45-s sampling period. A similar trajectory past the earth would have encountered unidirectional intensities as high as  $10^7 \text{ (cm}^2 \text{ s sr)}^{-1}$ , Ref. 8. Hence, as a purely observational matter it is clear that the radiation environment of Mars is vastly different than that of the earth.

### 5. Implications of the absence of radiation belts.

Assuming the applicability of the composite theoretical-observational knowledge of the magnetospheric transition region around the earth to that of a planet of much smaller magnetic moment, it is possible to use our negative results to place an upper limit on the magnetic moment of Mars.

The basic scaling law (Ref. 9) is given by

$$n m v^2 \approx \frac{B^2}{8\pi} \approx \frac{M^2}{R^6} \quad (1)$$

It is further supposed that  $v$  at Mars is the same as at the earth and that  $n$  is an inverse square function of heliocentric radial distance. Thus, it is supposed that the shock front and the magnetopause have the same geometric shapes as for the earth with the linear scale factor

$$\frac{R_M}{R_E} = 1.1 \left( \frac{M_M}{M_E} \right)^{1/3} \quad (2)$$

It is known that the shock front and the magnetopause have approximate cylindrical symmetry about the sun-planet line, more or less independent of the orientation of the magnetic moment of the planet.

The application of these ideas to the present situation is described by Fig. III-11. The curved line ABCDEFG represents the encounter trajectory of *Mariner IV* in areocentric polar coordinates  $R$  (radial distance from center of Mars) and  $\alpha$  (sun-Mars-probe angle). The cross section of the body of the planet is shown to the same scale. Data for the trajectory plot are from JPL's "IBSYS-JPTRAJ-SFPRO 062965 *Mariner IV* Mission Encounter Fine Print 03:10 GMT 15 July 61 Special", which is the first-order corrected, post-encounter ephemeris, believed to be in error by less than 100 km. Adopting a blended best bit to present knowledge of the geometric forms of the earth's shock front and magnetopause (Refs. 3, 10, and 11), geometrically similar curves have been drawn in Fig. III-11, scaled according to Eq. (2) for the case  $M_M/M_E = 0.001$ . The two connected squares labeled  $M$  are similarly transformed points from Fig. III-9 which represent the positions of easily detectable intensities of electrons  $E_e > 40$  keV at 23.0 and 25.7  $R_E$ , respectively, in the fringe of the earth's magnetosphere on November 28-29, 1964.

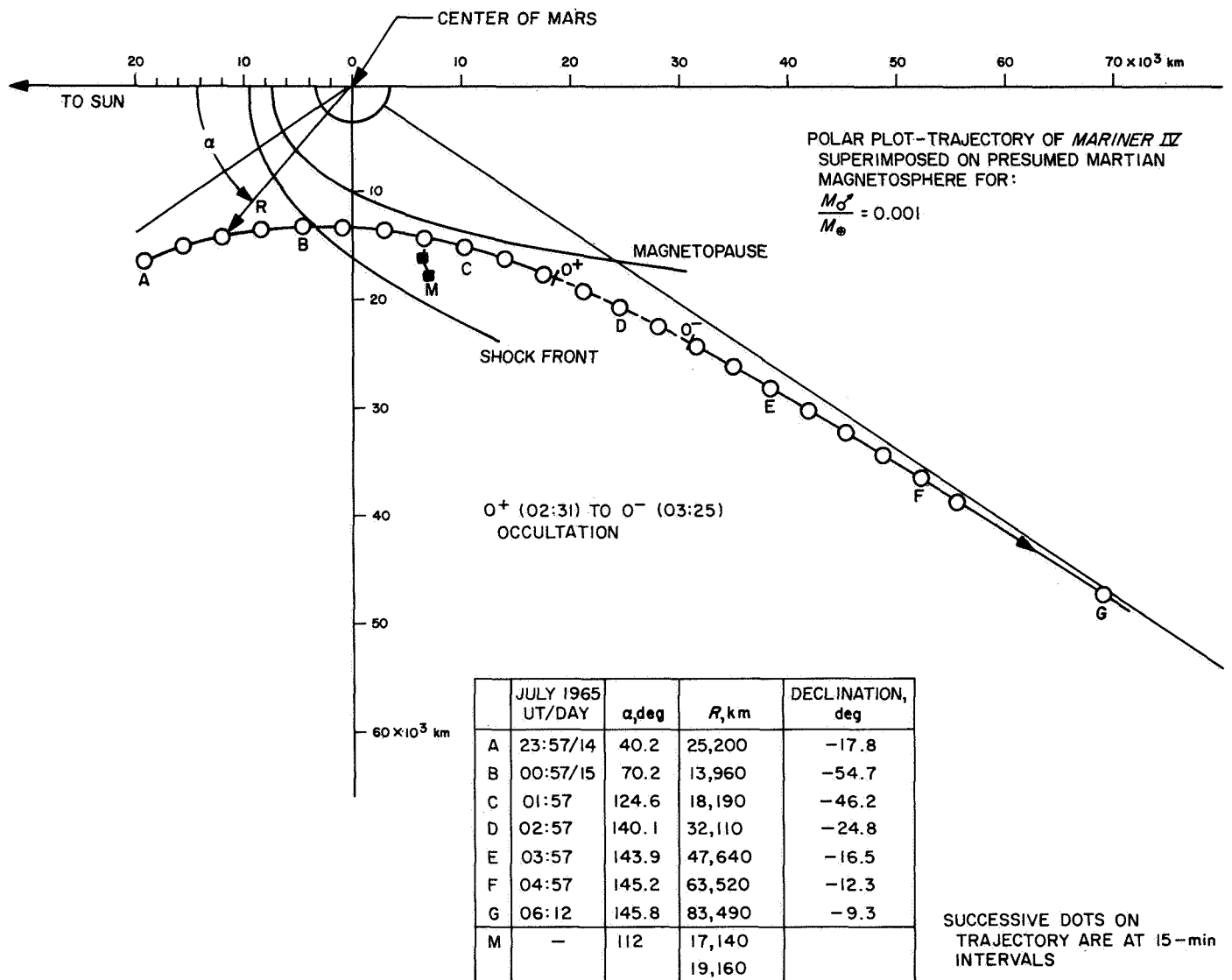


Fig. III-11. An analytical diagram used for inferring an upper limit to the ratio of the magnetic dipole moment of Mars to that of earth

From Fig. III-11, the conclusion is that  $M_M/M_E$  is surely less than 0.001. In fact, a literal interpretation of Fig. III-11 gives  $M_M/M_E < 0.0005$ . In view of the wide range of areocentric latitude and of  $\alpha$  while the spacecraft was flying more or less parallel to the scaled magnetopause, these conclusions are probably valid for any orientation of the Martian magnetic moment.

The foregoing results mean that the equatorial surface magnetic field of Mars is less than 200, and perhaps 100  $\gamma$  (radius = 3417 km), and hence suggest that the solar wind will, on occasion and perhaps usually, have a direct interaction with the Martian atmosphere. This

interaction may be of essential importance in determining the physical state of the atmosphere.

Also, it is evident that the Martian atmosphere and surface are exposed to the full effects of solar and galactic cosmic radiation irrespective of latitude.

The observed weakness of the Martian magnetic field will presumably contribute to the understanding of the internal structure of the planet, though we do not pretend competence in this field and make only a few general remarks. It is noted that the origin of the earth's

general magnetic field is not understood on the basis of *a priori* theory and that no significant prediction of the magnetic moment of any other celestial body exists. On the basis of the most widely accepted conjecture on the physical origin of the geomagnetic field (Refs. 12 and 13), it is believed necessary for a planetary body to be endowed with both rotation and a liquid, electrically conducting core in order that its externally apparent magnetization exceed the mean of the remanent values of its constituents. Mars has 0.107 the mass, 0.71 the mean density, and 0.536 the radius of the earth; it has 1.18 the mass and 1.97 the radius of the moon (Ref. 14). The period of rotation of Mars, 24.62 h, is nearly the same as that of the earth. It appears that its vastly weaker magnetic moment must be attributed to a

markedly different internal structure and/or composition such that it does not possess a liquid, electrically conducting core.

## E. Sources

In addition to the principal investigators, D. L. Chinburg and D. C. Enemark of SUI participated in the experiment. Dr. H. R. Anderson, R. K. Sloan, R. F. Lockhart, and D. K. Schofield of JPL contributed to various aspects of the effort.

Additional papers on the results of the TRD experiment are in preparation. The bibliography consists of papers from the SUI experiments on *Mariner IV*.

## References

1. Frank, L. A., Van Allen, J. A., and Macagno, E., "Charged-particle Observations in the Earth's Outer Magnetosphere," *J. Geophys. Res.*, Vol. 68, pp. 3543-3554, 1963.
2. Van Allen et al., "Absence of Martian Radiation Belts and Implications Thereof," *Science*, Vol. 149, p. 1288, 1965.
3. Ness, Norman F., Searce, Clell S., and Seek, Joseph B., "Initial Results of the IMP 1 Magnetic Field Experiment," *J. Geophys. Res.*, Vol. 69, pp. 3531-3569, 1964.
4. Coleman, P. J., Jr., Davis, L., Jr., Jones, D. E., and Smith, E. J., "Mariner IV Magnetometer Observations" (title only), *Trans. Am. Geophys. Union*, Vol. 46, p. 113, 1965.
5. Van Allen, J. A., Frank, L. A., Maehlum, B., and Acton, L. W., "Solar X-ray Observations by *Injun 1*," *J. Geophys. Res.*, Vol. 70, pp. 1639-1645, 1965.
6. Bryant, D. A., Cline, T. L., Desai, U. D., and McDonald, F. B., *Phys. Rev. Lett.*, Vol. 11, p. 144, 1963.
7. Bryant, D. A., Cline, T. L., Desai, U. D., and McDonald, F. B., *Phys. Rev. Lett.*, Vol. 13, pp. 481-484, 1965.
8. Frank, L. A., Van Allen, J. A., and Hills, H. K., "A Study of Charged Particles in the Earth's Outer Radiation Zone with *Explorer 14*," *J. Geophys. Res.*, Vol. 69, pp. 2171-2192, 1964.
9. Spreiter, J. R., and Jones, W. P., "On the Effect of a Weak Interplanetary Magnetic Field on the Interaction between the Solar Wind and the Geomagnetic Field," *J. Geophys. Res.*, Vol. 68, pp. 3555-3564, 1963.

## References (contd)

10. Heppner, J. P., Ness, N. F., Searce, C. S., and Skillman, T. L., "Explorer 10 Magnetic Field Measurements," *J. Geophys. Res.*, Vol. 68, pp. 1-46, 1963.
11. Frank, L. A., and Van Allen, J. A., "Measurements of Energetic Electrons in the Vicinity of the Sunward Magnetospheric Boundary with Explorer 14," *J. Geophys. Res.*, Vol. 69, pp. 4923-4932, 1964.
12. Elsasser, W. M., "The Earth's Interior and Geomagnetism," *Rev. Mod. Phys.*, Vol. 22, pp. 1-35, 1950.
13. Cowling, T. G., *Magnetohydrodynamics*, Interscience Publishers, Inc., New York, 1957.
14. Allen, C. W., *Astrophysical Quantities*, Athlone Press of the University of London, London, 1955.

## Bibliography

- Krimigis, S. M., and Armstrong, T. P., "Observations of Protons in the Magnetosphere with Mariner IV," *J. Geophys. Res.*, Vol. 71, pp. 4641-4650.
- Krimigis, S. M., and Van Allen, J. A., "Observations of  $\sim 500$ -keV Protons in Interplanetary Space with Mariner IV," *Phys. Rev. Lett.*, Vol. 16, pp. 419-423, 1966.
- Krimigis, S. M., and Van Allen, J. A., *Observations of the Solar Particle Event of 5 to 12 February 1965 with Mariner IV and Injun IV*, Univ. of Iowa Report 67-7, Feb. 1967.
- Krimigis, S. M., Van Allen, J. A., and Coleman, P. J., Jr., "Observation of  $\sim 500$  keV Protons in Interplanetary Space with Mariner IV," *Trans. Am. Geophys. Union*, Vol. 47, p. 153, 1966.
- Krimigis, S. M., Van Allen, J. A., and Frank, L. A., *Observations with University of Iowa Equipment on Mariner IV*, Univ. of Iowa Preliminary Report 65-36, May-Oct. 1965.
- Van Allen, J. A., "Absence of 40 keV Electrons in the Earth's Magnetospheric Tail at 3300 Earth Radii," *J. Geophysical Res.*, Vol. 70, pp. 4731-4739, 1965.
- Van Allen, J. A., "Further Remarks on the Absence of a Very Extended Magnetospheric Tail," *J. Geophys. Res.*, Vol. 71, pp. 2406-2407, 1966.
- Van Allen, J. A., Frank, L. A., Krimigis, S. M., and Hills, H. K., "Absence of Martian Radiation Belts and Implications Thereof," *Science*, Vol. 149, pp. 1228-1233, 1965.
- Van Allen, J. A., Frank, L. A., Krimigis, S. M., and Hills, H. K., *Observations with University of Iowa Equipment on Mariner IV*, Univ. of Iowa Preliminary Report 65-15, Feb., Mar., Apr., May 1965.

### Bibliography (contd)

- Van Allen, J. A., and Krimigis, S. M., "Impulsive Emission of  $\sim 40$  keV Electrons from the Sun," *J. Geophys. Res.*, Vol. 70, pp. 5737-5751, 1965.
- Van Allen, J. A., and Krimigis, S. M., "Interplanetary and Martian Particle Measurements with *Mariner IV*," *Trans. Am. Geophys. Union*, Vol. 46, p. 532, 1965.
- Van Allen, J. A., and Krimigis, S. M., "Interplanetary Observations of the Solar Particle Event of February 5 to 13 with *Mariner IV*," *Trans. Am. Geophys. Union*, Vol. 47, p. 153, 1966.
- Van Allen, J. A., Krimigis, S. M., and Frank, L. A., *Observations with University of Iowa Equipment on Mariner IV*, Univ. of Iowa Report 65-5, Nov. 1964-Feb. 1965.

## IV. Cosmic Dust Detector

### A. Introduction

The cosmic dust detector (CDD) experiment was conducted under the direction of W. M. Alexander, principal investigator, of Goddard Space Flight Center during the study. J. L. Bohn of Temple University was co-investigator for the program. B. V. Connor, cognizant scientist, and D. K. Schofield, cognizant engineer, both of the Jet Propulsion Laboratory, conducted studies, tests, and analyses in support of the experiment.

Knowledge concerning the origin, composition and dynamic properties of the cloud of dust surrounding the sun is fundamental to any extensive study of the solar system. Prior to the advent of rockets, satellites and space probes, information about the physical and dynamic characteristics of aggregates of particulate matter in space came from a variety of ground-based experiments. Meteor observations, using visual, photographic, and radar techniques, produced measurements of the mass, velocity, density and composition of individual meteoroids colliding with the earth's atmosphere. These studies were limited to particle masses greater than  $10^{-4}$  g until Gallagher and Eshleman (Ref. 1) and Eshleman (Ref. 2) reported radar observations of particles with limiting masses of approximately  $10^{-6}$  g. For particles with masses less than  $10^{-6}$  g, photographic observations of the zodiacal light, solar corona, and sky radiance have represented the major optical techniques used to obtain measurements of the sizes and dynamic properties of minute dust particles near the earth and in deep space. Composition, age, and

gross accretion rates of meteoroidal and dust particle material have been obtained from analysis of collections of remnants of these particles surviving passage through the earth's atmosphere. These collection studies include dust particles with masses as low as  $10^{-10}$  g. The direct study of the physical and dynamic properties of dust particles in space with masses between  $10^{-13}$  and  $10^{-8}$  g started with the in-situ measurements of various dust-particle parameters from experiments on many rockets, satellites, and space probes. Results of measurements obtained from previous ground-based and space experiments regarding dust particles with masses less than  $10^{-6}$  g are summarized in this report, as well as results of the in-situ measurement of the flux of minute dust particles comprising the bulk of the zodiacal dust cloud between 1.0 and 1.57 AU.

### B. Experiment Objectives

Ground-based photometric studies of the zodiacal light and the solar F-corona have produced the only measurements of the size distributions of dust particles in interplanetary space out to 1.0 AU. Observations of this scattered light define the integrated effects of a distribution of particles along the observing line of sight. No information is possible concerning the dynamic characteristics of these minute particles. Results of analyzing zodiacal light measurements within the past 3 or 4 years, for example, Giese (Ref. 3) and Weinberg (Ref. 4), have placed the radii of the predominate scattering particles between 0.08 and  $2\ \mu$ .



The orbital distribution of zodiacal dust particles cannot be determined by the ground-based photometric measurements. The only information concerning the shape of the heliocentric zodiacal dust cloud comes from studies of the shape of the isophotal contours of the zodiacal light and solar F-corona. Whereas the solar F-corona is spherically symmetric about the sun, the zodiacal light is not. The observations show that the cloud has the shape of an oblate spheroid with the axis of rotational symmetry being almost normal to the ecliptic plane; thus, the highest concentration of dust particles occurs near the plane of the ecliptic. However, the zodiacal light does not appear like an edge-on view of the rings of Saturn, which could only occur if the dust particle orbits were primarily of zero inclination. The isophotal contours do show that a sizable fraction of the particles have orbits of at least moderate inclinations. The measurements do not yield information concerning the eccentricities of the orbits.

Ground-based measurements capable of determining the orbit parameters of individual particles are limited to particles having much greater masses than those which produce the major portion of the scattered light of the zodiacal dust cloud. These particles are detected as they impinge on the earth's atmosphere at meteoric velocities with the resultant energy release detected by various ground observational techniques. The radio-radar techniques are the most sensitive observational methods used, and the orbits of a number of meteors with masses between  $10^{-6}$  and  $10^{-2}$  g have been determined in recent years. In a general sense, these measurements show mostly direct orbiting particles with moderate inclinations and eccentricities. However, the spectrum of these two quantities becomes broader for the smaller particles. Most of the orbits of these particles do indicate that they are predominately from the short period comets.

If the major portion of the zodiacal dust particles come from the short period comets, they would have to be of very recent origin because of the Poynting-Robertson effect. If they were originally associated with long period comets or primordial debris, they would have had to have been several hundred astronomical units (AU) from the sun to be near the earth's orbit now. The inclination of the former group of particles would be similar to that of the short period comets with a moderate range of orbital eccentricities. The orbits of the latter group of particles could exhibit almost random inclinations, but the eccentricities should be almost zero (Poynting-Robertson effect).

Almost all of the direct or in-situ measurements concerning the flux of minute dust particles from space

vehicles have been made from satellites near the earth. One measurement was obtained from an experiment on a cislunar probe, Dubin (Ref. 5), and one measurement from an interplanetary probe experiment, Alexander (Ref. 6). A summary of the major results from these measurements is that (1) the flux distribution near the earth is different than in deep space, and (2) the mass distribution is somewhat different near the earth than in deep space. The flux distribution in deep space indicated by the *Mariner II* experiment, Alexander (Ref. 6), was not statistically significant. However, it was in general agreement with the recent zodiacal light measurements. No measurement from a dust particle experiment on a space vehicle has yielded any information concerning the orbits of these particles in interplanetary space.

Prior to the *Mariner IV* measurement, the general knowledge we have regarding the physical and dynamic properties of zodiacal dust may be summarized as follows: (1) the predominate size of zodiacal dust is from  $0.08\mu \leq r \leq 2\mu$  in radius; (2) the flux distribution in deep space is markedly different (less than) from that near the earth; and (3) the particle orbits contain both moderate inclinations and eccentricities.

The nature and origin of the individual dust particles in the zodiacal dust cloud are of primary interest for the initial measurements of the physical and dynamic properties of these particles. The major parameters desired are:

- (1) The flux distribution.
- (2) The mass distribution.
- (3) The particle size distribution.
- (4) The approximate heliocentric radiant and velocity.

The weight and power limitations for the first Mars probe, *Mariner IV*, restricts the zodiacal dust measurements to the first three desired parameters. Therefore, the scientific objective of the *Mariner IV* cosmic dust experiment was to obtain in-situ measurements of the flux and mass distributions of zodiacal dust particles in the vicinity of the earth, in interplanetary space between the orbits of earth and Mars, and in the vicinity of Mars.

### C. Instrumentation

The experiment was designed to sample the number of dust particles over a given mass range along the *Mariner IV* trajectory. From this information, the zodiacal dust flux and mass distribution could be derived. Figure IV-1 is a

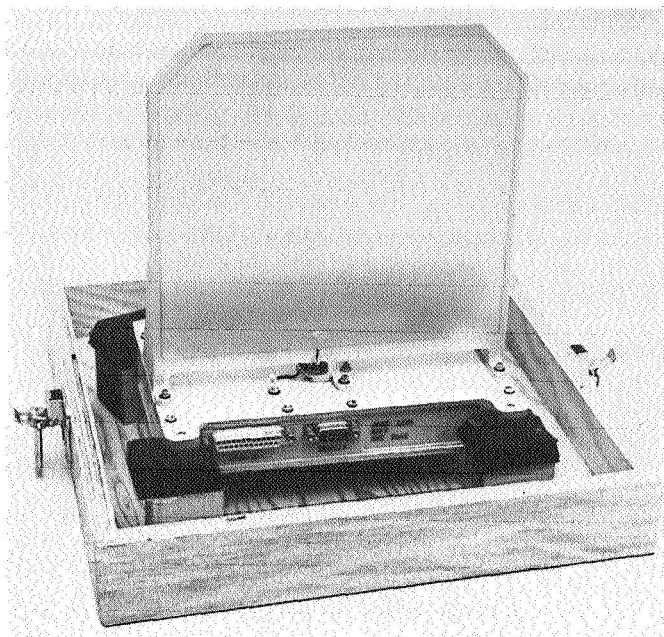


**Fig. IV-1. Cosmic dust detector**

photograph of the instrument, and the functional block diagram of the instrumentation is depicted in Fig. IV-2.

The detector is an aluminum plate (area =  $3.5 \times 10^{-2} \text{ m}^2$ ) which can be exposed to impacts of zodiacal dust in space. One sensor is a crystal microphone bonded to the impact plate. The crystal is a piezoelectric ceramic transducer (lead zirconate) which responds to the compression wave in the plate resulting from the impulse delivered to either side of the plate by the hypervelocity impact of the minute zodiacal dust particles. The second sensor consists of thin-film capacitors vacuum-deposited on both sides of the impact plate. The dielectric of the capacitors is a combination of  $\text{SiO}$  and  $\text{Al}_2\text{O}_3$ , about  $2 \mu$  thick. When a micro-particle impinges upon the plate and penetrates the dielectric of the sensor, a low impedance path through the dielectric momentarily occurs; the resulting voltage change across the capacitor is the electrical signal from the sensor denoting an impact. The impact plate is mounted on the spacecraft in such a manner that both sides of the detector are exposed to collisions of zodiacal dust. Signals from the capacitor sensors identify on which side of the plate an impact occurred.

Upon excitation, the crystal transducer generates a damped 100 kHz wave which is amplified, rectified and detected in the microphone amplifier. The resultant signal is applied to the input of the comparator, Z110-3 (see Fig. IV-2). When the amplitude of this signal is greater than the preset threshold, the output of the comparator

Z110-11 falls from 3 V to 0.1 V. This decreasing voltage is applied to a dual inverter, Z111-5, and the resultant increasing voltage from Z111-6 is used to start the 5-kHz clock, Z103. At the same time the signal from Z111-12 is used to trigger a 100- $\mu\text{s}$  positive-going one-shot, Z113. At the end of 100  $\mu\text{s}$ , the trailing/falling edge of the 100- $\mu\text{s}$  pulse (Z113-6) triggers Z115, a 30-ms one-shot. The positive-going output at Z115-6 activates the inhibit module Z109, whose outputs reduce the microphone amplifier gain to zero and thus prevent further signals from changing the amplitude of the detected signal. The peak detected amplitude of the initial signal will be attained before the end of 100  $\mu\text{s}$ , after which no signals will be accepted for 30 ms.

The maximum amplitude of the detected signal is generally attained between 50 and 70  $\mu\text{s}$  after particle impact and is the amplitude which decays through a precision RC network in the microphone-amplifier. As long as the detector output remains above the threshold of Z110-3, the 5-kHz clock applies pulses through Z104 to the three bit microphone-PHA (pulse-height analyzer) counter (Z121, Z122 and Z123). Z104 is enabled by Z107-6 at the end of each readout of the Z121-Z128 eight-bit register. After an impact and the above logic sequences occur placing PHA information in the readout register, the eight-bit accumulator is advanced one from the trailing edge of the 30 ms pulse, Z115-5 to Z129-7. Also, the trailing/falling edge of Z115-6 sets Z107-6 to a "0" state, disabling the NAND gate Z104, and preventing a further microphone PHA until the data in the register has been read out. The time for the decaying detector voltage to recross the Z110 threshold is thus a nonlinear function of the maximum amplitude of the microphone signal. When the threshold is recrossed, Z110-11 returns to 3 V; Z111-6 returns to 0.1 V; and, the clock is stopped until a new event. Only one microphone PHA is allowed during one readout period. However, if more than one event occurs during a readout period, the accumulator register will still advance from the toggle Z129-7 receives from Z115-5.

When the signal from the thin-film capacitor is amplified by Z146 or Z147 and exceeds the threshold set on the film trigger modules, Z101 or Z102, Z101-11 or Z102-11 rises from the "0" state to the "1" state causing a count to be put into the film accumulative counter (Z126, Z127 and Z128) through Z106. In addition, if a coincident film-microphone event has occurred, Z113-6 will have placed Z105-6 in an up state which allows the direct or retro film identification to be made in Z124 or Z125. The logic is so arranged that if there is no signal from Z113-6 at Z105-4, no film identification will occur; only a number in the film accumulator will occur.

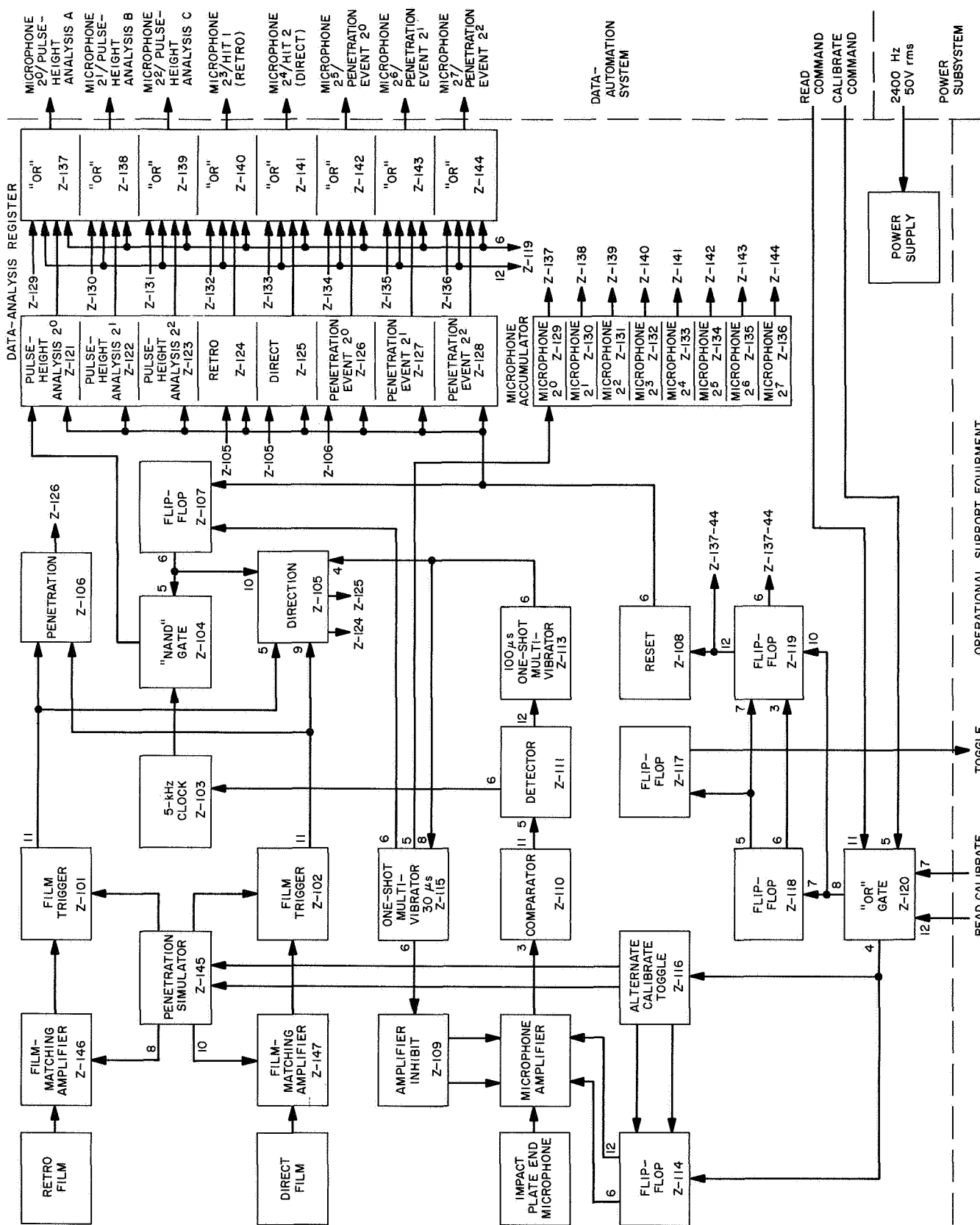


Fig. IV-2. Cosmic dust detector, functional block diagram

In summary, if an impacting zodiacal dust particle produces a detectable signal from the crystal transducer and one of the capacitor sensors, the following will occur:

- (1) The number in the microphone-accumulative eight-bit counter advances by one (via Z129-7).
- (2) A three-bit binary number, which is the PHA of the crystal transducer's detected signal, is stored in Z121-Z123. This is true only for the first hit after each readout.
- (3) The direction of the particle (capacitor identification) is stored in either Z124 or Z125 for the first event after readout only.
- (4) The film accumulator advances by one (via Z126). This three-bit counter accepts signals from either capacitor sensor and stores the total count between readouts. A film event is registered in the accumulator with or without a microphone coincident signal.

The experiment data is stored in two eight-bit registers. The accumulator for the microphone events comprises one of the registers (Z129 through Z136). This register is never reset. The microphone PHA data, film accumulator, and film identification comprise the information stored in the other register (Z121 through Z128), and is reset after every readout of the register.

The signals from these two storage registers are fed to logic modules Z137 through Z144 which perform an "OR" function so that the two registers are read out alternately upon readout command. The data readout is an eight-bit parallel readout with a 10- $\mu$ s 6-V pulse for a logical "1," and no pulse for a logical "0." The output pulses are applied to eight transformers; one output winding drives the data automation subsystem (DAS) of the spacecraft and the other winding is provided for monitoring the system by the operational support equipment (OSE).

Readout and calibrate commands may enter the experiment from either the DAS or OSE. The DAS readout command enters Z120-11 and produces a pulse at Z120-8; and the similar OSE command enters Z120-12 to produce the same pulse at Z120-8. If Z118-5 is in a logical "1" state, the Z120-8 pulse passes through Z119, appearing at Z119-12 where it strobes the logical "OR" gates Z137 through Z144 and transfers the data stored in the eight-bit register, Z121 through Z128. The trailing edge of this

strobing pulse produces a negative spike at Z108-6, which resets Z121 through Z128 so the register can accept new data. Z107 is also reset so that Z107-6 is in a logical "1" state, which enables Z104 and allows the PHA data of the first event after readout to be transferred to the data storage register.

The trailing edge of the positive pulse at Z120-8 changes the state of Z118 so that the next readout pulse will now appear at Z119-6. The pulse strobes the output "OR" gates again, but now transfers the data stored in the Z129 through Z136 register. The trailing edge of the readout pulse again changes the state of Z118 so that the next readout command will result in data from the microphone accumulator register. The experiment uses sixteen bits to store the data from the sensors. This information is alternately fed to the DAS in eight-bit groups.

A calibrate command is used for an in-flight calibration of the instrumentation. The calibration simulates an impact by feeding electrical signals to the inputs of the sensor amplifiers. The two film amplifiers are pulsed alternately while the pulse to the microphone amplifier alternately varies between two levels to provide a two-point check on the PHA system. The calibrate system operates in the following manner. The calibrate command pulse is received by the "OR" gate (Z120) from either the DAS or OSE. The pulse from Z120-4 drives Z114-7. The positive driving pulse causes either Z114-6 or Z114-12 to fall, depending on the state of Z116. The trailing edge of the Z120-4 pulse toggles Z116-7 and changes the state of Z116 at the end of the calibrate pulse, thus setting the state of Z114 for the next calibrate. The outputs of Z114 are divided down differently so that pulses of two different amplitudes are alternately applied to the microphone sensor input, thus simulating two levels of impact impulse. The shifting of the Z116 flip-flop sends signals to the penetration simulator module, Z145, and results in a signal being alternately fed to the two films by Z145-8 or 10. The above signals and logic occur within 10  $\mu$ s; thus, the simulation is fast enough for the event to be considered a single coincident impact as far as the logic circuits in the experiment electronics are concerned.

## D. Instrument Calibration

The instrument received low and high velocity calibrations. The high velocity calibrations were done using an electrostatic micro-particle hypervelocity accelerator. The minute particles used were iron spheres with diameters in the range of 1  $\mu$ . A typical set of fifty impacts during one calibration period contained particles having

the following ranges of mass ( $m$ ), velocity ( $V$ ) and momentum ( $p_i$ ) with the  $p_i$  referring to particle momentum prior to impact:

$$1.8 \text{ p-g} \leq m \leq 100 \text{ p-g}$$

$$1.6 \text{ km/s} \leq V \leq 6.7 \text{ km/s}$$

$$1.2 \mu \text{ dyn-s} \leq p_i \leq 26 \mu \text{ dyn-s}$$

In general, the value of  $p_i$  for the particles obtainable in the accelerator is below the threshold set for the A/D conversion in the experiment electronic instrumentation. This level is always a conservative one taking into consideration all possible protection against noise. With the accelerator, the signals due to impacts were observed in an analog state, and pulses from particles with  $p_i$  as low as  $5 \mu \text{ dyn-s}$  were observed.

The capacitor sensor was impacted using the iron spheres accelerated by the hypervelocity accelerator. These iron spheres penetrated the capacitor producing pulses from this sensor. The iron spheres used for these firings had momentums considerably less than required for microphone PHA level 1. Therefore, this sensor is more sensitive than the microphone sensor. However, this has to be qualified because the only particle it was possible to use was iron; thus, the capacitor calibrating statements are true only for minute iron particles.

The other calibration technique used particles of low velocity and greater mass. For example: a  $50\text{-}\mu\text{g}$  glass sphere which is dropped from a height of 1 cm from the plate (velocity vector normal to the plate) delivers an impulse of  $3 \times 10^{-3} \text{ dyn-s}$  (including the use of an effective coefficient of restitution). By using this technique and its possible variations in conjunction with the high velocity information, the threshold levels, in terms of  $p_i$  and normal incidence to the plate, were determined for the different PHA levels and are shown in Table IV-1. Level 8

**Table IV-1. Threshold levels in terms of momentum of particles for different PHA levels**

PHA level	$p_i, \text{ dyn-s} \times 10^{-5}$
1	$6.0 \pm 0.7$
2	$18.5 \pm 2.2$
3	$35.5 \pm 4.2$
4	$57.5 \pm 6.7$
5	$82.0 \pm 9.6$
6	$115.0 \pm 13.0$
7	$150.0 \pm 18.0$
8 <sup>a</sup>	$196.0 \pm 23.0$

<sup>a</sup>Saturated condition.

denotes the largest impulse received and is saturation for the system. The three-bit PHA counter is allowed to go past a logical "111" to "000" and then stop. If the microphone accumulator has advanced by one, and the adjacent PHA readouts show a microphone PHA of "000," then level 8 occurred.

## E. Trajectory

**1. Spacecraft position in space/time.** The spacecraft, *Mariner IV*, was injected into the earth-Mars transfer trajectory on November 28, 1964 at 15:07:57 GMT. At this time the earth was at 66.4-deg celestial longitude and was very nearly in the ecliptic plane. Mars encounter occurred on July 15, 1965 at 01:01 GMT (closest approach) when Mars was at 227.8-deg celestial longitude and was very nearly in the ecliptic plane. For practical purposes, one can consider the plane of the nominal spacecraft trajectory as lying in the ecliptic plane. (Figure IV-3 shows the distance above the ecliptic plane as a function of longitude.) Figure IV-4 is a polar plot of the flight path with the sun at the origin. The relative positions of earth and Mars to the spacecraft at various times are shown with the connecting dashed lines denoting simultaneous positions. It can be seen that the spacecraft is overtaken by the earth at some point and that Mars passes the spacecraft at encounter, so that the spacecraft as seen from Mars approaches the planet, generally, from ahead and from the solar direction.

Within a few planet radii of earth and Mars, the trajectory is influenced by the gravitational attraction of these

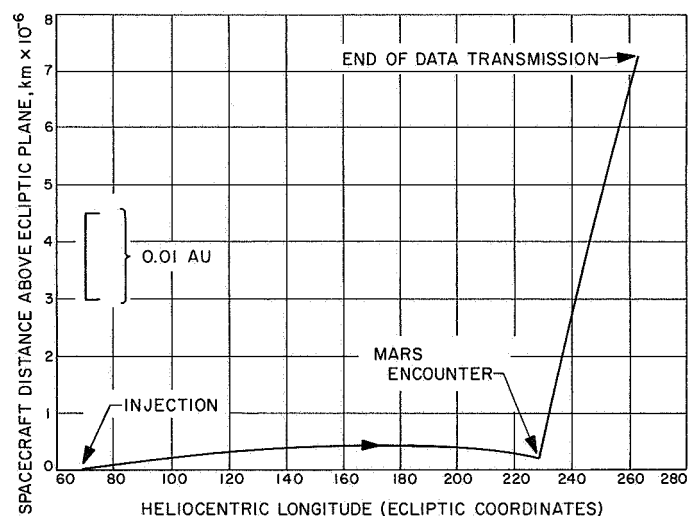


**Fig. IV-3. Mariner IV heliocentric longitude vs spacecraft distance above ecliptic plane**

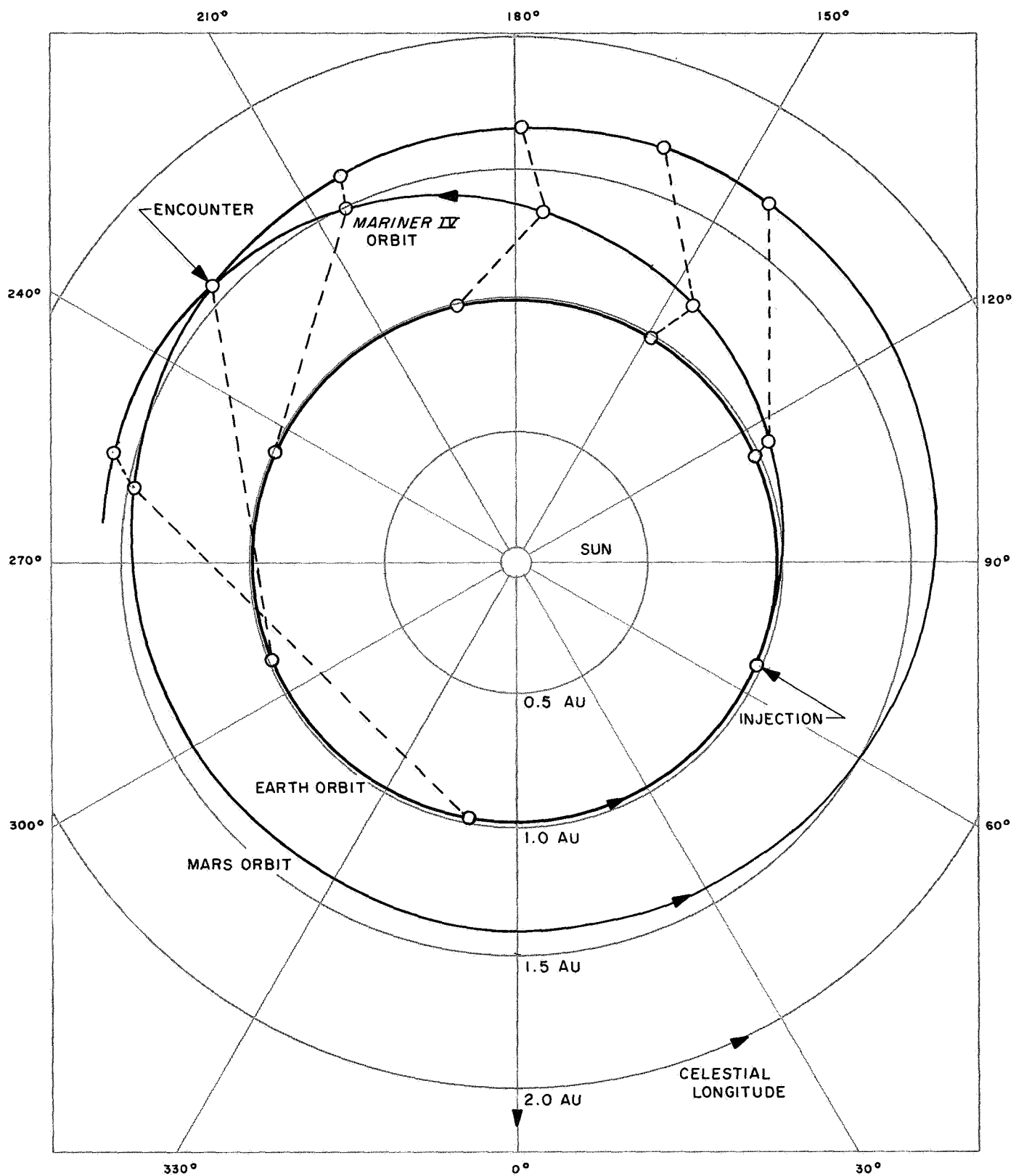


Fig. IV-4. Polar plot of spacecraft flight path with sun at origin

bodies, but for purposes of analysis of the interplanetary data, the transfer trajectory may be described as a sun-centered elliptical orbit. The equation of the orbit can be assumed to have the well known polar form of

$$r = \frac{a(1-e^2)}{1 + e \cos \nu} \quad (1)$$

where

$a$  = semi-major axis of the ellipse

$r$  = magnitude of the sun-spacecraft radius vector

$e$  = eccentricity of the ellipse

$\nu$  = angle measured eastward from perihelion to the sun-spacecraft radius vector of interest

The values of the pre-encounter parameters for *Mariner IV* are:

$$a = 1.9093 \times 10^8 \text{ km}$$

$$e = 0.2275$$

which, when substituted in Eq. (1) gives

$$r = \frac{1.8105 \times 10^8}{1 + 0.2275 \cos \nu} \text{ km} \quad (2)$$

Other elements to locate the orbit in space are:

$$\omega = \text{argument of perihelion} = 352.56 \text{ deg}$$

$$\Omega = \text{longitude of the ascending node} = 68.67 \text{ deg}$$

$$i = \text{inclination} = 0.126 \text{ deg}$$

$$T = \text{epoch of perihelion passage} = \text{November 23, 1964 at 23:10:59 GMT}$$

Since the inclination is negligible for our purposes, we can express the longitude of perihelion as  $\Omega + \omega$ . Let  $\lambda$  = celestial longitude measured eastward from the vernal equinox,  $\gamma$ . Then, the celestial longitude for any spacecraft position along the orbit is

$$\lambda = \Omega + \omega + \nu = 61.23 \text{ deg} + \nu$$

An alternate form of Eq. (2) using celestial longitude is

$$r = \frac{1.8105 \times 10^8}{1 + 0.2275 \cos (\lambda - 61.23 \text{ deg})} \text{ km} \quad (3)$$

(assuming  $r$  to always lie in the ecliptic plane).

The magnitude of the effect on the spacecraft trajectory by Mars passage can be appreciated by comparing the aphelion range and longitude calculated by Eq. (3) with actual tabulated values:

$$\text{calculated } r = 2.3437 \times 10^8 \text{ km}, \lambda = 241.23 \text{ deg}$$

$$\text{actual } r = 2.351 \times 10^8 \text{ km}, \lambda = 247.07 \text{ deg}$$

Since the spacecraft passed Mars over the southern hemisphere of the planet, the trajectory received an upward kick (see Fig. IV-3) increasing the inclination of the orbit to about 2.5 deg and rotating  $\Omega$  to about 227 deg.

To aid in analyzing time-tagged data, it is useful to know the spacecraft position as a function of time. Figure IV-5 is a plot of heliocentric range  $r$  and longitude  $\lambda$  as a function of earth days elapsed flight time. These values are taken from the actual *Mariner IV* ephemeris and may differ slightly from those derived from Eq. (3) and the epoch of perihelion.

**2. Cosmic dust sensor attitude in space.** Previously described were the position of the spacecraft (SC) in space with respect to the heliocentric ecliptic coordinates and a basis for an ephemeris to determine a date and time for a given position. This section deals with the spacecraft-fixed orientation of the sensor with respect to these coordinates and to the spacecraft space-fixed velocity vector.

The detection of a dust particle occurs when the particle impacts on the microphone plate. Inherently, the instrument is most sensitive to a particle arriving at right angles to either side of the plate, so we are especially interested in what happens to the orientation of the plate normal, both in the direct and retrograde directions and in the possible angles of accessibility to the plate.

The SC roll-axis is kept aligned with the sun-SC radius vector by the attitude control system, and the roll attitude is controlled by keeping the Canopus sensor's projection in the SC roll plane aligned with the star Canopus. The cosmic dust sensor plate is mounted in the roll axis-Canopus sensor plane. Figure IV-6 is a photograph of a *Mariner* model as seen looking along the plate-normal as the SC is approaching Mars. From this geometry, the plate-normal is seen to generally lie along the path of SC motion, but the eccentricity of the orbit and the fact that Canopus lies 14.16 deg away from the ecliptic south pole cause the plate-normal to vary somewhat in its angles to the ecliptic plane and to the velocity vector.



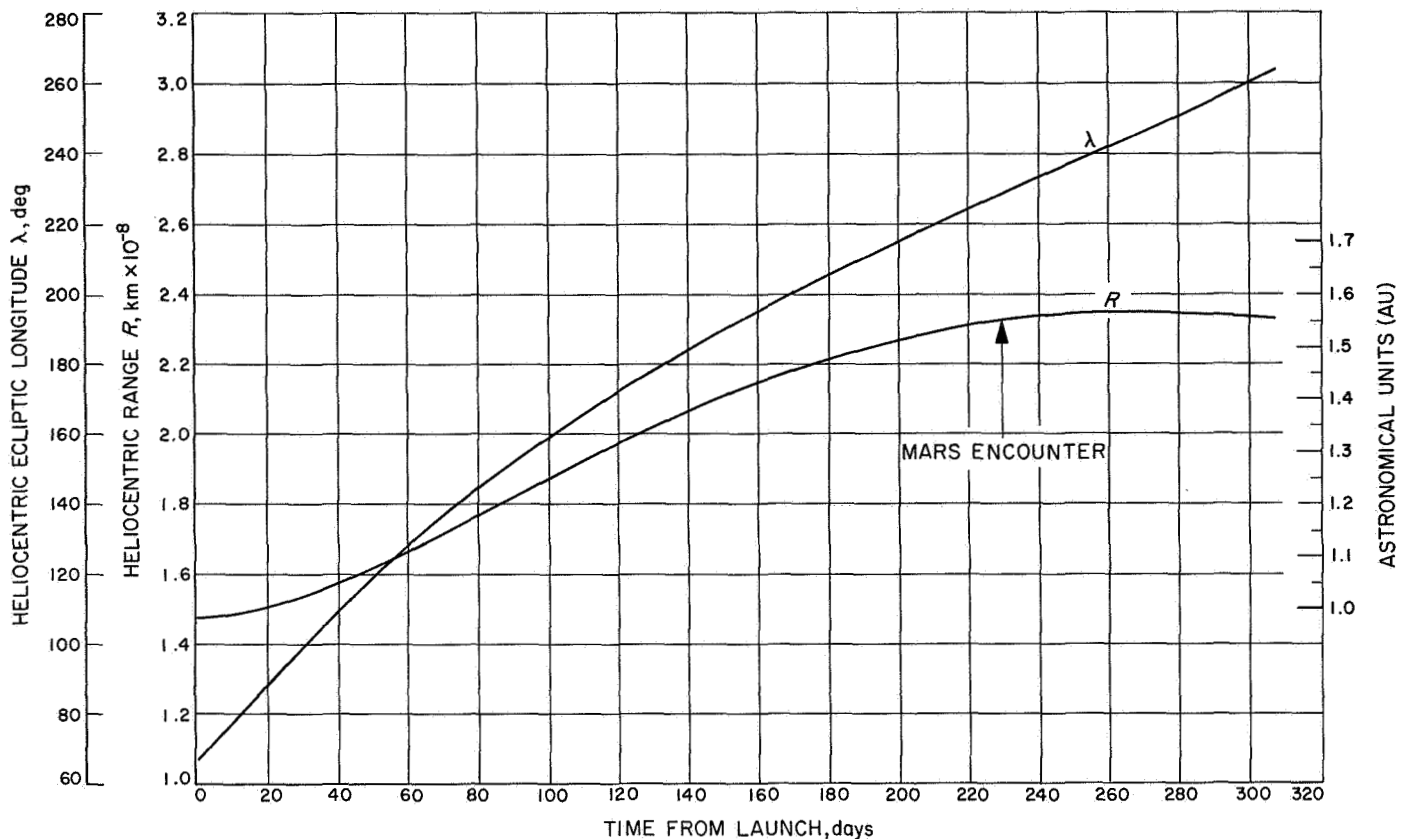


Fig. IV-5. Mariner IV heliocentric range and longitude vs time

Two assumptions can be immediately drawn concerning the plate-normal and the velocity vector:

- (1) The plate-normal always lies perpendicular to the sun SC radius vector and varies a few degrees in its angle to the ecliptic as the SC rolls to keep Canopus in view.
- (2) The velocity vector always lies very nearly in the ecliptic plane and varies a few degrees in its angle to the local heliocentric horizontal during flight.

In the illustration of Fig. IV-7,

$\hat{n}$  = unit vector along plate normal

$\vec{V}_s$  = SC velocity vector

$\vec{r}$  = sun-SC radius vector

$\chi_n$  = angle between  $\hat{n}$  and ecliptic plane

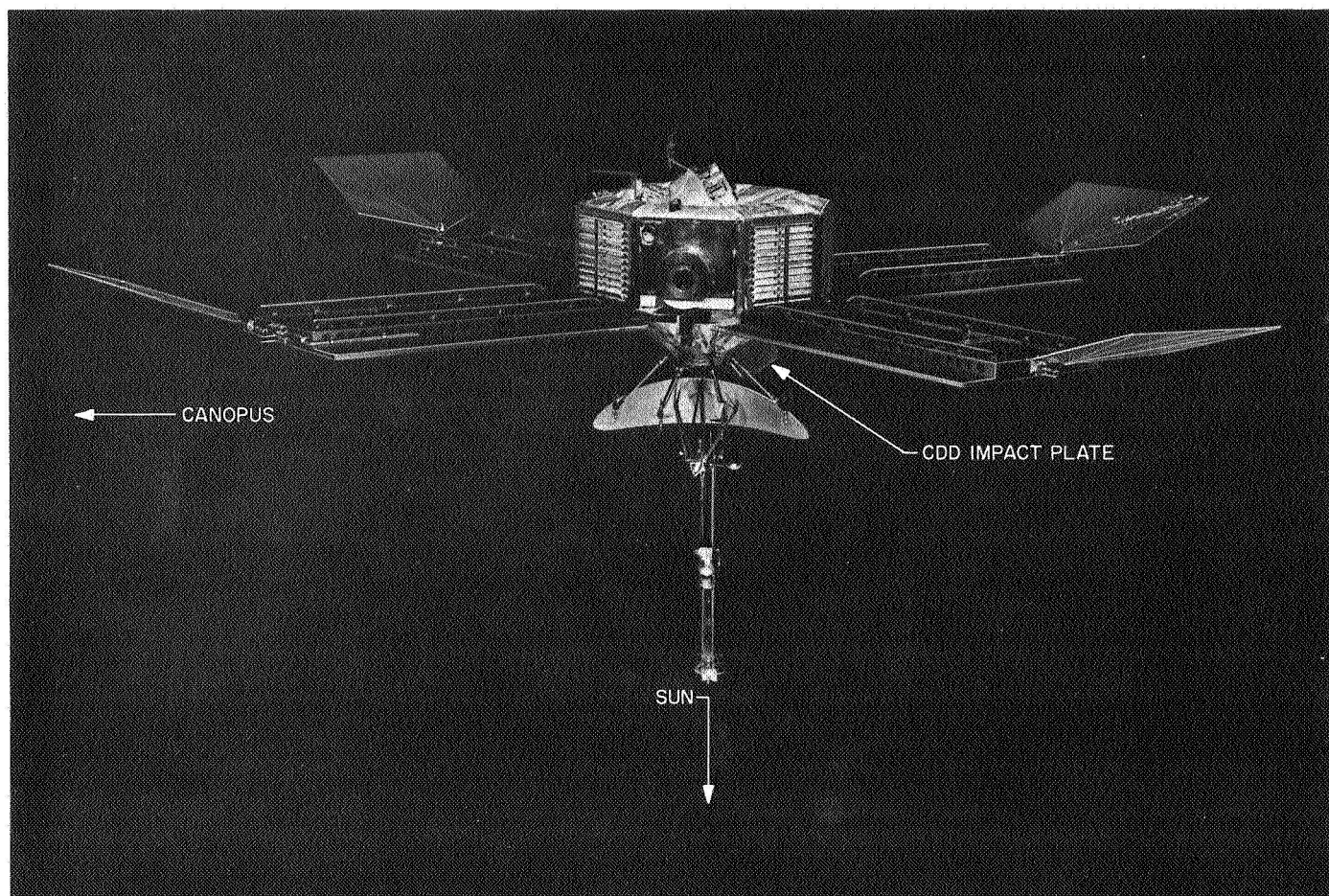
$\psi_s$  = angle between  $\vec{V}_s$  and local horizontal

Figure IV-8 is a plot of  $\chi_n$  and  $\psi_s$  as a function of days of flight, and Fig. IV-9 shows  $|\vec{V}_s|$  vs time.

The accessibility of a dust particle to the cosmic dust sensor plate is determined by: the relationship of the particle's velocity vector with respect to the spacecraft; the angle between this relative velocity vector and  $\hat{n}$ ; and the shielding effect of the spacecraft. To aid in describing the geometry of accessibility, it will be convenient to define a unit sphere with the sensor plate at the origin and the unit vector  $\hat{n}$  along the polar axis. The coordinates are defined such that  $\hat{l}$  is a unit vector directed outward along the SC heliocentric radius vector,  $\hat{n}$  is already defined, and  $\hat{m} = \hat{n} \times \hat{l}$ . ( $\hat{m}$  is directed toward the projection of Canopus in the local heliocentric horizontal.)

The path of a colliding particle can be visualized as a straight line entering the surface of the hypothetical sphere and ending at the origin. Since the particle's SC centered velocity vector lies along this line, the position of entry on the sphere describes the orientation of the vector in the sensor-centered coordinate system. Conversely, a set of values for the sensor-centered coordinates allowing measurable impacts describes the relative velocity vectors of particles having access to measurement.





**Fig. IV-6. View of the CDD impact plate as *Mariner IV* approaches Mars**

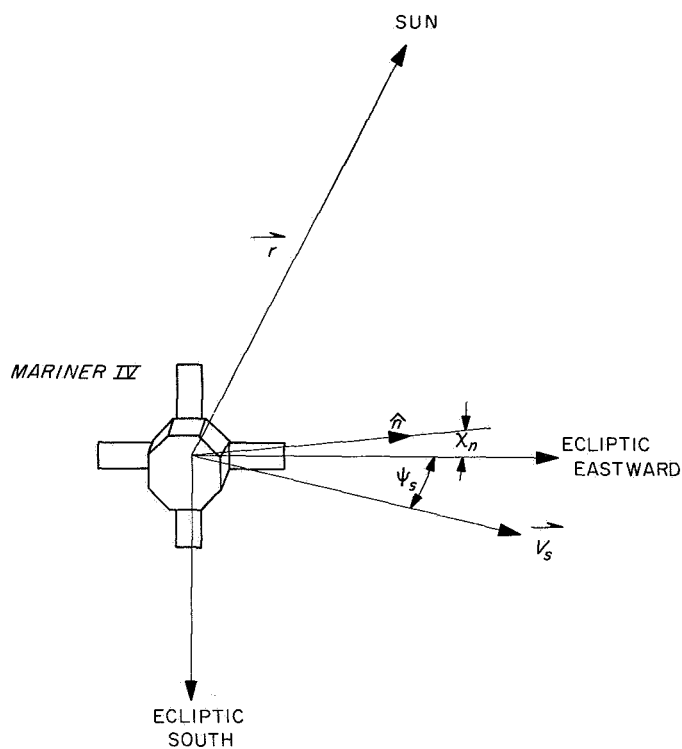


Fig. IV-7. Geometrical illustration of the relationships of the plate-normal  $\hat{n}$  and the heliocentric velocity vector  $\vec{V}_s$  in the heliocentric ecliptic system

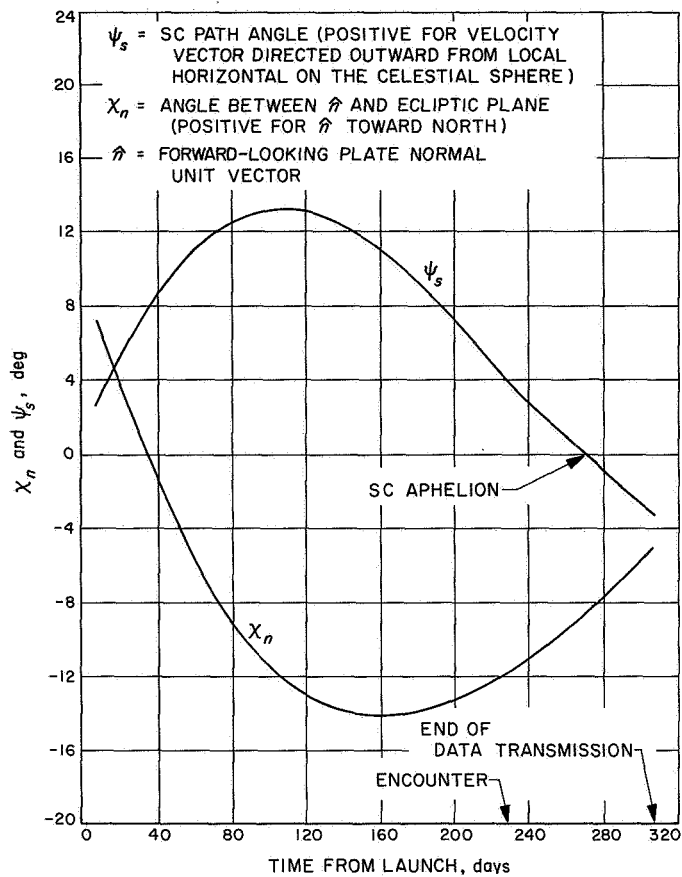


Fig. IV-8.  $X_n$  and  $\psi_s$  vs time from injection

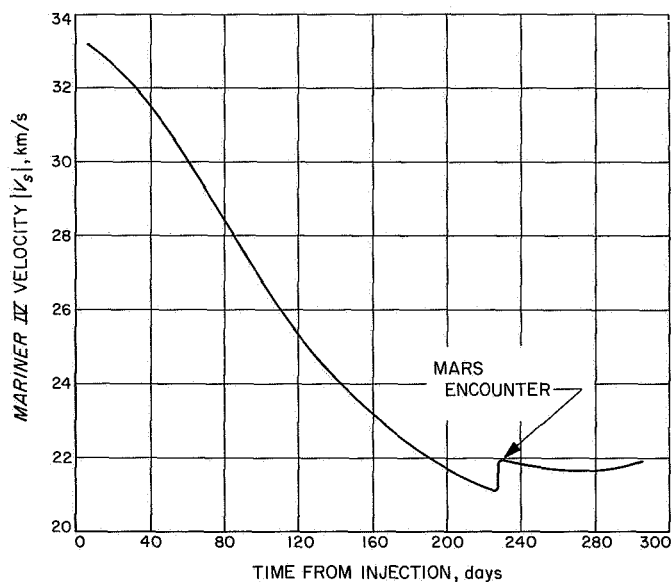


Fig. IV-9. Mariner IV scalar heliocentric velocity vs time

It will be convenient to define a co-latitude angle,  $\phi$ , measured from  $+\hat{n}$  (forward plate normal) to the position of interest on the unit sphere and longitude angle,  $\theta$ , measured in the right-hand direction from the  $\hat{l}\hat{n}$  plane to the point of interest. Figure IV-10 illustrates the geometry where the vector  $\vec{V}$  represents the relative velocity of an impacting particle entering the sphere at the small open circle. Using this system, we will define the accessibility to the sensor-plate as a contour line about  $+\hat{n}$  and  $-\hat{n}$  (retro-looking direction) on a plot showing the co-latitude and longitude lines projected in the  $\hat{l}\hat{m}$  plane (plane of the sensor-plate).

In the plot of Fig. IV-11, the forward-looking projection is shown so that  $+\hat{n}$  can be considered coming out of the paper at the origin. The heavy contour line represents the extent of the maximum  $\phi$  as a function of  $\theta$  for impact velocity vectors of measurable impacts. Particles entering outside this contour can be considered as not contributing to the measurement data. The uncertainty in locating the contour is approximately 5 deg in  $\phi$  and 5 deg in  $\theta$ . The two factors determining the contour limits are:

- (1) The lowest grazing angle ( $90 \text{ deg} - \phi$ ) of particle paths for which the instrument is sensitive.
- (2) The portions of the sensitive sector which are obscured (or shielded) by the physical location of the vehicle and its attachments.

The uncertainties mentioned are consistent with calibration accuracy and data-reduction capability at these limits and are considered reasonable approximations. Figure IV-12 is a similar plot for the retrograde or rear-looking side of the sensor, where  $-\hat{n}$  is perpendicular to the plane of the plot toward the viewer.

The relative particle velocity vector is

$$\vec{V} = \vec{V}_p - \vec{V}_s \quad (4)$$

where  $\vec{V}_p$  and  $\vec{V}_s$  are the heliocentric particle and SC velocities, respectively.

Since  $\vec{V}$  is directed inward, the direction cosines of the hypothetical point of entry on the unit sphere will be negative to those of the approach velocity vector itself. If we break  $\vec{V}$  into its components along  $\hat{l}$ ,  $\hat{m}$ , and  $\hat{n}$ ,

$$\tan \theta = \frac{V_m}{V_l} \quad (5)$$

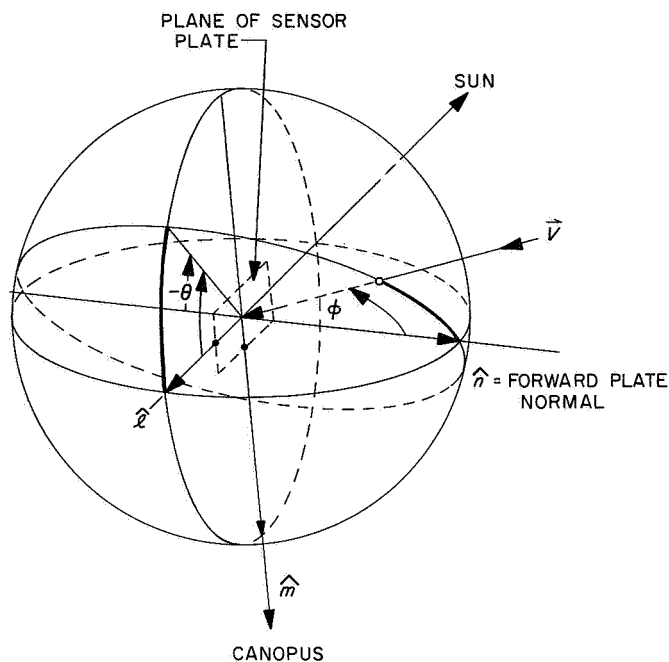


Fig. IV-10. Spherical geometry used to describe particle path relative to the sensor impact plate

and

$$\cos \phi = - \frac{V_n}{|V|} \quad (6)$$

For particles approaching the SC in retrograde motion (frontal impact),  $\cos \phi$  is positive ( $V_n$  is negative), and particles in direct relative motion result in a negative value ( $90 \text{ deg} < \phi < 180 \text{ deg}$ ) which is the condition for impact on the rear side of the plate. For a particle of heliocentric velocity  $\vec{V}_p$ , let:

$V_{p\lambda}$  = component at  $90 \text{ deg}$  to  $\vec{r}$  in the plane of particle motion

$V_{pr}$  = component along  $\vec{r}$

$i_p$  = inclination of its plane of motion to the ecliptic

$V_{p\lambda}$  is positive for conventional direct orbital motion,  $V_{pr}$  is positive in the direction of the radius vector (away from the sun), and  $i_p$  is positive at the ascending node and negative at the descending node (the SC position at time of impact is assumed to be very near a node of the particle's trajectory). Then

$$V_n = V_{p\lambda} \cos(i_p - \chi_n) - |V_s| \cos \psi_s \cos \chi_n \quad (7)$$

$$V_m = |V_s| \cos \psi_s \sin \chi_n - V_p \sin(i_p - \chi_n) \quad (8)$$

$$V_l = V_{pr} - |V_s| \sin \psi_s \quad (9)$$

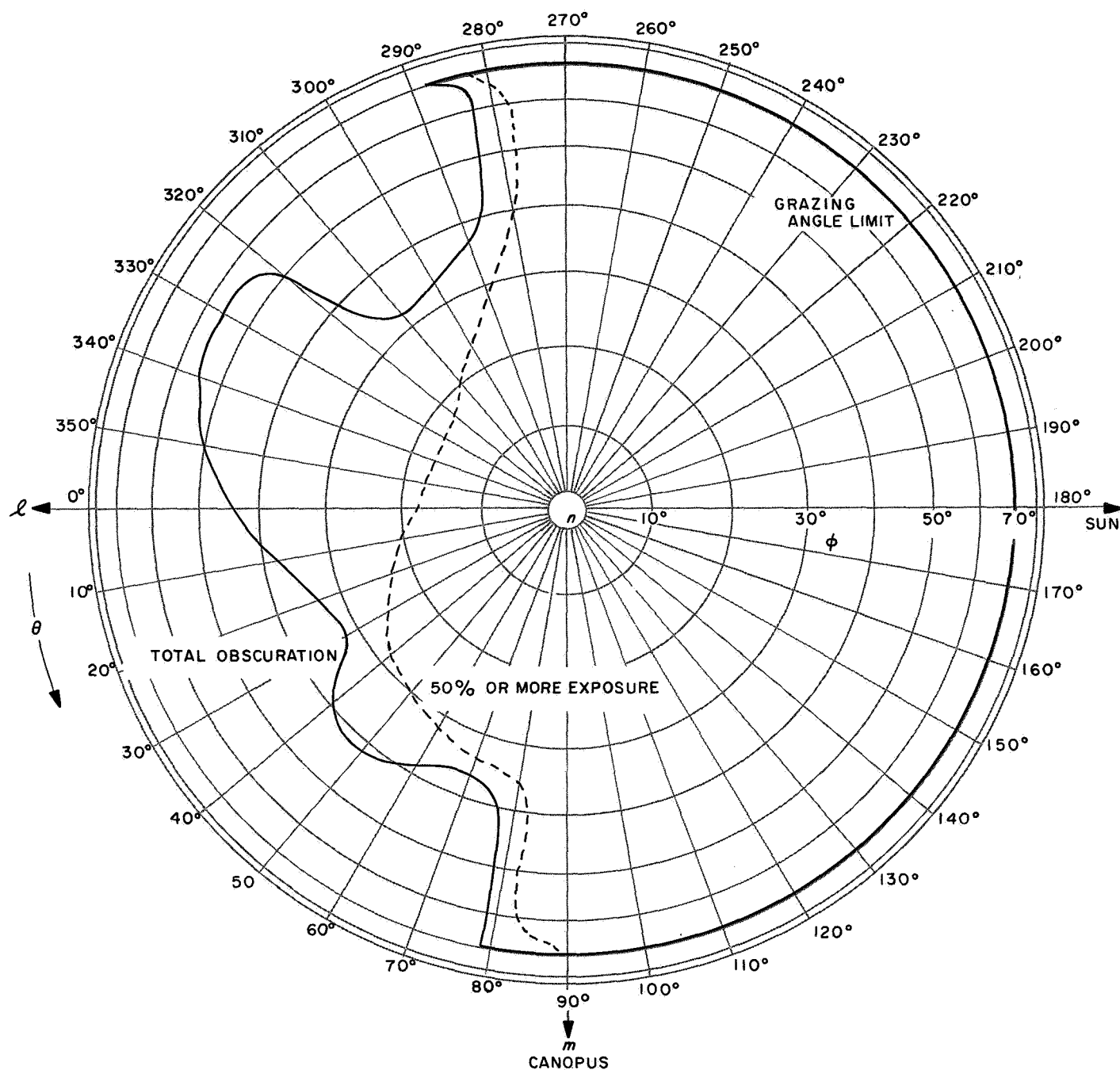


Fig. IV-11. Contour of accessibility-to-measurement of the forward-looking plate surface, *Mariner IV* CDD (projection of sensor-centered spherical coordinates on plane of impact plate)

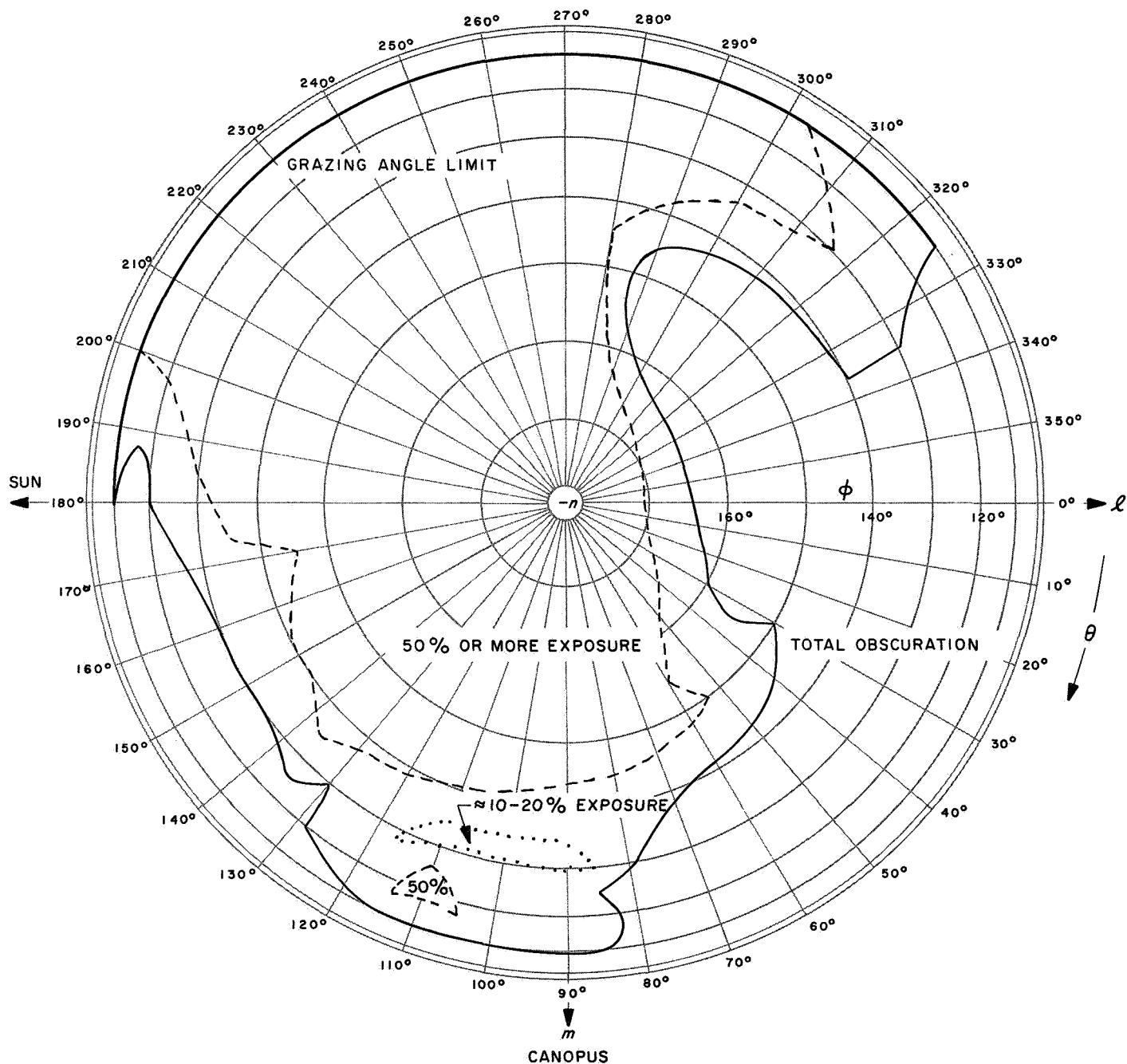


Fig. IV-12. Projection of the rear-looking contour of accessibility on the plane of impact plate

These equations relate the particle velocity vector to the angles of accessibility plotted in Figs. IV-11 and IV-12.

To illustrate the use of the plots and the relationships, consider the Geminid meteor stream. According to various listings, the orbital elements of the stream are approximately:

$$\begin{aligned}\omega_p &= 324 \text{ deg} \\ \Omega_p &= 260 \text{ deg} \\ i_p &= 24 \text{ deg} \\ a_p &= 1.39 \text{ AU} = 2.08 \times 10^8 \text{ km} \\ e_p &= 0.899\end{aligned}$$

Calculations of  $r$  at the descending node ( $\lambda = 80 \text{ deg}$ ) and reference to Fig. IV-5 show that the spacecraft should pass through the vicinity of the stream at a time centered on the 12th day from launch (December 10, 1964). To compute the relative velocity components,  $V_{p\lambda}$  and  $V_{pr}$  can be determined from the conic relationships:

$$V_{p\lambda} = \frac{\sqrt{p_p \mu}}{r} \quad (10)$$

and

$$V_{pr} = e_p \frac{\mu}{p_p} \sin \nu$$

$$(\nu = 540 \text{ deg} - \omega_p = 213 \text{ deg for descending node}) \quad (11)$$

where

$$p_p = a_p (1 - e_p^2) \text{ for the periodic orbit}$$

and

$$\mu = 1.327 \times 10^{11} \text{ km}^3/\text{s}^2$$

Solution of Eq. (10) and (11) gives  $V_{p\lambda} = 15.8 \text{ km/s}$  and  $V_{pr} = -30.4 \text{ km/s}$ .

$|V_s|$ ,  $\psi_s$  and  $\chi_n$  are taken from Figs. IV-8 and IV-9 for the date of interest.

Substituting in Eqs. (7), (8), and (9) and noting that the sign of  $i_p$  in Eqs. (7) and (8) is negative for the de-

scending node, we obtain

$$\begin{aligned}V_i &= -32.5 \text{ km/s} \\ V_m &= 10.9 \text{ km/s} \\ V_n &= -19.1 \text{ km/s} \\ |V| &= V_i^2 + V_m^2 + V_n^2 = 39.3 \text{ km/s}\end{aligned}$$

The negative sign of  $V_n$  shows that particles encountered will approach the spacecraft in retrograde relative motion, so that  $\phi$  is less than  $90 \text{ deg}$ . Equation (6) gives  $\phi = 61 \text{ deg}$ . The signs of  $V_m$  and  $V_i$  place the *entry* point in the 4th quadrant of the  $lm$  plane, and from Eq. (5) we get  $\theta = 341 \text{ deg}$ . Referring to Fig. IV-11, the entry point located by these angles lies outside the contour of accessibility; particles unique to the Geminids are, therefore, not measurable for the given orbital elements.

## F. Data from the Experiment

As the DAS frame counter went from 2047 to zero, it sent the in-flight experiment calibration command to the electronics. Except for the early portion of the mission, this resulted in a calibration about every 1.19 days. Since the calibrates throughout the mission were all proper, it is assumed that the electronic instrumentation functioned correctly. After encounter, there were several periods where the capacitor sensors were noisy. However, these signals did not interfere with the data from the acoustic transducer.

The acoustic transducer will respond to acoustic events other than an impulse delivered to the plate by an impacting micro-particle. Major sources for such anomalous responses are:

- (1) Normal in-flight mechanical functions of the spacecraft system.
- (2) "Creaks" in the structure caused by thermal expansion and contraction.
- (3) Particle impacts on surfaces other than that of the sensor plate.

The degree of instrument sensitivity to a given anomalous event depends on the distance from the sensor to the source, the ease of acoustic propagation through the structure, and the amplitude-time characteristics of the event. To minimize such sensitivity, the sensor design incorporates a considerable amount of acoustic isolation, and the microphone amplifier frequency response excludes events having excitation frequency components below about  $100 \text{ Hz}$ .

The mass of pre-launch test data shows that mechanical functions can be disregarded for the entire mission profile. Tests in the space simulator showed that thermal causes must be considered, particularly during the first few hours following launch when the spacecraft experienced a relatively rapid temperature transient and again

during midcourse maneuver. From the test data (see Fig. IV-13) a total of 4 false measurements can be predicted for the period immediately following launch. The time distribution and magnitude of the in-flight data during this short near-earth period compared with test data (see Fig. IV-14) indicate that approximately 25% of

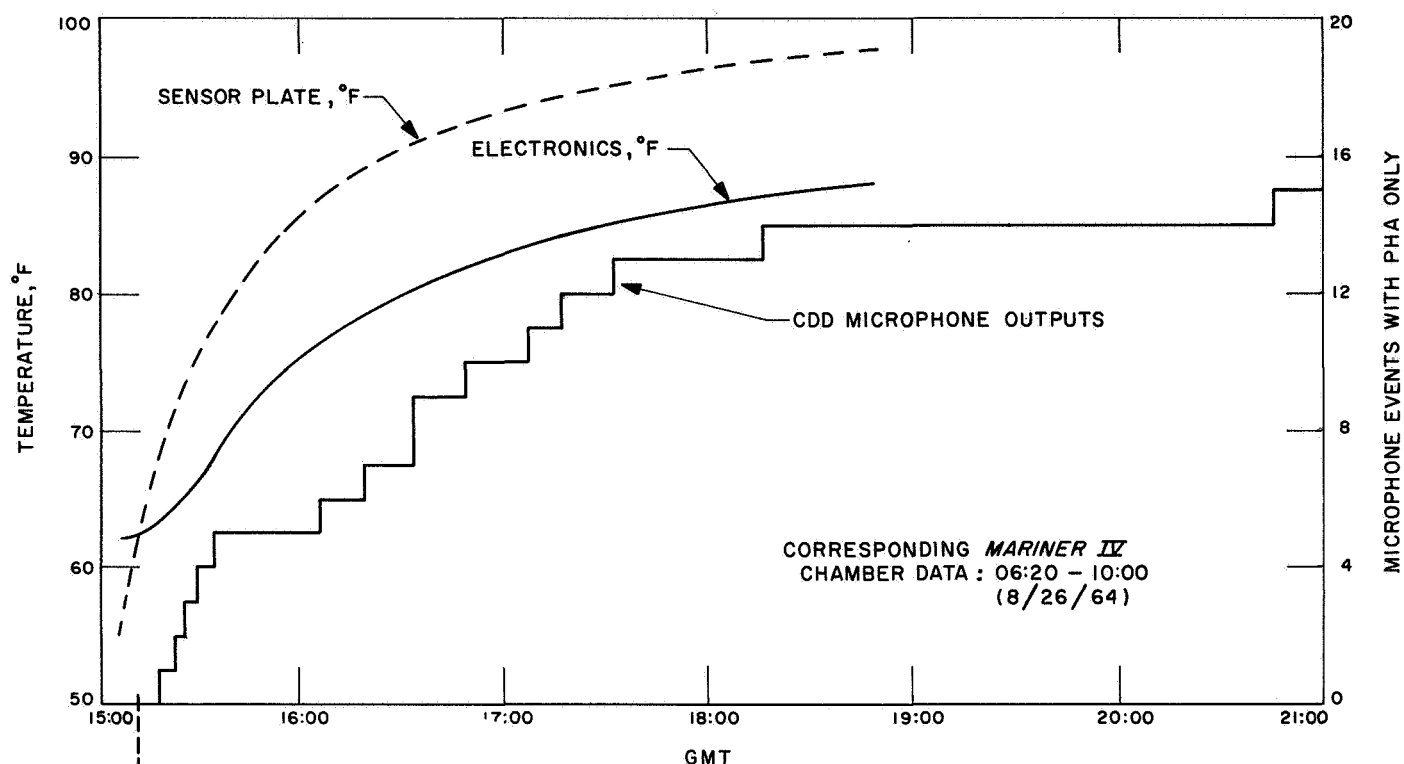


Fig. IV-13. Mariner IV CDD, solar simulator data, August 26, 1964

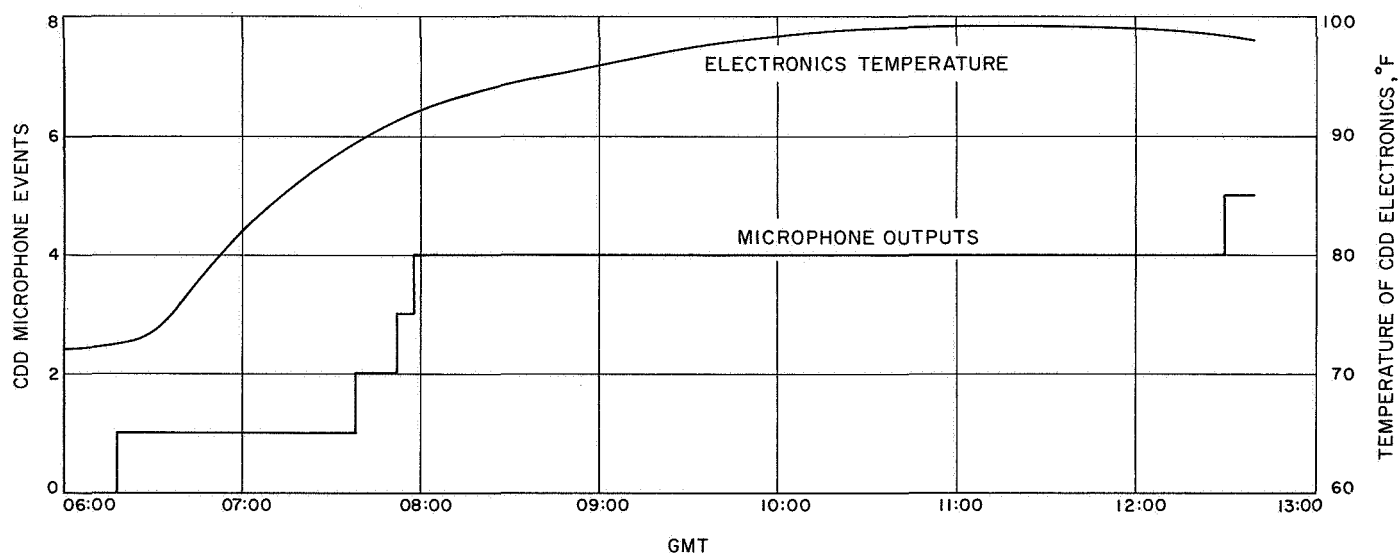


Fig. IV-14. Mariner IV CDD, estimated launch-temperature history

the indicated impacts during any time increment between 15:12 and 19:00 GMT on November 28, 1964 can be assumed to be a result of temperature "creaks."

Studies have recently been made concerning thermal gradient effects on ceramic transducers by Bohn (Ref. 7). Figure IV-15 shows the temperature range experienced by the acoustical sensor. The thermal gradient varies between 0.025°C/day and 0.2°C/day. The laboratory studies do not show sensor related thermal noise under these conditions. The possible contributions from this source are considered negligible except for a brief period following midcourse motor burn on December 5, 1964. Between 16:15 and 16:20 GMT on this date, six events were registered in comparatively rapid succession, which are assumed to be the result of the large, rapid temperature transient associated with the motor firing. (No mechanical interference was recorded during motor-burn because the instrument was turned off during the actual firing.)

To estimate the effect of particle impacts on surfaces other than those of the sensor, tests were performed to obtain a reasonable estimate of the effective mechanical isolation of the sensor from the spacecraft. Impulses of magnitude large enough to obtain a response from the cosmic dust detector were applied at various points on the spacecraft. By means of the test data, an isolation constant  $I$  (ratio of applied impulse to instrument momentum indication) was evaluated for each point. The values for  $I$  varied from a low of approximately  $10^8$  for points closely adjacent to the sensor to  $5 \times 10^8$  at the mid-point of the solar panels. From these results and from the characteristics of the measured data, an approximate prediction of indirect-impact contributions to the in-flight

measurements can be calculated in the form of a probability. The average number  $N_p$  of particle impacts per unit time over the area  $A_p$  of the sensor plate is

$$N_p = \Phi A_p \quad (12)$$

where  $\Phi$  is the average influx rate per unit area at the location of the spacecraft. From the in-flight data, the cumulative influx rate  $\Phi_c$  (a measure of total influx consisting of all particles having a momentum  $M$  and larger) can be related to the particle momentum over the measurement range by

$$\Phi_c = KM^\beta$$

where  $K$  and  $\beta$  are empirical constants. Then, Eq. (12) becomes

$$N_p = KM^\beta A_p \quad (13)$$

where  $N_p$  is now the number of particles of momentum  $M$  and larger, per unit time.

To cause an instrument output corresponding to a particle of momentum  $M$ , a particle impacting on a non-sensitive surface would have a momentum of  $MI$ . Then, the number  $N_s$  of these indirectly detected impacts is

$$N_s = K(MI)^\beta A_s \quad (14)$$

where  $A_s$  is the effective cross-sectional area of the spacecraft's hard surface.

The probability that a given detected impact is an indirect hit is

$$q = \frac{N_s}{N_p + N_s} \quad (15)$$

So, from Eqs. (13) and (14),

$$q = \frac{A_s I^\beta}{A_p + A_s I^\beta}$$

Since  $I$  is a function of position, a mean value for the cross-section used is selected. The selection of  $A_s$  is more difficult since the entry angle distribution is not known; however, a mean value here seems reasonable based on the relationships derived from the test data. The value for  $\beta$  is also difficult, since  $\beta$  varies somewhat as a function of spatial position of the spacecraft. We must also

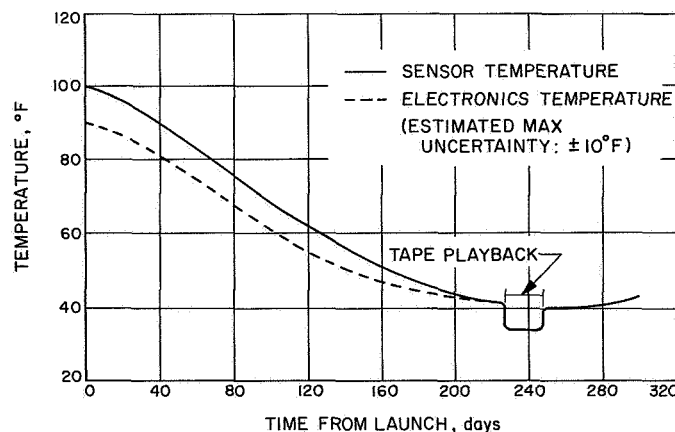


Fig. IV-15. Mariner IV CDD, estimated flight temperatures



extrapolate  $\beta$  considerably out of the dynamic range of the instrument. For this computation, a value of  $\beta$  of  $-0.5$  is used, which is considered a worst case. The values selected are:

$$A_p = 0.07 \text{ m}^2$$

$$A_s = 7 \text{ m}^2$$

$$I = 4 \times 10^6$$

$$\beta = 0.5$$

from which  $q \approx 0.05$ . Therefore, a 5% contribution to the measurement by comparatively large indirect impacts on the spacecraft is considered an upper limit for any time increment.

The data from the experiment for each event (impact) is given in Table IV-2. The time, event (impact) number, and PHA level define the impact. The data in Table IV-2 do not contain any events shown in Fig. IV-14. The last event shown in Fig. IV-14 occurred about 5 h and 40 min after experiment turn-on, or at 20:47 GMT. The next impact occurred over 12 days later and is event 1 in Table IV-2. The notation NPHA is used for an event when there was no PHA data. This happened most frequently when there was a data gap due to no reception of transmission from the spacecraft. Since the microphone-accumulator is never reset and the time of each calibrate command known, the number of events during a data gap is known. Of the 241 impacts, only 23 are without PHA information.

Table IV-2. Data from CDD experiment by time, event No., and PHA level

Mission day	GMT			Event no.	PHA level		Mission day	GMT			Event no.	PHA level
	'64 day	h	min					'65 day	h	min		
13	346	12	21	1	1		78	045	17	48	28	2
14	347	03	40	2	1		81	048	14	00	29	8
15	348	01	42	3	1		85	052	03	08	30	4
15	348	20	48	4	1		86	053	02	43	31	2
16	349	06	51	5	3		86	053	(s-23)	00	32	NPHA
18	351	20	42	6	1		87	054	(f-00)	15		
22	355	03	10	7	1		Data gap: one event during gap					
25	358	09	07	8	1		87	054	01	42	33	NPHA
39	006 ('65)	09	18	9	6		Garbled telemetry frame					
41	008	04	59	10	3		88	055	10	10	34	8
44	011	(s-21)	42	11	NPHA		91	058	03	44	35	1
Data gap: two events during gap							91	058	14	19	36	1
45	012	(f-03)	41	12	NPHA		93	060	23	41	37	1
45	012	(s-21)	40	13	NPHA		94	061	10	43	38	1
Data gap: one event during gap							94	061	10	50	39	2
46	013	(f-03)	41				95	062	21	01	40	1
46	013	14	14	14	8		99	066	03	11	41	4
47	014	07	35	15	8		99	066	17	09	42	3
49	016	01	33	16	NPHA		100	067	15	23	43	4
50	017	09	00	17	6		100	067	(s-15)	40	44	NPHA
51	018	11	50	18	1				(f-19)	05		
51	018	14	20	19	2		Data gap: one event during gap					
55	022	17	41	20	1		101	068	13	26	45	1
57	024	16	06	21	5		101	068	14	34	46	1
63	030	16	31	22	8		105	072	(s-16)	25	47	NPHA
71	038	04	36	23	2				(f-23)	30		
71	038	(s-18)	24	24	NPHA		Data gap: one event during gap					
72	039	(f-01)	26				106	073	04	48	48	2
Data gap: one event during gap							106	073	06	07	49	1
73	040	12	15	25	NPHA		106	073	12	27	50	2
Garbled telemetry frame							106	073	(s-16)	20	51	NPHA
75	042	(s-18)	05	26	NPHA				(f-23)	21		
76	043	(f-01)	14				Data gap: one event during gap					
Data gap: one event during gap							107	074	09	49	52	1
76	043	08	04	27	1							

Table IV-2 (contd)

Mission day	GMT			Event no.	PHA level		Mission day	GMT			Event no.	PHA level
	'65 day	h	min					'65 day	h	min		
107	074	(s-16)	11	53	NPHA		144	111	14	59	101	6
		(f-23)	20				144	111	15	47	102	1
	Data gap: one event during gap						145	112	00	32	103	5
110	077	05	36	54	1		145	112	12	26	104	3
111	078	09	54	55	1		146	113	01	20	105	1
112	079	(s-16)	06	56	NPHA		146	113	04	28	106	2
		(f-23)	21				146	113	07	06	107	1
	Data gap: one event during gap						147	114	06	58	108	8
113	080	(s-16)	02	57	NPHA		Coincident with thin film sensor; direct side					
		(f-22)	58				147	114	08	11	109	6
	Data gap: two events during gap			58	NPHA		147	114	13	54	110	2
114	081	(s-16)	01	59	NPHA		147	114	16	16	111	1
		(f-22)	58				148	115	11	08	112	2
	Data gap: one event during gap						149	116	08	01	113	2
115	082	07	05	60	1		149	116	19	05	114	1
117	084	04	34	61	8		150	117	09	50	115	2
118	085	03	41	62	1		150	117	10	19	116	1
118	085	07	02	63	1		150	117	11	41	117	1
118	085	18	29	64	2		150	117	18	13	118	8
118	085	22	25	65	1		Coincident with film sensor; retrograde side					
120	087	11	28	66	3		150	117	18	19	119	1
121	088	04	21	67	1		151	118	13	47	120	8
121	088	17	57	68	1		152	119	02	32	121	3
123	090	02	21	69	1		153	120	08	19	122	1
123	090	11	32	70	1		153	120	21	24	123	1
124	091	14	52	71	1		154	121	(s-04)	18	124	8
126	093	05	15	72	6				(f-04)	20	125	NPHA
127	094	08	28	73	1		Second event occurred before readout of event #126					
127	094	08	48	74	2		154	121	04	22	126	3
127	094	13	52	75	5		154	121	21	20	127	1
127	094	21	14	76	1		156	123	07	10	128	1
130	097	06	32	77	1		157	124	17	17	129	4
131	098	13	08	78	1		158	125	13	47	130	1
131	098	23	35	79	1		159	126	(s-03)	10	131	NPHA
132	099	12	21	80	1				(f-03)	45		
132	099	17	55	81	1		Data gap: one event during gap					
133	100	09	55	82	5		159	126	06	02	132	7
133	100	20	08	83	1		160	127	07	03	133	8
134	101	07	12	84	1		160	127	08	05	134	8
134	101	09	00	85	2		160	127	10	35	135	2
134	101	21	59	86	8		160	127	16	09	136	5
134	101	23	52	87	1		161	128	04	48	137	1
135	102	23	48	88	3		163	130	04	05	138	1
135	102	23	50	89	7		163	130	14	56	139	4
137	104	00	16	90	1		164	131	09	26	140	1
137	104	00	48	91	1		165	132	20	25	141	2
137	104	09	44	92	1		166	133	02	44	142	1
138	105	08	57	93	4		166	133	15	15	143	3
139	106	10	05	94	1		167	134	11	27	144	1
140	107	12	08	95	1		169	136	19	25	145	1
143	110	08	07	96	8		171	138	00	45	146	2
143	110	09	48	97	1		172	139	21	20	147	1
143	110	15	26	98	1		173	140	01	28	148	1
143	110	20	00	99	2							
144	111	05	04	100	2							

Table IV-2 (contd)

Mission day	GMT			Event no.	PHA level		Mission day	GMT			Event no.	PHA level
	'65 day	h	min					'65 day	h	min		
173	140	14	27	149	8		214	181	15	08	204	2
173	140	17	51	150	2		217	184	19	27	205	2
174	141	21	43	151	1		219	186	06	53	206	2
175	142	20	30	152	1		221	188	05	38	207	7
176	143	05	17	153	8		222	189	04	03	208	1
177	144	19	33	154	2		222	189	06	02	209	8
178	145	23	46	155	1		222	189	10	58	210	1
179	146	00	18	156	8		222	189	11	33	211	8
179	146	07	21	157	1		224	191	01	40	212	1
179	146	12	22	158	2		225	192	23	24	213	1
180	147	19	59	159	8		228	195	06	42	214	8
181	148	09	32	160	1		228	195	21	00	215	3
181	148	18	15	161	3		229	196	11	48		
182	149	07	41	162	1			Data transmission interrupted for picture playback				
182	149	08	05	163	1							
182	149	16	49	164	4		248	215	03	48		
183	150	19	05	165	3			Data transmission started				
183	150	20	20	166	2		248	215	04	10	216	2
184	151	09	55	167	2		249	216	03	48	217	1
184	151	13	10	168	1		251	218	13	53	218	5
184	151	20	35	169	1		252	219	12	00	219	2
185	152	14	34	170	2		252	219	22	23	220	1
186	153	00	39	171	1		253	220	22	11	221	8
188	155	10	43	172	1		254	221	03	44	222	1
189	156	01	41	173	4		258	225	(s-03)	58	223	NPHA
190	157	21	12	174	1				(f-04)	00		
190	157	23	06	175	1			Data gap: one event during gap				
191	158	00	13	176	3		258	225	13	53	224	1
191	158	00	25	177	1		258	225	18	31	225	1
191	158	05	41	178	2		261	228	01	55	226	1
191	158	08	36	179	1		273	240	(s-22)	49	227	NPHA
191	158	12	33	180	2				(f-22)	53		
191	158	13	05	181	3			Data gap: one event during gap				
192	159	02	33	182	3		276	243	(s-01)	14		
192	159	09	03	183	1		278	245	(f-12)	13		
193	160	09	17	184	4			No data; experiment turned off				
193	160	21	25	185	1		278	245	18	05	228	1
195	162	18	32	186	1		279	246	03	17	229	1
196	163	09	50	187	3		280	247	02	44	230	1
197	164	05	32	188	8		280	247	16	17	231	1
198	165	05	59	189	2		281	248	09	49	232	3
199	166	08	08	190	2		283	250	07	09	233	1
199	166	15	27	191	8		286	253	19	24	234	2
200	167	20	45	192	1		291	258	21	52	235	8
201	168	22	49	193	5		293	260	02	36	236	1
204	171	00	16	194	1		293	260	06	13	237	1
205	172	07	18	195	3		298	265	13	07	238	1
206	173	10	07	196	2		300	267	14	41	239	2
207	174	20	38	197	1		307	274	(s-10)	35	240	NPHA
208	175	02	45	198	1				(f-11)	11	241	
209	176	10	54	199	1			Occurred in low quality telemetry data				
210	177	14	14	200	2							
210	177	15	09	201	1		307	274	17	14		
211	178	19	44	202	1			End of experiment data				
212	179	15	22	203	1							

Events number 108 and 118 are the only impacts where there was a microphone sensor pulse and film sensor signal in coincidence. The capacitor sensor is more sensitive than the microphone sensor when micro-particles were impacted at high speeds onto the plate during calibrations. However, these particles were minute iron spheres and thus would have high penetrating power, as compared to a dust particle in space which may have a density approaching *one* and most probably would not be spherical in shape. Another factor is the calibration of the microphone sensor. At the present time, there is laboratory evidence that this sensor is not strictly related in a simple manner to the impulse delivered to the plate when the relative velocity of impact is in the hyper-velocity regime. The precise relationship has not yet been determined. The most likely result is that the microphone sensor detected particles of smaller mass than originally suspected. The two events mentioned above had PHA levels of 8, saturation. There are other saturation events which do not show a film coincidence; however, since level 8 is, in effect, a cumulative counter, the size of these impacting particles cannot be determined. For the above reasons and the long test history, these two events are considered real. It is interesting to note that each side was impacted.

The major characteristics of the data from the experiment from launch through encounter were reported in a preliminary paper by Alexander, McCracken, and Bohn (Ref. 8). The cumulative flux distribution for various heliocentric distances is shown in Table IV-3. The slope of the flux-mass distribution for the various intervals varies between 0.54 and 0.85.

*Note:* The cumulative flux can be related to particle mass by an expression of the form

$$\Phi_c \sim M^\beta$$

**Table IV-3. Cumulative flux-mass distribution for various heliocentric distances**

$N_p$	$\Delta t$ , days	psd, AU	$\phi$	$\beta$
44	100	1.0 -1.25	$7.3 \times 10^{-5}$	-0.54
43	34	1.25-1.36	$2.1 \times 10^{-4}$	-0.85
40	20	1.36-1.43	$3.3 \times 10^{-4}$	-0.57
39	29	1.43-1.49	$2.2 \times 10^{-4}$	-0.56
49	45	1.49-1.56 <sup>a</sup>	$1.8 \times 10^{-4}$	-0.68
26	57	1.56-1.58	$7.4 \times 10^{-5}$	-0.81

$N_p$ : number of impacts.  
 $\Delta t$ : time in days for data interval with first interval starting at 00:00 UT, November 29, 1964.  
<sup>a</sup>Data interval concluding with encounter; last data interval is complete post-encounter period.  
psd: probe-sun distance in AU for each data interval.

where  $\Phi_c$  is the mean cumulative flux for each data interval in particles  $m^{-2} s^{-1} (\pi \text{ steradian})^{-1}$ ; and  $\beta$  is the slope of the cumulative mass distribution.

## G. Sources

At the Goddard Space Flight Center, Lou Secretan, C. W. McCracken, and O. E. Berg gave valuable assistance to the planning, sensor development, and calibration of the systems. At Marshall Laboratories, Herbert Rosenberg and S. C. Baker were responsible for the design, testing, and fabrication of the electronic instrumentation.

References to material contained in this section provide primary sources of documentation on related observations and measurements. Other cross references and bibliographies can be obtained by examining the List of References at the end of this Section IV.

## References

1. Gallagher, P. B., and Eshleman, V. R., "Sporadic Shower Properties of Very Small Meteors," *Jour. Geophys. Res.*, Vol. 65, p. 1846, 1960.
2. Eshleman, V. R., "Radar Rate Measurements on Very Small Meteors," *Paper presented at the Symposium on Small Meteoritic Particles in the Earth's Neighborhood, 110th meeting of the American Astronomical Society*, Cambridge, Mass., 1962.
3. Giese, R. H., "Light Scattering by Small Particles and Models of Interplanetary Matter Derived from the Zodiacal Light," *Space Sci. Rev.*, Vol. 1, p. 589, 1962.
4. Weinberg, J. L., "White-Light vs Narrow-Band Observations of the Polarization of the Zodiacal Light," *Nature*, Vol. 198, p. 842, 1963.
5. Dubin, M., "IGY Micrometeorite Measurements," *Proceedings of the First International Space Science Symposium*, Nice, ed. by H. K. Kallmann-Bijl, Amsterdam: North-Holland Publishing Company, p. 1042, January 1960.
6. Alexander, W. M., "Preliminary Results of Interplanetary Dust Particle Flux from *Mariner II*," *Science*, Vol. 138, p. 1098, 1962.
7. Bohn, J. L., and Alexander, W. M., "A Study of Thermal Gradient Effects on Ceramic Transducers Used in Cosmic Dust Experiments: Part I," NASA Research Grant NsG-84-60, *Scientific Report*, March 1967.
8. Alexander, W. M., McCracken, C. W., and Bohn, J. L., "Zodiacal Dust: Measurements by *Mariner IV*," *Science*, Vol. 149 No. 3689, pp. 1240-1241, 1965.

## V. Ionization Chamber

### A. Introduction

H. Victor Neher of the California Institute of Technology was the principal investigator for the ionization chamber experiment conducted on the *Mariner IV* spacecraft. He was assisted by Hugh R. Anderson of Rice University and members of the Space Science Division of the Jet Propulsion Laboratory.

The ionization chamber experiment provided the means to measure charged particles in space. As a primary detector of radiation, the instrument used an integrating ionization chamber because of its long-term stability. The Geiger-Mueller (G-M) counter associated with the experiment provided the secondary means of detecting radiation. The purposes of the experiment included the following:

- (1) Measure ionizing radiation in interplanetary space with such stability and accuracy that changes amounting to less than a few percent could be observed during a period of several months.
- (2) Focus special interest on dependence of radiation intensity upon distance from the sun.
- (3) Focus special interest on dependence of the correlation between: (a) changes in radiation between two points, and (b) the distance between the points.
- (4) Observe the time history of the rise and decay of solar-flare radiation.
- (5) Determine the dependence of items 1 through 4 upon the phase of the solar cycle, requiring similar measurements to be made on more than one interplanetary spacecraft.
- (6) Measure any energetic, magnetically trapped particles at Mars.

### B. Instrument

The chamber and the counter had to be mounted on the spacecraft so that spacecraft components would subtend the minimum possible solid angle where the detectors were located. In addition, the two detectors had to be located close enough together to experience the same flux of radiation. For these reasons the instrument was mounted on the omnidirectional antenna, away from the body of the spacecraft. Mounting the instrument on the antenna mast with insulated washers provided electrical isolation and minimized effects due to scattering or absorption of the radiation to be measured.

**1. Measurements.** The time between successive output pulses was the important parameter to be measured

by the ionization chamber, whereas the parameter required of the G-M tube was the number of pulses per unit time. In both cases the respective pulses were transmitted on separate lines to the data automation subsystem (DAS), which measured the time interval between the beginning of a frame and the arrival of an ion-chamber output pulse in increments of 1.2 or 0.3 s, depending on the prevailing bit rate. In addition, the number of ion-chamber pulses per frame was also recorded. If the rate from the ion chamber was 1 pulse/frame or less (the usual case in quiescent space), the time between ion-chamber output pulses could be calculated. For more than 1 pulse/frame the exact time pulses could not be obtained, but the number of pulses/frame was more significant at these rates and was directly recorded. At rates of 7 pulses/frame or more, all interval-timing bits were reset and the entire ion-chamber data word was devoted strictly to counting pulses. An indicator bit was set by the eighth pulse in any one frame and was useful in reducing the data. In this mode the data register was capable of tabulating as many as  $2^9 - 1$  pulses/frame. Ion-chamber data were read out once every frame.

The G-M tube registers were capable of recording as many as  $5 \times 2^{19}$  pulses/frame. When 19 bits of the 20-bit register were filled ( $2^{19} - 1$  pulses/frame), the next pulse triggered a change of tabulating mode. Incoming G-M tube pulses were then prescaled by a factor of 4 before being recorded in the data register. The change to the prescale mode was signalled by an indicator bit to avoid ambiguity. Data from the G-M tube were commutated with data from other sensors and were consequently read out only every fourth frame. Pulses were accumulated for 45 or 11.25 s when the telemetry bit rates were  $8\frac{1}{3}$  and  $33\frac{1}{3}$  bits/s, respectively.

**2. Description.** The ion chamber used a G-M counter to measure the average omnidirectional flux of charged particles detected by the ion chamber. The stability of this instrument's calibration and because many instruments may be accurately calibrated ( $\pm 1\%$ ) to the same standard, not only makes the ion chamber useful for measuring radiation on long spacecraft missions, but also for comparing radiation observed by different spacecraft at different times. Figure V-1 shows the ion chamber

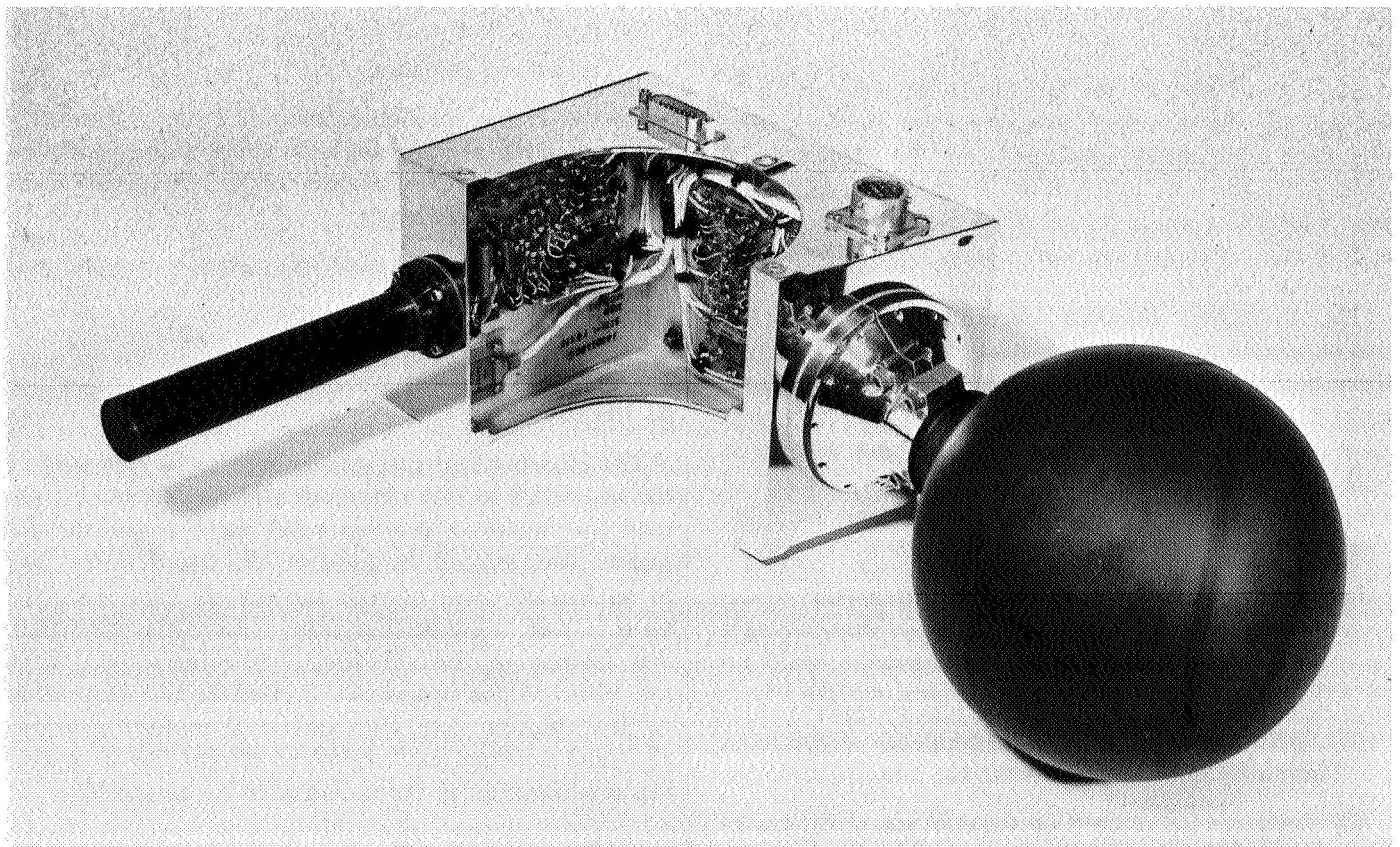


Fig. V-1. Ionization chamber, *Mariner Mars 1964*

and G-M counter system used on *Mariner IV*, similar to the combination used on *Mariner II*. The *POGO* (*OGO-C* and *-D*) instrument carried a slightly modified chamber, without the G-M tube.

The ion chamber generates a pulse signal after a fixed amount of charge ( $\sim 10^{-10}$  C) has been collected from the ionized filling gas. The time interval  $\Delta t$  between pulses is inversely proportional to the ionization rate. The G-M tube puts out a pulse for each ionizing particle that passes through it. The resultant pulse is amplified (see Fig. V-2), shaped, and delivered to the DAS. For each charged particle that penetrates the shield and enters the sensitive region of the G-M tube, an output pulse is generated and its pulse rate is directly proportional to the radiation flux.

When ionizing particles penetrate the sphere, the argon in the chamber ionizes and the ions are attracted to the grounded sphere, whereas the electrons are attracted to the collector, tending to neutralize its positive charge. When the collector's charge is sufficiently neutralized, the negative image charge on the Aquadag coating attains a magnitude sufficient to pull the fiber

into contact, and the collected charge discharges through the load resistor. This surge of electrons — a current pulse — is amplified, shaped, and presented to the DAS.

Each output of the ion chamber represents a fixed amount of charge collected from the argon gas, the average rate of ionization, whereas the output of the G-M tube measures the omnidirectional flux of energetic particles.

**3. Absolute calibration of ion chamber.** Absolute calibration of the ion chambers is made by measuring their pulsing rates  $\Delta t^{-1}$  in a flux of  $\text{Co}^{60}$   $\gamma$ -rays with known ionizing power. The ionization rate  $I$  is measured in units of ion pairs  $(\text{cm}^3 \text{ s})^{-1}$  of STP air by a set of standard ion chambers maintained at the California Institute of Technology. The calibration constant  $K$  of the flight instruments is calculated from the expression

$$K = I \Delta t \frac{\text{ion pairs}}{(\text{cm}^3 \text{ s})^{-1} \text{ STP air}} \text{ s}$$

where  $\Delta t$  is the time interval between pulses from the fiber electrometer.

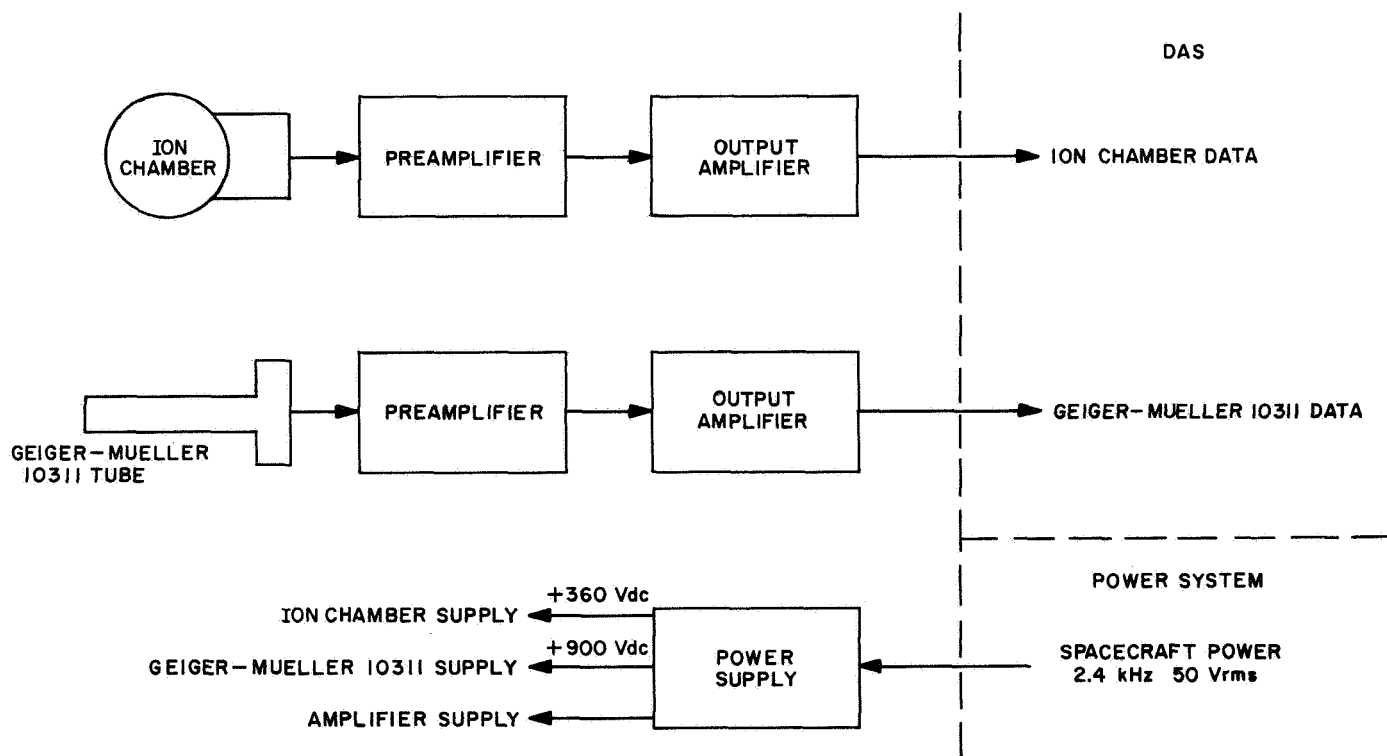


Fig. V-2. Block diagram of ionization chamber



The standard ionization chambers, which are similar to the model used in the balloon experiment, have a spherical wall 25.4 cm in diameter and 0.063 cm (0.5 g/cm<sup>2</sup>) thick and contain 8 l of argon at 8 atm pressure. A quartz-fiber electrometer measures the collected ion current. They have been calibrated in absolute units by a three-step procedure (Ref. 1). A total of 8 l of air at 1 atm pressure enclosed in a standard ion chamber shell was exposed to a reproducible  $\gamma$ -ray flux. The collected ion current was measured with an external absolute electrometer, sufficient voltage being applied to saturate the chamber; i.e., the current was independent of the collecting voltage. A second standard chamber similarly filled and equipped with a quartz-fiber electrometer was then mounted in place of the first instrument, and the pulsing rate of the electrometer was measured. This calibrated the fiber electrometer in units of coulombs collected per pulse.

Argon gas is used in these instruments because of the low rate of recombination of the ions and the consequent low temperature coefficients of recombination. In order to reduce this to free air ionization, one must calculate the effect of the chamber wall (which would be necessary with an air-filled chamber) and then calculate the ratio of ionization in air and in argon. Johnston (Ref. 1) did this and found that the 0.5-g/cm<sup>2</sup> wall increases the cosmic ray ionization by 1.4%, and that after this effect is subtracted the ratio of cosmic ray ionization in air to that in argon (both at STP) is as follows:

$0.672 \pm 0.017$  at 10 g/cm<sup>2</sup> depth in atmosphere

$0.659 \pm 0.017$  at 100 g/cm<sup>2</sup> depth

0.665 mean

In order to provide a large ion current, the ion chambers required argon at 8 atm pressure. Several instruments of from 1 to 8 atm of argon were flown by Johnston (Ref. 1) on the same balloon, and it was found that the ion current collected was proportional within  $\pm 2\%$  to the mass of argon used. These instruments had been calibrated as follows:

- (1) The chamber with the calibrated fiber electrometer was refilled with argon at 1 atm and placed in the standard  $\gamma$ -flux. The collected ion current was measured. This procedure was repeated with different argon pressures up to 8 atm. These data showed that the  $\gamma$ -ray ionization current was proportional to the mass of argon, and measured the ionizing power of the standard  $\gamma$ -ray flux in units

of ion pairs (cm<sup>3</sup> s)<sup>-1</sup> STP argon. (The ratio of  $\gamma$ -ray ion rate in air to that in argon, both at STP, was observed to be  $0.655 \pm 0.019$ , which is fortuitously close to the calculated values for cosmic rays.)

- (2) The pulsing rates of the flight instruments filled to various pressures were measured in the standard flux.

Subsequently a set of chambers, all filled with 8 atm of argon, were calibrated in the standard flux and set aside as standards. Their calibration constants, in units of ion pairs (cm<sup>3</sup> s)<sup>-1</sup> STP argon, were multiplied by the calculated mean cosmic ray ratio, 0.665, to give constants in units of ion pairs (cm<sup>3</sup> s)<sup>-1</sup> STP air. When new standard  $\gamma$ -ray fluxes have been established with these standard ion chambers, the ion rate  $I$  will have been expressed in units of ion pairs (cm<sup>3</sup> s)<sup>-1</sup> STP air effective for cosmic rays.

The smaller, spacecraft ion chambers were calibrated in a  $\gamma$ -ray flux that had been measured by standard chambers. As a check, a small instrument and a balloon-type chamber were flown together to a 10-g/cm<sup>2</sup> depth, and it was found that the smaller instrument measured an ionization rate 3.5% lower than the larger instrument at atmospheric depths less than 200 g/cm<sup>2</sup> (Ref. 2).

**4. Absolute calibration of Geiger-Mueller tube.** The absolute response of the G-M tube to penetrating charged particles is determined by the shape, size, and efficiency of the sensitive volume. It is assumed that the sensitive volume is a right circular cylinder with a diameter  $d$  equal to the internal diameter of the cathode. The counting rate of the tube was measured as a function of the position of a collimated beam of  $\beta$ -rays (Sr<sup>90</sup>) along its length, and the effective length  $l$  was set equal to the full width at half the maximum of the rate-vs-position plot. Typical values are  $d = 1.32$  cm,  $l = 6.03$  cm. If  $A$  is the surface area of the sensitive volume, then the omnidirectional geometric factor  $G_0$  is

$$G_0 = \frac{A}{4 \text{ cm}^2}$$

with

$$\frac{\text{count rate}}{4\pi j} = G_0$$

where  $4\pi j$  is the average omnidirectional flux.

With the above values of  $d$  and  $l$ ,  $G_0 = 6.9$  cm. In a nonisotropic flux the counting rate depends on the orientation of the tube.

The efficiency of a tube was measured by forming a coincidence telescope of three parallel tubes denoted A, B, and C; the middle tube being B. The telescope was oriented vertically and exposed to cosmic radiation in the laboratory for 112,000 s. The coincidences  $ABC$ ,  $A\bar{B}C$ , and the singles rate of A were measured with the following result:

$ABC$	3175 counts
$A\bar{B}C$	60 counts
A	75,987 counts or 40.7 counts/min

If the tubes are assumed to be identical and the inefficiency  $\epsilon \ll 1$ , then

$$\epsilon = \frac{A\bar{B}C}{ABC + 3 A\bar{B}C} = 1.79\%$$

These tubes are concluded to be 98% efficient for detecting penetrating charged particles.

It can be assumed that protons are detected with an efficiency of 98% if they penetrate the wall of the sensitive volume. This cylindrical-sided wall may be approximated as follows:

0.2 g/cm<sup>2</sup> steel, area 25 cm<sup>2</sup>

1.0 g/cm<sup>2</sup> carbon, area 2.75 cm<sup>2</sup>

With these data, the proton response shown in Fig. V-3 can be computed from a consideration of proton range.

The electron accelerator for calibrating the ion chamber was used in a similar manner to measure the response of a G-M tube to nonpenetrating electrons with energies of 30–100 keV. The tubes were operated without shielding and with various angles between a radius vector from the electron target to the tube and the axis of the tube. From these data we calculated the response curves shown in Fig. V-4, allowing for absorption of bremsstrahlung in the tube shield and the supporting rubber plugs.

Data in the energy range of 400–1350 keV were obtained by bombarding a shielded G-M tube with  $\beta$ -rays selected by a magnetic spectrometer. It was assumed

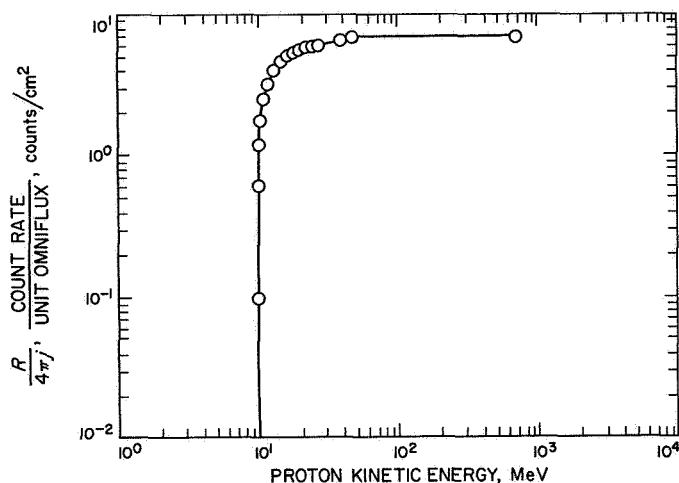


Fig. V-3. Proton response of G-M tube

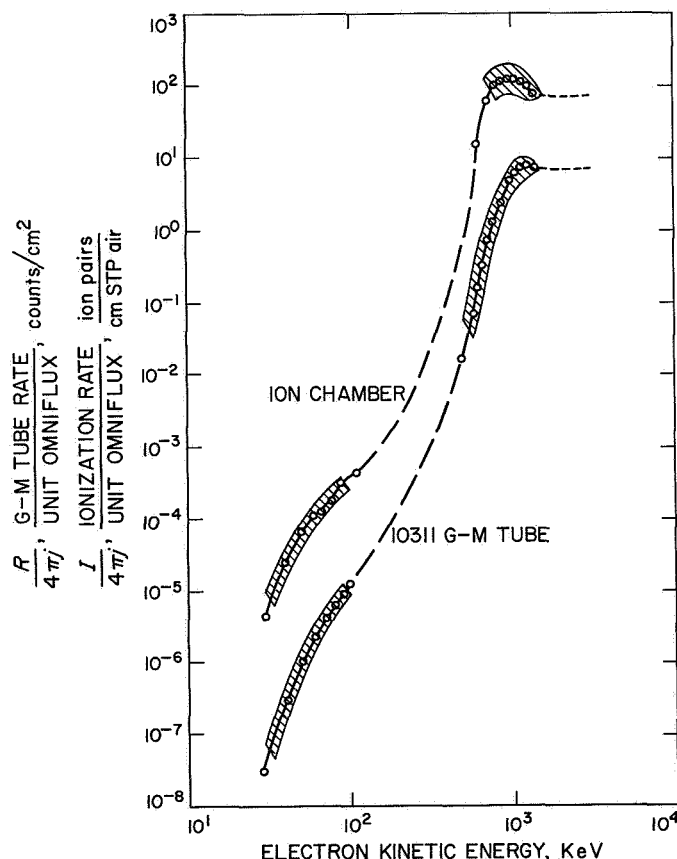


Fig. V-4. Response of ion chamber and G-M tube to electrons

that electrons with energies above 1,300 keV penetrate completely and are detected with an efficiency of 98%. Data in the range of 400–1,300 keV were normalized at 1,350 keV to the response to penetrating electrons.

**5. Construction.** The ion chamber (see Fig. V-5) consisted of a 5-in.-diam, 0.010-in.-thick, nonmagnetic stainless steel shell (0.2 g/cm<sup>2</sup>), which housed the fused quartz electrometer system. The quartz mechanism was rigidly mounted on the header in the *Mariner II* instrument, whereas in the *Mariner IV* it was attached to a friction damper to isolate it from vibration. The mechanism, consisting of the collector, fiber, and support arm, was made of quartz fused into a single piece. The

fiber,  $\sim 10\ \mu$  in diameter by 0.9 cm long, was mounted so that it laid approximately 0.038 cm from the collector when electrical forces were not present.

Aquadag applied to the collector made it conductive, and the conducting portion was insulated from the remainder of the instrument. The fiber and support arm were also coated with Aquadag, so that the resistance along the fiber to the point that touched the collector

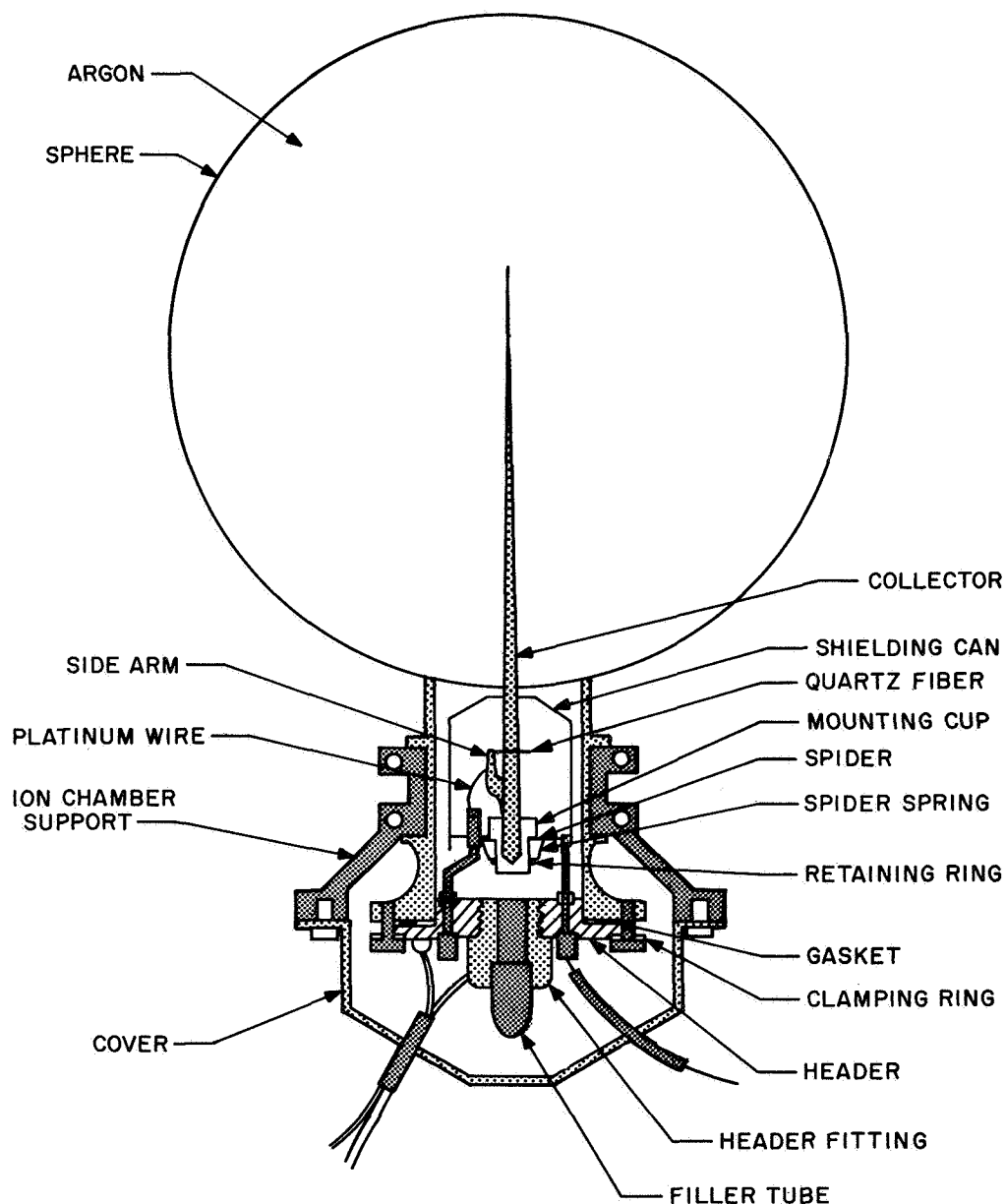


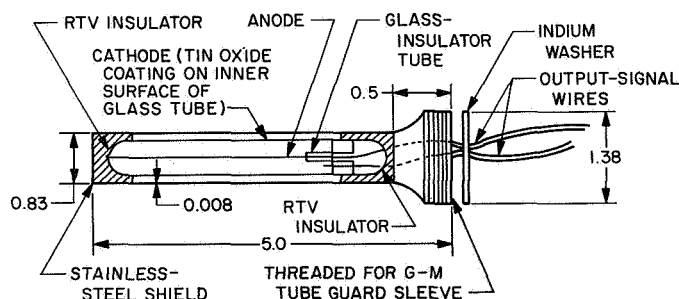
**Fig. V-5. Cross-sectional view of ion chamber**

during operation was 0.2–1.0 M $\Omega$ , and the fiber was connected to a header pin by a platinum–iridium wire.

On the *Mariner IV* and *POGO* instruments Neher used an improved method of coating the quartz fiber to make it conductive. Before the fiber and support were joined to the collector, a silver band was evaporated onto the fiber at the point of contact with the collector. Platinum was then evaporated onto the fiber and tip of the support, and a conductive coating was applied to the support so that the electrical resistance to the fiber was  $\sim 10$  M $\Omega$ . This technique limited the peak current conducted to the collector during the recharging cycle and extended the life of the electrometer to  $>3 \times 10^8$  pulses.

After assembly the chamber was evacuated, baked several hours at  $\sim 350^\circ\text{C}$ , cooled, and then filled with argon. In operation a potential  $V_0 \simeq 300$ –400 V with respect to the shell was applied to the inner shielding can; and, through an external load resistor ( $\simeq 0.2$  M $\Omega$ ) to the fiber. Attracted to the collector, the fiber charged it to  $V_0$  and returned to its rest position. Ion and electron current between the shell and collector discharged the latter, and the fiber was gradually pulled towards the collector until the potential between the two reached a critical value ( $\sim 150$  V). With a further decrease in the separation of the fiber and collector, the attracting electrostatic force increased more rapidly than the restoring mechanical force. The fiber then whipped against the collector, recharging it, and produced a voltage pulse across the external load resistor.

The G-M counter (shown in Fig. V-6) used a Radiation Counter Lab 10311 halogen quenched tube operating at  $\sim 900$  V. The tube has a stannous-oxide cathode on the inside of the wall and a 0.003-in. tungsten anode. A steel cylinder supports the tube and matches the shielding to



NOTE: DIMENSIONS IN INCHES

Fig. V-6. Cross-sectional view of G-M counter tube

the wall of the ion chamber. The shield has a mass thickness of 0.16 g/cm<sup>2</sup>, which matches the total shielding around the sensitive volume of the tube to the ion chamber shielding.

**6. Response to environment.** The operation of the sensors under various environmental conditions is measured using convenient sources of radiation as stimuli. Voltage plateaus of the G-M tubes counting Co<sup>60</sup>  $\gamma$ -rays are measured as a function of temperature prior to their selection for flight instruments. The effective lengths of selected tubes are measured with collimated  $\beta$ -rays. Each completed flight instrument is calibrated in a standard flux of Co<sup>60</sup>  $\gamma$ -rays reproducible to  $\pm 0.2\%$  when decay is taken into account. It is then subjected to an environmental test, shown in Table V-1. If the instrument survives these critical test specifications, it is recalibrated. Those characteristics that are different for each instrument are then measured for each instrument. Nonlinearity at high rates is determined with an X-ray beam, and the change of calibration with gravitational acceleration and with temperature are measured with Co<sup>60</sup>  $\gamma$ -rays. Flight instruments are usually operated for several months on the spacecraft prior to launching. They are recalibrated in the standard  $\gamma$ -ray flux several times during this period so that a check on long-term stability can be made.

Table V-1. Critical specifications of environmental test

Vibration	36 s of 14-g rms noise 600 s of 5-g rms noise + 15–2000 Hz sine wave at g levels from 2 to 9
Temperature	–30 to +65°C –46 to +65°C (thermal shock both at $<10^{-4}$ mm Hg air pressure)
Shock	200 g, 0.5 to 1.5 ms on each of three axes
Acceleration	$\pm 14$ g for 5 min along each of three axes

The other responses, listed in Tables V-2 and V-3, have been measured with only a few instruments. The minimum rates correspond to approximately 10 ion pairs (cm<sup>3</sup> s)<sup>–1</sup> of STP air and an average omnidirectional flux of 0.07 particles/cm<sup>2</sup> s. These are close to the expected sea-level cosmic-ray rates, and are small compared with the primary cosmic-ray rates of 650–1,000 ion pairs (cm<sup>3</sup> s)<sup>–1</sup> STP air and 3–4 particles/cm<sup>2</sup> s, which have been measured in interplanetary space. Instrumental background rates are therefore neglected.

Table V-2. Response of ion chamber to environment<sup>a</sup>

Parameter	Response or quantity	Comment
Filling pressure vs pressure $\times \Delta t$ , %/atm	-0.8	1 to 10 atm of argon, 300 V applied
$\Delta t$ vs collection voltage, $V_{or}$ , %/V	<0.002	200 to 500 V applied, 10 atm of argon
$\Delta t$ vs $\Delta V$ , %/V	5	POGO, high sensitivity
$\Delta t$ vs temperature, %/°C	~0.01	Normal sensitivity
	~0.1	High sensitivity, POGO -25 to +75°C
Stability of calibration, % change	$\leq \pm 0.5$	Includes 3 mo or more of test and operation
rms deviation of $\Delta t$ , %	0.3	Mariner instrument deviations result from random effects in the mechanical electrometer
Dynamic range of pulse rates, s	$\leq 3.10^{-5}$ to $10^2$	See Fig. V-7
$\Delta t$ vs acceleration in direction of fiber motion, % g	4	Normal sensitivity
	22	POGO, high sensitivity
Lifetime, pulses	~ $3.10^7$	Fibers with Aquadag coating
	> $3.10^8$	Fibers with Ag and Pt coating
Calibration constant, K, ion pairs/(cm <sup>3</sup> s) <sup>-1</sup> STP air	~350,000	Mariner instrument
	~150,000	POGO, normal sensitivity
	~15,000	POGO, high sensitivity
Volume of chamber, l	1	
Pressure, atm absolute	4	Mariner
	10	POGO

<sup>a</sup>Unless otherwise noted, data apply to both Mariner and POGO instruments.

Table V-3. Response of G-M tubes to environment

Parameter	Response	Comments
Count rate vs voltage, % per 100 V on voltage plateau	3	900 to 1000 V
Count rate vs temperature: (tube only), %/°C	0.03	100/s; -40 to +75°C
Tube and preamplifier, %/°C	0.05	10 <sup>4</sup> /s; -25 to +75°C
Stability of calibration, % change	$\leq \pm 1$	Includes 3 mo or more of calibration and test
Dynamic range of counting rate, s	$\leq 0.5$ -50,000	See Fig. V-8
Lifetime, counts	>10 <sup>10</sup>	For good tubes; see performance
Geometric factor, cm <sup>2</sup> omnidirectional	7 cm <sup>2</sup>	

The ion chambers are quite linear up to that ionization rate for which the pulse rate approximates the natural mechanical frequency of the fiber. At that point they depart abruptly from linearity. The G-M tubes depart gradually from linearity in a way that depends on the tubes' dead and recovery time and on the preamplifiers' sensitivity and double-pulse resolution. Figures V-7 and V-8 show the true counting rates vs the observed rate of an ion chamber and a G-M counter. On Fig. V-7 the ionization rate is obtained by dividing a constant (~350,000) by true  $\Delta t$ . On Fig. V-8 the average omnidirectional flux of charged particles is obtained by dividing the true rate by a constant ( $\approx 7.0$ ).

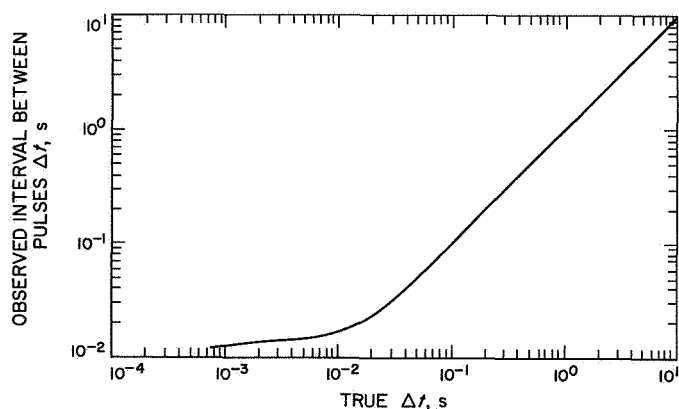


Fig. V-7. True counting rates vs observed rate of an ion chamber

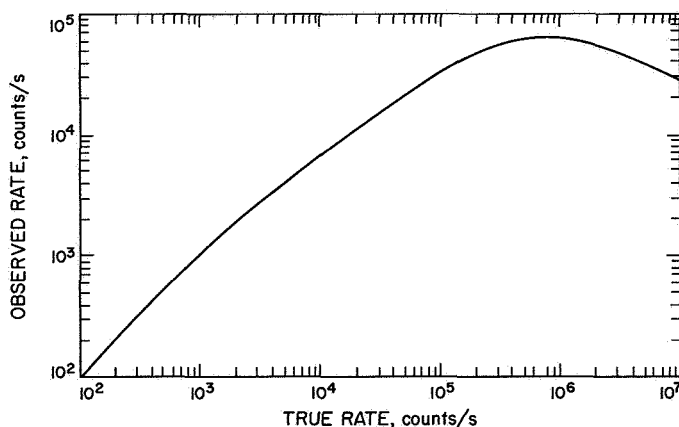


Fig. V-8. True counting rates vs observed rate of G-M counter

## C. Results

On February 5, 1965, the 69th day of the mission, a large flux of particles associated with a solar flare was observed. On the 73rd day, as the ionization rate decayed to its preflare level, the G-M tube rate remained 30% above the preflare value. This condition continued for 10 days and then the G-M tube rate rose to  $\sim 18,000$  counts/s indicating a self-sustaining discharge, while the ion chamber continued to function normally. On the 109th day of the mission (March 17, 1965) the G-M tube rate and ion chamber pulsing rate dropped to zero. No further data were obtained from these sensors, but other portions of the spacecraft were not affected. The G-M tube failed after approximately  $8 \times 10^8$  counts, although in laboratory tests similar tubes from the same lot produced  $3\text{--}10 \times 10^9$  counts before failure. Apparently, in the normal counting process, the quenching gas is depleted. After this occurs, the resulting discharge transports tungsten from the anode wire to the cathode.

Continual erosion of the anode in this manner eventually severs it, and the free charged end is electrostatically attracted to the cathode. If the free end touches the cathode, the high-voltage supply common to both the ion chamber and G-M tube is shorted, and the ion chamber also ceases to function.

**1. Galactic cosmic rays.** Galactic cosmic rays consist of protons, alpha particles, and heavier nuclei, mostly with energies exceeding 200 MeV. Outside the earth's atmosphere, their flux was constant within 10% for the first 230 days of the *Mariner IV* mission, as judged by terrestrial and earth-satellite measurements. The ion chamber experiment measured 4 particles  $(\text{cm}^2 \text{ s})^{-1}$  and  $1.7 \text{ mrad/h} \simeq 1,000$  ion pairs  $(\text{cm}^3 \text{ s})^{-1}$  of STP air from launch until March 17, 1965, when the instrument ceased operating. In 230 days at these rates the dose amounted to  $7.9 \times 10^7$  particles/ $\text{cm}^2$  and 9.5 rad. The 6-h averages of these quantities for the first portion of the mission are shown in Fig. V-9.

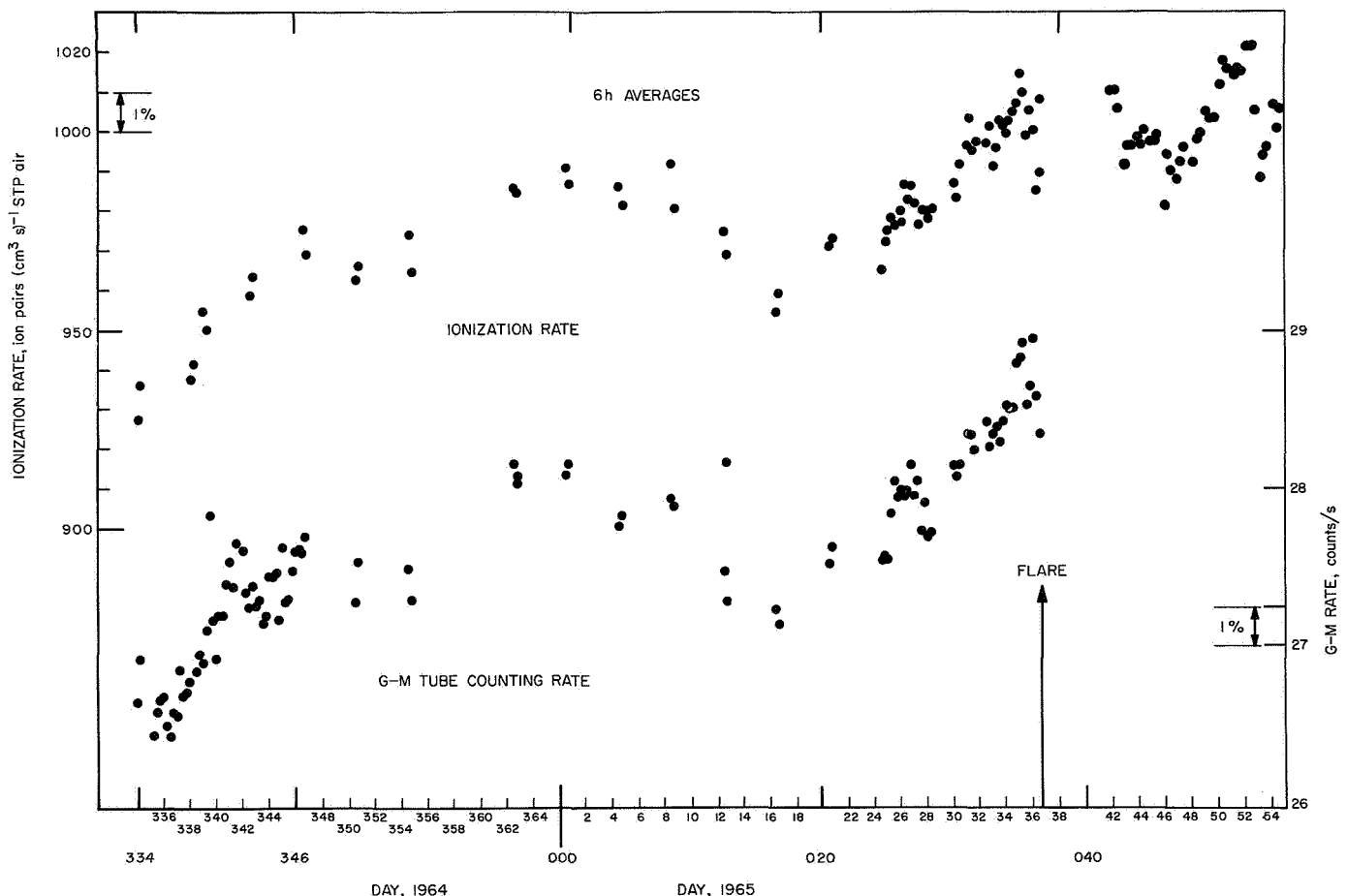


Fig. V-9. Averages (6-h) of ionization rate and G-M tube counting rate for the first portion of the *Mariner IV* mission

Because the radiation was penetrating, these doses were uniform within 20% throughout the spacecraft. The average specific ionization was about 5.5 MeV/g/cm<sup>2</sup>, i.e., about three times the minimum ionization. There are large local fluctuations about this figure due to nuclear stars produced in the material of the spacecraft. As solar activity increases toward the maximum predicted for 1968 and 1969, the flux and ionization rate of galactic cosmic rays will gradually decrease by about a factor of 2.

**2. Solar protons.** Almost all of the solar protons encountered by *Mariner IV* through March 17, 1965, occurred in the 2 days following a solar flare at 18:00 GMT on February 5. The counting and ionization rates measured by the ion chamber experiment during this period are shown in Fig. V-10. The total dose using 0.2-g/cm<sup>2</sup> shielding was  $1.3 \times 10^7$  particles/cm<sup>2</sup> and 4.2 rad.

Unlike the galactic cosmic rays, the average energy from these particles (mostly protons according to data from the cosmic ray telescope) was 30–40 MeV. Other measurements made near the earth suggest that there are 3% as many particles above 80 MeV as there are above 10 MeV; hence, the dose diminished by a factor of approximately 30 in going from 0.2- to 7-g/cm<sup>2</sup> depth in the spacecraft. The number of protons with ranges between 0.001 and 0.2 g/cm<sup>2</sup> (0.5–10 MeV) was

of the order of  $10^8$ /cm<sup>2</sup>, judging from preliminary data returned by the trapped radiation detector experiment.

**3. Trapped particles at earth.** The counting and ionization rates measured by the ion chamber experiment in the earth's Van Allen radiation belts are shown in Fig. V-11. The dose measured for the inner belt (mostly protons of energy from 10 to 100 MeV) using 0.2 g/cm<sup>2</sup> shielding was  $0.36 \times 10^7$  particles/cm<sup>2</sup> and 1.9 rad. For the outer belt (mostly electrons of energy greater than 1 MeV), the dose measured was  $13.4 \times 10^7$  particles/cm<sup>2</sup> and 8.2 rad. Thus, the total dose measured in the Van Allen radiation belts was  $13.8 \times 10^7$  particles/cm<sup>2</sup> and 10.1 rad.

The particles trapped in the earth's radiation belts are mostly of low energy. Thus, the number of particles having ranges between 0.001 and 0.2 g/cm<sup>2</sup> was of the order of 100 times greater than the numbers given, whereas the number of particles reaching 3 g/cm<sup>2</sup> or greater must have been of the order of 100 times less.

**4. Failure of G-M tube and ion chamber.** It was calculated that the G-M tube had first failed (by spontaneous discharge) after having counted approximately  $8 \times 10^8$  counts, i.e., after expending only 8% of its rated  $10^{10}$  count life. In an attempt to understand this phenomenon, 10 tubes were taken from the batch from

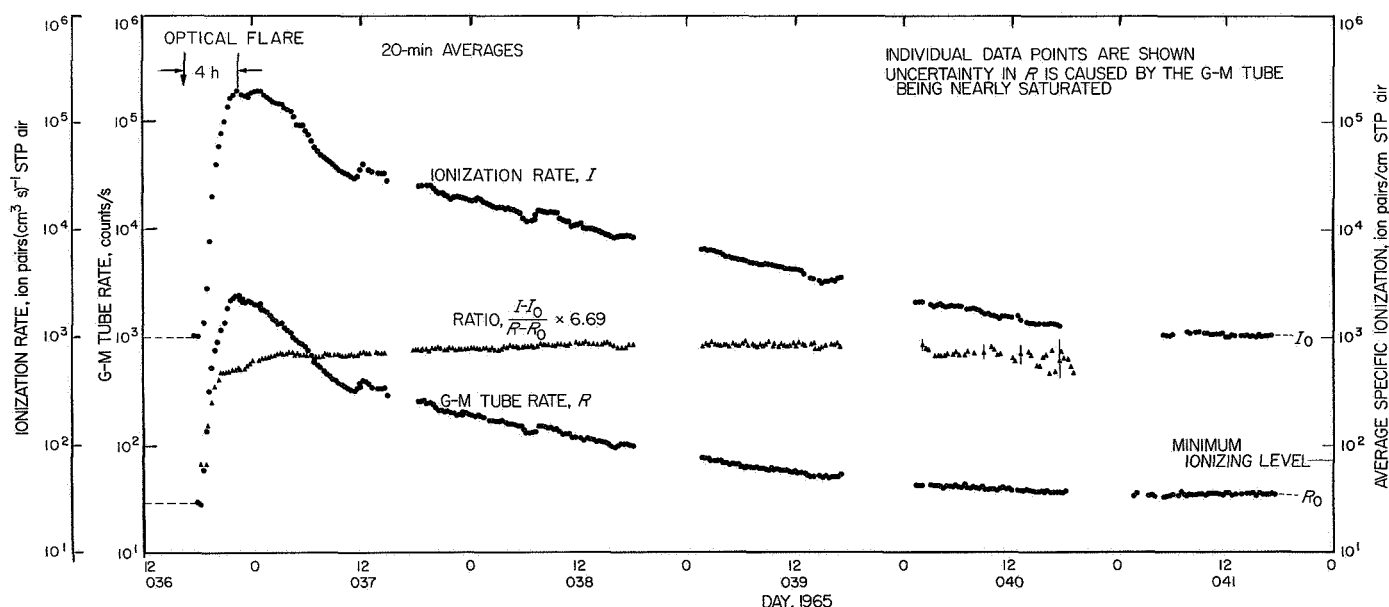


**Fig. V-10. Averages (20-min) of ionization rate, true G-M tube counting rate, and average specific ionization for the period following solar flare of February 5, 1965**

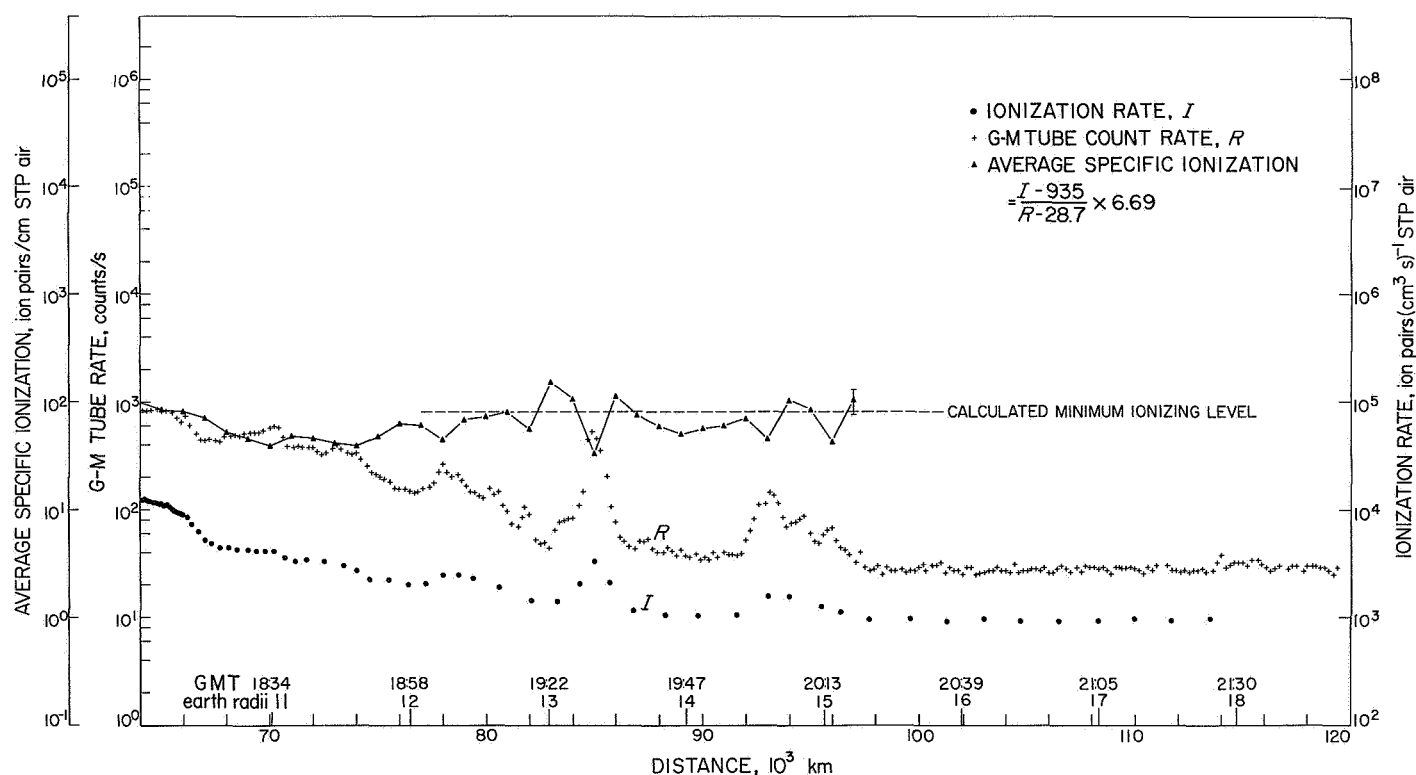
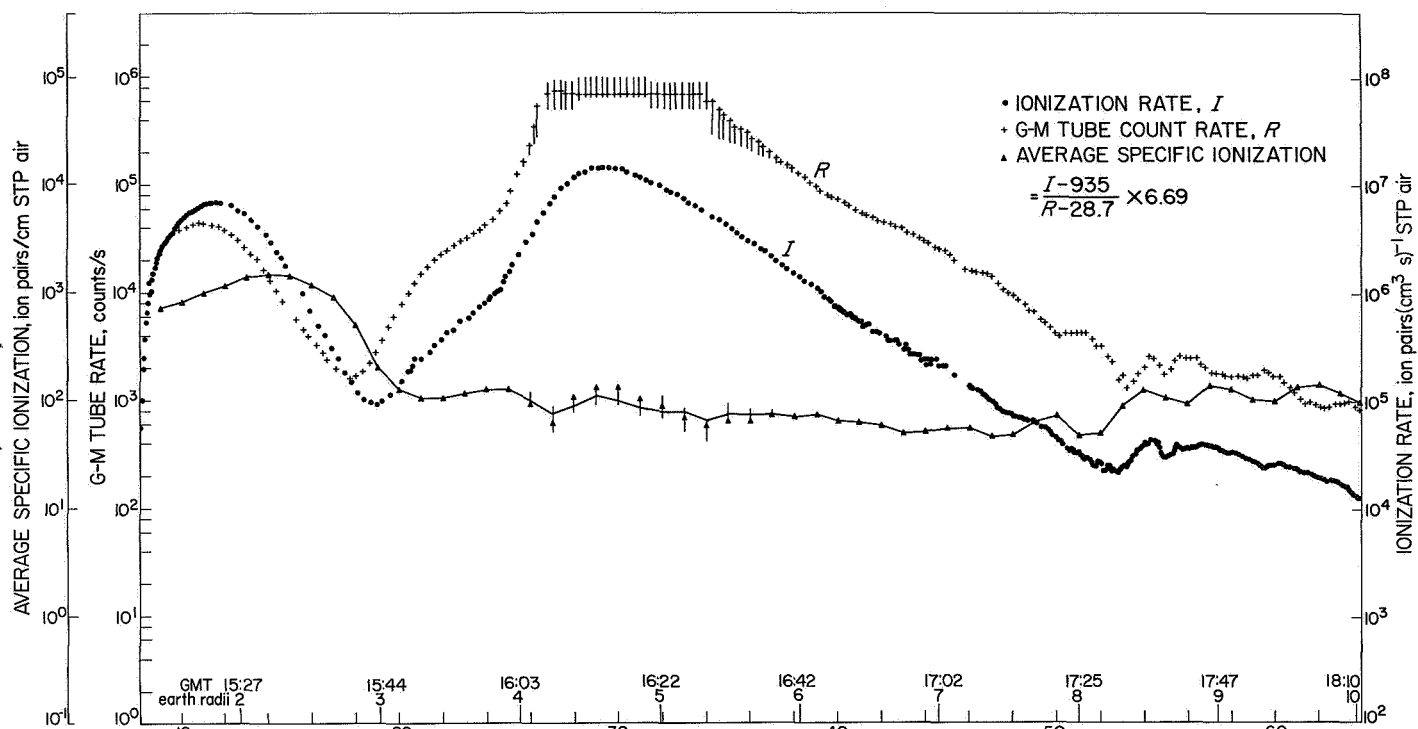


Fig. V-11. Ionization rate, true G-M tube counting rate, and average specific ionization in the earth's Van Allen radiation belts



which the flight tubes were selected. Seven tubes were operated at various fixed count rates until such time as each tube failed by continuous discharge. Three tubes were exposed to the higher flux levels, but without power applied. No significant shift in the voltage plateaus of these latter tubes was observed.

The tentative conclusion from the results was that the total life-count of a tube depends upon the rate at which the tube counts; the higher the count rate, the more counts a tube will assimilate before the onset of spontaneous discharge. Since each pulse is smaller at higher rates, it is likely that the tubes fail by spontaneous discharge after a certain amount of charge has passed through them. It also appears that the tube selected for *Mariner IV* may have been an especially short-lived tube in spite of the excellent stability displayed in selection and prelaunch tests. It appears that any other tube in the batch would have had a life-count capacity capable of finishing the mission.

In an effort to understand the mechanism of the failure mode, it was speculated that perhaps the quench gas, a mixture of chlorine and silicon tetrafluoride, was depleted. This would explain the sustained count rate in the absence of sources. With this in mind, good tubes and failed tubes were submitted to chemical analysis. The analysis of the filling gas as performed by a mass spectrometer indicated no significant differences between gas from good tubes and gas from expended tubes. However, this test was deemed inconclusive due to the poor sensitivity of the available spectrometer.

A darkening of the transparent cathode of the expired tubes was noted as they were allowed to operate in the spontaneous counting mode. Chemical analysis of cathode washings showed chlorine — one of the quenching gases — to be present on the cathodes of both good and expired tubes. The most significant and entirely unexpected finding occurred when the tin oxide cathode of a blackened tube was carefully scraped and the scrapings submitted to spectrographic analysis. Tests showed a remarkable 72% (by weight) tungsten content. The mechanism for tungsten transport from anode to cathode is not yet understood.

The subsequent failure of the ion chamber portion of the instrument on the spacecraft, accompanied by the apparent simultaneous drop to zero in the G-M tube rate gave rise to speculation that perhaps the power sup-

ply, which is common to both detectors, had failed or had been shorted. This speculation was made more credible in view of the tungsten transport phenomenon. It was hypothesized that the anode was steadily weakened by the emission of tungsten until electrostatic attraction by the cathode was sufficient to break the anode. Further, it was theorized that the slender anode might be attracted to the cathode to the extent that physical contact might be made, the ensuing arc providing the energy necessary to weld the anode to the cathode, resulting essentially in a short circuit of the power supply. In order to provide a method of quickly testing the feasibility of the hypothesis, it was necessary to find a means of severing the anode of the tube while the tube was counting normally under applied high voltage. To accomplish this feat, a good tube was mounted to the breadboard circuit. By means of optical lenses, the beam from a ruby laser was focused through the glass envelope of the tube onto the anode. With the tube in normal counting operation and powered by the breadboard ion chamber circuit, the laser was pulsed. The anode burned in two and the energized segment was attracted to the cathode as postulated. However, welding of the anode to the cathode did not occur immediately, but required a period of approximately 40 min during which time the arcing between the electrodes was visible through the glass tube. A possible reason why the welding was not instantaneous in this case, but may have been instantaneous with the unit in space, was that burning the anode in half seemed to result in the formation of a small ball of tungsten on the melted ends of the anode. The additional mass of tungsten, slightly larger than the diameter of the anode wire, might be expected to require considerably more energy for welding than an anode wire eroded to the breaking point by tungsten emission. Also, an eroded wire might have significantly less restoring force to counter the electrostatic attraction.

Additional evidence in favor of the shorted power supply hypothesis occurred when the life test unit failed in a manner much the same as the *Mariner IV* instrument. The G-M tube output dropped to zero after a count rate profile and a time interval comparable to that of the spacecraft instrument. Simultaneously, the test voltages at all monitor points dropped in a manner that suggested a shorted supply. However, the ion chamber sensor continued to function with only slight increase in the expected period as opposed to the immediate failure of the chamber in space. This apparent discrepancy in the failure modes seems to have been resolved by subsequent tests on the breadboard circuit. If it is assumed that the

power supply is shorted through the G-M tube, breadboard tests indicate that if the life test unit (operating at ambient room temperature) were subjected to cold temperatures comparable to those experienced by the unit in space, the high voltage would decrease to a value below the ion chamber pulsing threshold.

Further evidence for the postulated failure mode has been obtained. Three failed tubes functioning in their spontaneous discharge modes have successively been operated on the breadboard circuit until output

from the tubes ceased. In all three cases when each tube finally quit producing the spontaneous output pulses, it was noted that the filaments had broken. In two of the tubes, the anode was observed to have been instantaneously welded to the cathode, resulting in a short-circuit of the power supply. The third tube proved to have an open circuit within the tube. This occurred because the break in the anode was located so close to the glass feedthrough sheath as to provide insufficient length for the energized end of the broken anode to reach the cathode.

## References

1. Johnston, A. R., *The Absolute Cosmic-Ray Ionization in the Atmosphere at Balloon Altitudes*, thesis, California Institute of Technology, Pasadena, Calif., 1956.
2. Neher, H. V., and Anderson, H. R., "Cosmic-Ray Intensity at Thule, Greenland during 1962 and 1963, and a Comparison with Data from Mariner II," *J. Geophysical Res.*, Vol. 69, pp. 807-814, 1964.

## Bibliography

- Anderson, H. R., Despain, L. G., and Neher, H. V., "Response to Environment and Radiation of an Ionization Chamber and Matched Geiger Tube Used on Spacecraft," *Nuclear Instruments and Methods*, June 1966.
- Anderson, H. R., "Ionizing Radiation Measured Between Earth and Venus by Mariner II," in *Space Research V*, pp. 521-543. North Holland Publishing Co., Amsterdam, 1965.
- Camerini, U., Lock, W. O., and Perkins, D. H., "The Analysis of Energetic Nuclear Encounters Occurring in Photographic Emulsions," in *Prog. in Cosmic-Ray Phys. I*, pp. 1-62. North Holland Publishing Co., Amsterdam, 1952.
- Evans, R. D., *The Atomic Nucleus*, pp. 605-606. McGraw-Hill Book Company, Inc., New York, 1955.
- Frank, L. A., "Efficiency of a Geiger-Mueller Tube for Non-penetrating Electrons," *J. Franklin Inst.*, Vol. 273, pp. 91-106, 1962.
- "Mariner IV Ionization Chamber Failure Analysis," in *Space Programs Summary 37-34. Vol. VI*, Jet Propulsion Laboratory, Pasadena, Calif., July 31, 1965.

### Bibliography (contd)

- Neher, H. V., and Johnston, A. R., "Modification to the Automatic Ionization Chamber," *Rev. Sci. Instr.*, Vol. 27, pp. 173-174, 1956.
- Neher, H. V., "An Automatic Ionization Chamber," *Rev. Sci. Instr.*, Vol. 24, pp. 99-102, 1953.
- Neher, H. V., "Variable Sensitivity Automatic Ionization Chamber," *Rev. Sci. Instr.*, Vol. 32, pp. 48-49, 1961.
- Rich, M., and Madey, R., *Range Energy Tables UCRL-2301 USAEC*, Technical Information Service, Oak Ridge, Tenn., 1954.
- Whaling, W., "The Energy Loss of Charged Particles in Matter," *Handbuch der Physik*, Vol. 34, pp. 193-217, Springer Verlag, Berlin, 1958.

## VI. Cosmic Ray Telescope

### A. Introduction

The cosmic ray telescope (CRT) was developed under the direction of Professor John A. Simpson, the principal investigator, and Mr. J. J. O'Gallagher, co-experimenter, both of the University of Chicago. This telescope, shown in Fig. VI-1, was designed to measure the absolute and relative flux levels and the energy spectra of the two main components of primary cosmic radiation, namely protons and ionized helium, in the energy range from 1-180 MeV/nucleon. Thus, the CRT was capable of identifying He ions in the 180 MeV/nucleon- $\infty$  range and electrons over a small range of energies with low efficiency. The specific aims of these measurements were directed both towards measurements of fluxes in interplanetary space and toward measurements to be conducted in the vicinity of Mars (Ref. 1).

The separation of spatial from temporal variations of the proton and helium spectra and fluxes was to be attempted from data obtained with instruments (from the University of Chicago) launched into earth orbits in September 1964, *Orbiting Geophysical Observatory 1* (OGO-1) and *Interplanetary Monitoring Probe 2*

(IMP-2), in May 1965 (IMP-3), and from the Neutron Intensity Monitor network (Ref. 2).

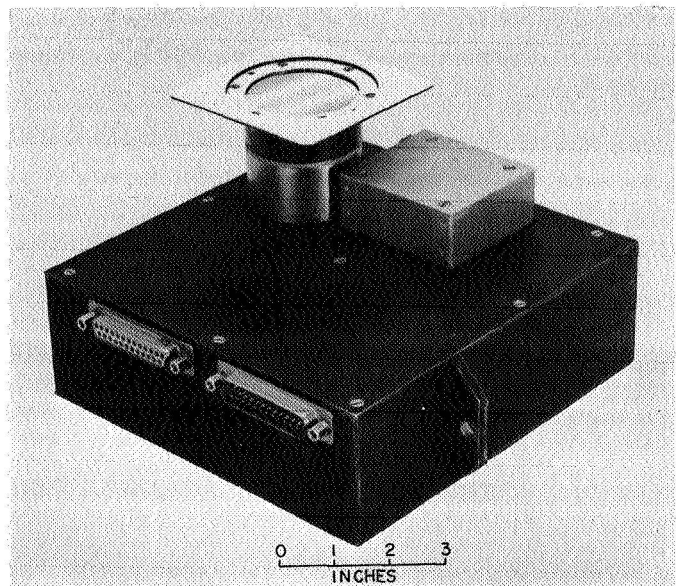


Fig. VI-1. Cosmic ray telescope

## B. Objectives

The objectives of the cosmic ray telescope experiment included:

- (1) To measure the radial gradient in the low-energy cosmic-ray intensity in the inner solar system between 1 and 1.5 AU.
- (2) To measure the ratio of low-energy protons and He ions as a function of radial distance from the sun.
- (3) To search for trapped protons and electrons at Mars.
- (4) To search for shock front accelerated electrons near Mars.
- (5) To study the time dependence, composition, and spectra of solar flare particles in interplanetary space.
- (6) To search for a persistent solar contribution to the low-energy proton spectrum at solar minimum.
- (7) To determine whether high-energy electrons are present by comparison of results with the Geiger-Müller counters and ionization chamber.

## C. Instrument

The measurements were made using a three-element energy loss ( $dE/dx$ ) versus range telescope. This telescope consists of three gold-silicon surface barrier detectors (labeled  $D_1$ ,  $D_2$ , and  $D_3$ ) that are arranged with absorbers between  $D_1$ - $D_2$  and between  $D_2$ - $D_3$ , as shown in Fig. VI-2.

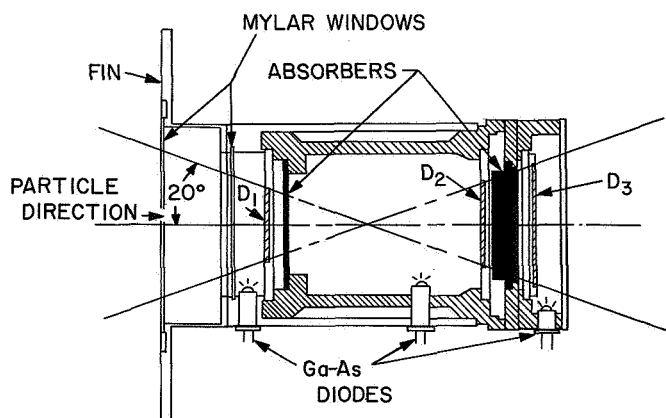


Fig. VI-2. Cross section of telescope showing sensors

When any energetic charged particle passes through matter, it loses energy through ionization. When such a particle passes through a solid-state detector, it creates a number of electron-hole pairs that are swept out of the silicon, before recombination can occur, by an electric field set up by bias voltage. A packet of charge thus produced in any detector is deposited at the input of a charge-sensitive preamplifier and is converted to a voltage pulse that is directly proportional to the amount of charge produced in the detector and, hence, to the energy lost by the particle.

Associated with the detector-preamplifier combination  $D_1$ ,  $D_2$ , and  $D_3$  are five pulse-height discriminators with levels labeled  $D_1$ ,  $D_1'$ ,  $D_2$ ,  $D_3$ , and  $D_3'$ . In addition, the  $D_1$  detector amplifier combination has associated with it a 128-channel pulse-height analyzer, so that, under certain conditions (described below), the energy loss in the  $D_1$  detector may be measured. The outputs of the five discriminators are fed to coincidence-anticoincidence logic such that, in the normal mode of operation, events are classified as to how much absorber they have penetrated, i.e., according to particle range in matter. The coincidence resolving time of these circuits is 4  $\mu$ s, which leads to a negligible accidental coincidence rate of approximately  $2 \times 10^{-5}$  counts/s, when taken in conjunction with an individual detector count rate of 1-2 counts/s. The number of each type of coincidence event occurring between readouts is recorded and results in three basic counting-rate channels:  $D_1' \bar{D}_2$ ,  $D_1' D_2 \bar{D}_3$ , and  $D_1' D_2 D_3$  ( $D_1' \bar{D}_2$  is read:  $D_1'$  and not  $D_2$ ).

Each of these rate channels corresponds to energetic particles of known ranges. The  $D_1' \bar{D}_2$  rate corresponds to the number of particles having enough energy to penetrate the protecting windows of the telescope to  $D_1$ , but not enough to penetrate the aluminum absorber between  $D_1$  and  $D_2$ . This corresponds to particles with energies of 0.8 to 15 MeV/nucleon for vertical incidence. The  $D_1' D_2 \bar{D}_3$  rate includes those particles penetrating to  $D_2$  but not through the platinum absorber to  $D_3$ , or particles with energies between 15 and 70 MeV/nucleon. The  $D_1' D_2 D_3$  rate includes all particles which pass through all three detectors and all absorbers while leaving enough energy in all three detectors to exceed the associated discriminator levels of each. Figure VI-3 shows the energy loss versus energy per nucleon curves for protons and He ions. From this graph it can be seen that, as particle energy increases, the proton energy loss decreases until it is less than the  $D_1$ ,  $D_1'$ ,  $D_2$ , and  $D_3$  threshold levels (all set at approximately 210 keV) for

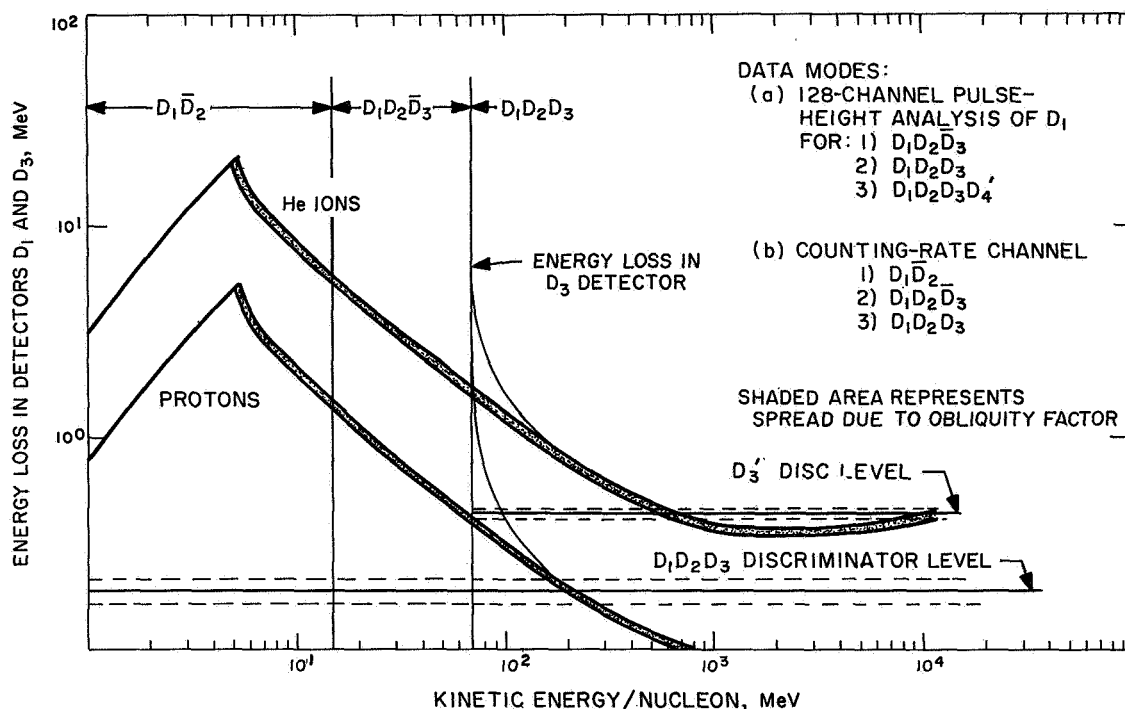


Fig. VI-3. Energy loss of particles in  $D_1$  and  $D_3$  detectors vs incident particle energy

protons with energies greater than 170 MeV. In contrast, the minimum energy loss of a He ion remains above threshold for all energies. This gives rise to the differing sensitive ranges of 70 to 170 MeV for protons and 70 MeV/nucleon- $\infty$  for He ions in the  $D_1D_2D_3$  channel.

The coincidence requirement between the detectors  $D_1$  and  $D_2$ , which is in effect for the last two of the rate channels discussed previously, defines a cone of half angle 20 deg limiting the directions from which the incident particle can arrive in order to pass through both detectors. The  $D_1$  and  $D_2$  detectors are 2.5 cm<sup>2</sup> in sensitive area and the  $D_3$  detector has a 5-cm<sup>2</sup> sensitive area with spacings that result in a geometrical factor of 0.24 cm<sup>2</sup>-sr for forward incident particles. Particles incident from the back side of the telescope can contribute to the  $D_1D_2D_3$  rate; however, allowance for this correction has been made.

A fin in front of the  $D_1$  detector acts as an aperture for nucleons  $\sim 0.8$  to  $\sim 30$  MeV/nucleon and for low-energy electrons so that the geometrical factor for  $D_1$  is  $\sim 7$  cm<sup>2</sup>-sr.

In addition to the three counting rate measurements discussed, the energy loss spectrum of all particles pro-

ducing at least a double ( $D_1D_2$ ) coincidence is *sampled* by recording the digitalized pulse height corresponding to the energy loss in the  $D_1$  detector of the *first*  $D_1D_2$  event occurring after each readout. Indicator bits record whether this event was a double or triple coincidence and, if triple, whether the  $D_3$  level was high or low. The  $D_3'$  discriminator level at  $\sim 420$  keV on the  $D_3$  detector is used partially as an aid to the identification of particles as either forward or backward moving and, in addition, to provide better separation between protons and He ions in the  $D_1D_2D_3$  range. In this way the energy loss-range "signature" of a given event is recorded, from which the particle may be identified as a proton or He ion and its approximate total energy can be determined by means of known range-energy relations.

Further study of Fig. VI-3 will show that protons and He ions are separable over almost the entire range of sensitivity. The pulse-height analyzer has a range from 200 keV at threshold to 5.7 MeV at saturation to include the greatest possible energy loss by a He nucleus. Energetic particles with  $Z > 2$  will lose more energy than He ions and the resulting pulse will saturate the pulse-height analyzer, but will be distinct from He. In this manner, the components of the double and triple coincidence rates can be identified and their relative contributions measured.

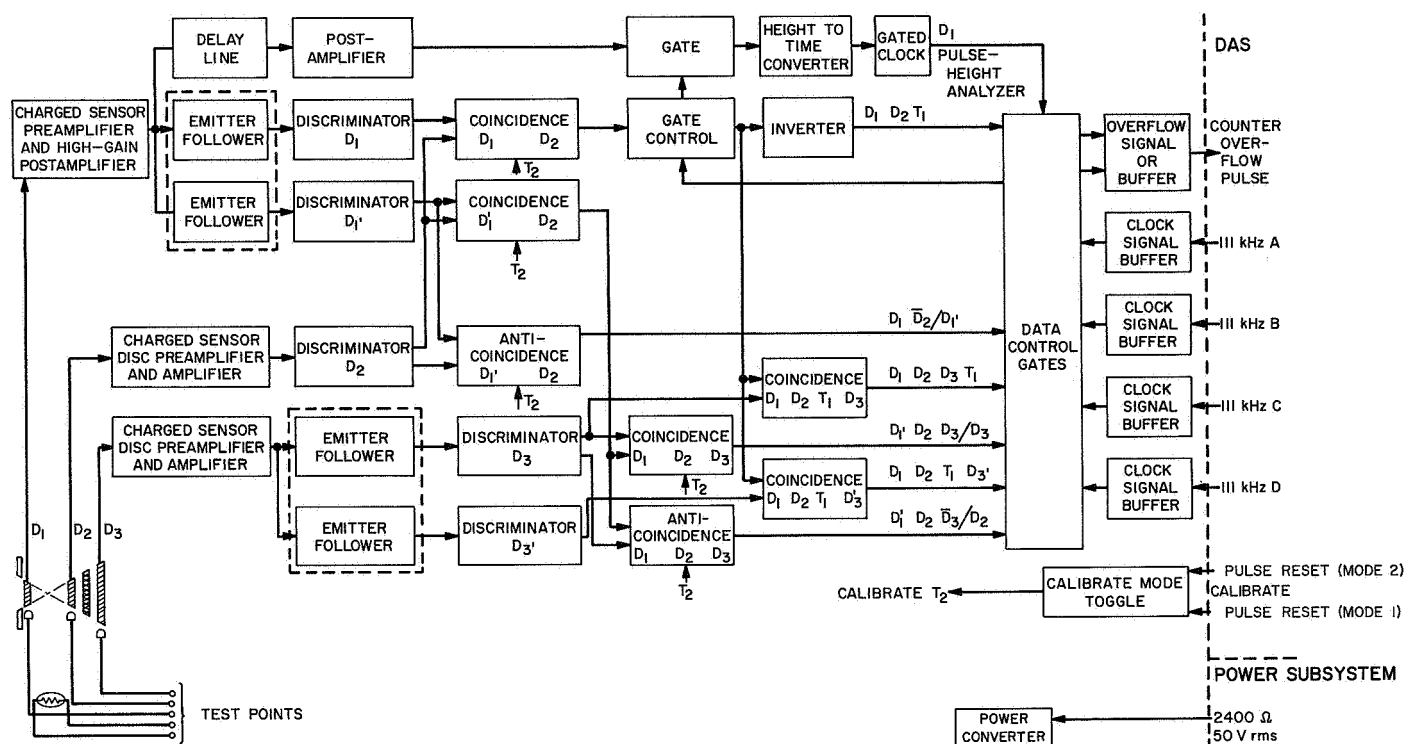
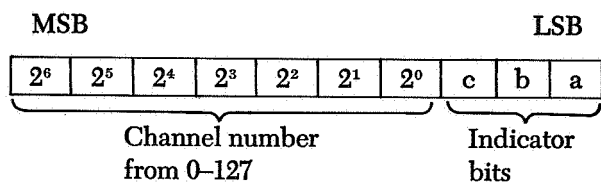


Fig. VI-4. CRT block diagram showing logical functions

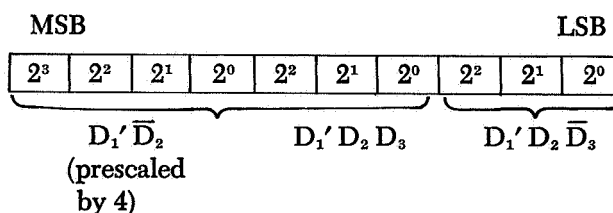
The block diagram in Fig. VI-4 depicts the logic used in making these measurements. In addition to the three coincidence rates, the coincidence logic controls a linear gate, which allows the pulse from the  $D_1$  amplifier to proceed to the analog-to-digital converter (A/D) only if there is a  $D_1 D_2$  coincidence and if the toggle  $T_1$  is in the reset state. This toggle is then set by the trailing edge of the coincidence pulse preventing further pulses from being analyzed until  $T_1$  is reset at the time of readout.

**1. Accumulation, readout, and format of data.** The three coincidence rates and the pulse-height channel and indicator bits are accumulated and stored between readouts by the data automation system (DAS) in two 10-bit registers within the CRT as follows:

(1) Particle analysis register



(2) Count rate register



In the analysis register, seven bits are allotted to storing the channel number. Bits "b" and "c" are 1 if  $D_3$  and/or  $D_3'$  are respectively fired in coincidence with the analyzed event. Bit "a" is 1 if there was one or more  $D_1 D_2 \bar{D}_3$  event(s) between readouts (not necessarily corresponding to the event analyzed). In the "rate" word, three bits each are allotted for the number of double or triple coincidences between readouts, and four bits are allotted for recording the number of  $D_1' \bar{D}_2$  events prescaled by 4. Both registers are reset to zero after readout by the DAS.

The registers are each read out serially by the DAS, which supplies a train of 111-kHz pulses to the register, and in parallel into a register within the DAS. The eventual overflow of the CRT register generates a pulse that, when received in the DAS, shuts off the pulse train leaving the DAS register containing a number that is one

more than the one's complement of the CRT binary register. The numbers in the DAS register are transmitted and recorded as raw data at earth.

The DAS reads out the particle-analysis and count-rate registers in even and odd numbered frames, respectively, and in any given frame, words 6 and 22 (also 30 during encounter mode at Mars) are CRT data from the corresponding register. This results in accumulation times of 72 and 19.2 s for words 6 and 22, respectively, at the  $8\frac{1}{3}$ -bit/s transmission rate, and one quarter of these times at the  $33\frac{1}{3}$ -bit/s rates. These times are short enough to insure that the storage capacity of the coincidence rate channels should exceed the expected count rates of  $\sim 1.5$  counts/min by at least a factor of 15 under normal conditions.

**2. Calibration and checkout procedures.** The three means of calibration used for the cosmic-ray telescope use both artificial pulse generation and energetic particle measurements, using natural radioactive sources or accelerated particles from laboratory accelerators. The most accurate measurements are made using a pulse generator to feed voltage pulses through a calibrated probe input to each of the three charge-sensitive preamplifiers. These pulses deposit at these inputs an amount of charge corresponding to a known energy. By varying the amplitude of the pulse, the thresholds of the five discriminators and the input response curve of the pulse-height analyzer is measured in terms of energy with an accuracy of  $\pm 0.5\%$ .

For operation in flight and during spacecraft testing, a calibrate mode of instrument operation has been incorporated in the CRT. This operation uses the permanent installation of low-level  $^{241}\text{Am}$  alpha particle sources in front of each of the three detectors. These sources are encapsulated between two thin layers of Mylar and have only enough energy to penetrate to the detector on which they are mounted. Hence, in the data mode of operation, they produce no coincidences or pulse-height analysis, but only contribute to the  $D_1\overline{D}_2$  rate. In the calibrate mode of operation, the coincidence circuits are disabled, allowing the individual count rates on  $D_2$  and  $D_3$  to be recorded and the pulse-height analysis of the  $D_1\overline{D}_2$  events to proceed. Large shifts in the counting rates of  $D_2$  or  $D_3$  would indicate significant shifts in the corresponding threshold. The source on  $D_1$  is constructed so as to provide a peak in the pulse-height distribution at a known energy, which would thus reflect any changes in amplifier or A/DC gain. The plot of such a distribution is shown in Fig. VI-5. These measurements are pri-

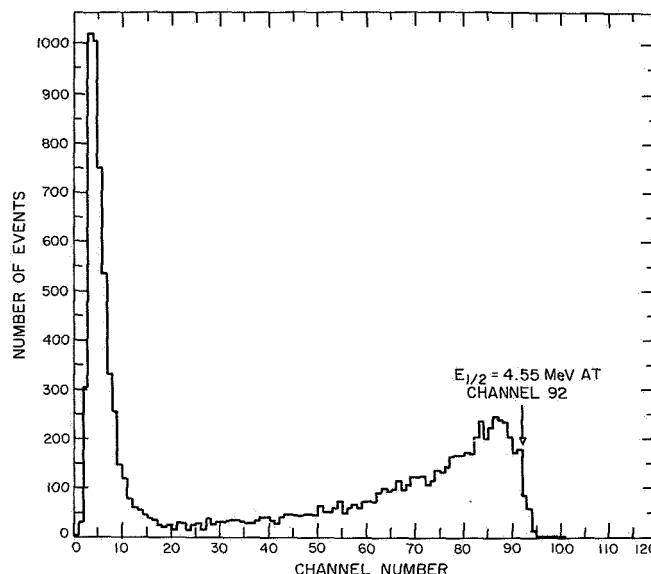


**Fig. VI-5. Typical pulse-height spectrum produced in  $D_1$  by internal  $^{241}\text{Am}$  source with instrument in calibrate mode**

marily designed to be gross checks, since the rates of all of these sources lie between 1 and 10 counts/min, thus a long time would be required to build up statistics for accurate measurements. However, they will provide a continuous monitoring of the gain and threshold levels throughout the mission. In flight, the instrument is put into the calibrate mode by command from the spacecraft DAS for a little more than 1 h out of every 27 h.

In addition to these measurements, all flight units have been exposed to high-energy proton beams from the University of Chicago 170-in. synchrocyclotron. This use of penetrating charged particles measures the actual energy ranges produced by the absorbers used in the telescopes. Also, the sensitivity of this type of detector to high fluxes of electrons of less than 30 keV and to somewhat lower fluxes of less than 200 keV electrons has been measured, using a small electron accelerator at the University of Chicago.

In addition to the calibration procedures, periodic checks of the coincidences and A/DC logic are performed. Since there are no natural radioactive sources of protons or alpha particles with sufficient energy to produce coincidences in the cosmic-ray telescope, a method of artificial stimulation of the individual detectors, in such a way as to simulate coincidences from protons and alpha particles and exercise the logic, has been designed at the University of Chicago. This method uses three,



infrared producing, Ga-As diodes mounted so that each diode views one solid-state detector in the telescope, as shown in Fig. VI-2. These Au-Si detectors are sensitive to infrared radiation, producing electron-hole pairs when such radiation is incident on their surface. The three diodes are driven by a program generator capable of delivering to any combination of detectors a preset number of pulses in coincidence at a large number of preset rates. The flexibility of the program generator thus allows the logic and storage to be exercised completely.

A further but somewhat limited logic check is obtained periodically by mounting a  $^{90}\text{Sr}$  source on the front radiating fin of the telescope. This source produces 2.2-MeV electrons to which the telescopes have a small sensitivity, in that a small fraction of the electrons can penetrate the aluminum absorber to  $D_2$  after passing through  $D_1$ , thus producing double (never triple) coincidences at a rate of about 0.5 counts/min. This check does not provide any calibration points, nor does it exercise all logic, and is thus intended only as a go-no-go check.

**3. Stability and degradation modes.** The drifts in the electronic circuitry of the CRT under the expected time and environmental variations during the mission are not expected to exceed  $\pm 1\%$  for the pulse-height analyzer or  $\pm 3\%$  on the discriminator levels. Such drifts are well within the limits required for accurate measurement of the desired quantities. It should be noted that the  $D_1 D_2 \overline{D}_3$  rate channel has been designed to depend on physical properties of charged particles passing through matter, i.e., their range and energy loss characteristics. These properties are governed by known physical laws making this channel totally insensitive to drifts as long as the detectors and discriminators are functioning.

The only degradation mode for the CRT outside of circuit failure is the breakdown of a solid-state detector, which might result from excessive heating or mechanical strain. This breakdown would produce an increase in the background noise level of the detector and a corresponding increase in the individual count rate from that detector, thus increasing the probability of accidental coincidences. The radiating fin (Fig. VI-1) is expected to maintain the telescope elements at a low temperature throughout the mission and prevent any such breakdown.

**4. Leading particulars.** The following is a summary of the CRT characteristics.

- (1) Overall characteristics:
  - (a) Weight: 2.7 lb.
  - (b) Power supply: 2400-Hz square wave, 100 V peak to peak.
  - (c) Power consumption: 400 mW (continuous).
- (2) Sensor characteristics:
  - (a) Type: three-element  $dE/dx$  versus range telescope using solid-state detectors and aluminum and platinum absorbers, which use coincidence techniques to define the range and limit the direction of incident particles.
  - (b) Detector characteristics:
    1. Type: gold-silicon surface barrier detectors, labeled  $D_1$ ,  $D_2$ , and  $D_3$ .
    2. Bias voltage (nominal): 50 V.
    3. Sensitive area:  $D_1$  and  $D_2$  of  $2.5 \text{ cm}^2$  and  $D_3$  of  $5 \text{ cm}^2$ .
    4. Depletion depth:  $200 \text{ }\mu\text{m}$ .
  - (c) Geometrical factor:  $0.24 \text{ cm}^2\text{-sr}$  for double and triple coincidences, and  $7 \text{ cm}^2\text{-sr}$  for  $D_1$  detector individually.
  - (d) View angle: cone of half angle of  $20 \text{ deg}$  from axis of telescope.
  - (e) Sensitive ranges: protons at  $0.8\text{--}170 \text{ MeV}$  and alpha particles at  $0.8 \text{ MeV/nucleon--}\infty$ .
- (3) Electronics:
  - (a) 128-channel pulse-height analyzer measuring amplitude of energy loss in  $D_1$  detector with a dynamic range extending from  $200 \text{ keV}$  to  $5.7 \text{ MeV}$ .
  - (b) Five discriminators:
    1.  $D_1$ ,  $D_1'$ ,  $D_2$ , and  $D_3$  at a nominal level  $210 \text{ keV}$ , used for both rate and pulse-height analysis functions.
    2.  $D_3'$  at a nominal level  $420 \text{ keV}$ , used only in conjunction with pulse-height analysis to provide further information on energy loss in  $D_3$  for better separation of protons and helium ions.

(c) Five coincidence and two anticoincidence circuits to control the pulse-height analysis gating and to provide coincidence rate outputs; coincidence resolving time is 4 ms.

(d) Prescaling and 20 binaries for accumulation and storage of the pulse-height channel number and coincidence rate data.

(4) Data outputs:

(a) Pulse-height channel numbers from 0-128, plus range indications.

(b) Three coincidence counting rates:

1.  $D_1\overline{D}_2$  protons and helium ions at 0.8 MeV/nucleon to 30 MeV/nucleon.

2.  $D_1D_2\overline{D}_3$  protons and helium ions at 15-70 MeV/nucleon.

3.  $D_1D_2D_3$  protons at 70-170 MeV, and helium at 70- $\infty$  MeV/nucleon.

## D. Results

During the *Mariner IV* mission to Mars from November 28, 1964 until October 1, 1965, one moderately large solar proton event and several much smaller events associated with solar activity (i.e., solar flares or "27-day" recurring regions) were observed by the cosmic-ray telescope. Almost all of these events, including the large event, were observed simultaneously by University of Chicago instruments on earth orbiting satellites, especially *IMP-3*. The analysis of the time and spatial relations between these simultaneous observations yields several new conclusions that would *not* have been evident from measurements at a single point in interplanetary space (Ref. 3).

First, it is apparent that the particles propagate by *anisotropic diffusion*, that is, they are strongly directed along rather than across the spiral interplanetary magnetic fields.

Second, the particles are sometimes injected, stored, and transported in already existing corotating magnetic field regions for periods on the order of days. These properties are not plainly evident from measurements at a single position in space where observations have usually been brought in agreement with one of the many isotropic diffusion models.

Third, there is also evidence for at least one series of so called "27-day" regions, recurring for at least three solar rotations of a type similar to those observed earlier on the *IMP-1* satellite (Ref. 4).

To illustrate these general conclusions, the first item to be considered is the large solar proton event associated with the Importance 2+ flare occurring at 1750 UT on 5 February 1965 and located at 8 deg N, 25 deg W on the sun (Fig. VI-6). Solar protons from this flare were observed by University of Chicago instrument on *IMP-2* in earth orbit and by the *Mariner IV* cosmic-ray telescope at 1.14 AU, 1.3 deg E of the earth. The decay time  $t_0$  for proton fluxes from this flare was observed to be shorter at earth than at *Mariner IV*. In Fig. VI-7 is displayed the integrated pulse-height distribution for protons 15-70 MeV observed on *Mariner IV*. These data show the absence of a helium component in this energy/nucleon interval and were used as the basis for constructing the time-varying proton spectrum (Refs. 5 and 6). Comparison of this time variation with the *IMP-2* time-varying spectrum showed that the near-earth spectrum steepened at a rate faster than at *Mariner IV*.

The most striking disparity between the two measurements, however, is shown in Figs. VI-8 and VI-9, which compare the onset and decay phases of the event as observed at the two points for particles in the 15-70-MeV range. Late in the flare when the flux should become nearly isotropic, there is still discrepancy in the decay phase where the two levels of intensity actually cross. This behavior can also be attributed to a spatial variation in intensity between these two points of observation even though they are relatively close together on an interplanetary scale.

The general properties of the spatial and temporal variations for events associated with two classes of solar related events (i.e., solar flares and "27-day" recurring regions) may be understood from a comparison of the counting rates of the front detector  $D_1$  on the *Mariner IV* and *IMP-3* instruments for the period from May 20 to October 1, 1965 (five successive "27-day" periods). During this time period, a number of very small increases in particle intensity were observed. The continuous time-intensity profile of these observations is shown in Fig. VI-10 for successive solar rotations Nos. 1804-1808. The counting rate channel shown is protons of energy  $> 1$  MeV and electrons  $> 200$  keV for both instruments. The roman numerals I, II, and III at the top of the figure give the range of onset times at which "27-day"

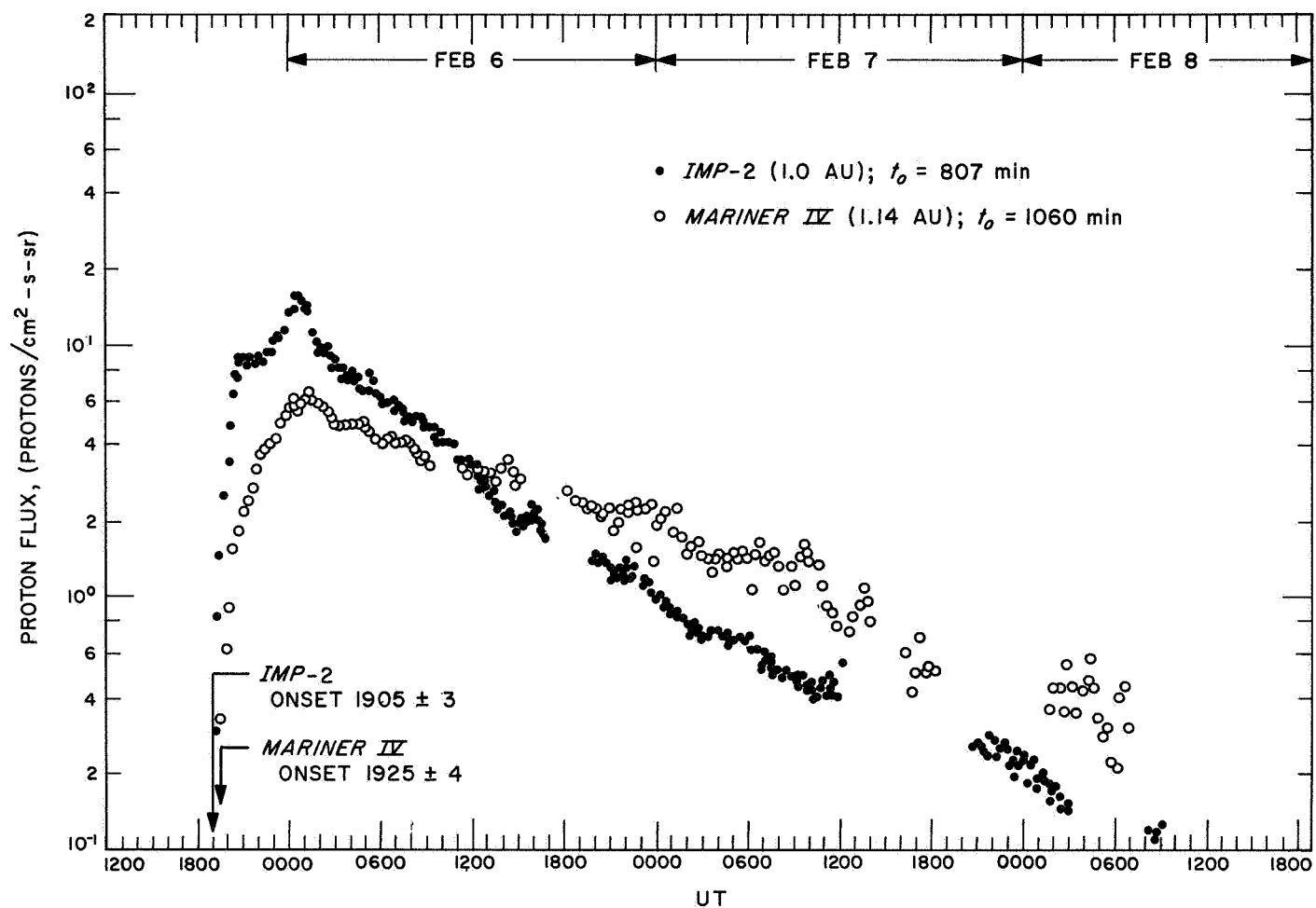
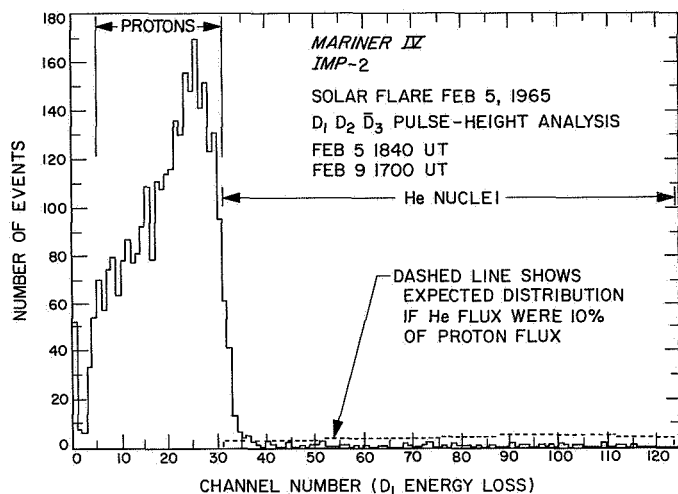
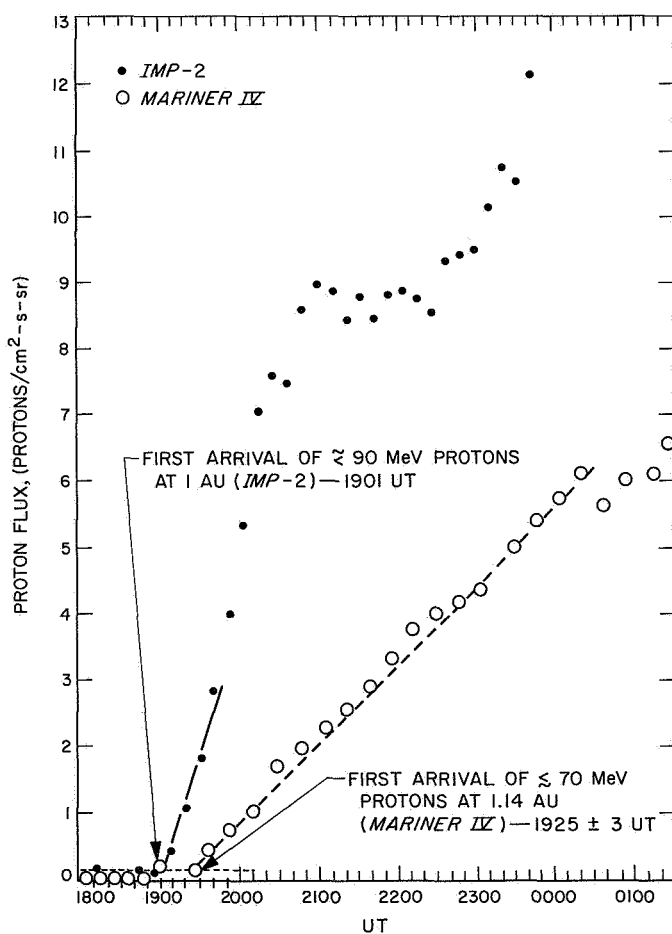


Fig. VI-6. Solar flare protons  $E > \text{MeV}$ , 5 February 1965



**Fig. VI-7. Integrated pulse-height distribution for protons 15-70 MeV**



**Fig. VI-8. Onset phase of solar proton event, 5 February 1965**

recurring modulation of galactic cosmic radiation was detected by the Climax neutron intensity monitor. The dots represent the *Mariner IV* counting rate and the light solid line represents the *IMP-3* data. The gaps in the *IMP-3* data correspond to times when the satellite was passing through the earth magnetosphere. Some fragments of *OGO-1* satellite data have been inserted to extend the data coverage at earth.

The trajectory of *Mariner IV* was such that for most of the mission the probe was falling steadily behind the earth as both moved around the sun. Thus, corotating regions arrived at *Mariner IV* before they arrived at earth for most of the last half of the mission, as shown in Fig. VI-11. In this figure, the spiral lines, representing the idealized interplanetary magnetic field configuration, are separated by an amount equivalent to one day of solar rotation. By relating the observations in Fig. VI-10 to the heliographic longitude of the pertinent solar activity (if it can be determined) and to the relative radial and angular separation of the two observations (as determined from Fig. VI-11 for each event individually), the following general qualitative conclusions are evident:

- (1) The separation in time between observations of some events at *Mariner IV* and *IMP-2* becomes increasingly well-defined with each successive solar rotation, indicating *corotation* of magnetic regions containing enhanced particle intensities first past *Mariner IV* and then past *IMP-2*.
- (2) The magnitudes of the time separations agree with that expected for regions following the general Archimedes spiral shape of the interplanetary magnetic field lines controlled by the solar wind.
- (3) The longitudinal spread of the events is limited as seen by the detection of some events by only one instrument when the angular separation of the two spacecraft is large. This limitation is also suggested by the profile of the corotating regions. This profile indicates that the propagation is anisotropic with the particles diffusing outward along the lines of force more easily than across them.
- (4) There is evidence that at least two of the events, which corotate past the two spacecraft, originate in a solar flare occurring somewhat prior to detection by either spacecraft. The subsequent storage of these particles eventually allows them to be transported in corotating magnetic fields to the detector location.

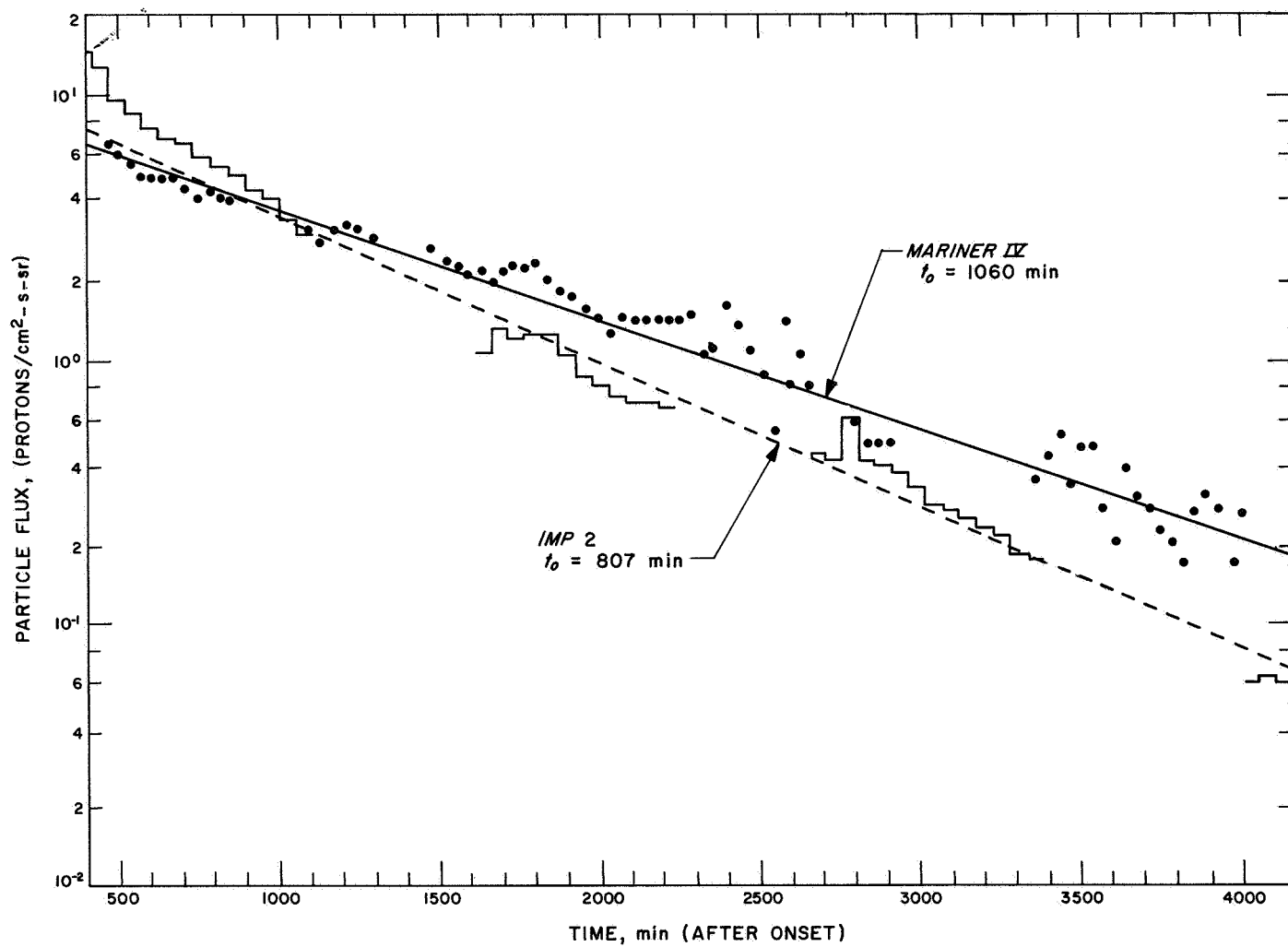


**Fig. VI-9. Decay of intensity of solar event, 5 February 1965**

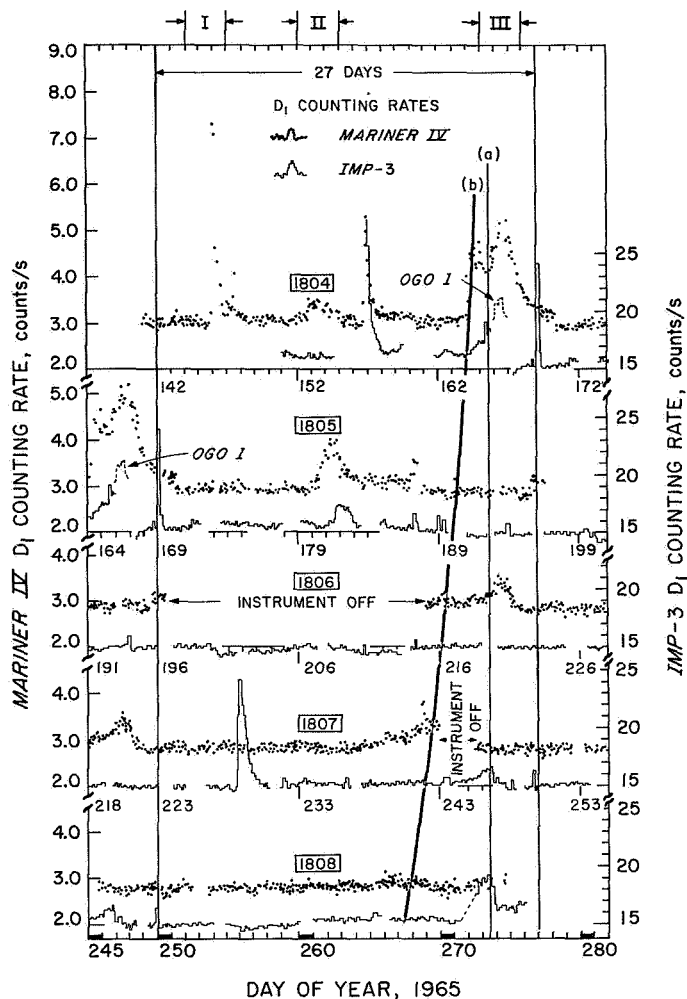


**Fig. VI-10. Continuous time-intensity profile for successive solar rotations Nos. 1804-1808, Mariner IV and IMP-3**

- (5) There is also evidence for at least one series of so-called "27-day recurring events" associated with corotating magnetic field regions that sweep past the two spacecraft with increasingly greater separation in time.

These particles are likely of the same origin as those observed on *IMP-1* and *OGO-1* and considered as either issuing from solar active regions or accelerated in interplanetary space (Ref. 4).

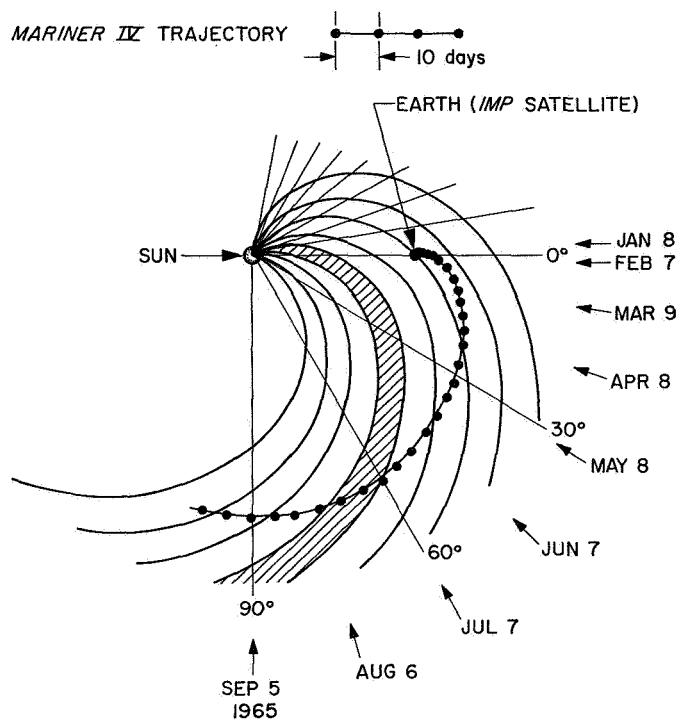


**Fig. VI-11. Mariner IV trajectory and idealized interplanetary magnetic field configuration**

Finally, it should be noted that at least two events have been identified as being composed of electrons only by the University of Iowa equipment on *Mariner IV*. From the shape of the intensity profiles of these events observed by the University of Chicago instrument, it can be concluded that the propagation of these electrons of energy greater than 200 keV is much the same as protons of 1 MeV, despite the large difference in magnetic rigidity for the two kinds of particles (Ref. 7).

The two major conclusions from the study of these small events, namely strongly anisotropic diffusion along spiral magnetic lines of force and corotation of stored particles in limited angular regions, serve to explain in a qualitative way the differences between the two observations of the larger flare of 5 February 1965.

## References

1. O'Gallagher, J. J., and Simpson, J. A., "Search for Trapped Electrons and a Magnetic Moment at Mars by *Mariner IV*," *Science*, Vol. 149, pp. 1233-1239, 1965.
2. Simpson, J. A., and O'Gallagher, J. J., "The Cosmic-Ray Telescope," paper presented at Western Electronic Show and Convention, Session 4, San Francisco, Calif., Aug. 24-27, 1965.
3. O'Gallagher, J. J., and Simpson, J. A., "The Interplanetary Propagation of Solar Flare Particles Simultaneously Observed by Earth Satellites and the *Mariner IV* Space Probe," *Bull. Am. Phys. Soc.*, Series II, Vol. II, No. 3000, 1966.
4. Fan, C. Y., Gloeckler, G., and Simpson, J. A., "Protons and Helium Nuclei Within Interplanetary Magnetic Regions Which Co-rotate with the Sun," in *Proceedings of the Ninth International Conference on Cosmic Rays, Accel. 3, London, 1965*. The Physical Society and London Institute of Physics, London, 1966.
5. Simpson, J. A., and O'Gallagher, J. J., "Proton and Alpha Particle Studies on *Mariner IV*," *Trans. Am. Geophys. Union*, Vol. 46, p. 15, 1965.
6. O'Gallagher, J. J., and Simpson, J. A., "Preliminary Results of Cosmic Ray and Mars Encounter Studies on *Mariner IV*," *Trans. Am. Geophys. Union*, Vol. 46, p. 533, 1965.
7. O'Gallagher, J. J., and Simpson, J. A., "Low-Energy Proton and Alpha Particle Studies on *Mariner IV*," paper presented at Midwest Conference on Cosmic Rays, Jan. 1965.

## VII. Helium Magnetometer

### A. Introduction

The magnetometer experimenters were Edward J. Smith (principal investigator) of Jet Propulsion Laboratory, Paul J. Coleman, Jr. of University of California at Los Angeles, Leverett Davis, Jr. of California Institute of Technology, and Douglas E. Jones of Brigham Young University.

Measurements in interplanetary space have added significantly to our knowledge of the large scale features and dynamics of interplanetary magnetic fields and plasma. Knowledge of the interplanetary field is important in understanding the propagation of solar cosmic rays and flare particles from the sun to the earth, in understanding the modulation of galactic cosmic rays, in treating the origin of the solar wind near the sun, and as a clue to solar magnetic fields above the photosphere. By studying the interaction scale structure of the interplanetary field, information may be obtained concerning magnetic storms, shocks, and other large fluctuations in interplanetary space. The magnetometer experiment of *Mariner IV* represents the first opportunity to sample magnetic fields at heliocentric distances significantly greater than 1 AU.

The magnetic field of Mars was investigated by making measurements along the *Mariner IV* trajectory

during encounter. A general planetary field, perhaps associated with a molten planetary core, would be directly measurable if part of the trajectory lies inside the hydromagnetic cavity or if conditions are like those observed near earth, where the solar plasma flow containing embedded magnetic fields is strongly affected outside the cavity, and instabilities generate magnetic disturbances that propagate outward to considerable distances. Thus, the existence or absence of a planetary field would be indicated by possible transitions from magnetic conditions characteristic of interplanetary space to magnetic conditions associated with the nearby presence of the planet. If the Martian dipole moment were greater than 1/10 that of earth, the probe would have reached the region where the dipole field is not grossly disturbed by the solar wind, and it would be possible to determine some of the structural characteristics of the field, such as the orientation of the dipole.

### B. Purpose

The objectives of the helium magnetometer experiment were:

- (1) Investigate the existence of a planetary field associated with Mars and, if one were observed, determine the characteristics of the field, including magnitude, direction, multi-polarity, and orientation relative to the planetary rotational axis.



- (2) Investigate the nature of the interface between the planetary and interplanetary magnetic fields.
- (3) Measure the magnitude and direction of the steady and slowly varying components of the interplanetary magnetic field and determine their variation with heliographic altitude and longitude.

### C. Instrument

The *Mariner IV* instrument is a low-field, vector, helium magnetometer that is not to be confused with either the rubidium magnetometer (Ref. 1) or the high-field, scalar, helium magnetometer (Ref. 2). This instrument, like the other two magnetometers, is a resonance magnetometer in which a specimen gas is examined spectroscopically, using optical pumping to detect changes in state caused by the presence of weak magnetic fields (Ref. 3). However, this vector helium magnetometer is not an absolute instrument like the others that produce tones, the frequencies of which are proportional to the field magnitude. Instead, it generates three steady or dc

voltages, each proportional to a component of the ambient field.

The basic operating principles of the *Mariner* instrument can be understood with the aid of the simplified diagram shown in Fig. VII-1. The pumping light,  $1.08\text{-}\mu$  radiation obtained from an electrodeless discharge helium lamp, is circularly polarized and focused on an absorption cell, where it is partially absorbed by metastable helium atoms. Absorption and pumping are observed by an infrared lead sulfide detector. Since simple Zeeman absorption depends on both the polarization of the resonant radiation and its direction of incidence with regard to the magnetic field, the pumped condition can be destroyed by changing the direction of the magnetic field. When a rotating field is applied to the cell, the field causes a periodic variation in the transparency of the gas. A sweep oscillator produces two sinusoidal currents, 90 deg out of phase in two mutually perpendicular sets of Helmholtz coils (represented in the figure by a circle) placed around the absorption cell. This generates a  $100\text{-}\gamma$  field rotating at a rate of 50 rev/s. Empirically, it is

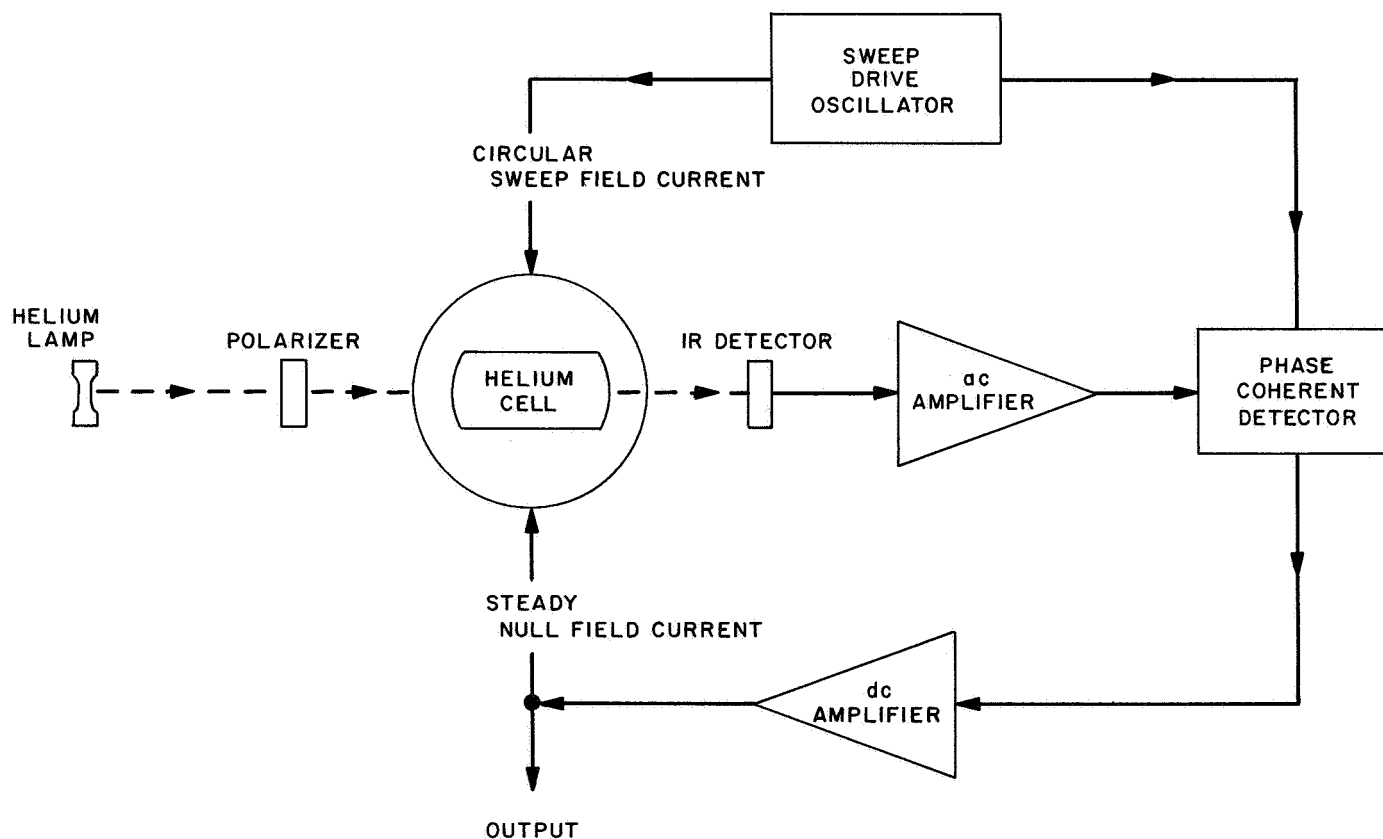


Fig. VII-1. *Mariner IV* vector helium magnetometer, simplified functional block diagram

found that the absorption is proportional to the square of the cosine of the angle between the light beam (optical axis) and the magnetic field. Thus, in the absence of an ambient field, the detector output is a second harmonic of the sweep frequency. If a dc field is present, the detector output contains a component at the sweep frequency whose phase depends on the angle between the optical axis of the sensor and the dc field. The ac amplifier passes a signal containing only the fundamental frequency component that is used to generate, by phase coherent detection, a dc current that is applied to the Helmholtz coils to null the external field. Thus, the magnetometer functions as a closed loop, or feedback, system with a resulting improvement in output linearity and stability.

A photograph of the *Mariner IV* magnetometer is shown in Fig. VII-2. The triaxial Helmholtz coils lie on

a 4-in. diameter sphere with the helium lamp and igniter at one end and the detector and a preamplifier at the other end. These units weigh 1.25 lb. The two modules containing the rest of the electronics weigh 4.5 lb. The left module houses the magnetometer power supply, igniter logic, RF power supply, and the analog-to-pulse-width (A/PW) converters. The right module contains the basic signal-chain circuits and ancillaries. The average power input to the instrument is 7 W. During the 10-s ignition periods, the instrument power consumption increases by 3 W.

As shown in Fig. VII-3, the magnetometer processes error signals ( $e_x$ ,  $e_y$ ,  $e_z$ ) to generate voltage outputs proportional to the components of a low magnetic field. The helium lamp provides the source of  $1.08\text{-}\mu$  resonant radiation. The collimated light beam passes through a linear polarizer and a quarter-wave plate, both of which

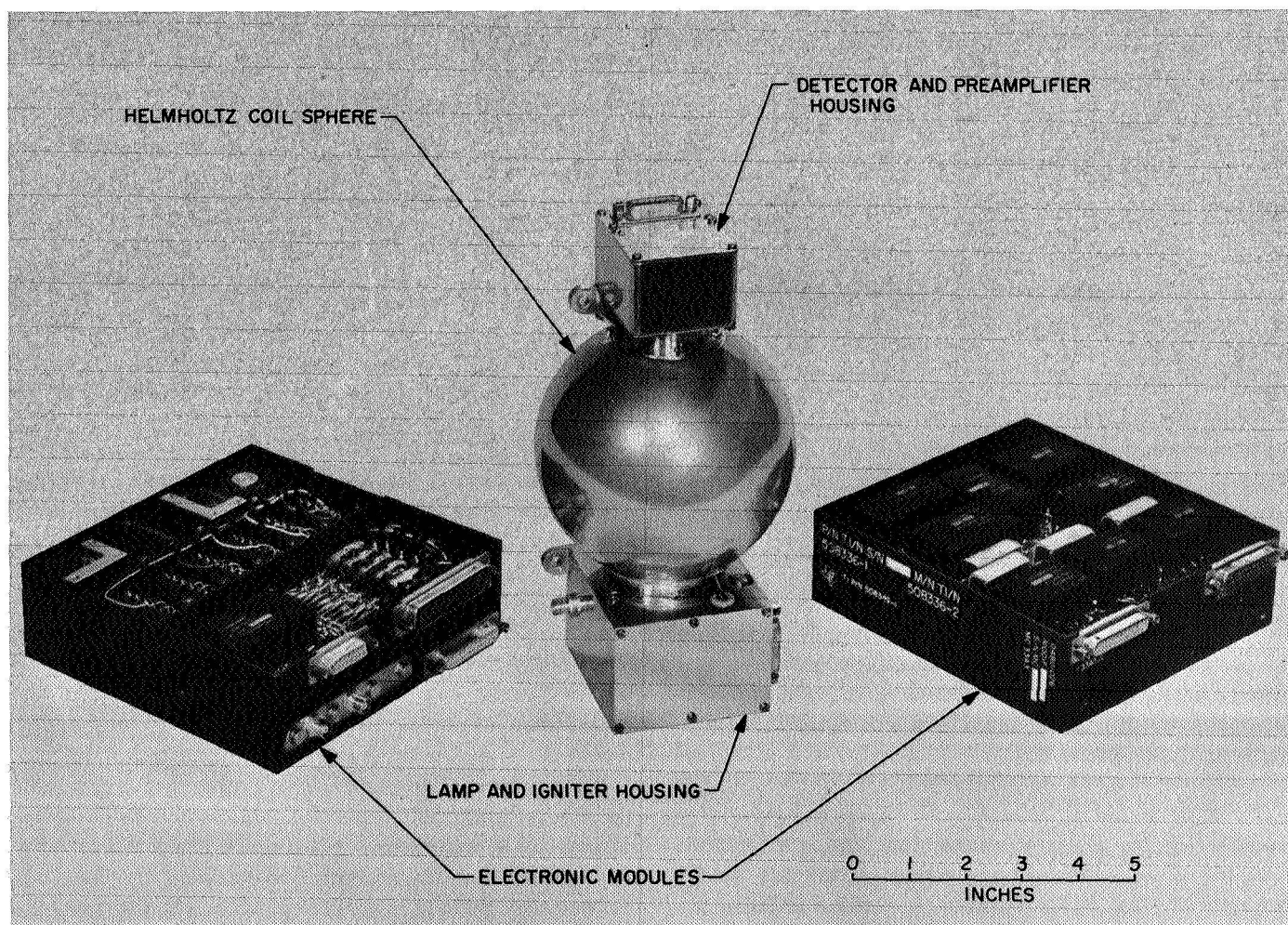


Fig. VII-2. *Mariner IV* magnetometer

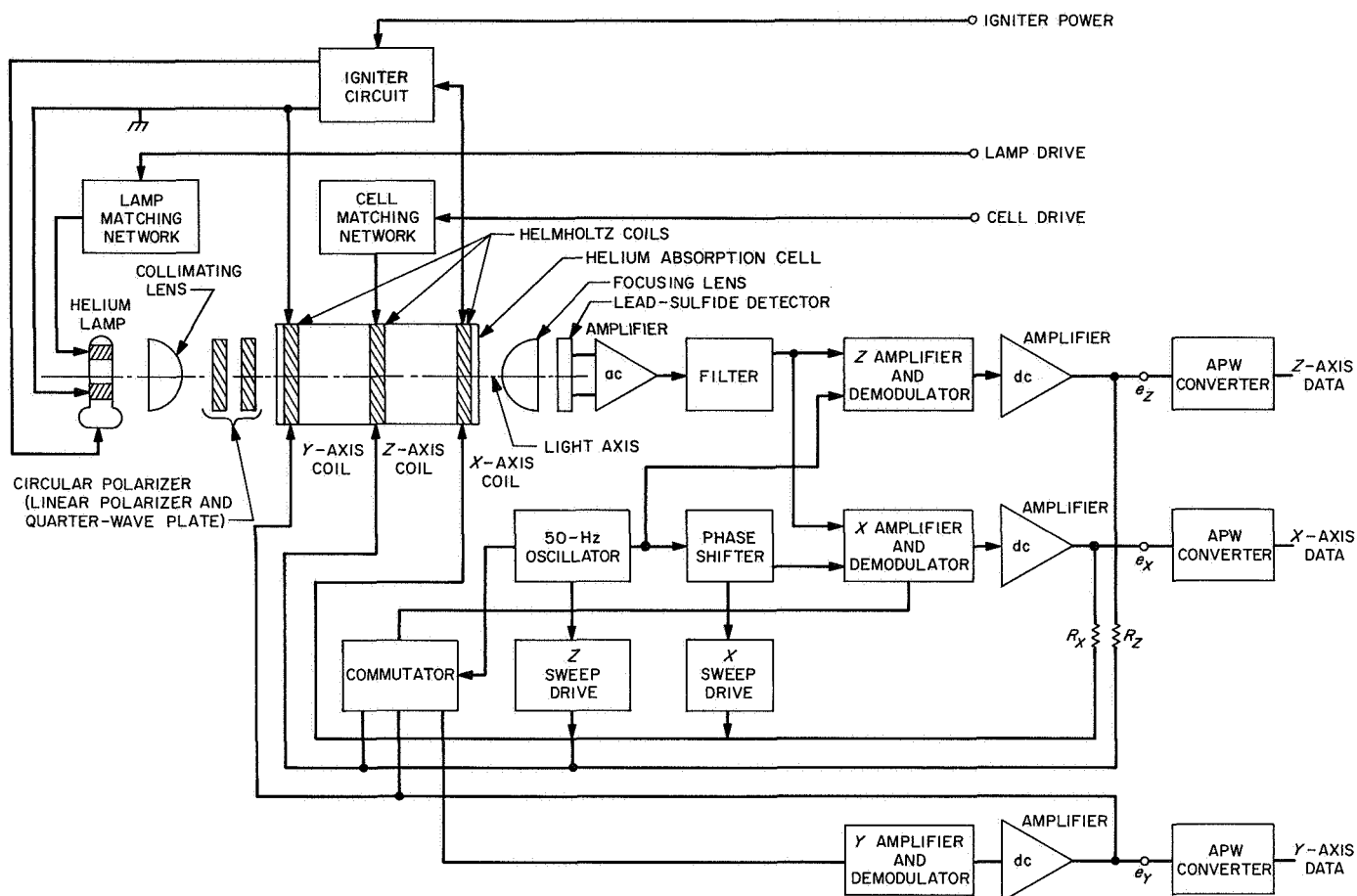


Fig. VII-3. Mariner IV magnetometer, simplified schematic

combine to polarize the light circularly. The triaxial set of Helmholtz coils surrounding the cell elements generate a magnetic sweep vector and null out the ambient magnetic field at the cell. A 50-Hz oscillator provides sinusoidal currents to drive the coils surrounding the cell to produce the components of the sweep vector.

The output from the lead sulfide detector is amplified, filtered to remove the second harmonic, and then fed to the X- and Z-bandpass amplifiers and demodulators. The Z demodulator is driven synchronously with the oscillator, and the X demodulator is driven synchronously with the phase shifter.

The error signal associated with the Z component is detected by the Z demodulator that converts this ac error signal to a dc voltage, which drives the Z-axis dc amplifier. The Z-axis output  $e_Z$  is applied to a resistor  $R_Z$  in series with the Z-axis coil. The X-axis signal is processed in the same manner as the Z-axis signal to produce

an output voltage proportional to the X component of the field.

Three-axis magnetometer action is achieved by adding a third coil (Y-axis) and commutating both sweep drive and demodulation on alternate cycles between X- and Y-axes. Decommutors internal to the amplifier loop are driven synchronously with the commutators in the X and Y sweep-drive circuits to extract the information for the X and Y planes. When the sweep vector is rotating in the Z-X plane, the X-axis error signal is gated to the X-axis demodulator, while the Y-axis decommutor blocks the signal from the X-axis demodulator. The commutator and decommutor drive is obtained by dividing the 50-Hz oscillator output by 2 and applying the 25-Hz square wave, with proper phasing, to the X and Y commutators. When the outputs are sampled by the Data Automation System, the commutation scheme provides measurements on all three magnetometer axes simultaneously.

## D. Results

For the purposes of scientific analysis, the *Mariner IV* magnetometer data fall into three distinct and separable magnetic regimes. The first of these is the region *near earth*, where the observed magnetic fields are either the earth's field, or interplanetary magnetic fields that have been deformed by a complicated interaction between the earth's field and the interplanetary medium. The second regime lies wholly in *interplanetary space* and contains weak magnetic fields transported outward from the sun by the streaming solar wind. Finally, the observations at the time of Mars *encounter* are of special significance because of the information they contain about the intrinsic magnetic field of Mars.

**1. Near-earth measurements.** The basic interest in making magnetic measurements near earth is to explore further the nature of the complex interaction between the streaming interplanetary medium and the geomagnetic field. Much of the scientific interest stems from the unique opportunity such measurements provide to investigate the physics of tenuous, highly ionized gases under conditions that have, thus far, not been reproduced in the laboratory.

The fields and particles measurements prior to *Mariner IV* have been concerned with two objectives: first, to characterize the different regimes surrounding the earth and to determine the position and shape of large scale features, such as the bow shock, the outer boundary of the geomagnetic field, and the earth's magnetic tail; second, to investigate the dynamic, time-dependent phenomena occurring in the different regions. The major scientific accomplishments in these areas prior to the *Mariner IV* measurements have been reviewed recently by W. N. Hess, et al. (Ref. 4).

The *Mariner IV* data were first scrutinized to identify the various magnetic regimes through which the spacecraft passed. Then, special attention was given to a rather comprehensive study of magnetic fluctuations observed behind the earth's bow shock.

Scientists are keenly interested in this kind of investigation because of the potential information about the nature of the shock, the effect that the shock has on the portions of the solar wind passing through it, and the properties of the medium between the shock front and the earth's field. *Mariner IV* did not obtain the first data of this kind, but the *Mariner* observations are unique in

that they were acquired in a relatively unexplored region of space near earth and were free of certain limitations associated with earlier measurements.

**a. Classification of data according to magnetic regime.** The 10-min averages of the total field magnitude  $|B|$  and the magnitude of the solar radial component  $|B_r|$  are given in Fig. VII-4 as functions of GMT or, alternatively, geocentric distance. During this time interval, which began shortly after the magnetometer came on scale and ended just prior to complete attitude stabilization, *Mariner IV* rotated slowly (approximately 2 rev/h) about an axis oriented toward the sun. The changing orientation, relative to the ambient field, of the two sensor axes transverse to the sun-oriented axis allowed the corresponding components of the spacecraft field to be derived. The value of  $|B_r|$  was adjusted to agree with the radial component of the unperturbed geomagnetic field near the earth. The three spacecraft field components, which total 28  $\gamma$  at the sensor, were subtracted from the data before  $|B|$  was computed.

The data show four distinctly different magnetic regimes separated by transitions, designated in Fig. VII-4 as 1, 2, and 3. The data from nearest the earth to the first transition (at approximately 12 earth radii) show the same general dependence on geocentric distance as the unperturbed geomagnetic field. The average field from transition 1 to transition 2 (at approximately 22 earth radii) is essentially constant in magnitude, with an enhanced radial component that points away from the sun (no directional information is given in Fig. VII-4). The smaller (5- to 10- $\gamma$ ) average field in the region between transitions 2 and 3 is irregular in magnitude and direction. Transition 3 (at approximately 35 earth radii), not completely obvious in the 10-min averages, marks the edge of a zone in which regions of rapidly fluctuating fields alternate with regions of relatively stable fields.

The locations of the three major transitions along the *Mariner IV* trajectory and the relationship of these transitions to the different regions of interaction between the solar wind and the magnetosphere are illustrated in the top half of Fig. VII-5. Shown are the asymmetric magnetosphere, consisting of a torus formed by field lines that corotate with the earth; an elongated magnetic tail pointing away from the sun; and the detached hydro-magnetic bow shock. The boundary between the corotating magnetosphere and the tail identifies transition 1, the boundary between the tail and the turbulent magnetosheath identifies transition 2, and the standing shock front boundary identifies transition 3. These

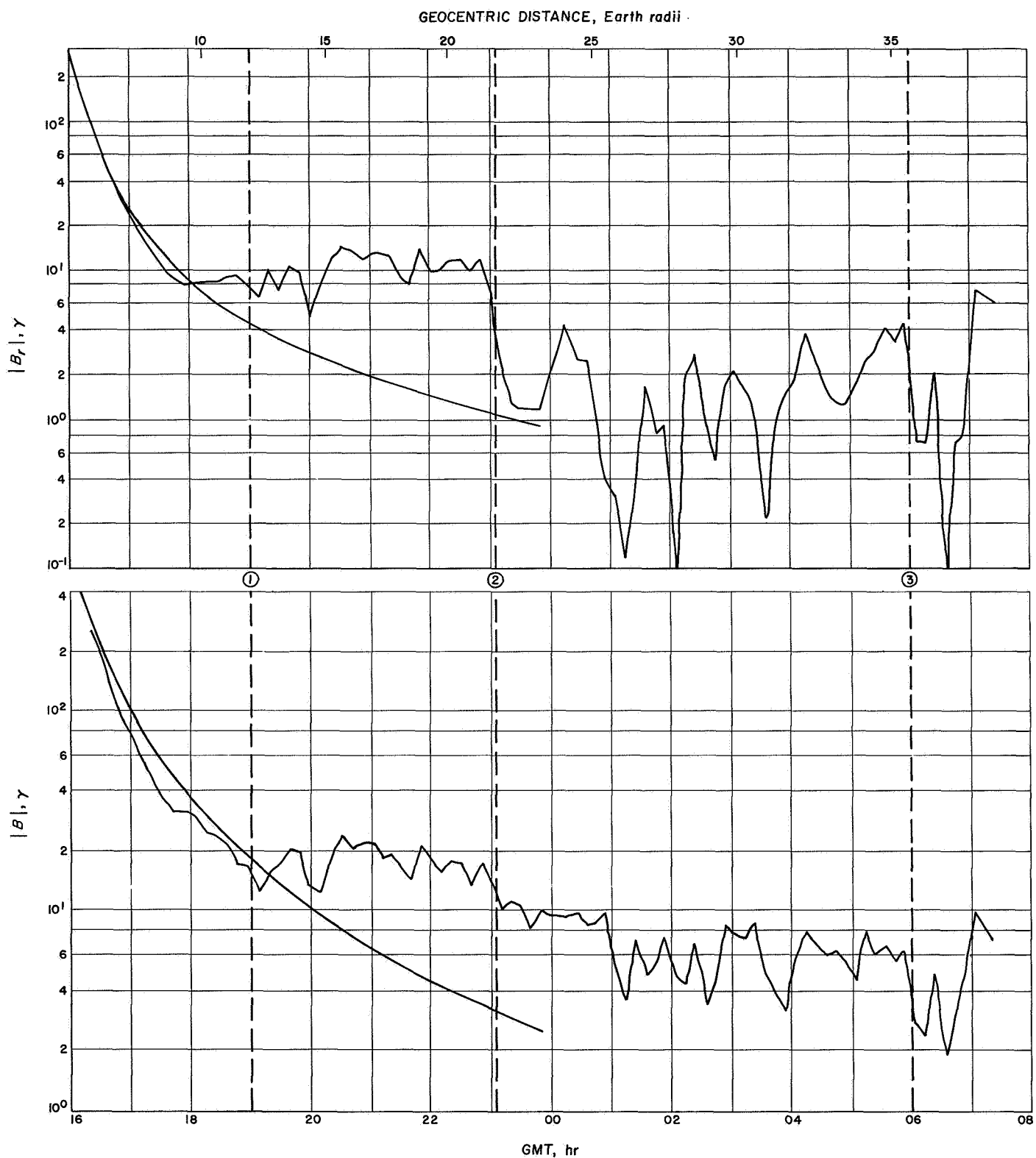


Fig. VII-4. Mariner IV magnetometer data acquired near earth

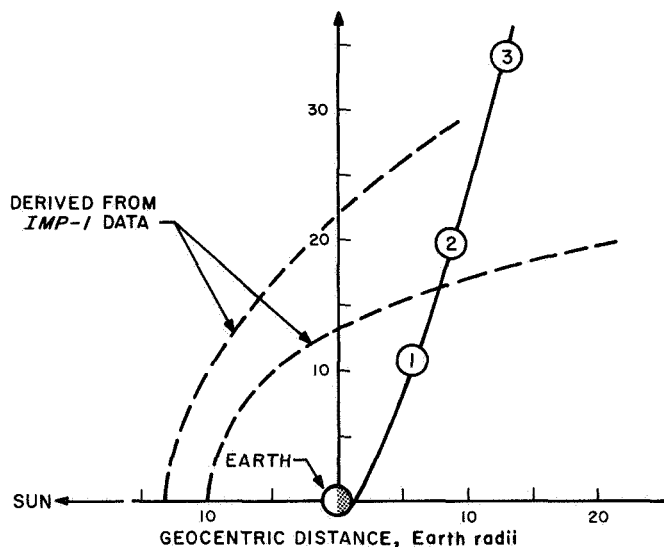
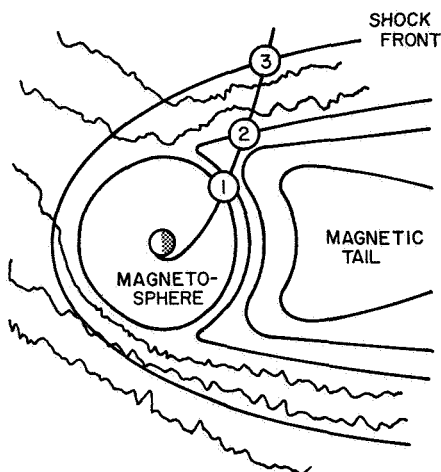


Fig. VII-5. *Mariner IV* near-earth trajectory

boundary locations agree reasonably well with corresponding transitions in the *Mariner IV* plasma and energetic particle data, as well as with previous field and particle measurements by other spacecraft.

The bottom half of Fig. VII-5 is essentially a polar plot of the near-earth trajectory, and is not a simple projection into a fixed plane, such as the ecliptic. The dashed curves show the average location of the magnetopause and shock front as derived from *IMP-1* (*Interplanetary Monitoring Probe 1*) magnetometer data. Transition 3 occurs near the extension of the outer contour. Transition 2 lies beyond the inner contour, but is generally consistent with the spread in the individual boundary penetrations by *Explorer 10*, *Explorer 14*, and *IMP-1* at approximately the same sun-earth-spacecraft

angle. The innermost transition detected by the *Mariner IV* magnetometer is associated with a general feature in the distribution of trapped electrons with energies greater than 40 keV.

Omnidirectional flux contours first obtained by the *Explorer 14* instruments showed a bifurcation behind the dawn line, at an average geocentric distance of approximately 9 earth radii, that is associated with the change from the magnetosphere proper to the magnetic tail. The characteristics of the electrons in and near the tail have been further investigated on *IMP-1* by K. Anderson and their relation to the observed magnetic field has been discussed by K. Anderson and N. Ness (Ref. 5).

The data acquired beyond transition 3 merit special attention because the important features are associated with the fine structure of the field, which is obscured by averaging. Figure VII-6 is a plot of all the magnetic measurements made during a 1-h interval corresponding to the range of geocentric distances between 36 and 38 earth radii. The radial component  $B_r$  is parallel to the Z axis of *Mariner IV*, which was continuously pointed at the sun.

The spacecraft was rolling about the Z-axis at a gyro-controlled rate, causing sinusoidal variations to appear in the two transverse field components  $B_x$  and  $B_y$ . No attempt was made to remove the effect of the spacecraft roll, which caused the variations with periods of approximately 30 min.

Vertical lines corresponding to the instantaneous shock front (SF) position divide the data in Fig. VII-6 into intervals when *Mariner IV* was inside the transition region (TR) and outside the shock in the interplanetary (IP) medium. The four triaxial measurements in each 12.6-s period reveal regions of higher noise levels that alternate with regions of relative quiet. The last such observation occurring at 07:18 GMT is not shown.

The abrupt changes from the transition region to interplanetary space represent successive passages through the shock front. This interpretation is supported by the *Mariner IV* plasma measurements, which show penetrations into the free-streaming solar wind to be coincident with several of the shock-front transitions in the magnetometer data. The multiple passages through the shock front show that it is not stationary, but surges back and

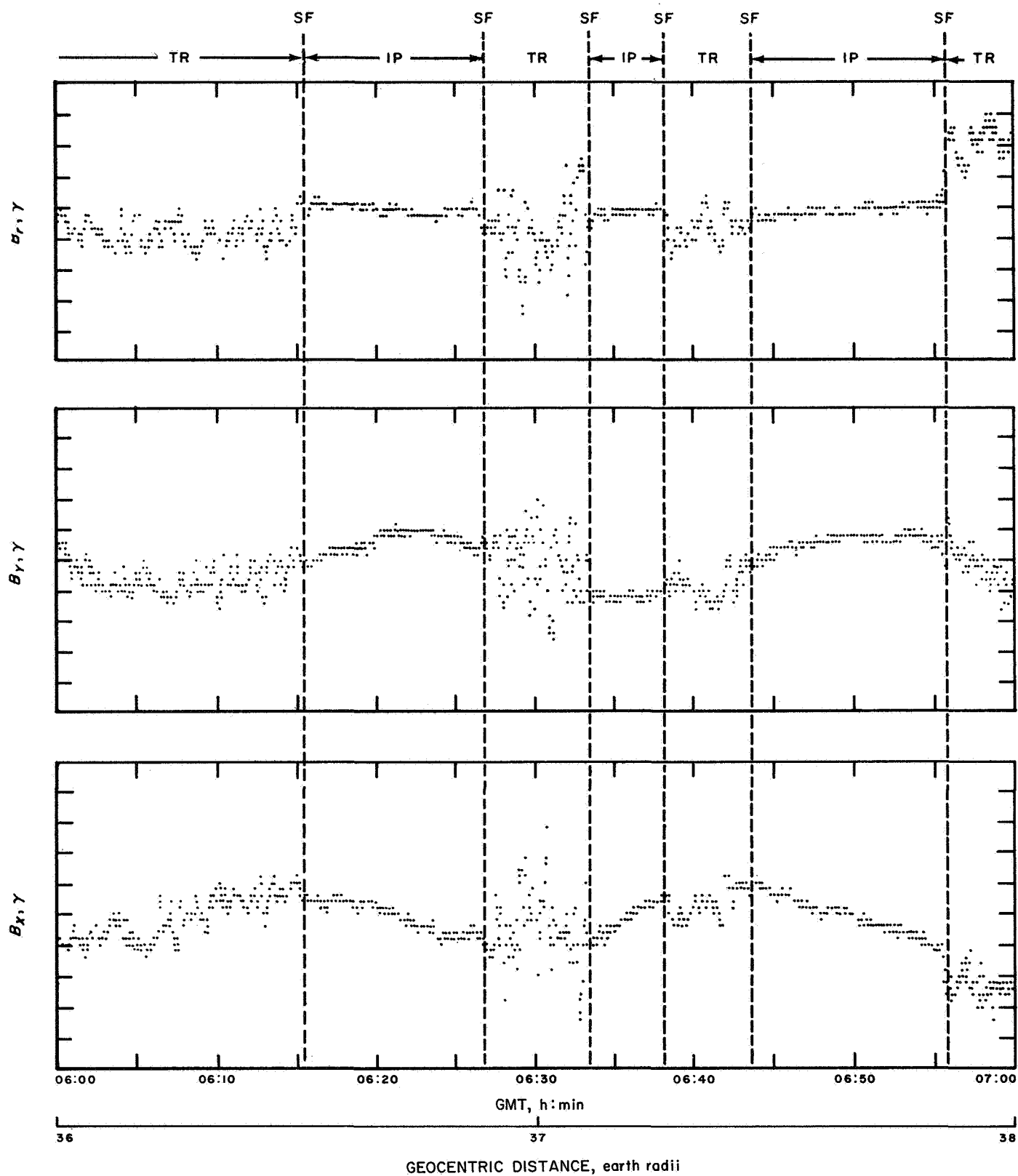


**Fig. VII-6. Mariner IV magnetometer data showing multiple passages of shock front**



forth over distances of several earth radii with typical periods of 5-20 min, at least for this time and location.

These results seem quite reasonable, as it has been suggested that hydromagnetic shocks resemble hydraulic phenomena in which irregular and fluctuating fronts with considerable structure and precursors ahead of the main shock are typical. The sharp nature of most of the observed transitions suggests that the shock front makes a large angle with the trajectory and moves a considerable distance, rather than suggesting that the trajectory lies nearly tangent to the front. Presumably, it is the unknown velocity of motion of the front, and not the known velocity of the spacecraft, that determines the apparent duration of the crossing from one region to the other. The average interval between successive observations of the shock is comparable to the time required for the solar wind to slide around the magnetosphere; thus, it is not clear whether the local variations in the position of the front are caused by fine structure in the solar wind or by some form of instability.

The outstanding feature of the magnetic data was the occurrence of irregular fields behind the shock with or without an accompanying change in average field magnitude. The same feature was used to identify the *IMP-1* shock-front locations, and was also obvious in the *OGO-1* (*Orbiting Geophysical Observatory 1*) search coil magnetometer data. The fluctuations inside were, very roughly, five times as great as those outside the front.

*b. Magnetic fluctuations in magnetosheath.* The following is a description of the data obtained in and adjacent to the magnetosheath, the transition region between the termination of the geomagnetic field (magnetopause) and the earth's bow shock. The results of the present analysis contribute to the growing store of magnetosheath information (Refs. 6-10).

*Mariner IV* observations, which were made near 04:00 local time near the ecliptic plane and at a time of very quiet geomagnetic activity, confirm the usual picture of a magnetically active region terminated on the sunward side by a sharp discontinuity in field intensity, direction, and level of activity. The present treatment reveals a high level of activity in the hydromagnetic regime (frequencies less than the proton gyrofrequency) and extends the study of the magnetic fluctuations by analyzing the behavior of both the compressional and torsional components.

*General characteristics of field in frequency range  $10^{-3}$  to 0.5 Hz.* The average value and standard deviation of the absolute magnitude  $B$  together with the average direction for five-minute intervals from 23:00 on Nov. 28 to 07:00 on Nov. 29 are shown in Figs. VII-7 and VII-8. The angles giving the average direction (Fig. VII-8) refer to a solar ecliptic coordinate system in which  $\lambda_s$  is the longitude measured in the ecliptic plane east from the solar direction, and  $\beta$  is the latitude with  $\beta = 90$  deg as the north ecliptic pole.

Although magnetic conditions on the ground were very quiet, the average field magnitude in the transition region showed marked variations. Several regions of variations also appeared in the average angle plots; although, in general, the angles did not change much. To simplify the treatment of short-period magnetic fluctuations, detailed analyses were made using data segments during which the changes in long-period average field were relatively small. Large-amplitude oscillations analyzed in this way are presented in paragraph 2-b of this section.

The 5-min standard deviations of  $B$  were relatively large, as is typical for the transition region. The value dropped abruptly near 05:00 GMT, marking the first shock transition. This transition is also indicated by an abrupt change in the field direction. The complex series of events that occurred between 05:40 and 08:00 GMT involving multiple shock transitions was discussed previously.

To define more clearly the frequency regions in which the oscillations occurred, power spectra of  $B$  were made for nine consecutive intervals of 42-min duration beginning at 23:09 GMT. The nine spectra are shown superimposed on each other in Fig. VII-9. It is seen that relatively narrow frequency intervals showing greater power density than adjacent frequencies occur at one time or another all along the frequency axis from 0.005 to 0.04 Hz. This occurrence suggests that the entire frequency range is excited, but with different frequencies at different times being more important. The region around 0.005 Hz shows activity most often and with greatest intensity during the time interval analyzed.

A single power spectrum of  $B$  covering a time interval of 7 h (2000 frames) beginning at 22:17 GMT is shown in Fig. VII-10. The rapid increase in power toward low frequencies for  $f < 10^{-3}$  Hz is probably due to the secular decrease of the field intensity during the 7-h interval.



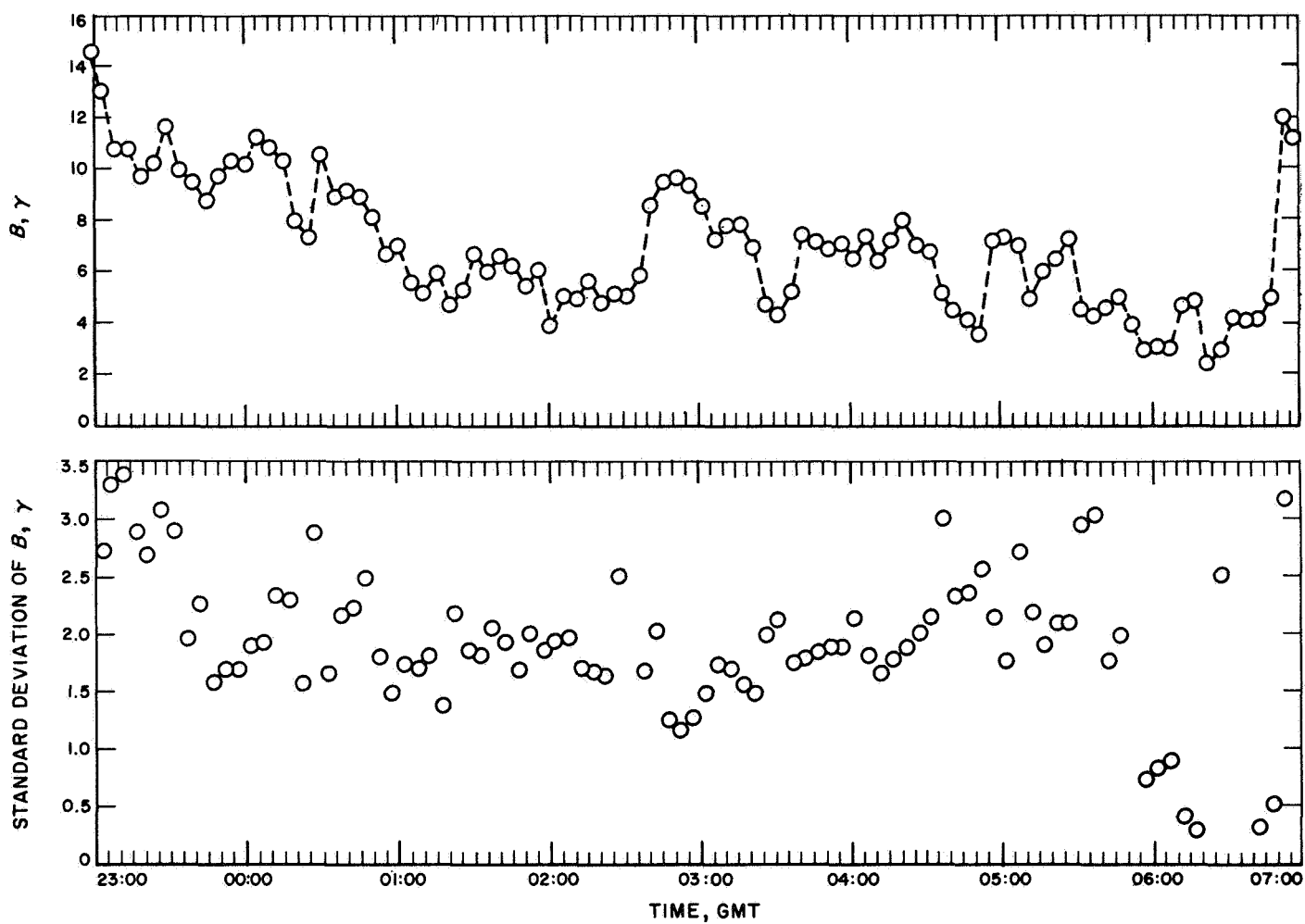
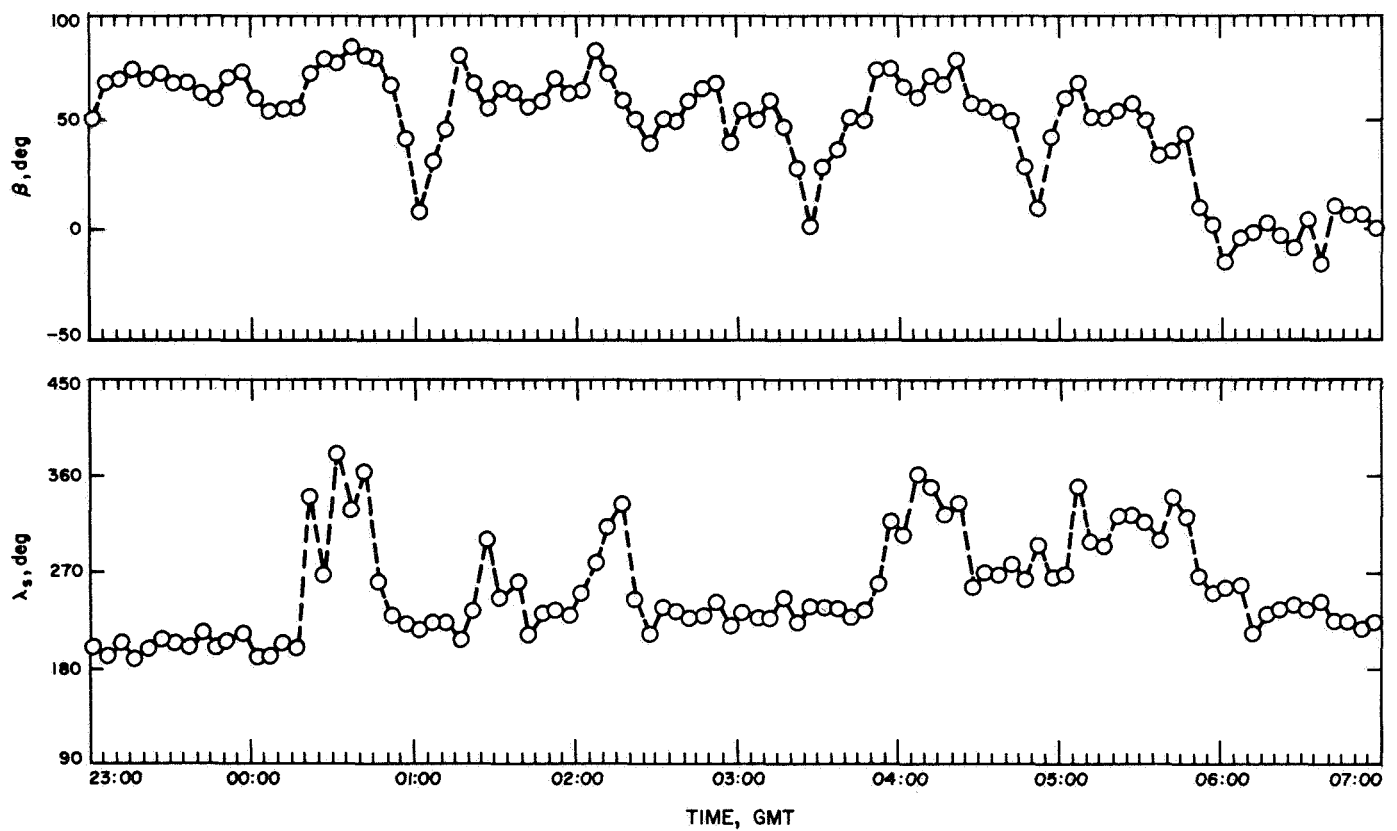


Fig. VII-7. Five-minute averages and standard deviations of absolute field magnitude in magnetosheath



**Fig. VII-8. Five-minute averages of field direction angles in solar ecliptic coordinates**

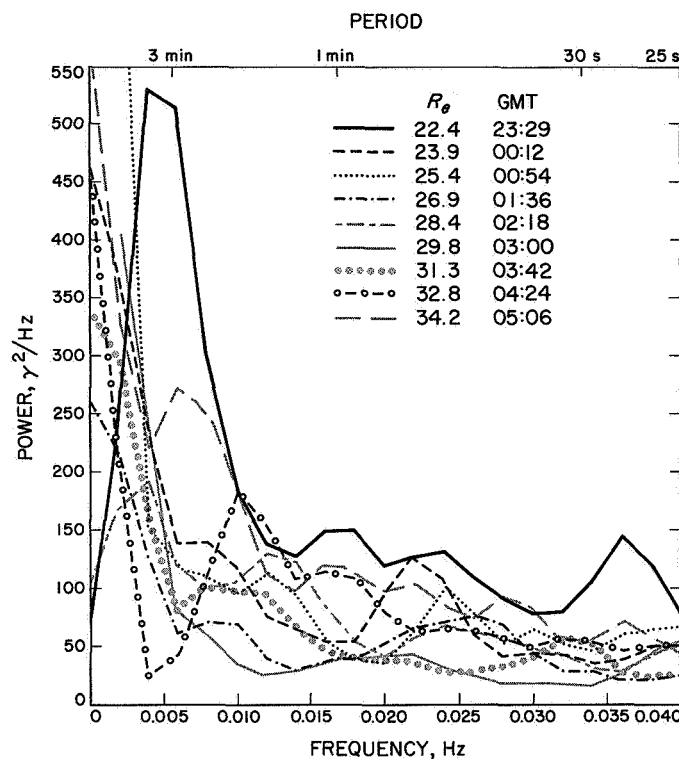


Fig. VII-9. Power spectra of B

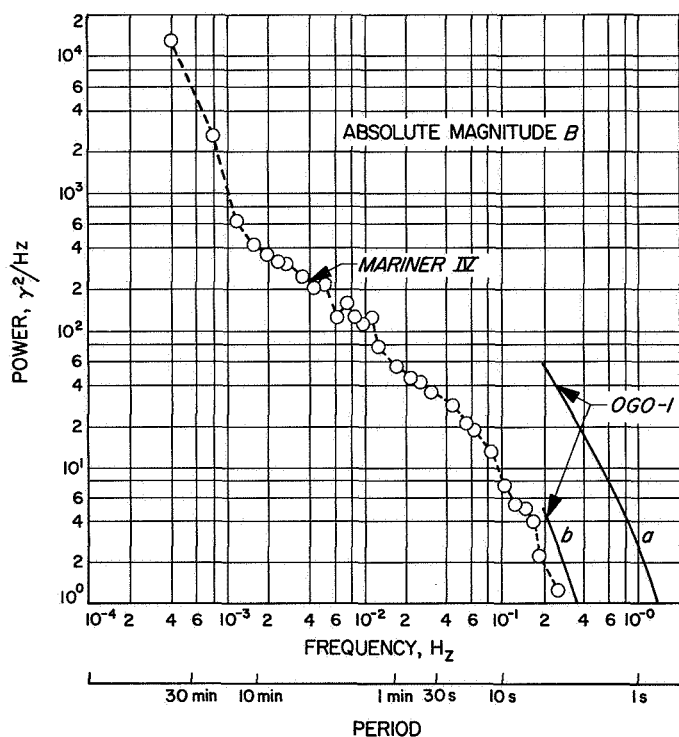


Fig. VII-10. Power spectrum of B

However, the power density from  $10^{-3}$  Hz to approximately  $5 \times 10^{-2}$  Hz is seen to decrease approximately as  $f^{-1}$  (or more accurately, as  $f^{-0.85}$ ) in a relatively smooth manner. The smooth dependence of the power density on frequency indicates that the power in the activated frequency intervals that cover this range have blended together during the 7 h to produce a time-averaged smooth dependence. That the frequency range characterized by the  $f^{-1}$  dependence is excited can nevertheless be inferred. If the  $f^{-1}$  dependence were to continue indefinitely to higher frequencies, the variance, which is the area under the curve, would approach infinity. In this sense, the slope in the excited region is less than normal.

The frequency dependence of the power density for  $f > 0.1$  Hz is approximately  $f^{-2}$ . The region separating the two regions of slope  $-1$  and slope  $-2$  is approximately  $0.05 < f < 0.1$ , which essentially coincides with the upper limit of the hydromagnetic regime. The hydromagnetic regime is bounded above by the proton gyro-frequency, which, for a  $10\text{-}\gamma$  field, is  $0.16$  Hz.

For comparison, power spectra are shown for data obtained in the transition region by OGO-1 (Ref. 10). The curves labeled *a* and *b* in Fig. VII-10 correspond to noisy and quiet regions, respectively. Curve *b*, which nearly coincides with the Mariner IV curve, was obtained at a quiet time and in a quieter region away from the bow shock.

Summarizing the previous paragraphs, Mariner IV data suggest that magnetic oscillations in the transition region are excited throughout the hydromagnetic frequency regime, possibly with the greatest excitation at any one time occurring in a reasonably narrow frequency range. At the time of the Mariner IV measurements, frequencies near  $0.005$  Hz showed the greatest activity in B.

*Decomposition of large amplitude wave train.* A large amplitude wave train observed in the interval from 23:09 to 23:40 GMT is further analyzed here to try to isolate the longitudinal and transverse parts of the oscillations and to investigate the polarization of the transverse oscillations. This interval was chosen because the longitudinal oscillations were especially pronounced and the average direction of the field was quite steady compared to other half-hour intervals. It provides the best example of a wave in the hydromagnetic regime that can be studied in detail.

The field is decomposed into a longitudinal part  $B_{\parallel}$  parallel to the direction of the average vector field  $\mathbf{B}$ , and a transverse part  $\mathbf{B}_{\perp}$  perpendicular to  $\mathbf{B}$ . Plots of  $B_{\parallel}$  and  $\mathbf{B}_{\perp}$  smoothed as before by five frame (63 s) sliding averages are given in Figs. VII-11 and VII-12.  $B_{\parallel}$  displays large-amplitude oscillations with periods around 200 s. The oscillations occasionally have an amplitude of  $4 \gamma$  that should be compared with the average value for  $B_{\parallel}$  of about  $10 \gamma$ .

In Fig. VII-12, each point gives the components of  $\mathbf{B}_{\perp}$  in an arbitrary coordinate system in a plane perpendicular to  $\mathbf{B}$ . The origin of the coordinate system is indicated by a cross, and the average field direction  $\mathbf{B}$  is out of the paper. The data for  $\mathbf{B}_{\perp}$  are shown on 11 separate plots, each corresponding approximately to a complete oscillation of the  $\mathbf{B}_{\perp}$  vector. Correlation between  $\mathbf{B}_{\perp}$  and  $B_{\parallel}$  is achieved through the measurement sequence number which is shown on all plots. Time increases by 12.6 seconds between measurement sequence numbers. The solid dots on the  $\mathbf{B}_{\perp}$  plots indicate the position of a maximum for  $B_{\parallel}$  and the open circles indicate a minimum.

Figure VII-12 reveals that the  $\mathbf{B}_{\perp}$  component of the wave is elliptically polarized, describing approximately one rotation for each oscillation of  $B_{\parallel}$ . The sense of the polarization with respect to the direction of  $\mathbf{B}$  is seen to change between the fifth and sixth, sixth and seventh, and seventh and eighth cycles. The average value of  $|\mathbf{B}_{\perp}|$  over the interval is  $1.4 \gamma$ , indicating that the transverse component of the wave is somewhat weaker than the longitudinal component.

A description of the magnetic oscillations that emerges from the data is as follows. The field vector of average magnitude  $10 \gamma$  changes in magnitude by  $2-4 \gamma$  with a period near 200 s while rotating with essentially the same period around its average direction. The angle

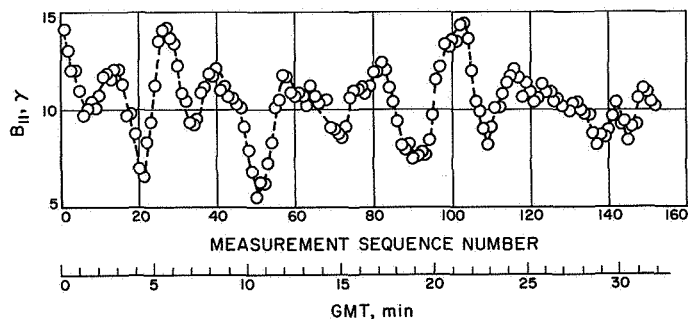


Fig. VII-11. Smoothed  $B_{\parallel}$

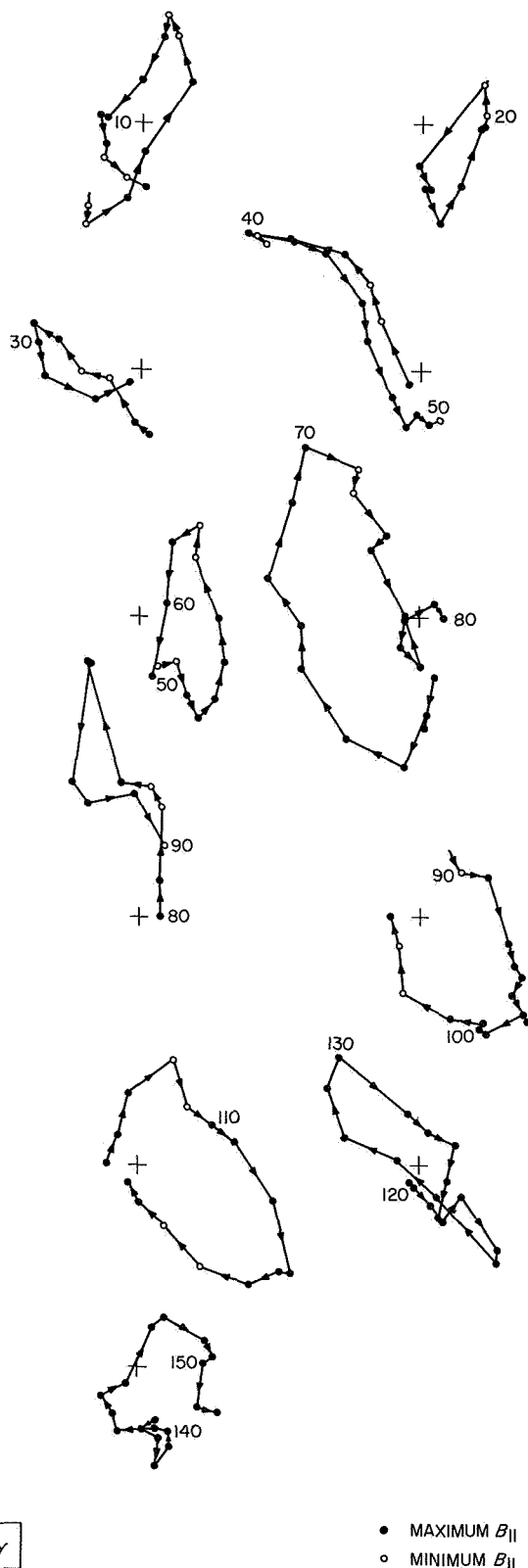


Fig. VII-12. Smoothed  $\mathbf{B}_{\perp}$

between the field vector and the average direction typically fluctuates from about 3 deg to about 12 deg during an oscillation, the fluctuation covering a moderately eccentric ellipse whose polarization remains correlated for 3 or 4 oscillations and then tends to reverse.

**Shock aligned magnetic oscillations.** Field irregularities in the magnetosheath have been investigated in some detail, using an analytical technique that has also been employed successfully to study torsional discontinuities in the interplanetary field. This technique identifies intervals when the magnetosheath field variations consisted principally of planar rotations. When the magnetic field rotates in a plane, the technique also yields the normal to that plane. The normals so derived appear to be aligned with the normal to the shock front (or, alternatively, the plane of the oscillations is parallel to the shock front). Thus, this technique appears to be use-

ful in finding the local shock normal direction observationally. Comparison with the traditional shock analysis, as applied to the same data, supports such a view and suggests that the study of planar oscillations may yield many more estimates of the direction normal to the shock than the traditional approach has yielded.

Figure VII-13 shows  $B$ , the absolute magnitude of the vector field smoothed by 63-s (five data frames) sliding averages from 05:00 to 07:22 GMT, 29 November 1964. This figure shows several transitions between fields characteristic of the magnetosheath (M) and those characteristic of interplanetary (I) space. The most interesting interval is that from 05:35 to 05:50 GMT, when several transitions occurred involving changes in field strength of about a factor of 2. The low-field-strength region, which persisted from 05:51 to 06:15 GMT, was not the undisturbed interplanetary field, but rather a

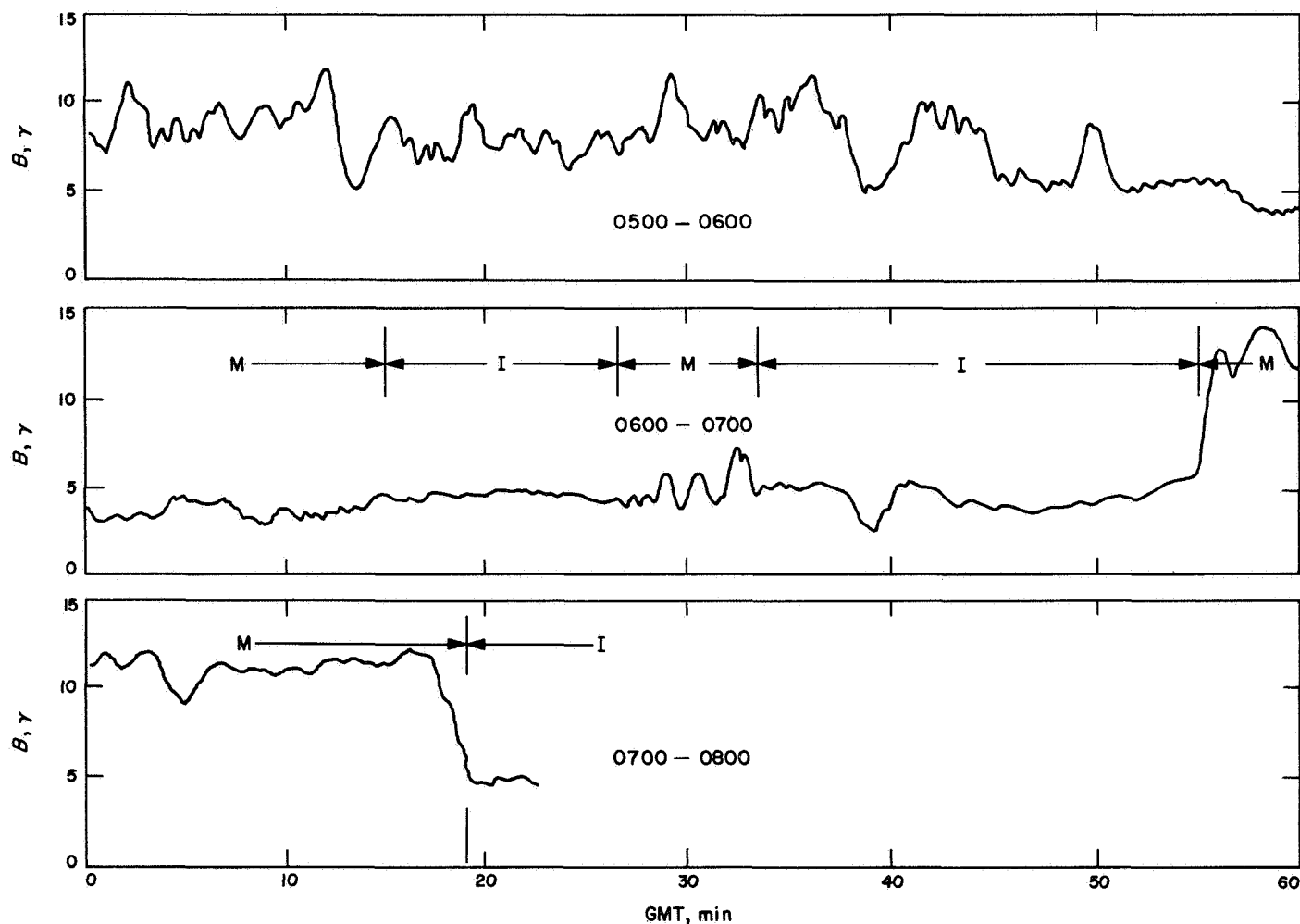


Fig. VII-13. Absolute magnitude of magnetic field

field displaying torsional oscillations with periods around 1 min in the spacecraft frame and higher frequency fluctuations. The quiet interplanetary field appeared abruptly at 06:15 GMT.

Detailed examination of the data turned up several intervals, each of a few minutes duration, when the projection of the magnetic field vector on the expected plane of the shock rotated more or less continuously in a counterclockwise direction when looking inward toward the earth, the rotation periods being of the general order of 1 min. Typically,  $B$  had its larger values during such intervals. These torsional oscillations cause the four vectors (measured within 4.8 s in each data frame) to sweep through an arc of 30–60 deg in the plane of the oscillation.

The orientation of this plane can be determined by a technique that has also been applied to discontinuities in the interplanetary field (Ref. 11); only the essentials of the method will be given here. If the four vectors  $B^i$  observed in a frame tend to lie in a plane, its normal  $n$  can be found by minimizing

$$\sum_{i=1}^4 (B^i \cdot n)^2 = s^2 \quad (1)$$

This is equivalent to determining the three orthogonal eigenvectors of the real, symmetric matrix

$$(T_{\mu\nu}) = \left( \sum_{i=1}^4 B_{\mu}^i B_{\nu}^i \right)$$

where  $\mu\nu = R, T, N$ , a spacecraft-centered, right-handed Cartesian coordinate system in which the  $R$  axis is radially away from the sun, the  $T$  axis is normal to  $R$  and parallel to the solar equatorial plane with  $+T$  in the direction in which the planets move, and  $+N$  is northward.

These eigenvectors are denoted by  $s_z^2 \leq s_x^2 \leq s_y^2$ ; thus, introducing a Cartesian coordinate system ( $X, Y, Z$ ) in which  $n$ , as defined for Eq. (1), is along the  $Z$ -axis, the  $XY$ -plane is the plane of the variation, and  $s_z$  is the root-mean-square (rms) deviation from this plane. If, as in Fig. VII-14, the four vectors describe approximately a plane arc, the  $Y$ -axis nearly bisects the arc, and the rms deviation in the plane  $s_x$  measures the extent of the rotation. The ratio  $s_z/s_x$  can be used to identify planar variations. The variation is planar by definition if in any

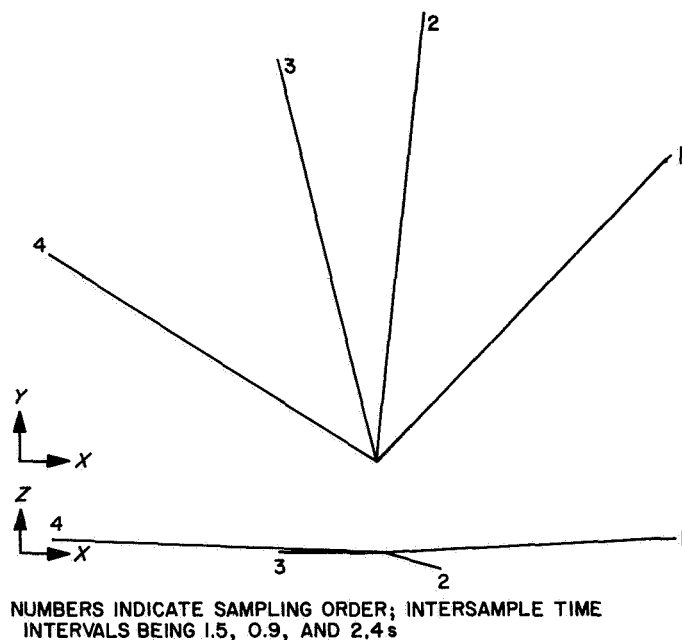


Fig. VII-14. A plane, torsional oscillation projected onto  $XY$  and  $XZ$  planes

data frame  $s_z/s_x \leq 1/4$ ; i.e., the average variation in the plane is four or more times larger than the average deviation *out of the plane*. The planar variation shown in Fig. VII-14, which occurred at 05:36 GMT, had  $s_z/s_x = 0.055$ .

An analysis of the directions of the normals to significant, planar, intraframe variations in the interval from 05:00 to 06:15 GMT revealed that, from 05:35 to 05:50 GMT, there was a moderately strong alignment of these normals with the expected shock normal. Before and after this 15-min interval, there was no such noticeable alignment. The sudden onset of alignment was probably due to a motion of the compressional transition that brought it close to the spacecraft at 05:35 GMT, where it then remained for some time. The inward-pointing shock normal is expected, from the high-speed gas dynamics model of Ref. 12 using a 5-deg aberration of the solar wind, to lie approximately in the  $RT$ -plane and at an angle of 65 deg from the  $+R$ -axis.

Figure VII-15 is a polar representation showing the orientation of the 31 planar frames (out of a total of 72) obtained during the 15-min interval previously mentioned, as well as planar frames obtained during later intervals. The radial coordinate of a point in the figure is the angle from the expected shock normal to the plane of the variation, and the azimuthal angle in the figure is the angle between the plane of these two normals and

○ 05:35–05:50 GMT  
 + 06:27–06:33 GMT  
 △ 07:16–07:19 GMT

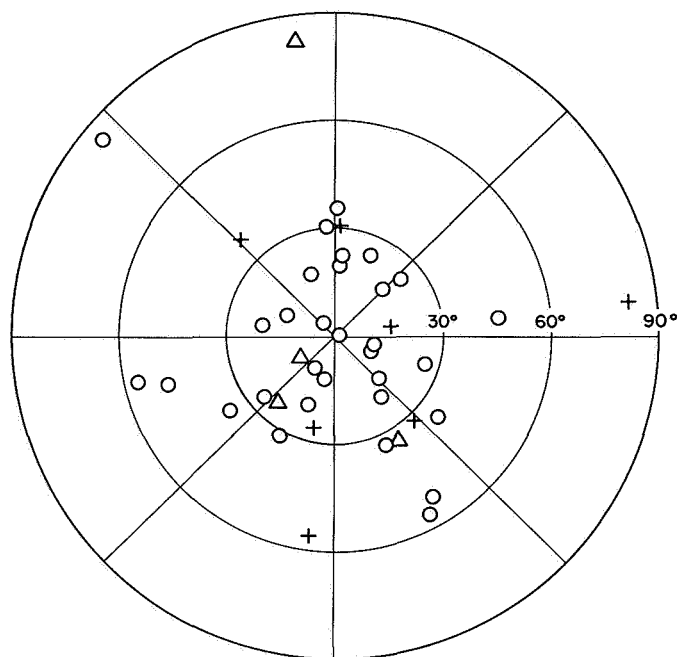


**Fig. VII-15. Directional distributions of normals to planar variations**

the *RT*-plane, essentially the plane of the ecliptic. The concentration of points toward the center is clearly noticeable. A quantitative measure of the degree of alignment of the 31 events is the ratio of the number of normals observed lying in concentric rings 10-deg wide to the number expected for an isotropic distribution. Over six times as many normals lie within 20 deg of the expected direction than would be expected for an isotropic distribution.

Finally, by projecting the oscillation onto the shock plane, it was observed that, although they were quite elliptical rather than circular, the polarization of the torsional oscillations in the high field intensity regions was always left-handed with respect to the outward-pointing shock normal. The average value of the field component along the outward shock normal during the oscillation was  $+2.4 \gamma$ . Hence, the oscillations were also left-hand polarized with respect to the normal field component.

**2. Interplanetary magnetic field measurements.** Several rather complete observations of the interplanetary magnetic field existed prior to the *Mariner IV* mission. There were good reasons, however, for extending these

observations by continuously monitoring the interplanetary field during the *Mariner IV* flight to Mars.

First, it is generally supposed that the character of the interplanetary medium, including the magnetic field, will change with the 11-yr solar cycle. The *Mariner* measurements happened to be made during the especially interesting period corresponding to the solar cycle minimum or the quiet sun. Thus, a unique opportunity existed to make measurements during an important phase of the solar cycle that, in combination with previous and subsequent magnetometer experiments on other spacecraft, should reveal the way in which the interplanetary medium is affected by changing solar conditions.

Second, *Mariner* shares the advantages that all space probes have as compared to earth satellites with regard to interplanetary studies. Even the highly eccentric satellites, such as *IMP-1* and *OGO-1*, only spend a fraction of their observing period in interplanetary space, namely the time they are outside the earth's bow shock. The rest of the time, they are inside the magnetosheath and the magnetosphere. Of greater consequence is the precession of the satellite orbit around the earth-sun direction, which typically prevents the satellite from penetrating into interplanetary space at all for about half a year at a time. Since the short term variability of the interplanetary field is one of its most important characteristics, there is a definite advantage in continuously monitoring the field; this monitoring is done best on a space probe.

Finally, *Mariner IV* was the first space probe to go substantial distances farther from the sun than the orbit of earth. In addition to studying the interplanetary field under varying temporal conditions, the present state of our knowledge made it advisable to extend the observations to regions of space far from the vicinity of the earth.

The preliminary analysis of the *Mariner IV* magnetometer data upon which this present report is based has concentrated on several important areas of investigation. The average characteristics of the field have been asayed, partly to make comparisons with earlier measurements during the declining portion of the solar cycle.

In this regard, both the average magnitude and direction of the field are important. Since the single most striking feature of the interplanetary magnetic field is its variability, it is not surprising that this general area of study has received a great deal of attention.

One of the fundamental problems associated with the measurement of highly variable phenomena involves distinguishing spatial from temporal effects. This differentiation has been done successfully in several ways:

- (1) The major element of variability in the field turns out to have the same period as the 27-day solar rotation, thereby making certain time variations readily recognizable. The most obvious changes in the field exhibiting such a solar periodicity are associated with the *polarity* of the field; i.e., whether the field lines tend to point away from, or toward, the sun.
- (2) Since changes in the interplanetary medium are responsible for various geomagnetic phenomena including magnetic storms, it is natural to expect and seek correlations between the interplanetary measurements and changing geomagnetic activity. Such correlations can also be used to identify temporal and spatial variations.
- (3) Where measurements exist that have been made simultaneously near earth on satellites, such as *OGO-I*, they can be used to separate spatial from time variations.

To the extent that one can resolve the time-varying component of the *Mariner* data, a dependence of the average field properties on spatial parameters can be investigated, the most obvious such spatial parameter being the distance from the sun.

The subsequent discussion of the scientific analysis of *Mariner* data includes all of the previous topics. Although the topics were summarized from the point of view of using them to distinguish spatial from temporal effects, they are all actually of considerable scientific interest in their own right.

Thus, the study of field polarity is important, because it is one of the field properties that is not readily predictable from existing theories. Furthermore, the subject is intimately related to the study of solar magnetic fields and to the relation between solar fields in the photosphere and those in the corona, where the solar wind originates.

In the same way, the correlation between interplanetary field properties and geomagnetic activity is important because of what can be learned about the origin of magnetic storms and aurorae, or the earth's radiation zones. Simultaneous *Mariner*-earth satellite measure-

ments can help to establish the typical scale of the irregularities in the interplanetary field, as well as their velocities of propagation through space. It is actually in terms of their intrinsic importance that the various topics will be discussed except insofar as they bear on the question of radial gradients; i.e., the dependence of the field properties on heliocentric distance.

*a. Average characteristics of interplanetary field near 1 AU.* The components of the interplanetary magnetic field will be described in terms of a spherical, polar coordinate system for which the sun's axis of rotation is the polar axis. Thus, the components of the field **B** at the point ( $r, \theta, \phi$ ) are  $B_r, B_\theta$ , and  $B_\phi$ , with  $B_r$  radially outward from the sun,  $B_\phi$  parallel to the solar equatorial plane and positive in the direction of planetary motion, and  $B_\theta$  southward, completing the usual right-hand system.

The fields of the spacecraft were measured before the flight. They were also checked during the flight, using the following procedure. During the first day of the flight, the spacecraft was allowed to roll about an axis coincident with the sun-spacecraft line. The two components of the spacecraft field transverse to the roll axis were checked using the data taken during this "roll" period. The third component, held parallel to the sun-spacecraft line during the entire flight, was checked by assuming trial values and obtaining, for each value, a distribution over a 27-day period for the spiral angle  $\alpha_B = \tan^{-1} (-B_\phi/B_r)$ . The value selected was that which provided a distribution that was most symmetrical about  $\alpha_B \approx 50$  deg and  $\alpha_B \approx 50$  deg + 180 deg. This requirement fixed the value of the roll-axis component within  $\pm (1/3) \gamma$ . The selected value of 50 deg is consistent with the values of the solar wind velocity measured with the *Mariner IV* plasma probe (see subsection 2-b).

Figure VII-16 contains the amplitude distributions  $B_r, B_\theta, B_\phi$ , and  $B$  obtained during solar rotation period (SRP) 1799, 7 January through 2 February 1965. Also shown are distributions of the field strength  $B$  and of the magnitude of the component transverse to the radial direction  $B_p = (B_\theta^2 + B_\phi^2)^{1/2}$ . The distribution of  $B_r$  suggests a smaller peak near  $B_r = -2 \gamma$  as well as the more obvious peak near  $B_r = +2 \gamma$ . During SRP 1799, the heliocentric range of *Mariner IV* increased from  $157 \times 10^6$  to  $169 \times 10^6$  km.

The mean value of  $B$  during this interval is  $4.5 \gamma$ . This preliminary result also shows a tendency for  $B_\theta$  to have



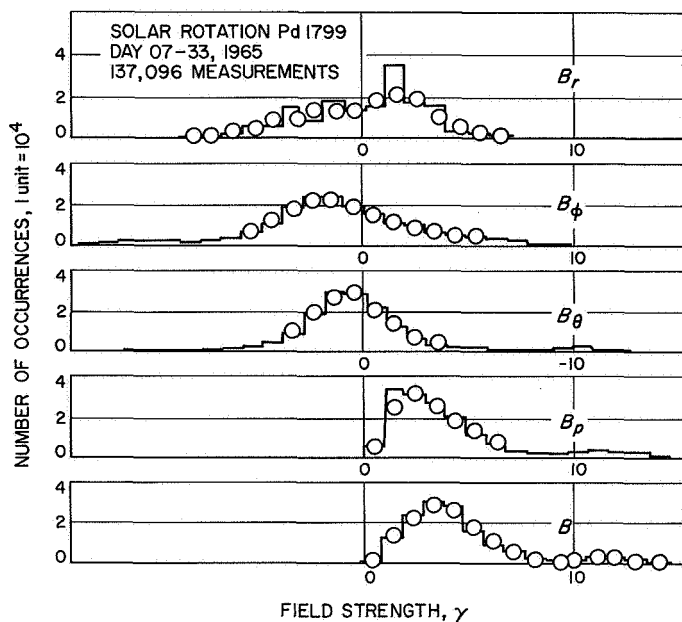


**Fig. VII-16. Mariner IV distributions of component magnitudes**

a non-zero mean. This corresponds to a slight, average, southward direction for the interplanetary field. The possible existence of such a component has excited some controversy over the last few years; there are excellent theoretical reasons for expecting this component to be zero on the average. The violation of this condition, as shown in Fig. VII-16, is probably best interpreted as an indication of the accuracy with which the preliminary values of the spacecraft field were estimated.

The distributions indicate that variations in the magnitudes of the various components of the field are greater than the variations in  $B$ , suggesting that the field variations are for the most part produced by changes in the orientation of a relatively constant field. However, the greatest contribution to the variations of  $B_r$  and  $B_\phi$  arises from the polarity reversals of the roughly spiral field.

*b. Long-period variations in polarity of interplanetary field.* Between August and November 1962, during the flight of *Mariner II*, the interplanetary magnetic field exhibited a well-defined 27-day periodicity. This periodicity was interpreted as evidence for a connection between the field at 1 AU and the large-scale patterns in the solar magnetic field that are observed to persist over several periods of solar rotation (Refs. 13-16). Between November 1963 and February 1964, a 27-day periodicity in the interplanetary field was again observed, this time

with the *IMP-1* magnetometer, and a correlation was established between the field patterns indicated by the *IMP-1* data and patterns in the photospheric fields (Ref. 17). The specific form of the variations recorded during the flight of *IMP-1* showed that the field pattern at 1 AU was different from the one previously observed on *Mariner II*. During the flight of *Mariner IV* (a year later), the variations in the recorded field over 27-day periods showed much less of the well-defined periodicity that had characterized the earlier observations.

The angle from the positive  $r$  direction to the projection of  $\mathbf{B}$  on the  $r\phi$ -plane is denoted by

$$\alpha_B = \tan^{-1} (-B_\phi/B_r)$$

According to the spiral-field model of Ref. 18, this angle, disregarding the sense of the field lines, is

$$\alpha_p \simeq \tan^{-1} [(\Omega_S r \sin \theta)/V_p]$$

where  $V_p$  is the radial velocity of the solar wind and  $\Omega_S$  is the angular velocity of the sun. Then  $\alpha_B = \alpha_p$  if the spiral-field lines of force lead away from the sun (+ polarity), and  $\alpha_B = \alpha_p + 180$  deg if the field lines lead toward the sun (- polarity). The component  $B_w$ , in the direction of the ideal spiral field, is given by

$$B_w = B_r \cos \alpha_p - B_\phi \sin \alpha_p$$

so that  $B_w$  is positive if the line of force in the spiral-field direction leads away from the sun.

The values of  $B_w$  computed from the *Mariner IV* data during the first two and one-half solar rotations are shown in Fig. VII-17. For each 3-h period, the amplitude distribution of  $B_w$  was obtained. These distributions were quantized into ranges 1.0- $\gamma$  wide. Each value plotted in Fig. VII-17 indicates the most frequently occurring 1- $\gamma$  range of  $B_w$  determined from the amplitude distribution for the indicated 3-h period.

In order to examine the records for phenomena that recurred at *Mariner* and at the earth due to the sun's rotation, it was necessary to estimate the effect of the changing heliocentric range and longitude of *Mariner IV* upon the expected times of recurrences. If a constant, radial streaming velocity is assumed for the solar wind, then  $\Delta t$ , the time interval from the arrival at the earth to

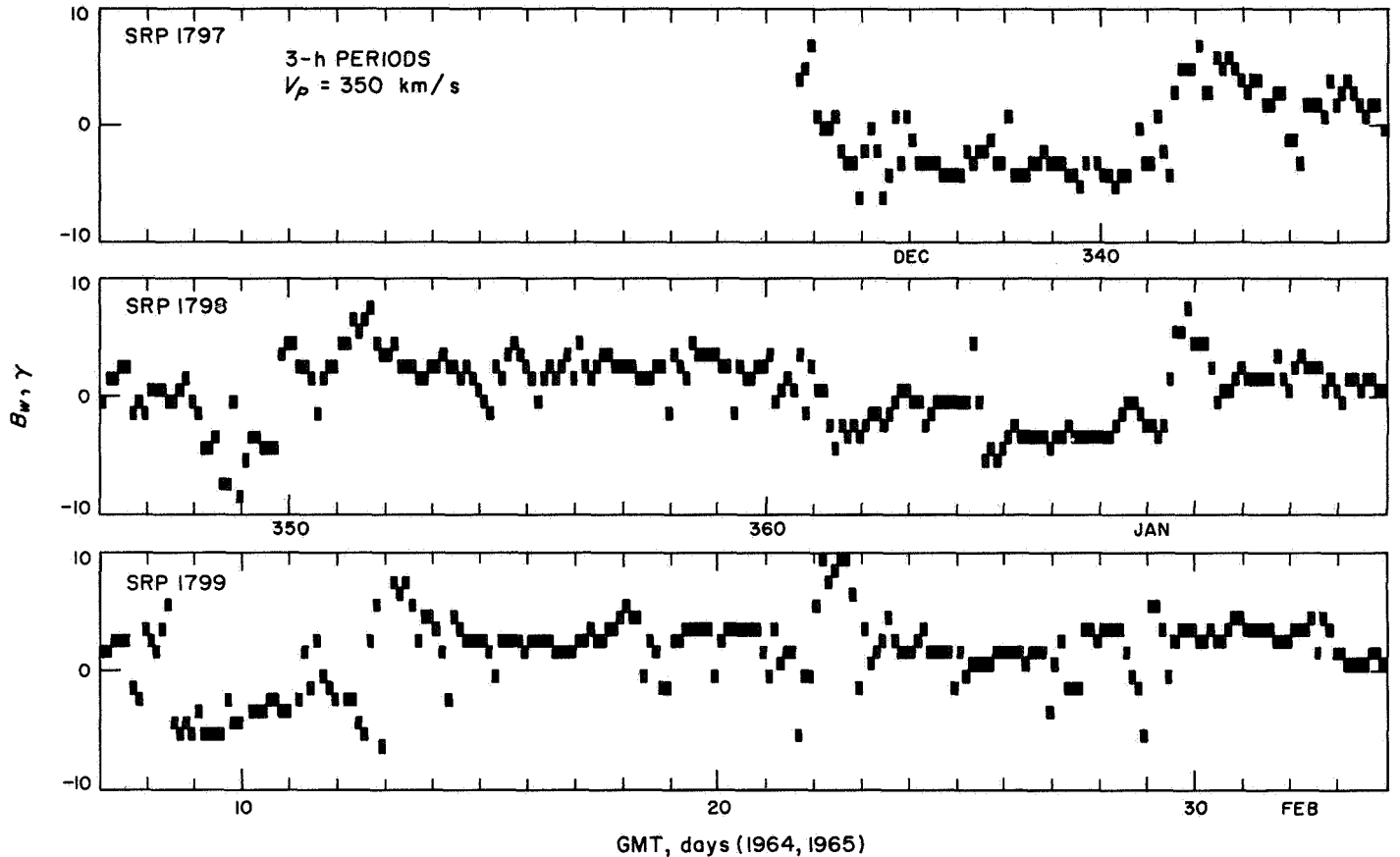


Fig. VII-17. Spiral field component, preferred values

the arrival at *Mariner IV* of the plasma streaming from a particular solar meridian, is

$$\Delta t = (\Omega_s / \Omega'_s) [(r_m - r_e) / V_p] + (\phi_m - \phi_e) / \Omega'_s$$

where  $\Omega'_s$  is the synodic angular velocity of the sun, or

$$\Delta t = [(r_m - r_e) / V_p] + [(\phi_m - \phi_e) / \Omega_s] \quad (2)$$

where the subscripts  $m$  and  $e$  refer to *Mariner IV* and earth, respectively.

In Fig. VII-18, the periods of constant polarity are indicated for more than 10 solar rotation periods. In this case, the times of polarity changes recorded at *Mariner IV* have been adjusted using Eq. (2) with  $V_p \doteq 350$  km/s. Thus, the times shown for polarity changes in Fig. VII-18 are estimates of the times at which the changes would have occurred in the near-earth region of interplanetary space.

The properties of the polarity patterns observed with the *Mariner IV* magnetometer may be summarized as follows. In late 1964, during the latter half of SRP 1797 and SRP 1798, the pattern was similar to the four-sector pattern observed with *IMP-1* during the period 26 November 1963 through 7 February 1964 (Ref. 19). This four-sector pattern had evidently evolved from the two-sector pattern observed with *Mariner II* during the period 30 August through 15 November 1962.

However, the *Mariner IV* data showed that a considerable additional evolution of the pattern occurred throughout the first part of 1965. During the first four periods of solar rotation in 1965, SRP 1799–1803, the pattern changed considerably from the four-sector pattern observed at the end of 1964. In fact, early in 1965, considerable evolution was observed to occur from one rotation of the sun to the next. Often, for periods of days, the polarity was so variable that neither polarity could be assigned. (In general, the polarity had to remain roughly the same for at least one day before a definite algebraic sign was assigned.)

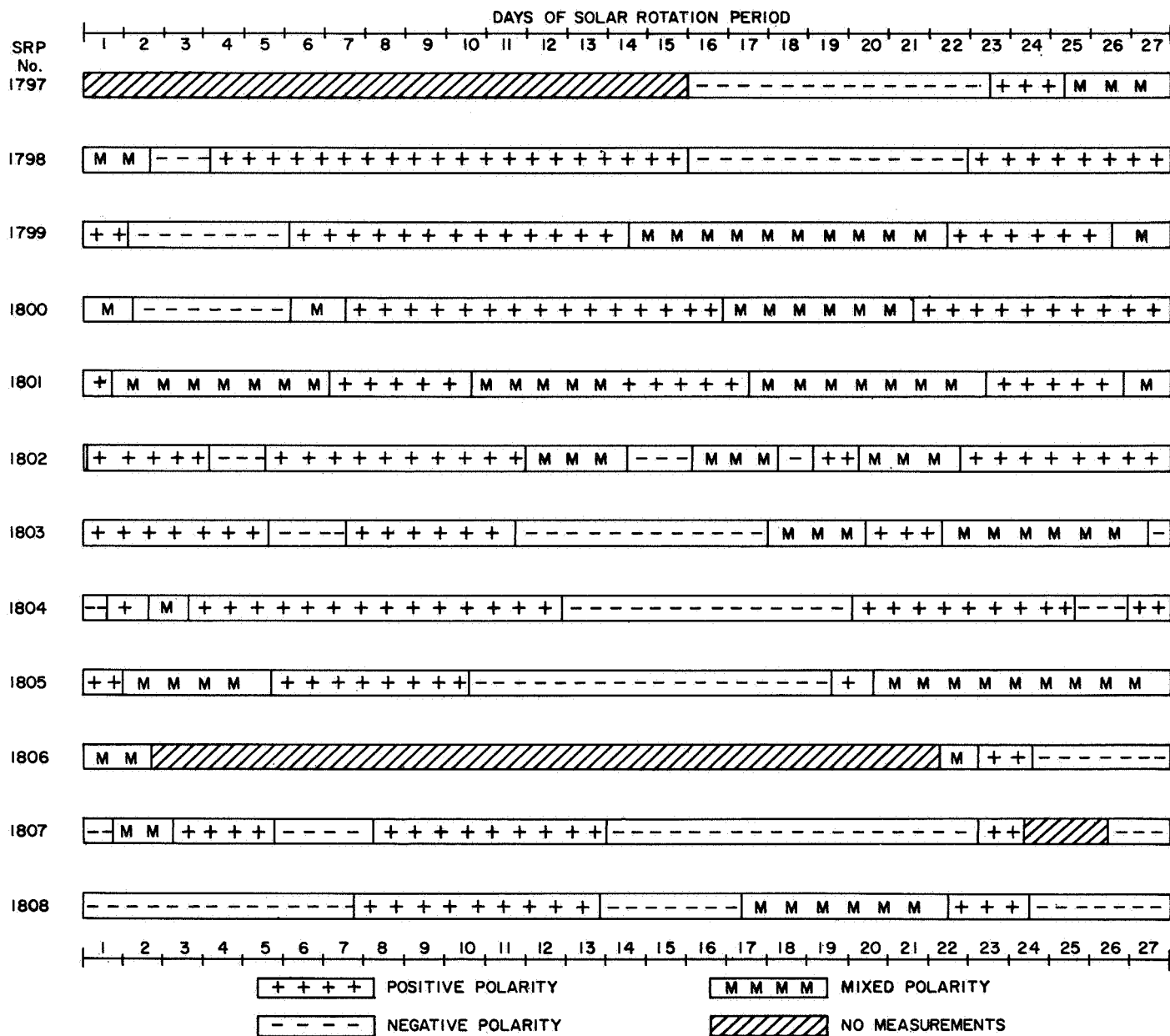


Fig. VII-18. Polarity distribution of interplanetary field during solar rotations 1797-1808 as derived from Fig. VII-17

A new, relatively well-defined pattern appeared during SRP 1804. However, the pattern exhibited three rather narrow sectors, as well as three sectors that were six days or more in width. The pattern of SRP 1805 was again less well defined, as were those of SRP 1799-1803. Data were taken during less than one third of SRP 1806. The pattern observed during SRP 1807 was again relatively well defined, and again of six sectors, but still different from that recorded during SRP 1804. The pattern of SRP 1808 was again evidently different from that

of SRP 1807, although it was also somewhat less well defined. Thus, it is apparent that polarity patterns varied considerably during these ten periods of solar rotation.

It is most reasonable to assume that the variations observed in the polarity patterns were due to similar variations in the polarity of the field leaving the sun, presumably from regions near the solar equator, rather than to changes in the position of the point of observations.

It may be recalled that the polarity pattern during the flight of *Mariner II* was produced by two well-defined sectors that remained stable for the three periods of solar rotation covered by the observations. During the flight of *IMP-1*, the pattern was produced by four sectors, which were stable for the duration of the three periods of solar rotation that could be covered. The results from *Mariner IV*, indicating that there were usually four or more sectors of generally uncertain stability, were consistent with a model for the dynamics of the solar magnetic field in which the patterns of polarity distribution near the equator became more finely divided and less stable during the declining part of the solar cycle.

A comparison with the plasma velocity  $V_p$  obtained by the *Mariner II* plasma probe (see Figs. 1a and 4 of Ref. 20) shows that each of the four field reversals occurred at the time of a local minimum in  $V_p$ . The same correlation was also observed during the flight of *IMP-1* (Ref. 21). Further, each *Mariner II* reversal was followed within 2.5 days by a local maximum in  $V_p$ . For three of the four events, the interval between the reversal and the maximum in  $V_p$  was about 1.5 days.

The relationship between the occurrence of reversals and the occurrences of minima and maxima in  $V_p$  indicated that each of the higher velocity streams originated in regions that contain fields of a single magnetic polarity. Thus, if adjacent streams happen to have opposite polarities, a field reversal will occur at the boundary between the two streams. During the flight of *Mariner II*, each of the polarity reversals occurred just before the plasma velocity began to increase. However, it seems likely that such a reversal may occur between any two streams regardless of their relative velocity. The *Mariner II* data also showed that adjacent plasma streams often contained fields of the same polarity. Thus, while there were at least five fairly well-established high-velocity streams observed during each solar rotation period, there were only two polarity reversals during each period.

c. *Relation between disturbances in interplanetary magnetic field and geomagnetic variability.* The variability of the earth's magnetic field has been studied with great interest for hundreds of years. Transient magnetic variations having periods less than one day have long been known to originate exterior to the earth. Such variations have been correlated with other terrestrial phenomena, such as aurorae, and with solar activity. It has been established beyond reasonable doubt that the

primary source of magnetic disturbance is solar activity communicated to the earth by causing changes in the interplanetary medium.

It is known that the electrical conductivity of the earth's magnetosphere prevents the interplanetary magnetic fields from penetrating directly to the earth's surface, but the precise mechanisms that couple solar wind energy into the geomagnetic field to cause magnetic storms or lesser variations have proven to be elusive. It is important, therefore, to seek possible clues in the form of a relation between geomagnetic activity and the properties of the interplanetary field.

The unique trajectory of *Mariner IV* kept it behind, but very near, the earth for several months and provided a long-term monitor of the magnetic character of the plasma streaming by and confining the geomagnetic field. Figure VII-19 illustrates this trajectory in a geocentric coordinate system. As indicated, the spacecraft first led the earth by as much as  $844 r_E$  on December 31

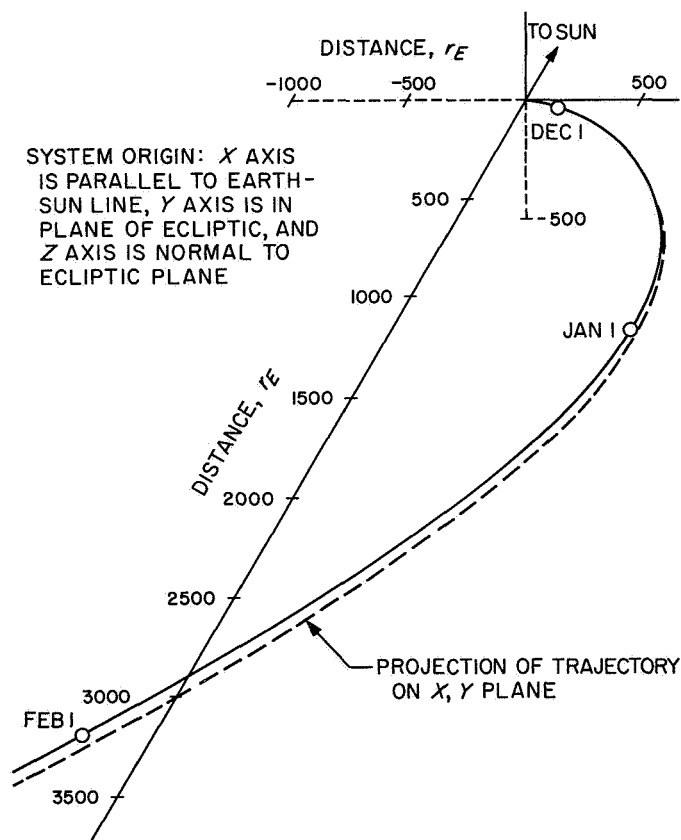


Fig. VII-19. Trajectory of *Mariner IV* in geocentric coordinate system

and then drifted backward, passing behind the earth on January 28 at  $3015 r_E$  while  $50.6 r_E$  above the sun-earth axis. During this time, the earth and *Mariner* were enclosed in a small solid angle from the sun and were, therefore, exposed to nearly the same solar wind.

Large scale disturbances in the interplanetary field at *Mariner* have been compared to magnetic disturbances seen at earth as indicated by the planetary magnetic index  $K_p$ . Several investigators, including P. J. Coleman, et al. (Ref. 22) and C. P. Sonett, et al. (Ref. 23), have already presented evidence showing that increased interplanetary magnetic fields occur in conjunction with specific geomagnetic events. The following results corroborate and extend the earlier work.

The relation between the daily mean values of the interplanetary field  $B$  at the probe and  $\Sigma K_p$ , the daily total of  $K_p$ , for the early months of the *Mariner IV* flight are shown in Fig. VII-20. The figure also displays the expected time lag between the arrival of a disturbance at the earth and its arrival at the probe. Two estimates are shown. Quantity  $\tau_R$  is obtained from the known distance to the probe and the velocity of the plasma computed from the empirical relation  $V_p$  (km/s)  $\cong (8.44 \Sigma K_p + 330)$  as given in Ref. 20. Quantity  $\tau$  is the lag expected when the effect of the angular difference between the earth, sun, and *Mariner* is added to  $\tau_R$ .

Inspection of Fig. VII-20 shows that, during the first two months of the flight, there is a simultaneous

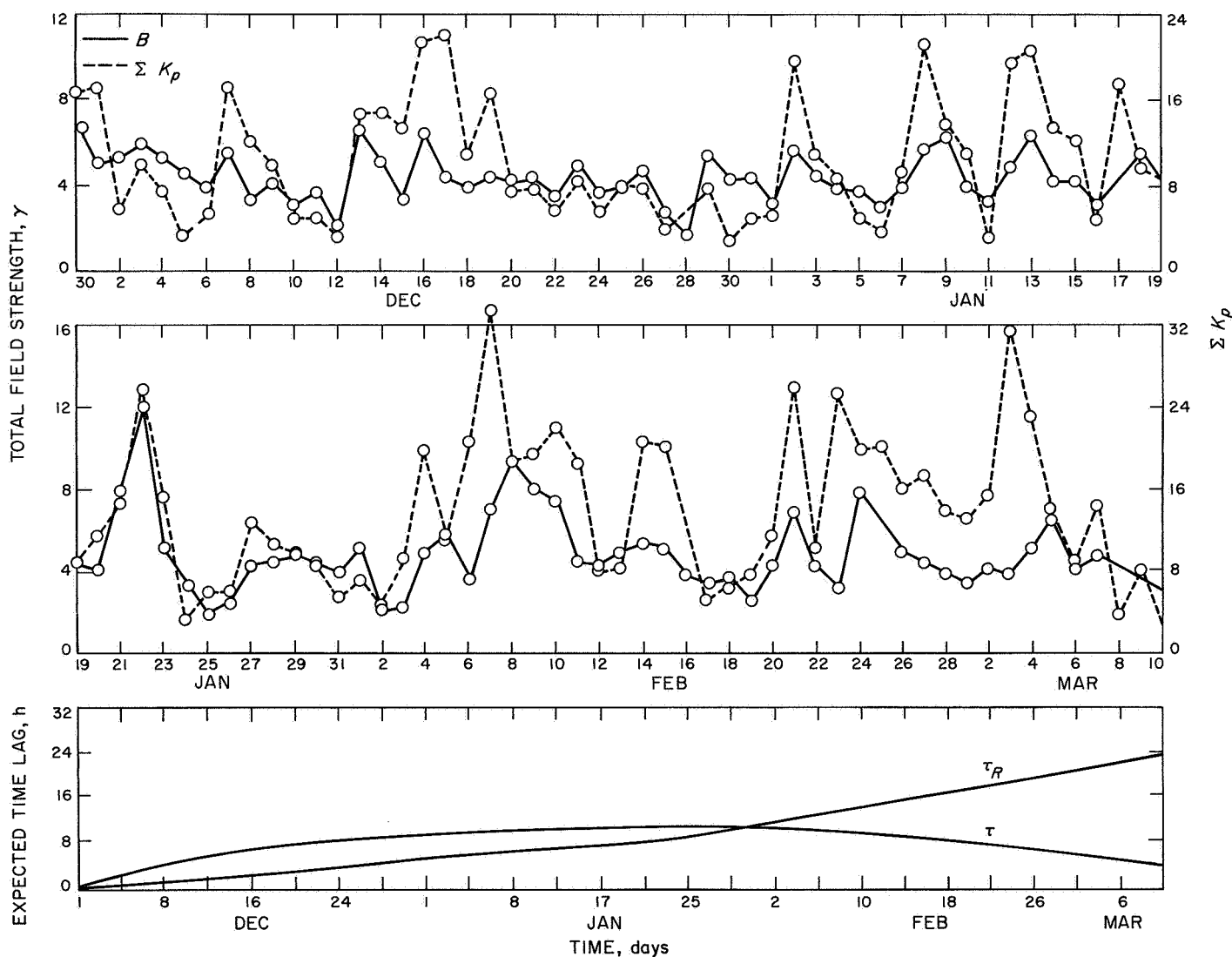


Fig. VII-20. Distribution of  $K_p$  for period from November 29, 1964 to March 12, 1965

peak in  $\Sigma K_p$  for every peak in the daily interplanetary field strength. The correlation is somewhat less obvious during the last month of the period, but this is not surprising when consideration is given to the expected lag time and the assumptions made in its formulation. When the effect of the time lag is included, the correlation coefficient for the entire period is 0.61. This correlation seems remarkably high for being obtained over such a long and geomagnetically quiet period. On the other hand, even though the total field is closely related to geomagnetic variability on the daily scale, the field com-

ponents are not. Quantities  $B_T$ ,  $B_N$ , and  $B_E$  have coefficients of  $-0.19$ ,  $-0.32$ , and  $0.15$ , respectively. This somewhat surprising result suggests that averaging the field components over one-day intervals may mask their relation to geomagnetic activity.

Although there is a significant correlation between daylong averages of total field strength and  $\Sigma K_p$ , as indicated in Fig. VII-20, a much higher correlation exists between geomagnetic activity and the fluctuating component of the interplanetary field. Figure VII-21 displays

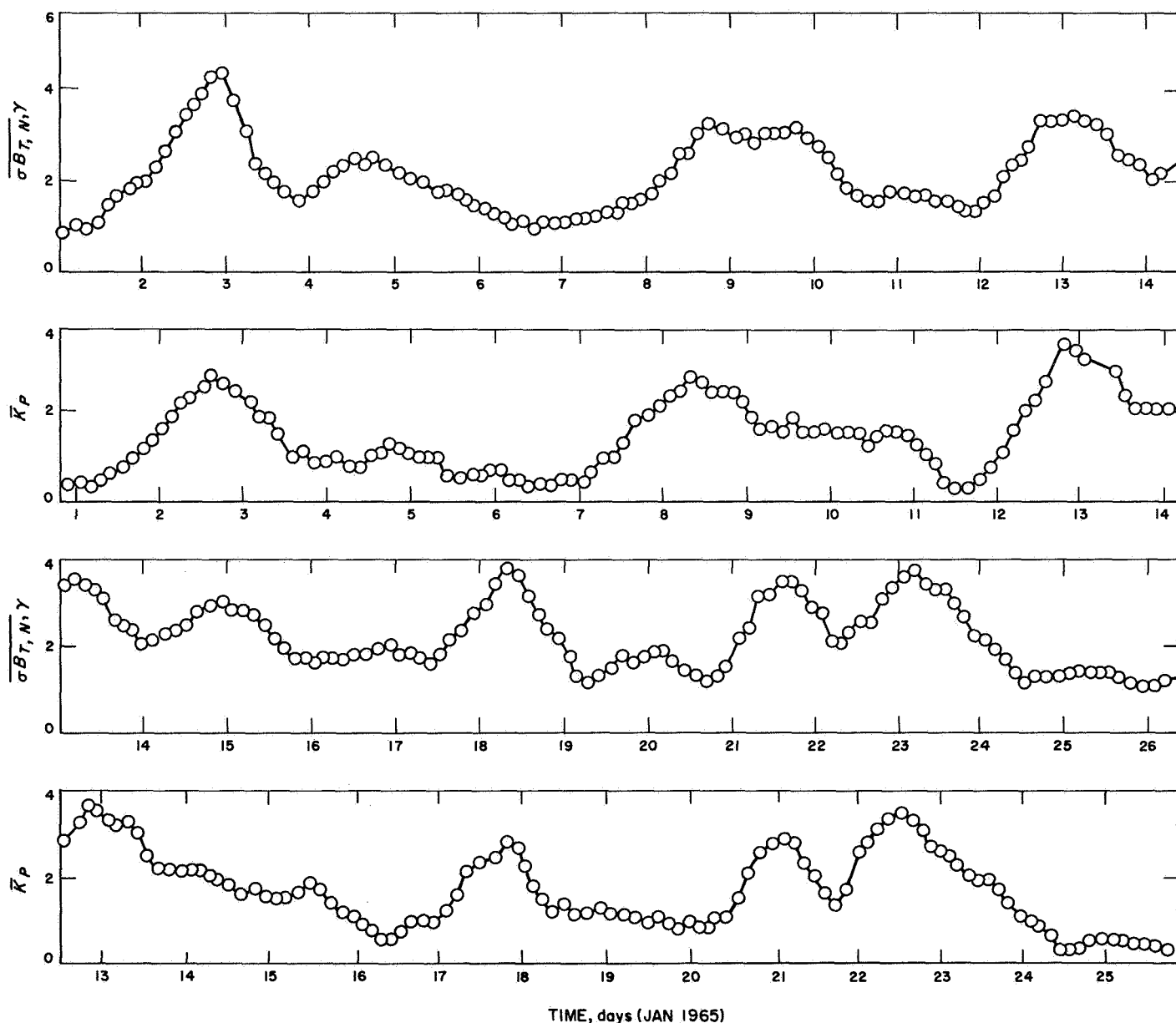


Fig. VII-21. Plots of  $\sigma B_{T, N, Y}$  a function of transverse oscillation in interplanetary field and  $K_p$

the quantity  $\overline{\sigma B_{T,N}}$  computed for 3-h blocks of 1-min averaged data and displays the geomagnetic parameter  $\overline{K_p}$ . The quantity  $\overline{\sigma B_{T,N}} = [(\sigma B_T)^2 + (\sigma B_N)^2]^{1/2}$  where  $\sigma B_T$  and  $\sigma B_N$  are the variances of the components of the interplanetary field in the plane normal to the sun probe line. Both  $\overline{\sigma B_{T,N}}$  and  $\overline{K_p}$  have been smoothed using a 21-h running mean. The  $\overline{K_p}$  plot has been offset so that the first day of each segment is corrected for the expected lag.

The relationship between the value of  $\overline{\sigma B_{T,N}}$  and  $\overline{K_p}$  is again illustrated in the scatter diagram of Fig. VII-22. Assuming a linear relationship, a least squares fit to the data yields a line which has the equation

$$\overline{\sigma B_{T,N}} = 0.73 \overline{K_p} + 0.95$$

The root mean square of the deviation is 0.44.

When an average lag is assumed for the entire period shown in Fig. VII-22, the correlation coefficient is 0.79. When the period is broken into two segments and an average lag is used for each, the correlation increases to 0.80 and 0.87, respectively. Thus, even though the geomagnetic activity is relatively low during this period, there is a remarkable correspondence between the planetary magnetic variability and the magnitude of the transverse fluctuations of the interplanetary field.

From Figs. VII-19 and VII-20, it is noted that the two events of highest interplanetary field magnitude observed during the early part of the flight occurred while

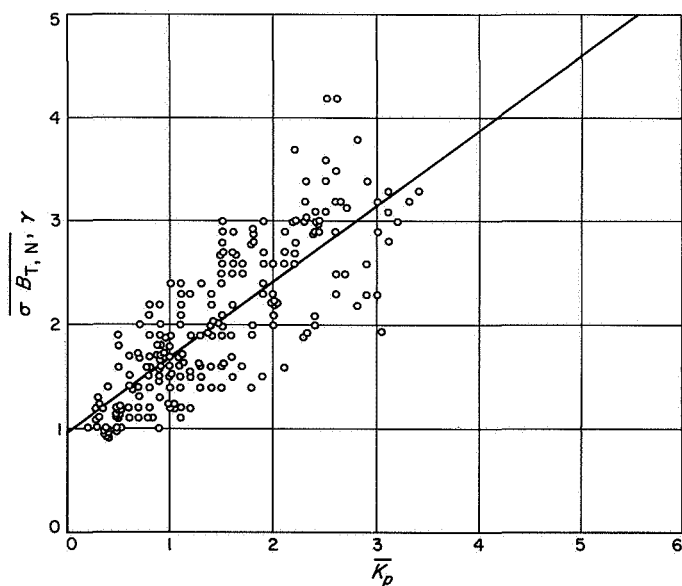


Fig. VII-22. Relationship between values of  $\overline{\sigma B_{T,N}}$  and  $\overline{K_p}$

the earth and probe were seeing very nearly the same solar winds. Furthermore, they were the only two events, during this period, that correspond to sudden commencement storms observed at the earth.

d. *Simultaneous measurements of interplanetary magnetic field on Mariner IV and OGO-1.* OGO-1 was launched in September 1964 prior to Mariner IV, and it continued to make interplanetary magnetic field measurements, as well as measurements inside the earth's magnetosheath and magnetosphere, using a search coil magnetometer. Simultaneous interplanetary field measurements were available during two intervals from November 28 to December 16, 1964 and from March 8 to May 4, 1965 (OGO-1 was inoperative during the intervening period). Data obtained in the first time interval, during which the distance between the two spacecraft increased from  $1/3 \times 10^6$  to  $5 \times 10^6$  km, have been employed to investigate simultaneous time variations in the interplanetary field at two widely separated locations. Simultaneous observations afforded a direct means of measuring the velocities of propagation and the representative scale sizes of interplanetary disturbances.

As a consequence of the 66-h orbital period of OGO-1 and the fact that it was inside the magnetosphere during the Mariner launch (even when Mariner was "near" the earth), a time delay on the order of an hour is to be expected for features frozen into the solar wind. This time delay suggests that correlations in the two sets of data will involve field changes that are slow compared to an interval of an hour or so. Consequently, the initial phase of the investigation has involved studying the steady and slowly varying components of the interplanetary field.

The digitized Mariner helium magnetometer data provided continuous measurements of the interplanetary field from 0 to  $\sim 1/3$  Hz. Due to the spin of the spacecraft, the OGO-1 search coil magnetometer also measured the steady field component or, actually, its projection into the satellite equatorial plane, which is perpendicular to the spin axis. In this case, the two equatorial components of the field can be obtained by synchronous demodulation of the search-coil sinusoidal voltage, using a reference sinusoid having the same period as the satellite spin ( $\sim 12$  s). The two components can be converted to cylindrical coordinates  $B_{\perp}$ , the magnitude of the field component perpendicular to the spin axis, and  $\phi$ , the direction of the perpendicular component (referred, in this case, to an arbitrary direction so that only changes are meaningful).

As part of the *Mariner* data analysis, the three components of the interplanetary field were averaged over a time interval of  $2^{-9}$  days (168.75 s). For the purpose of comparison, the *Mariner* measurements were transformed into *OGO-1* coordinates (based on the known *OGO-1* spin-axis orientation and the direction from the spacecraft to the sun);  $B_{\perp}$  and  $\phi$  were computed. Similarly, the *OGO-1* data were averaged over the same time interval ( $2^{-9}$  days) to provide a common basis for comparison.

The results of the earliest possible data comparison for the first interval when both spacecraft were simultaneously in interplanetary space are shown in Figs. VII-23 and VII-24. During the interval shown, *OGO-1* was moving toward apogee on the afternoon side of the earth (the sun-earth-satellite angle increased gradually from 35 to 53 deg) and *Mariner* was moving ahead of the earth in its orbital motion around the sun just behind the extended dawn-line (at a sun-earth-probe angle of  $-110$  deg). The separation between the two spacecraft increased from  $\sim 90$  to  $\sim 140$  earth radii.

At the beginning of the interval, the theoretical time delay for a structure frozen-into the solar wind traveling from *OGO-1* to *Mariner IV* is  $32 \pm 3.5$  min (the uncertainty corresponds to assuming a solar-wind speed of  $350 \pm 100$  km/s). The major part of the delay (10.3 min) is contributed by the azimuthal velocity of a feature assumed to be corotating with the sun. However, there is also a substantial contribution ( $12.5 \pm 3.5$  min) due to the radial velocity component. The azimuthal separation of *OGO-1* and *Mariner IV*, at this time, is  $77 r_E$  and the radial separation is only  $37 r_E$ .

Figure VII-23 shows a reasonably close correspondence between the directions of the perpendicular component of the interplanetary field at the two locations. The *OGO-1* data have been displaced 30 min with respect to the *Mariner IV* data and this results in the close agreement that is observed. By the end of the time interval shown in Fig. VII-23, the theoretical time delay has increased to  $49 \pm 5$  min. Since no allowance has been made in this figure for a variable time delay, slight discrepancies have developed in the time of occurrence of distinct field changes. In general, however, the results have substantiated expectations based on having the field irregularities propagate at wave velocities that are slow compared to the solar-wind speed.

Figure VII-24 contains the two measures of  $B_{\perp}$ , which are also shifted by 30 min relative to each other. The

average magnitude of the component at the two locations is quite similar. However, the detailed correspondence between successive distinct field changes that was noted in Fig. VII-23 is much less obvious. Apparently the direction of the interplanetary field tends to be uniform over distances in which the field magnitude can vary substantially. It is as though the flux tubes of the interplanetary field had a similar direction over a scale of  $\sim 100 r_E$ , but were either compressed or inflated over the same scale.

The data shown in Figs. VII-23 and VII-24 pertain to conditions approximately 2 days after the *Mariner IV* launch. Within  $\sim 1$  wk after the launch, it had become difficult to recognize readily correlatable features in either  $B_{\perp}$  or  $\phi$  in the two sets of data. This suggests that the transverse dimensions of typical interplanetary field irregularities are on the order of 10 million km (0.06 AU) or less.

Such a characteristic scale size is consistent with earlier observations. As seen on a single spacecraft, major changes in the interplanetary field (usually a change in direction) typically occur every few hours or so. For a wind speed of 400 km/s, this change occurrence implies a scale (either radial, tangential, or a composite) of a few times  $10^6$  km. Furthermore, simultaneous variations in the direction of arrival of solar protons and the direction of the interplanetary field as observed on *Pioneer 6* suggest that the interplanetary field is organized into distinct tubes of flux within which the field has a reasonably well-defined direction. The *Pioneer 6* observations suggest a typical transverse dimension of  $6 \times 10^6$  km for the flux tubes. Evidence from *Mariner IV* concerning the observation of such tubes or ropes of flux, and the nature of the discontinuous change in field across their boundaries, are presented in the following subsection 2-g.

*e. Dependence of properties of interplanetary field on heliocentric distance.* Several parameters pertaining to the interplanetary trajectory of *Mariner IV* are plotted in Figs. VII-25 and VII-26. The heliocentric range of the spacecraft varied from 1.00 to 1.58 AU during the part of the flight covered by the measurements, while the solar-equatorial latitude varied from  $+3.0$  to  $-7.3$  deg.

An attempt has been made to determine the radial dependences of the various properties of the "quiet-day" interplanetary field. It is not possible to unambiguously separate long-term temporal effects from spatial effects.



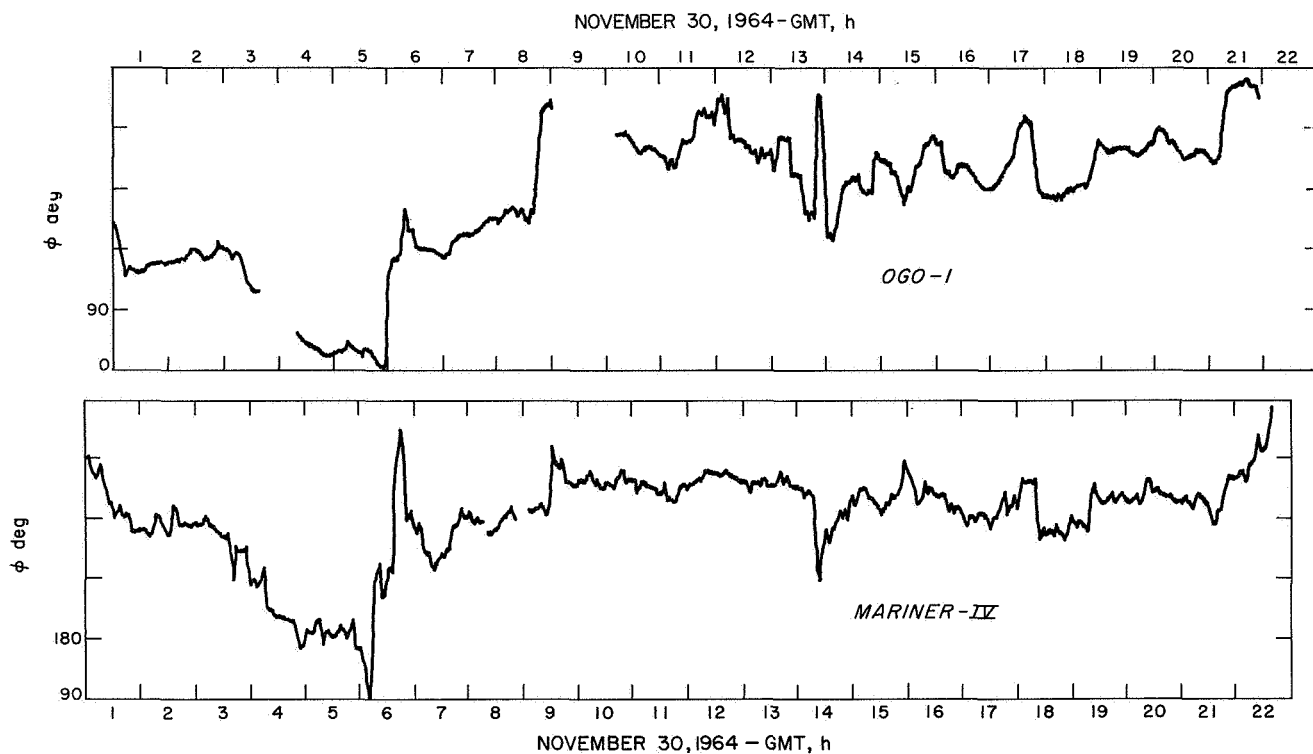


**Fig. VII-23. Simultaneous measurements of interplanetary magnetic field direction  $\phi$**

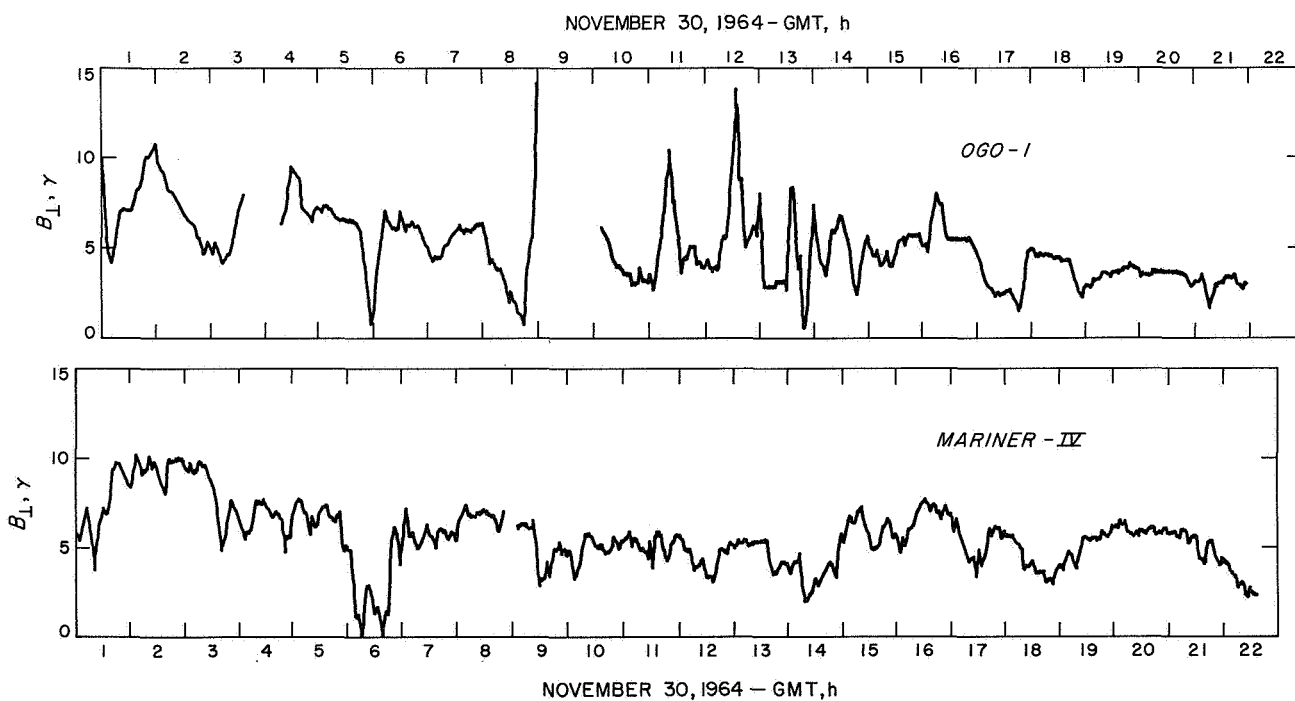


**Fig. VII-24. Simultaneous measurements of interplanetary field magnitude  $B_{\perp}$**

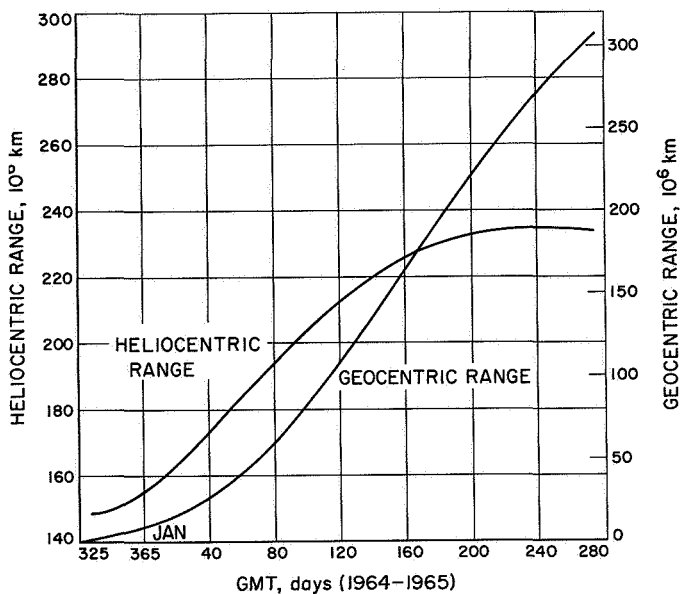


Fig. VII-25. Range parameters of trajectory of Mariner IV as functions of time

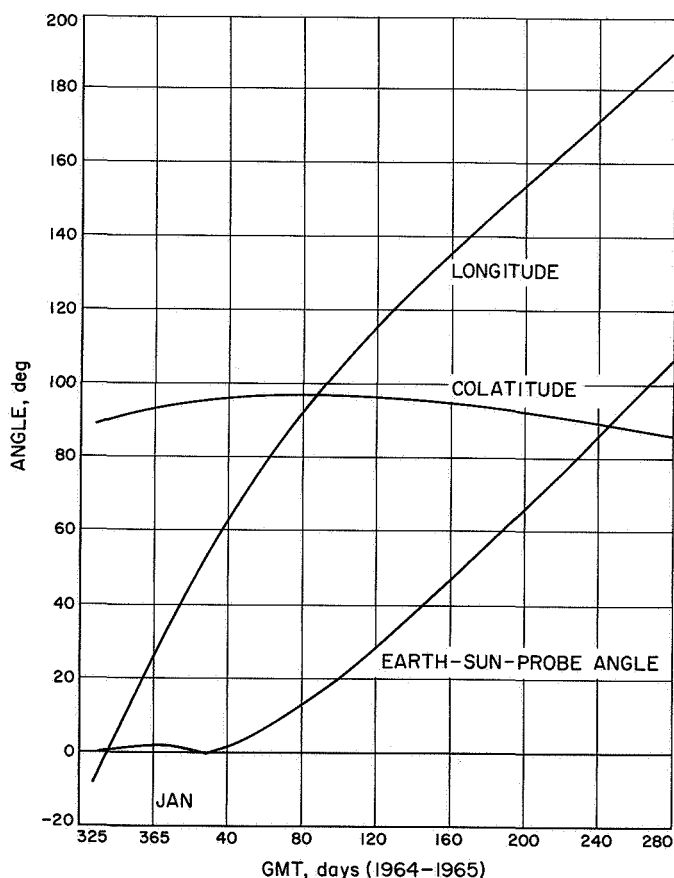


Fig. VII-26. Solar-equatorial system parameters of trajectory of Mariner IV as functions of time

However, in this study, it was assumed that the spatial dependences might be determined by comparing data taken when conditions in the interplanetary medium were similar. Conditions were taken to be similar during periods when indices of geomagnetic activity and the cosmic-ray influx at the earth were similar. Specifically, the daily indices of geomagnetic activity  $A_p$  and  $\Sigma K_p$ , and the mean neutron intensity (at Climax, Colorado)  $C_N$  were employed.

Of primary concern are properties of amplitude distributions of various quantities. Each of the distributions employed in this analysis consists of the measurements obtained during a single period of rotation of the sun.

Due to the motion of *Mariner IV* relative to the earth, specific periods of the sun's rotation (in GMT or UT) were, in general, different at the earth and at *Mariner IV*. The time differences depend on the solar-wind velocity, as well as the position of the spacecraft relative to the earth.

The procedures employed in this analysis were the following:

- (1) The period of the flight was divided into 68 overlapping 27-day periods taken at intervals of 3 days. These 27-day periods were selected so that they included, as a subset, the conventional solar rotation periods. The flight of *Mariner IV* began during SR 1791 and the data transmissions were uninterrupted until SR 1805. During each of the 68 periods, mean values of  $A_p$ ,  $\Sigma K_p$ , and  $C_N$  were calculated for each period. These mean values are denoted respectively by  $\langle A_p \rangle_s$ ,  $\langle \Sigma K_p \rangle_s$ , and  $\langle C_N \rangle_s$ , with the subscripts indicating means taken over periods of one solar rotation. The resulting three series of 68 values for each of these three quantities are plotted versus time in Figs. VII-27 and VII-28.
- (2) The corresponding time interval was computed for each 27-day period at earth, during which the spacecraft was most likely to encounter solar-wind plasma from the same sources on the sun and in the same sequence. If a constant radial streaming velocity  $V_p$  is assumed for the solar wind, then the time difference between the arrival at earth and the arrival at *Mariner IV* of the plasma streaming from a particular solar meridian is

$$\Delta t \simeq [(r_m - r_e)/V_p] + [(\phi_m - \phi_e)/\Omega_s]$$

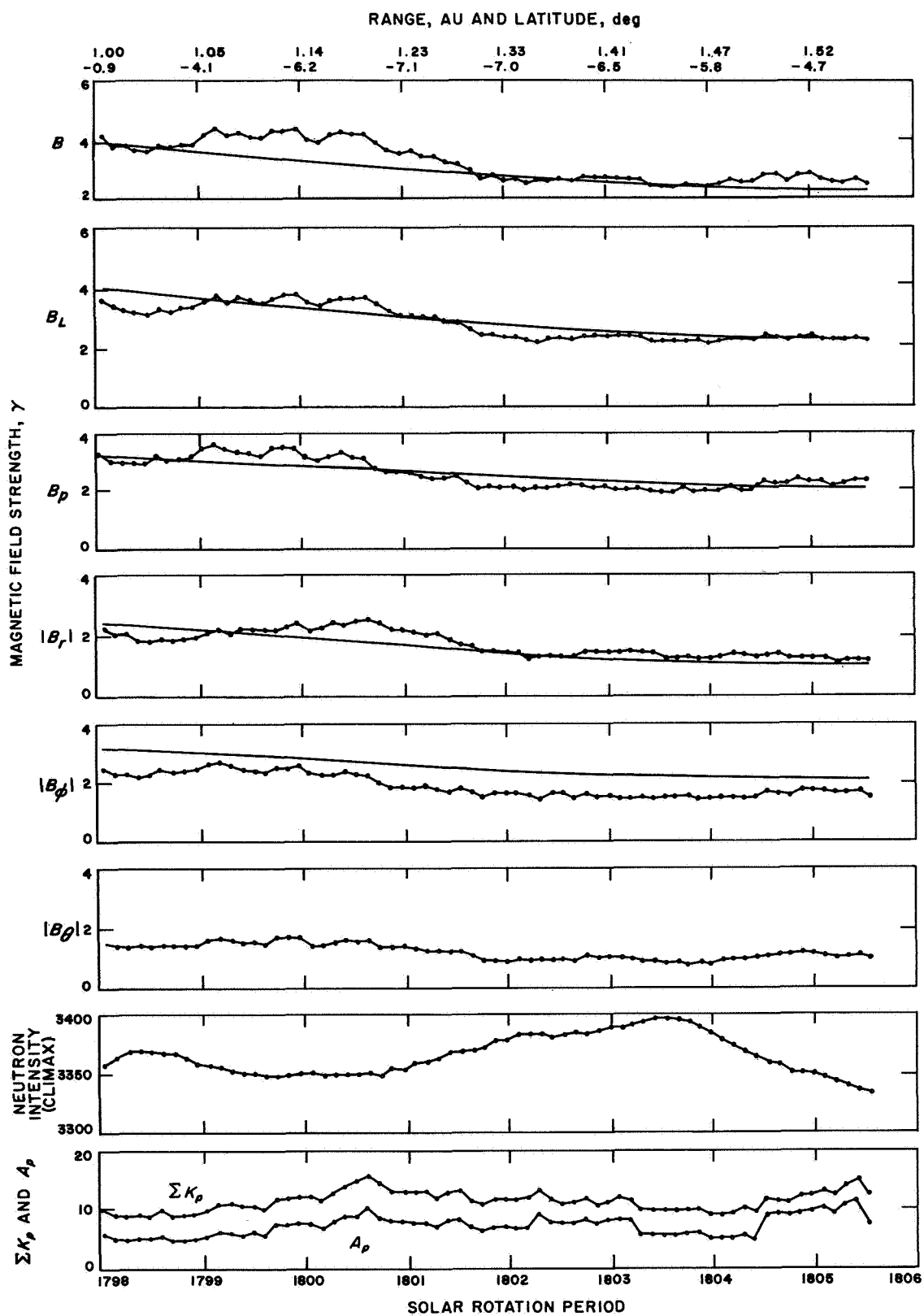
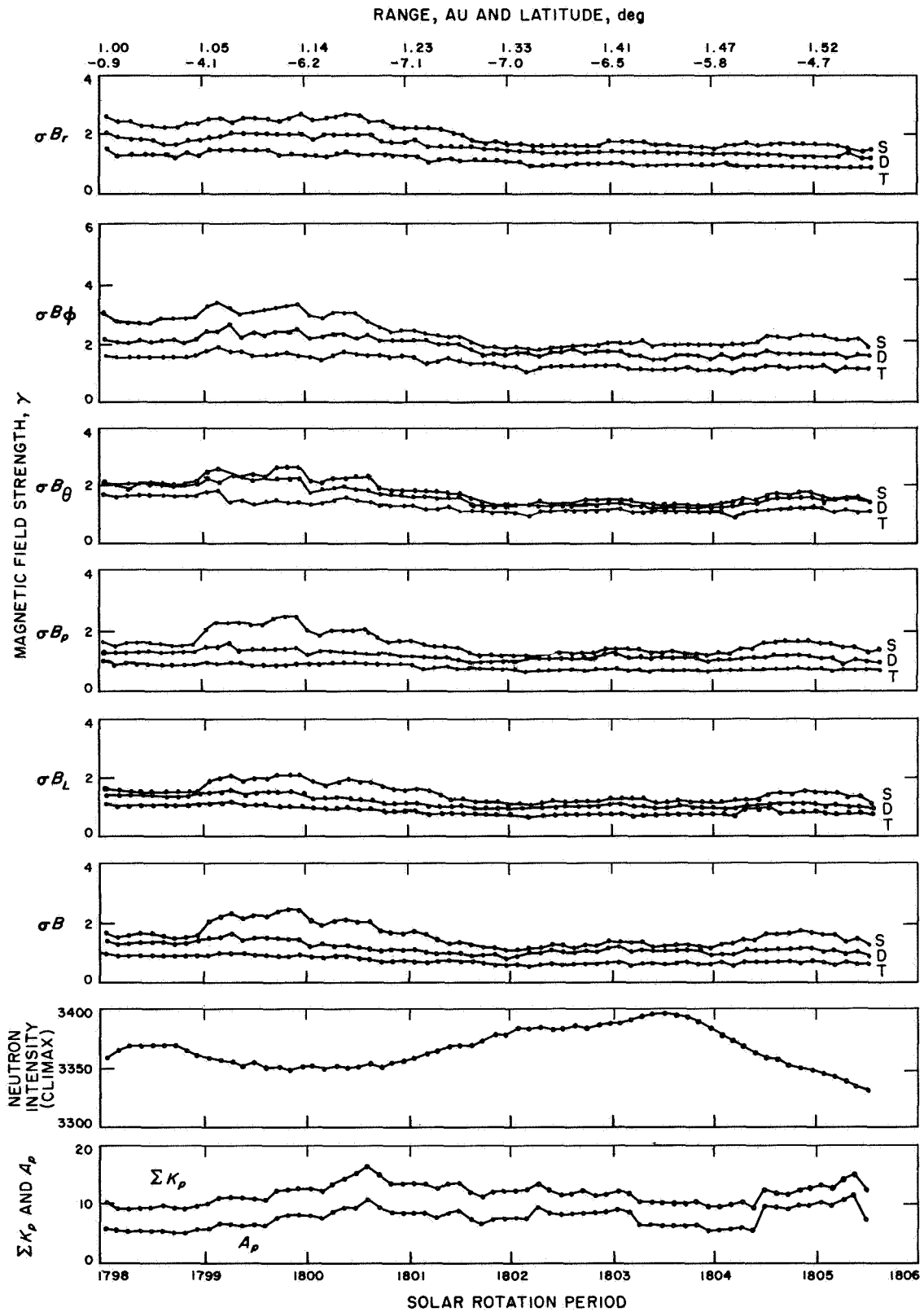


Fig. VII-27. Mean values of magnitudes of various components of interplanetary magnetic field versus time, heliocentric range, and latitude



**Fig. VII-28. Standard deviations of various components of interplanetary magnetic field versus time, heliocentric range, and latitude**

where the subscripts  $m$  and  $e$  refer to *Mariner IV* and earth, respectively. In computing  $\Delta t$ , a constant value of  $V_p = 350$  km/s was assumed. For each of these 68 overlapping periods of 27 days appropriate to *Mariner IV*, the amplitude distributions of various field variables were obtained and their means and standard deviations were derived from these distributions.

Figure VII-27 contains the 27-day running means obtained in this way from the measured values of  $B$ ,  $B_p$ ,  $|B_r|$ ,  $|B_\phi|$ ,  $|B_\theta|$ , and  $B_L$ .  $B_L = (B_r^2 + B_\phi^2)^{1/2}$ . The corresponding standard deviations are shown in Fig. VII-28. The curves labeled "S" are rms deviations taken over one period of the sun's rotation. Those labeled "D" are rms deviations taken over 24-h periods and averaged over solar rotation periods. Those labeled "T" are rms deviations taken over 3-h periods and averaged over solar rotation periods.

The mean values of the total field strength  $B$ , taken over solar rotation periods, are compared in Fig. VII-27 with the values expected for an idealized spiral field of magnitude  $4.0 \gamma$  at 1.0 AU in a solar wind at a velocity of 350 km/s. If the values obtained during periods of relatively high geomagnetic activity are neglected, the results indicate that the radial dependence of the field strength is very nearly that expected from the spiral-field model.

The theoretical values corresponding to  $\langle B_L \rangle_s$ ,  $\langle B_p \rangle_s$ ,  $\langle |B_r| \rangle_s$ ,  $\langle |B_\phi| \rangle_s$ , and  $\langle |B_\theta| \rangle_s$  are also shown in Fig. VII-27. The theoretical value of  $\langle |B_\theta| \rangle_s$  is zero for an ideal spiral field. Quantity  $\langle B \rangle_s$  exhibits the predicted behavior, but it is interesting to note that only  $\langle B_p \rangle_s$  also behaves roughly as expected. The other quantities are, in general, somewhat smaller than predicted. Further, the radial dependences of these quantities exhibit considerable scatter about the predicted values. Most of these discrepancies between the observed and theoretically predicted magnitudes of the individual components are probably due to the presence of relatively large-amplitude disturbances, which produce coherent variations in the various components of the field, as described by P. J. Coleman (Ref. 24). The primary effect of these disturbances is to cause changes in field orientation.

Perhaps the most significant result from the analysis of the variations is that the radial dependences of  $\sigma(B)$ ,  $\sigma(B_p)$ , and  $\sigma(B_L)$  are somewhat weaker than the radial

dependences of  $B$ ,  $B_p$ , and  $B_L$ . All mean rms deviations are compared to the mean values of  $B$ . The radial dependence of these ratios is also estimated. The result of the greatest immediate significance is for the function  $\sigma(B)/B$ . Thus, at 1.0 AU,  $\sigma_s/B \simeq 0.4$ ; while the calculations of the radial dependence indicate  $\Delta B/B \simeq r^{0.6}$ . For disturbances with periods shorter than one day,  $\sigma_D/B \simeq 0.3$  at 1.0 AU and  $\Delta B/B \propto r^{0.5}$ .

The measurements of the amplitudes of the variations in the field components indicate that a considerable component of the variations is produced by dynamic phenomena in the solar-wind plasma (e.g., waves and disturbances of greater magnitude). The properties of small-scale, small-amplitude disturbances have been discussed in recent reviews by E. N. Parker (Ref. 25) and by A. J. Dessler (Ref. 26). For the simplest cases, under the assumption that the plasma behaves as an ideal gas and that damping is negligible, the amplitudes of disturbances would increase relative to the mean field strength as the distance from the sun increased. E. N. Parker provides examples for small-amplitude waves (e.g., waves with  $\Delta B/B = 0.05$ ) near the sun. At 1.0 AU, such waves would yield  $\Delta B/B \simeq 1.0$ . Quantity  $\Delta B/B$  would increase with  $r$  at least as fast as  $r^{0.5}$ . These theoretical expectations compare well with the results derived from the *Mariner IV* observations.

*f. Power spectra of interplanetary field fluctuations.* Power spectra of fluctuations in the interplanetary field have been computed from *Mariner IV* data acquired over 24-h intervals. The fluctuations are of relatively short duration, 1 s to approximately 1 h, and can be viewed as superimposed on, or as additional detail to, the general spiral field pattern and the polarity sector structure (see previous subsection 2b). Power spectra of interplanetary field fluctuations have also been obtained from *Pioneer 5* (Ref. 8), *OGO-1* (Ref. 10), *Mariner II* (Ref. 27), and *Pioneer 6* (Ref. 28). Such results are useful both for interpreting the nature of the magnetic fluctuations (Ref. 24) and for studying the propagation of cosmic rays in the interplanetary medium (Ref. 29).

Power spectra of the three components of the field ( $B_R$ ,  $B_T$ ,  $B_N$ ) and the absolute magnitude  $B$  were obtained for six days during the high-bit-rate interval. Three days were selected near the beginning of the flight, and three days were selected near the end of the high-bit-rate interval, approximately one to three weeks later. Each group of three days contains a very quiet, a very disturbed, and an intermediate day. The

days analyzed are 24-h intervals that began: active 08:00 GMT, 7 December 1964 and 13:00 GMT, 2 January 1965; intermediate, 00:00 GMT, 2 December 1964 and 01:00 GMT, 26 December 1964; quiet, 00:00 GMT, 6 December 1964 and 00:00 GMT, 12 December 1964.

Figures VII-29 and VII-30 show the superimposed results for the three components and  $B$ . The frequency scale is shifted two decades between different days. The spectra are computed using the standard method of finding the auto correlation function for each data interval and then computing its Fourier transform (e.g., see R. B. Blackman and J. W. Tukey in Ref. 30).

Digitization noise is responsible for the flattening out of the curves at high frequencies and hence this region should be disregarded. This artificial noise results when the field is near the edge of a digitization window so that very small field fluctuations produce an apparent

field change of one window width ( $0.7 \gamma$ ). Although noise levels of  $(0.35)^2/F_N \approx 0.2 \gamma^2/\text{Hz}$ , where  $F_N$  is the Nyquist frequency, can be produced in this manner, the actual noise is usually less. When the field is very noisy as on 2 January 1965, it almost never comes to rest near the edge of a digitization window; consequently, very little flattening of the spectrum is observed.

Away from the region affected by digitization, the curves for all levels of activity tend to follow straight lines with slopes of  $-3/2$ . Several interesting relationships are apparent from these curves. First, the power in  $B$  at a given frequency is usually appreciably less than the power for the three components. This power difference indicates that the field fluctuations are more torsional than compressional; that is, changes in field direction are more important than changes in magnitude. Quiet days might be an exception to this rule, since the differences between the power spectra are not as large.

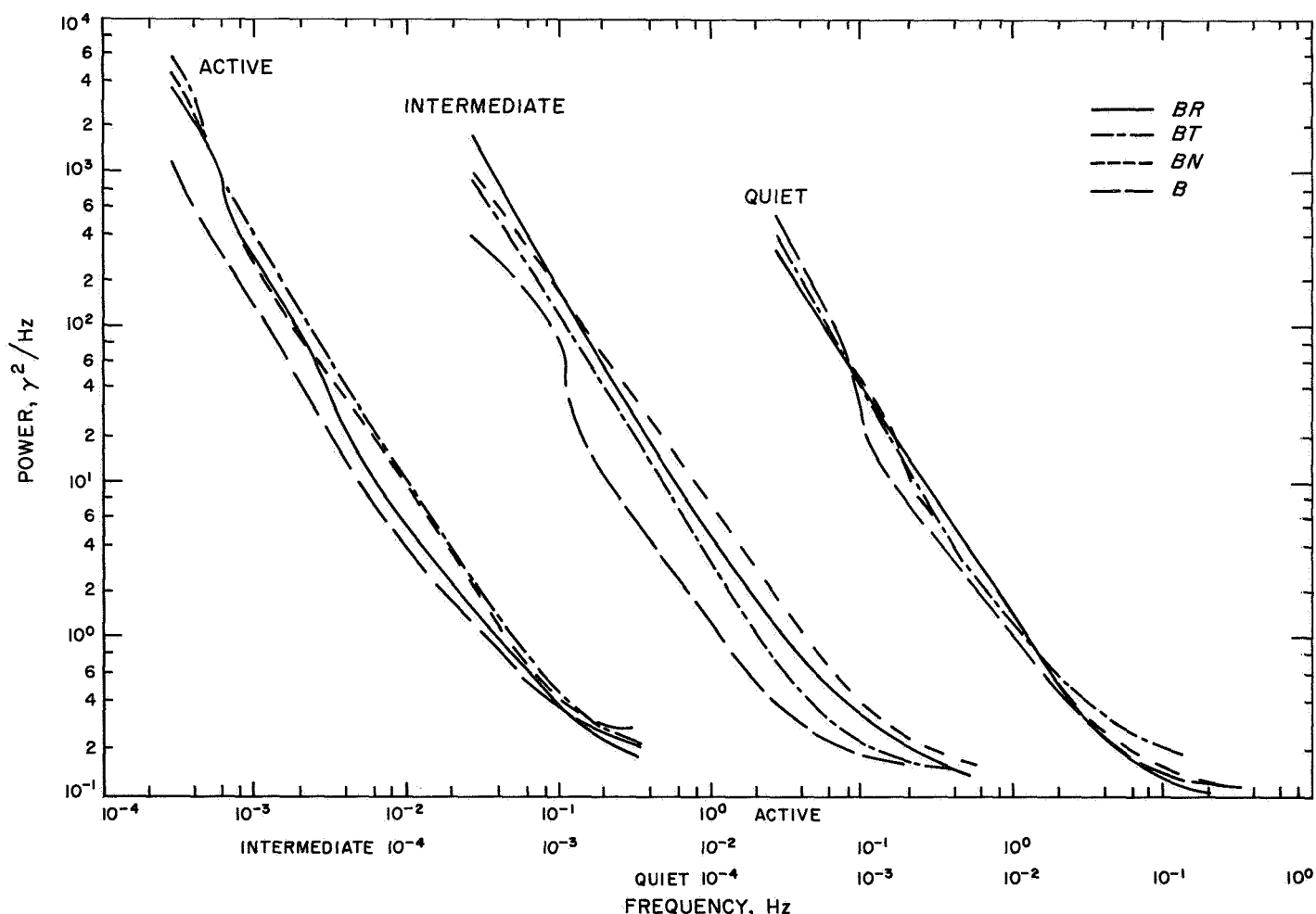


Fig. VII-29. Power spectra of field obtained for three days near beginning of flight

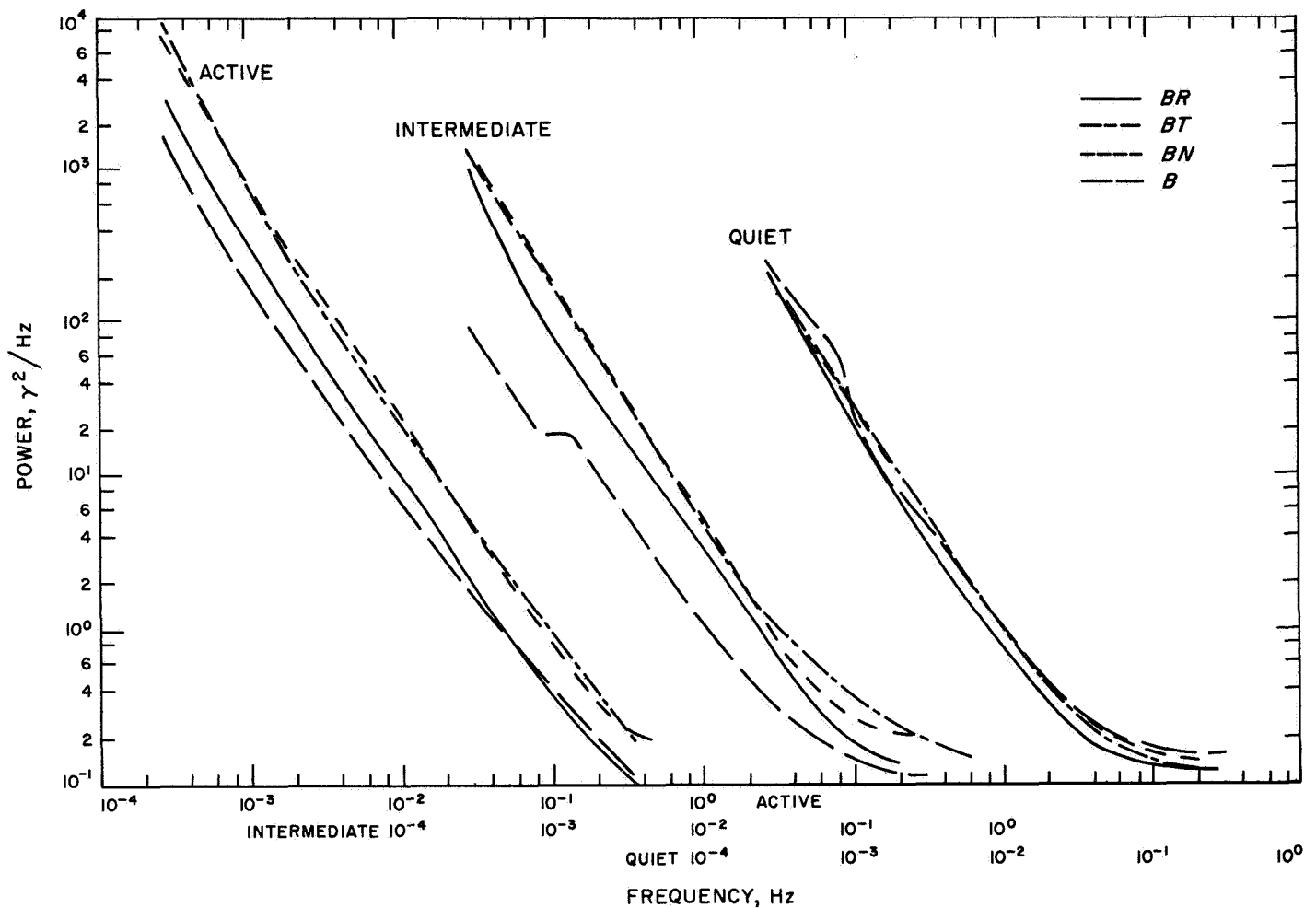


Fig. VII-30. Power spectra of field obtained for three days near end of high data rate interval

Second, the kink in the  $B$  curves near  $10^{-3}$  Hz on both quiet days and intermediate days might indicate a transition between modes of wave propagation. Alternatively, the transition frequency ( $10^{-3}$  Hz) corresponds very nearly to the expected 17-min period associated with the granulation pattern of the solar photosphere. This period is the time required for a granulation cell, which typically has a dimension of 2000 km, to rotate through the meridian plane containing the spacecraft.

Third, there is a tendency for the power in  $B_R$  to be less than that in either  $B_N$  or  $B_T$ . The tendency is more noticeable on disturbed than quiet days (see previous discussion in subsection 2-c). These properties of the power spectra all strongly suggest that the major contribution comes from waves, probably hydromagnetic waves, such as those observed on *Mariner II* (Ref. 24).

*g. Discontinuities in interplanetary magnetic field.* The interplanetary field typically has an intensity of  $5 \gamma$

and a direction that on the average agrees with a spiral pattern. Fluctuations in these values occur; some quantitative information about the fluctuations is given in the previous section. However, a false impression of the field behavior would be obtained by superimposing a long series of harmonic functions with random phases and with amplitudes that depend on frequency according to the power spectra given earlier. There is considerable detail and discrete structure in the interplanetary field. One particular aspect of this structure is the subject of the present section.

The field is often observed to change from one more-or-less steady direction to another more-or-less steady direction within a time span that is short in comparison to the time that it previously or subsequently remains nearly constant. The general impression where this occurs is that of a discontinuous change in the field direction. There may also be an associated change in magnitude, but this change is usually less noticeable.

Examples of this type of discontinuity are shown in Fig. VII-31. Each such event indicates the passage by the spacecraft of a current sheet. Most likely the current sheets are semipermanent structures in the interplanetary medium and are advected past the spacecraft by the solar wind.

The general subject of discontinuities in the solar wind has been reviewed by D. S. Colburn and C. P. Sonett (Ref. 31). Discontinuities are classified either as shock waves or as contact surfaces; both have been observed in the interplanetary medium. A shock wave was identified (Ref. 23) in the *Mariner II* data with a transition time less than 3.7 min (the plasma sampling spacing); hence, its thickness was less than about  $10^5$  km. Although the boundary between sectors was often thick and complicated, on at least one occasion (Ref. 21) a sector boundary was identified between successive 5-min averages, implying a contact surface that again had a thickness less than about  $10^5$  km. The recent model (Refs. 28, 32, and 33) in which the interplanetary field was composed of a large number of filamentary tubes that originate on the sun was based on observations of contact surfaces and associated changes in solar cosmic-ray anisotropies. The contact surfaces between filaments

passed *Pioneer 6* in time intervals on the order of 1 min or less, indicating thicknesses less than about  $2 \times 10^4$  km.

The present study concerns contact surfaces, few well-defined shock waves having been identified in the *Mariner IV* data in interplanetary space. A contact surface may involve a change in magnetic field strength or direction, a change in gas composition and pressure, and a change in gas velocity. Almost always currents are in a contact surface, perhaps a thin-layered structure of currents. Since we have studied only the magnetic observations, which give information about the current sheets and not about the plasma properties, we shall mostly think of contact surfaces as current sheets.

An analysis of the distribution of the thicknesses of the current sheets revealed a strong concentration toward small thicknesses. During nondisturbed times, over half of all the current sheets producing changes of  $4 \gamma$  or more within 5 min had thicknesses less than about 3500 km, and an estimated 10% had thicknesses less than 500 km; i.e., of the order of the thermal proton gyro diameter. During disturbed times, there was an even stronger concentration toward small thickness.

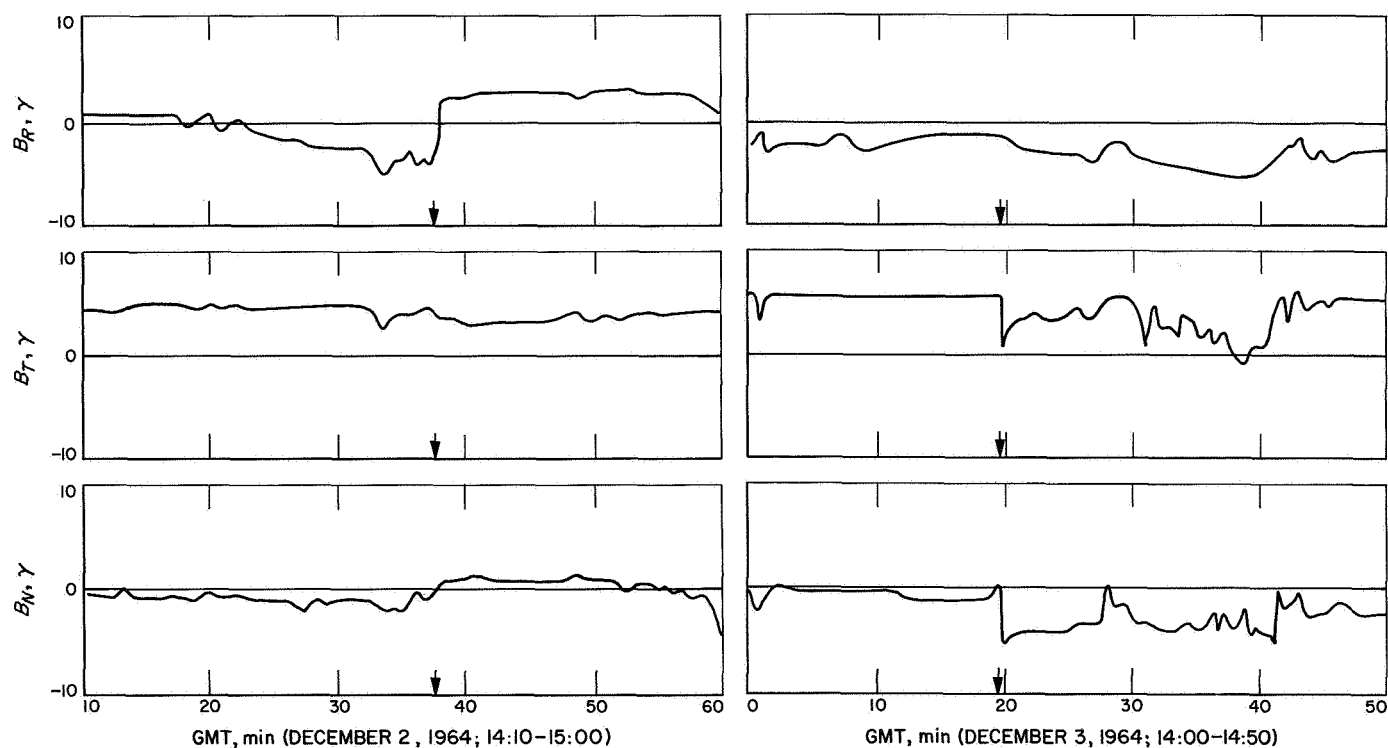
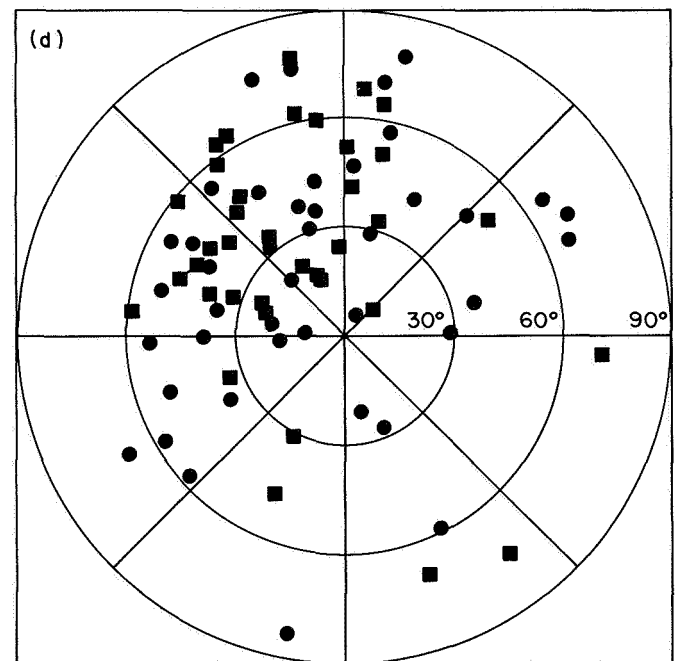
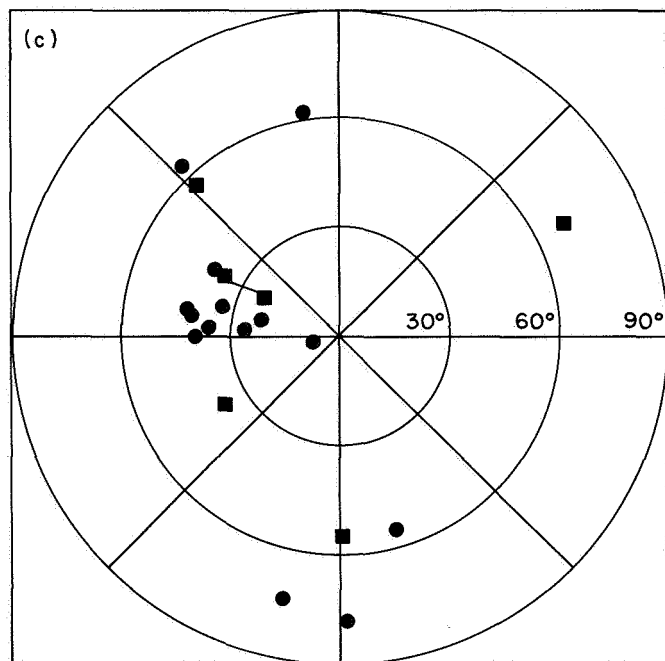
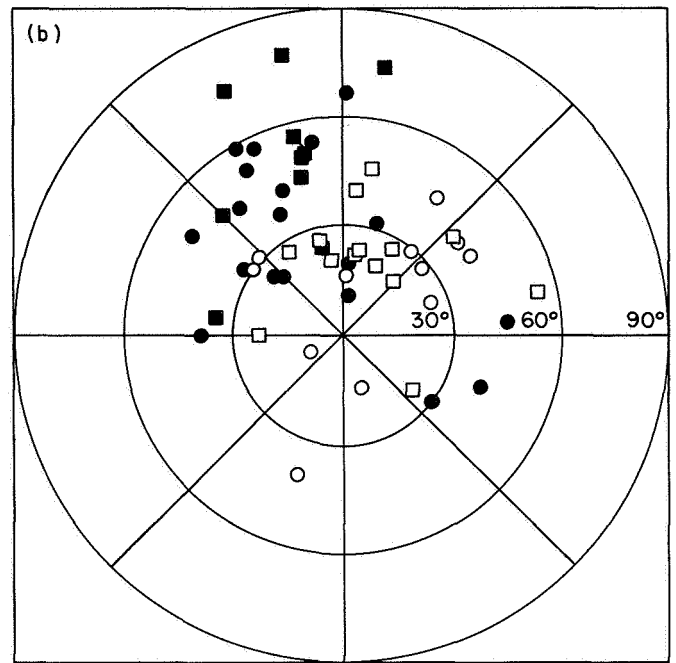
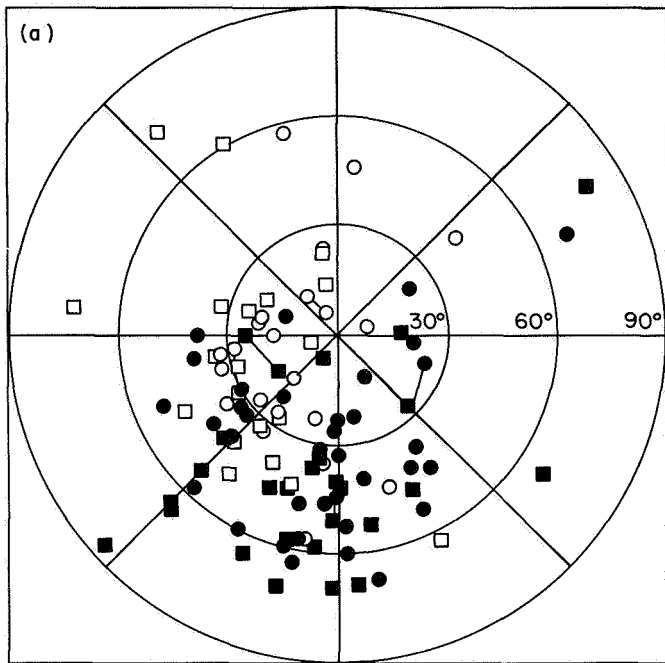


Fig. VII-31. Examples of discontinuities in interplanetary magnetic field





**Fig. VII-32. Directional distribution of current sheet normals**

Detailed analysis of the structure of simple discontinuities (i.e., discontinuities characterized by a more-or-less direct, uncomplicated change from one vector field to another) indicates that the field changes its direction by rotating in one plane from its initial to its final direction. This indication strongly suggests that the simple discontinuities are tangential discontinuities (in the sense of Ref. 31) characterized by zero normal field and velocity components. That is, they are shielding currents separating regions of plasma and fields with different histories or origins on the sun. This result is consistent with the filament model, if we interpret the discontinuities as filament boundaries.

Determinations of the normal vectors to the current sheets are useful, because they give the local orientation of the current sheet in space. The normals to the plane of rotation of the magnetic field were determined using the technique described in the previous discussion of shock aligned magnetic oscillations under subsection 1b. The results are plotted in Fig. VII-32. The center of the polar plot corresponds to the radial direction from the sun (+  $R$  direction). The distance from center represents the polar angle from the radial direction. The angle about the center measured from the horizontal gives the angle from the  $T$  direction in the  $TN$  plane. The four figures correspond to four polarity sectors. The first two sectors (a and b of Fig. VII-32) were sampled twice, the normals observed the second time being represented by open characters. Squares have been used for simple discontinuities and circles for other kinds. Filament boundaries are connected by straight lines.

The analysis of the current sheets observed by *Mariner IV* revealed a sector-dependent asymmetry in the directional distribution of current sheet normals. There was an east-west asymmetry, which was the same in three out of four sectors and was consistent with the spiral pattern. There was also a north-south asymmetry, which differed from sector to sector, requiring additional assumptions about the solar wind or the magnetic field for an explanation.

A possible explanation, which has been pursued, involves a latitudinal shear in the solar wind speed whose sense can vary from sector to sector. To explain the observations, the model requires higher wind speeds at latitudes north of the spacecraft latitude (positive shear) in one sector, a local negative shear in two sectors, and slightly negative shear in the fourth sector. The basic physical effect is seen in Fig. VII-33, which shows the intersection with the  $RN$  plane of a current sheet,

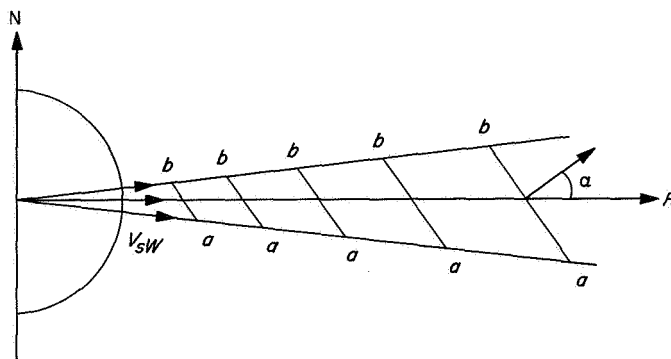


**Fig. VII-33. Illustrating north-south orientation of radially convected (ab) current-sheet normal due to negative latitudinal solar-wind shear**

the north side of which is moving more slowly than the south side, as a result of a latitudinal wind shear.

Filament transitions, characterized by two clearly associated discontinuities (the filament boundaries) before and after which the field often has the same direction, have also been studied. The time separation between filament boundaries from *Mariner IV* observations varies from less than 1 min to more than 1 h. Analysis of the normals to these boundaries suggests that they are nearly parallel (the average angular difference between the normals in the nine cases analyzed being 8.8 deg) and that they have the north-south direction prevailing for their sector. Hence, the cross-section of the filaments must be highly elliptical rather than more-or-less circular. This conclusion is consistent with the assumption of a local latitudinal wind shear, which stretches the filaments out into an elliptical cross section.

**3. Measurements near Mars.** From a naive point of view, it seems surprising that one can hope to learn something about the interior of Mars by conducting an experiment on a spacecraft that never gets closer to the surface of the planet than *Mariner IV* did. However, one of the objectives of the magnetometer experiment was to look for an intrinsic magnetic field associated with the planet. The best scientific information available, based on a long history of studying the earth's magnetic field, indicates that the source of such a field is a system of large-scale electric currents flowing inside a molten planetary core. Since Mars is known to have a relatively low density, it has been generally supposed that it lacks a dense fluid core, such as comprises the earth's center. Prior to the *Mariner IV* observations, the scientific consensus was that the absence of an intrinsic Martian field would represent further evidence that Mars lacked such

a core and, in this sense, was distinctly different from earth.

The question of whether or not a planet has a large-scale magnetic field also has important implications regarding its charged-particle environment. In the absence of a magnetic field, the planet cannot sustain a radiation belt, such as surrounds the earth. Furthermore, much of the planet's surface and atmosphere are not shielded from cosmic rays, and the flux of high-energy particles should everywhere be comparable to what is observed at earth only in the polar regions. Another consequence worth noting is the possible long-term effect that continuous bombardment by the solar wind could have on the atmosphere of the planet, including its removal at a rate that is important to any understanding of its composition or evolution.

*a. Encounter data and estimated bound on magnetic dipole moment of Mars.* No magnetic effects definitely attributable to the presence of the planet were observed. This conclusion is based on a comparison of the encounter data with the measurements recorded by the same instrument within the region of interaction between the earth's magnetic field and the solar wind, as well as in interplanetary space during the 7-mo interval between launch and encounter. It is assumed that the interaction of the solar wind with a significant Martian dipole moment would have produced effects geometrically similar to those observed near the earth, but with a scale determined by the magnitude of the dipole moment. This assumption is used in the following discussion to establish an upper limit for the Martian dipole moment. Since the bow shock is the feature of a planet's interaction with the solar wind that occurs farthest from the planet (except possibly for the magnetic tail which *Mariner IV* was never in a position to detect because of the nature of the trajectory), the ability to detect such a shock forms the basis of the discussion. The ability of the *Mariner IV* magnetometer to detect a planetary shock front depended on the spatial resolution and sensitivity of the measurements, on the nature of the encounter trajectory, and on the character of the interplanetary field fluctuations during encounter.

The resolution of the telemetered magnetic data was  $0.35 \gamma$  per axis ( $1 \gamma = 10^{-5} \text{ G}$ ), a limit imposed by the uncertainty inherent in converting the magnetometer output analog signals to digital numbers before transmission to earth. The noise threshold of the *Mariner IV* vector helium magnetometer was significantly smaller, being equivalent to only  $0.1 \gamma$  rms per axis. During

passage through the earth's bow shock, the sensitivity was the same, but each interval between data points was only one quarter as long. Data obtained slightly behind the extended dawn line showed clear evidence of the geomagnetic bow shock as it repeatedly surged back and forth past the spacecraft. The bow shock around Mars should occur at a position where the field strength has a value determined by the solar-wind pressure (i.e., its momentum flux), and hence should be largely independent of the Martian magnetic moment and quite similar to what is observed at the earth.

The *Mariner IV* flight path approached Mars from a direction  $13 \text{ deg}$  above the equatorial plane and at 09:40 local time. It crossed the noon meridian at a latitude of  $-50 \text{ deg}$  and an areocentric distance of  $14,500 \text{ km}$  or  $4.3 r_M$  (Martian radii); it dipped down  $21 \text{ min}$  later to a latitude of  $-67 \text{ deg}$  at closest approach, where the local time was 14:35 and the areocentric distance is  $13,200 \text{ km}$  or  $3.9 r_M$ . *Mariner IV* did not pass into the shadow of the planet, but moved away in a direction making an angle with the sun-Mars line of about  $145 \text{ deg}$ , the local time being 21:50 and the latitude being  $-3 \text{ deg}$ . Beginning at 02:19 UT (about  $1 \text{ h}$  after closest approach), *Mariner IV* was occulted by Mars for  $54 \text{ min}$ , and no telemetry data were received. However, this gap in the record does not significantly affect our estimate of the Martian dipole moment, since a moment large enough to cause a significant effect during this interval would have caused detectable effects before occultation.

The *Mariner IV* trajectory near Mars is shown in Fig. VII-34 as a function of areocentric distance and the

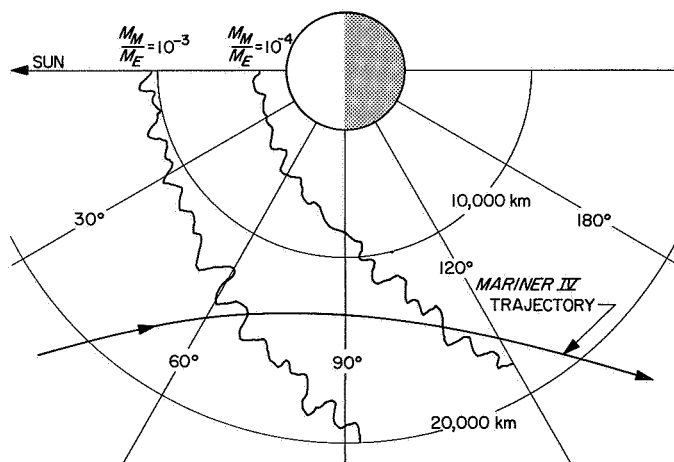


Fig. VII-34. *Mariner IV* encounter, shock front locations

sun-Mars-probe angle (the actual angle was used, not a planar projection). The two irregular contours show the expected shock-front locations for two values of the Martian magnetic dipole moment (given in terms of the ratio of that quantity  $M_M$  to the dipole moment of the earth  $M_E$ ). The shock-front locations were derived by scaling the earth's shock-front contour, using the measured momentum flux of the solar wind near Mars for various values of the planetary dipole moment. The irregularity of the contours drawn in the figure emphasizes some of the uncertainties involved in this procedure, as well as the variability in the actual location of the shock front observed near earth. This figure shows that *Mariner IV* would have penetrated the shock front well before closest approach, if Mars dipole were as large as 0.1% of the earth dipole. The other contour ( $M_M/M_E = 10^{-4}$ ) intersects the trajectory near the point at which a "shock-like" structure was seen in the *Mariner IV* magnetometer data.

Throughout the 7-mo period in interplanetary space, the *Mariner IV* magnetometer data show a pattern of alternating disturbed and quiet intervals, which has come to be expected of these kinds of data and which is related to daily changes in solar activity. Fortunately, the time interval before and during encounter was one of relative magnetic calm, even though the *Mariner IV* energetic particle detectors were recording a solar proton event that began about 23 h prior to encounter.

The three components of the measured magnetic field and the total magnitude  $B$  are shown in Fig. VII-35. Quantity  $B_R$  is directed radially outward from the sun;  $B_N$  is normal to the solar equatorial plane directed northward; and  $B_T$  completes the right-handed set and lies parallel to the solar equatorial plane pointing in the direction of motion of the planets. The effects of a spacecraft field (of  $\sim 30$   $\gamma$  magnitude whose components were determined by analyzing the many months of interplanetary data) have been subtracted from the measurements to obtain the values shown. The data are plotted as a function of both areocentric range and GMT (reckoned at the spacecraft by correcting for telemetry propagation times). Quantity CA, marked with an arrow at the top of the figure, designates closest approach. Individual data are not shown. Each dot represents averages over  $2 \cdot 10^9$  days (169 s). The vertical lines are two standard deviations long and are computed over the same 169-s interval, as were the averages. A gap in the data due to occultation occurs just after closest approach.

During the interval from 18:00 on 14 July to 01:23 UT, 22 min after closest approach, the field was unmistakably interplanetary in character, having fluctuations roughly an order of magnitude smaller than those behind the earth's bow shock. At 01:23 UT, a period of disturbance began abruptly with a 5  $\gamma$  jump in the field and an approximate doubling of the amplitude of the fluctuations. This condition continued for about 3 h, after which the components returned to near their previous values. This disturbance could be interpreted as evidence for a weak bow shock associated with Mars, but our preliminary analysis does not exclude the possibility that it is just one of many similar disturbances seen in interplanetary space during the preceding 7-mo period.

Satellite and space probe measurements made near the earth must be scaled to make them applicable to a planet having a different dipole moment. Essentially, the same approach was used that was applied to the *Mariner II* data obtained near Venus (Ref. 34). It assumed that the locations and the shapes of the magnetopause and the shock front are approximate surfaces of revolution about the solar direction and are reasonably insensitive to orientations of the magnetic dipole. Then the dipole moment of Mars  $M_M$  can be expressed in terms of the earth's dipole moment  $M_E$ , the typical solar-wind pressure at the planet  $P_M$ , the areocentric distance to a point on the encounter trajectory at which an effect, such as the magnetopause or shock, occurs  $R_M$ , and the geocentric distance  $R_E$  to the corresponding feature near earth at the same sun-planet-spacecraft angle:

$$M_M/M_E = (R_M/R_E)^3 (P_M/P_E)^{1/2} \quad (3)$$

This equation was used to derive the contours shown in Fig. VII-34 and an upper limit for  $M_M$  based on the observation that no magnetic disturbance was seen before 01:23 UT, when *Mariner IV* was 14,700 km from the center of Mars at a sun-Mars-spacecraft angle of 110 deg. Near earth at a sun-earth-spacecraft angle of 110 deg, the *Mariner IV* data showed that the position of the shock front varied between 233,000 and 246,000 km at a time when the velocity of the solar wind was 400 km/s and the density was about 6  $\text{cm}^{-3}$ . These data, when combined with the *IMP-I* shock-front data (Ref. 35), led to a reasonable, smooth contour for the average shock-front location.

The typical value for  $R_E$  at an angle of 110 deg is 240,000 km ( $\sim 37.5 r_E$ ). Average values for the solar-wind parameters during the *IMP-I* observations (8  $\text{cm}^{-3}$  and 340 km/s) correspond to an average pressure  $P_E$  of



and earth are nearly the same, a very small fluid core is suggested for Mars, in agreement with earlier proposals (Refs. 36-38). The Martian interior now appears definitely to be more like the interior of the moon than that of the earth. A moment of  $3 \times 10^{-4} M_E$  implies a surface field at the magnetic equator of only 100  $\gamma$ . It also means that the flux of cosmic rays above the atmosphere should everywhere be comparable to what is observed at earth only over the polar regions. The elevation of the magnetopause in the sub-solar region is, at most, 5,000 km or  $1.5 r_M$ . The very weak fields and low  $L$  value for the magnetopause imply that any belts of trapped radiation on Mars must be very small and weak. If the dipole moment is zero, there can be no trapped radiation.

### E. Sources

The magnetometer investigators were assisted in the analysis of scientific data by G. L. Siscoe of California Institute of Technology and J. R. Ballif of Brigham Young University. The low-field helium magnetometer was manufactured by Texas Instruments, Inc. of Dallas, Texas. The cognizant engineers at JPL were James Lawrence,

David Norris, and James Bunn. The project engineer at Texas Instruments was F. N. Reilly of the Apparatus Division. Other JPL personnel who contributed directly to the success of the experiment were A. M. A. Frandsen, J. Van Amersfoort, and B. V. Connor (experiment calibration and magnetic mapping of the *Mariner* spacecraft); G. Walker, G. Fagg, L. Simmons, and F. G. Olson (magnetometer testing and evaluation); J. G. Bastow and R. Christy (spacecraft materials testing and control); S. Z. Gunter and M. Sander (data handling); R. Norman and J. A. Stallkamp (design and construction of spacecraft magnetic mapping fixture); P. Fisher, P. McKay, and S. Harami (mathematical assistance); R. Collins and W. Hodges (experiment-spacecraft coordination). Data analysis was supported by NASA under research grants and contracts.

Discussions, analyses, and findings of magnetometer experiments have been well documented by members of the investigating team. These primary sources, as well as related astrophysics reports, are listed as references for the material contained in this section. Other references and bibliographies can be found by examining these publications.

## References

1. Ruddock, K. A., "Optically Pumped Rubidium Vapor Magnetometer for Space Experiment," *Space Res.*, Vol. 2, p. 692, 1961.
2. Keyser, A. R., Rice, J. A., and Schearer, L. D., "Metastable Helium Magnetometer for Observing Small Geomagnetic Fluctuations," *J. Geophys. Res.*, Vol. 66, p. 4163, 1961.
3. Slocum, R. E., and Reilly, F. N., "Low Field Helium Magnetometer for Space Applications," *IEEE Trans. Nucl. Sci.*, NS-10, p. 165, 1963.
4. Hess, W. N., Mead, G. D., and Nahada, M. P., "Advances in Particles and Field Research in the Satellite Era," *Rev. Geophys.*, Vol. 3, No. 4, p. 521, 1965.
5. Anderson, K. A., and Ness, N. F., "Correlation of Negative Field and Energetic Electrons on the *IMP-1* Satellite," *J. Geophys. Res.*, Vol. 71, p. 3705, 1966.
6. Sonett, C. P., and Abrams, I. J., "The Distant Geomagnetic Field," *J. Geophys. Res.*, Vol. 68, pp. 1233-1263, 1963.
7. Cahill, L. J., Jr., and Amazeen, P. G., "The Boundary of the Geomagnetic Field," *J. Geophys. Res.*, Vol. 68, pp. 1835-1843, 1963.
8. Coleman, P. J., Jr., "Characteristics of the Region of Interaction Between the Interplanetary Plasma and the Geomagnetic Field: *Pioneer V*," *J. Geophys. Res.*, Vol. 69, pp. 3051-3076, 1964.

## References (contd)

9. Heppner, J. P., *Recent Measurement of the Magnetic Field in the Outer Magnetosphere and Boundary Regions*, Report X-612-65-490. Goddard Space Flight Center, Greenbelt, Md., 1965.
10. Holzer, R. E., McLeod, M. G., and Smith, E. J., "Preliminary Results from the OGO-1 Search Coil Magnetometer: Boundary Positions and Magnetic Noise Spectra," *J. Geophys. Res.*, Vol. 71, pp. 1481-1486, 1966.
11. Siscoe, G. L., Davis, L., Jr., Smith, E. J., Coleman, P. J., Jr., and Jones, D. E., "Power Spectra and Discontinuities of the Interplanetary Magnetic Field: *Mariner IV*," *J. Geophys. Res.*, Vol. 73, pp. 61-82, 1967.
12. Spreiter, J. R., and Jones, W. P., "On the Effect of a Weak Interplanetary Magnetic Field on the Interaction Between the Solar Wind and the Geomagnetic Field," *J. Geophys. Res.*, Vol. 68, pp. 3555-3564, 1963.
13. Davis, L., Jr., Smith, E. J., Coleman, P. J., Jr., and Sonett, C. P., "The Interplanetary Magnetic Field Measurements of *Mariner II*," *Trans. Amer. Geophys. Union*, Vol. 45, p. 79, 1964.
14. Davis, L., Jr., Smith, E. J., Coleman, P. J., Jr., and Sonett, C. P., "Interplanetary Magnetic Measurements," in *The Solar Wind*. Edited by R. J. Mackin and M. M. Neugebauer. Pergamon Press, New York, 1966.
15. Davis, L., Jr., "Mariner II Observations Relevant to Solar Fields," in *Stellar and Solar Magnetic Fields*, pp. 202-207. Edited by R. Lust. North-Holland Publishing Company, Amsterdam, 1965.
16. Davis, L., Jr., "Models of the Interplanetary Fields and Plasma Flow," in *The Solar Wind*, p. 147. Edited by R. J. Mackin and M. M. Neugebauer. Pergamon Press, New York, 1966.
17. Ness, N. F., and Wilcox, J. M., "Solar Origin of the Interplanetary Magnetic Field," *Phys. Rev. Letters*, Vol. 13, pp. 461-464, 1964.
18. Parker, E. N., "Dynamics of the Interplanetary Gas and Magnetic Field," *Astrophys. J.*, Vol. 128, pp. 664-676, 1958.
19. Ness, N. F., and Wilcox, J. M., "Sector Structure on the Quiet Interplanetary Magnetic Field," *Science*, Vol. 148, p. 1592, 1965.
20. Snyder, C. W., Neugebauer, M., and Rao, U. R., "The Solar Wind Velocity and Its Correlation with Cosmic-Ray Variations and with Solar and Geomagnetic Activity," *J. Geophys. Res.*, Vol. 68, pp. 6361-6370, 1963.
21. Wilcox, J. M., and Ness, N. F., "Quasi-stationary Co-rotating Structure in the Interplanetary Medium," *J. Geophys. Res.*, Vol. 70, pp. 5793-5805, 1965.
22. Coleman, P. J., Jr., Sonett, C. P., Judge, D. L., and Smith, E. J., "Some Preliminary Measurements of the *Pioneer V* Magnetometer Experiment," *J. Geophys. Res.*, Vol. 65, pp. 1856-1857, 1960.
23. Sonett, C. P., Colburn, D. S., Davis, L., Jr., Smith, E. J., and Coleman, P. J., Jr., "Evidence for a Collision-Free Magnetohydrodynamic Shock in Interplanetary Space," *Phys. Rev. Letters*, Vol. 13, pp. 153-156, 1964.
24. Coleman, P. J., Jr., "Wave-like Phenomena in the Interplanetary Plasma: *Mariner II*," *Planetary Space Sci.*, Vol. 15, pp. 953-973, 1967.
25. Parker, E. N., "Dynamical Theory of the Solar Wind," *Space Sci. Rev.*, Vol. 4, pp. 666-708, 1965.

## References (contd)

26. Dessler, A. J., "Solar Wind and Interplanetary Magnetic Fields," *Rev. Geophys.*, Vol. 5, No. 1, 1967.
27. Coleman, P. J., Jr., "Variations in the Interplanetary Magnetic Field: *Mariner II*, I: Observed Properties," *J. Geophys. Res.*, Vol. 71, pp. 5509-5531, 1966.
28. Ness, N. F., Scarce, C. S., and Cantarano, S., "Preliminary Results from the *Pioneer VI* Magnetic Field Experiment," *J. Geophys. Res.*, Vol. 71, pp. 3305-3313, 1966.
29. Jokipii, J. R., "Cosmic-Ray Propagation: I. Charged Particles in a Random Magnetic Field," *Astrophys. J.*, Vol. 146, pp. 480-487, 1966.
30. Blackman, R. B., and Tukey, J. W., *The Measurement of Power Spectra*. Dover Publications, New York, 1958.
31. Colburn, D. S., and Sonett, C. P., "Discontinuities in the Solar Wind," *Space Sci. Rev.*, Vol. 5, pp. 439-506, 1966.
32. McCracken, K. G., and Ness, N. F., "The Collimation of Cosmic Rays by the Interplanetary Magnetic Field," *J. Geophys. Res.*, Vol. 71, pp. 3315-3318, 1966.
33. Bartley, W. C., Bukata, R. P., McCracken, K. G., and Rao, U. R., "Anisotropic Cosmic Radiation Fluxes of Solar Origin," *J. Geophys. Res.*, Vol. 71, pp. 3297-3304, 1966.
34. Smith, E. J., Davis, L., Jr., Coleman, P. J., Jr., and Sonett, C. P., "Magnetic Measurements Near Venus," *J. Geophys. Res.*, Vol. 70, p. 1571, 1965.
35. Ness, N. F., "The Earth's Magnetic Tail," *J. Geophys. Res.*, Vol. 70, pp. 2989-3005, 1965.
36. Urey, H. C., "Boundary Conditions for Series of the Origin of the Solar System," *Phys. Chem. Earth*, Vol. 2, p. 46, 1957.
37. MacDonald, G. J. F., "On the Internal Constitution of the Inner Planets," *J. Geophys. Res.*, Vol. 67, p. 2945, 1962.
38. Lyttleton, R. A., "On the Internal Structure of Planet Mars," *Monthly Notices Roy. Astron. Soc.*, Vol. 129, p. 21, 1965.

## Bibliography

- Akasofu, S.-I., "Dynamic Morphology of Auroras," *Space Sci. Rev.*, Vol. 4, pp. 498-540, 1965.
- Akasofu, S.-I., and Chapman, S., "The Development of the Main Phase of Magnetic Storms," *J. Geophys. Res.*, Vol. 68, pp. 125-129, 1963.
- Axford, W. I., "Interaction Between the Solar Wind and Earth's Magnetosphere," *J. Geophys. Res.*, Vol. 67, pp. 3791-3796, 1962.
- Axford, W. I., Petschek, H. E., and Siscoe, G. L., "Tail of the Magnetosphere," *J. Geophys. Res.*, Vol. 70, pp. 1231-1236, 1965.
- Colegrove, F. D., and Franken, P. A., "Optical Pumping of Helium in the  $^3S_1$  Metastable State," *Phys. Rev.*, Vol. 119, No. 2, pp. 680-690, July 15, 1960.



## Bibliography (contd)

- Coleman, P. J., Jr., Smith, E. J., Davis, L., Jr., and Jones, D. E., "Measurements of Magnetic Fields in the Vicinity of the Magnetosphere and in Interplanetary Space: Preliminary Results from *Mariner IV*," in *Space Research VI*. Interscience Publishers, a division of John Wiley and Sons, New York, 1966.
- Coleman, P. J., Jr., Davis, L., Jr., Smith, E. J., and Jones, D. E., "Variations in the Polarity Distributions of the Interplanetary Magnetic Field," *J. Geophys. Res.*, Vol. 71, pp. 2831-2839, 1966.
- Dessler, A. J., and Fejer, J. A., "Interpretation of  $K_p$  Index and M-Region Geomagnetic Storms," *Planetary Space Sci.*, Vol. 11, pp. 505-511, 1963.
- Dessler, A. J., and Walter, G. K., "Hydromagnetic Coupling Between Solar Wind and Magnetosphere," *Planetary Space Sci.*, Vol. 12, pp. 227-234, 1964.
- Fairfield, D. H., and Cahill, L. J., Jr., "Transition Region Magnetic Field and Polar Magnetic Disturbances," *J. Geophys. Res.*, Vol. 71, pp. 155-169, 1966.
- Kellogg, P. J., "Flow of Plasma Around the Earth," *J. Geophys. Res.*, Vol. 67, pp. 3805-3811, 1962.
- McCracken, K. G., "The Cosmic-Ray Flare Effect: 3. Deductions Regarding the Interplanetary Magnetic Field," *J. Geophys. Res.*, Vol. 67, pp. 447-458, 1962.
- Ness, N. F., Searce, C. S., and Seek, J. B., "Initial Results of the *IMP-1* Magnetic Field Experiment," *J. Geophys. Res.*, Vol. 69, pp. 3531-3569, 1964.
- Patel, V. L., and Dessler, A. J., "Geomagnetic Activity and Size of Magnetospheric Cavity," *J. Geophys. Res.*, Vol. 71, pp. 1940-1942, 1966.
- Siscoe, G. L., Davis, L., Jr., Smith, E. J., Coleman, P. J., Jr., and Jones, D. E., "Magnetic Fluctuations in the Magnetosphere: *Mariner IV*," *J. Geophys. Res.*, Vol. 72, pp. 1-16, 1967.
- Spreiter, J. R., and Jones, W. P., "On the Effect of a Weak Interplanetary Magnetic Field on the Interaction of the Solar Wind and Magnetosphere," *J. Geophys. Res.*, Vol. 68, pp. 3555-3564, 1963.
- Spreiter, J. R., Summers, A. L., and Alksne, A. Y., "Hydromagnetic Flow Around the Magnetosphere," *Planetary Space Sci.*, Vol. 14, pp. 223-253, 1966.
- Stirling, K. H., *Some Large-Scale Variations in the Interplanetary Magnetic Field Observed by Mariner IV Spacecraft and Their Relationships to Geomagnetism*, M.S. Thesis. Brigham Young University, Provo, Utah, 1966.
- Smith, E. J., "Interplanetary Magnetic Fields," in *Space Physics*, pp. 350-396. Edited by D. P. LeGalley and A. Rosen. John Wiley and Sons, New York, 1964.
- Wilcox, J. M., "On a Possible North-South Asymmetry in the Solar Wind," *Irish Astron. Soc.*, Vol. 7, pp. 82-84, 1965.
- Wilcox, J. M., "Solar and Interplanetary Magnetic Fields," *Science*, Vol. 152, pp. 161-166, 1966.
- Wilcox, J. M., and Ness, N. F., "Solar Source of the Interplanetary Sector Structure," *Solar Phys.*, Vol. 1, p. 437, 1967.

## VIII. Solar Plasma Probe

### A. Introduction

The solar plasma probe (SPP) experiment was conducted under the direction of Professor Herbert S. Bridge and Dr. Alan J. Lazarus of MIT, and Dr. Conway W. Snyder of JPL. Similar probes have been carried on *Explorer* and *Pioneer* missions. The SPP was designed to collect protons of the solar wind with energies between 30 and 10,000 eV. The detector was divided into three equal pie-shaped sectors to provide directional information on the flow of the solar wind. The kinetic energy of the plasma was determined by measuring successively the flux within each of 32 logarithmically spaced energy intervals that covered the total energy range.

About 1 wk after launch, approximately 17:00 UT on Dec. 6, 1964, the plasma-probe high-voltage monitor indicated that the instrument's high voltage was degrading. The high-voltage waveform became increasingly distorted due to an opening resistor. Although the instrument continued to operate, it supplied data in a form that required complex and time-consuming analysis, and

part of the time it did not make any measurements at energy levels where useful data might have been obtained.

### B. Purpose

The objectives of the SPP experiment were to:

- (1) Determine the positive ion flux density in the range  $5 \times 10^{-5}$  to  $5 \times 10^{-9}$  particles  $(\text{cm}^2 \text{ s})^{-1}$ .
- (2) Measure the energy spectrum of the solar wind in the range of 30 eV to 10 keV.
- (3) Determine arrival direction of the plasma flux within a cone of 15-deg half-angle centered 10 deg off the probe-sun line.
- (4) Measure the temporal and spatial variations of the above quantities.
- (5) Correlate the above measurements with those of the magnetic field, since the physical state of the plasma is intimately related to that of the magnetic field.

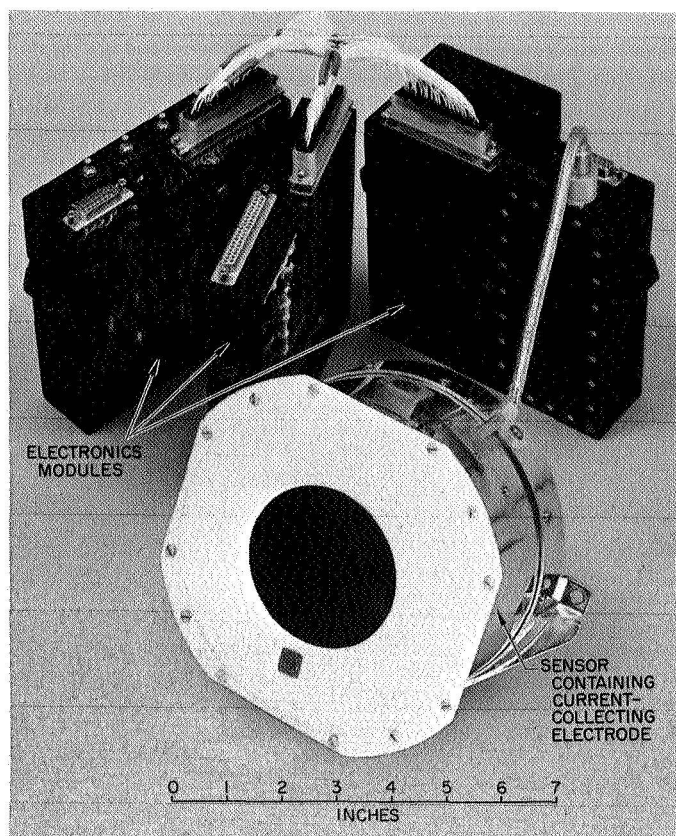


Fig. VIII-1. Solar plasma probe

### C. Instrument

The SPP, Fig. VIII-1, weighed 6.1 lb and required an average of 2.65 W of power for operation. The plasma-measurement circuit, basically a narrow-band ac amplifier and a synchronous detector, responds to the intermittent dc component of the positively charged part of the plasma current that enters the sensor. The detector, a modified Faraday current cup, Fig. VIII-2, was oriented so that its axis was 10 deg from the spacecraft-sun line. Positive ions and electrons enter the cup and produce a current on the collector plates at the back of the cup. A positive voltage applied to the modulator grid switches between two levels,  $V_1$  and  $V_2$ , and modulates that portion of the collector current due to positive ions which enter the sensor with energy/charge between  $V_1$  and  $V_2$  electron volts. The pulsating component of the current striking the collector plates was capacitively coupled to a logarithmic amplifier with a useful operating range between  $\sim 5 \times 10^{-12}$  and  $3 \times 10^{-9}$  A. Each current measurement was converted to digital form and supplied to the telemetry system in real time. The collector plates were 120-deg circular sectors, considerably

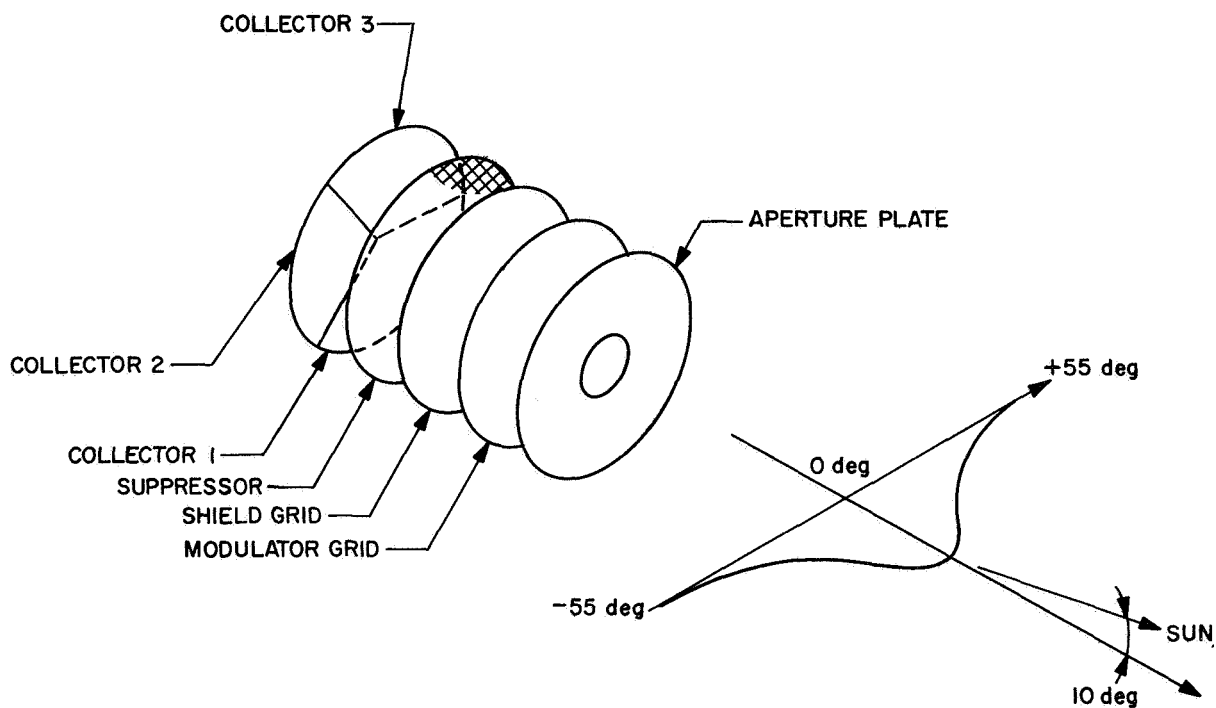
larger than the 3-in. circular aperture of the cup. The relative current from the three collectors was used to give an indication of the flow direction of the plasma.

Modulator grid voltages  $V_1$  and  $V_2$  were varied to produce a sequence of 32 logarithmically related energy windows, shown in detail in Fig. VIII-3. The time scale is appropriate for low bit rate data, i.e., after Jan. 3, 1965. A typical decay curve for the dc voltage is shown to indicate the effect of the high-voltage supply failure. The decay time became longer as the flight progressed. The measurement sequence was arranged so that at first the currents from the three collectors were summed together as the modulator voltage was stepped through a set of 16 *low* windows, shown as the dotted voltage intervals in Fig. VIII-3. Then the same 16 energy windows were again scanned, but this time the current from each individual collector was measured.

The *low* measurement sequence was followed by eight calibration and identification measurements to check the gain of the preamplifier for each collector plate and measure the high voltage at a level equal to step 7 of the voltage sequence. The whole set of 72 measurements was then repeated, but all of the 16 energy windows were shifted upward by the fourth root of 2 in order to form the *high* sequence shown in Fig. VIII-3. Thus, a total of 32 energy windows were sampled by the instrument. Since the data were telemetered in real time, the time taken to complete a sequence of measurement depended upon the telemetry bit rate. After Jan. 3, 1965, it took 30.24 min to complete a sequence of measurements.

**1. Circuits.** The measurement chain consisted of three preamplifiers, a summing amplifier, bandpass filter, a logarithmic compression amplifier, a synchronous detector, and temporary storage, Fig. VIII-4. The gated preamplifiers were low-noise linear amplifiers which amplified currents in the range  $10^{-12}$  to  $10^{-7}$  A and produced a proportional voltage output. The outputs of the individual preamplifiers were selected by appropriate logic. Each gated preamplifier was used with a corresponding collector, and the amplified outputs were added linearly by the summing amplifier. The bandpass filter was provided to limit the bandwidth of the system to a center frequency of 2 kHz and to improve the signal-to-noise figure.

The synchronous detector produced a dc output proportional to the amplitude of the ac signal leaving the logarithmic compression amplifier which took the output of the filter and amplified it in a non-linear manner. A



THE WAVEFORM OF THE MODULATING VOLTAGE IS INDICATED NEAR THE MODULATOR GRID; EFFECTIVE AREA OF THE SENSOR IS  $11.4 \text{ cm}^2$

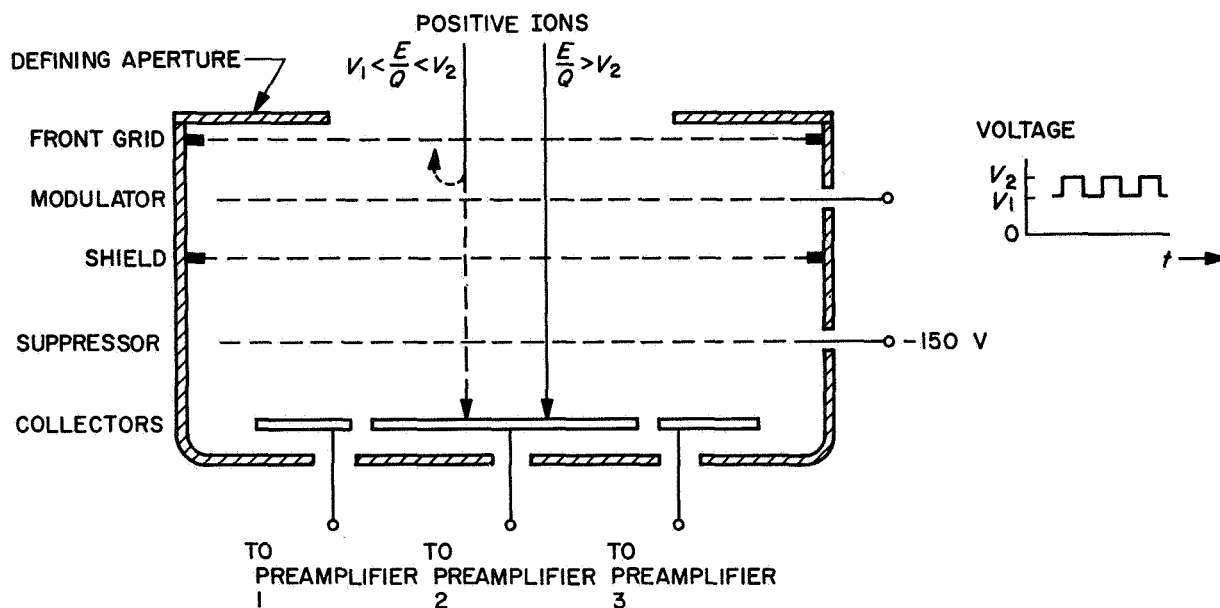


Fig. VIII-2. Plasma detector cup

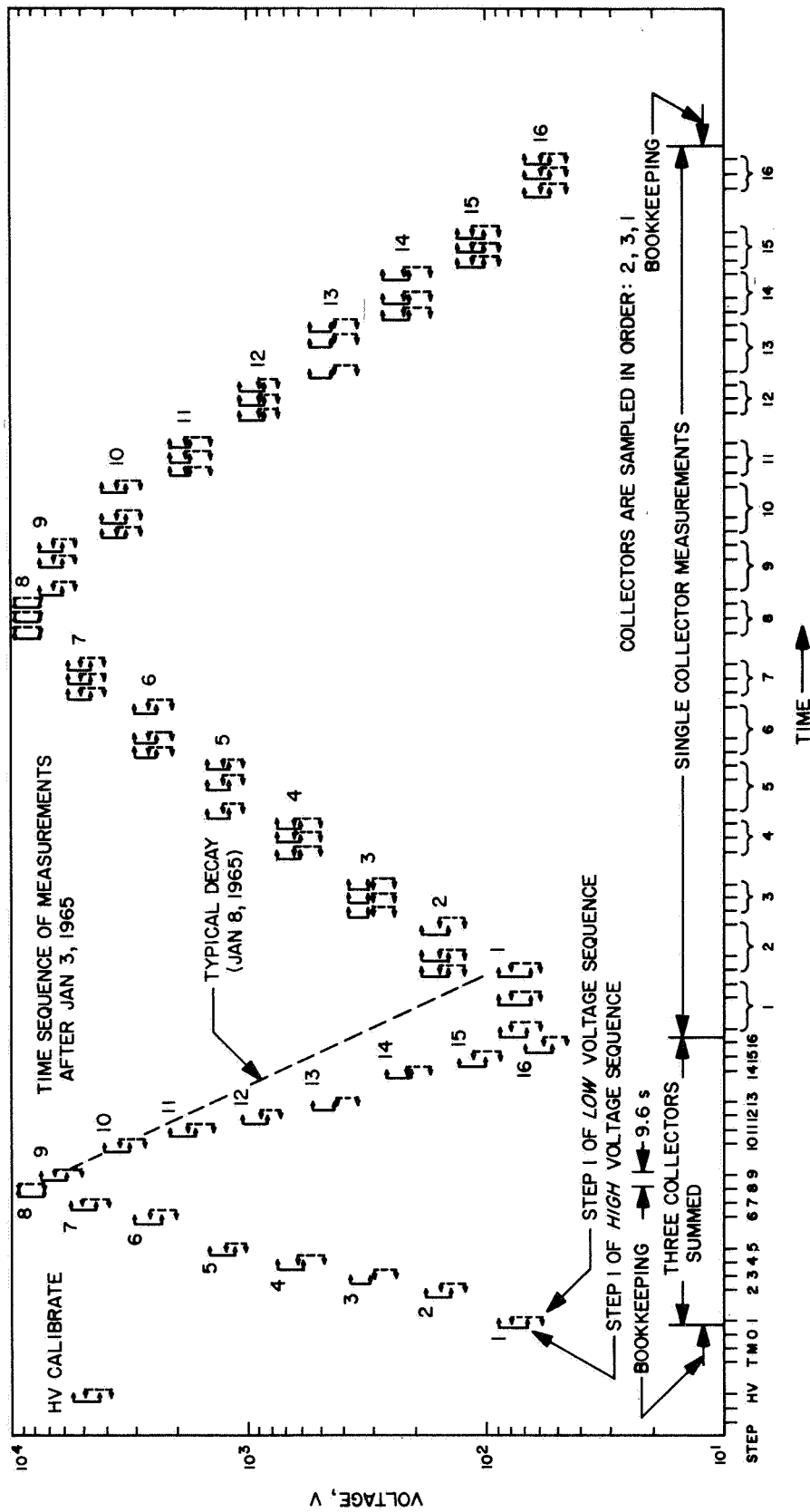


Fig. VIII-3. Sequence of energy measurements

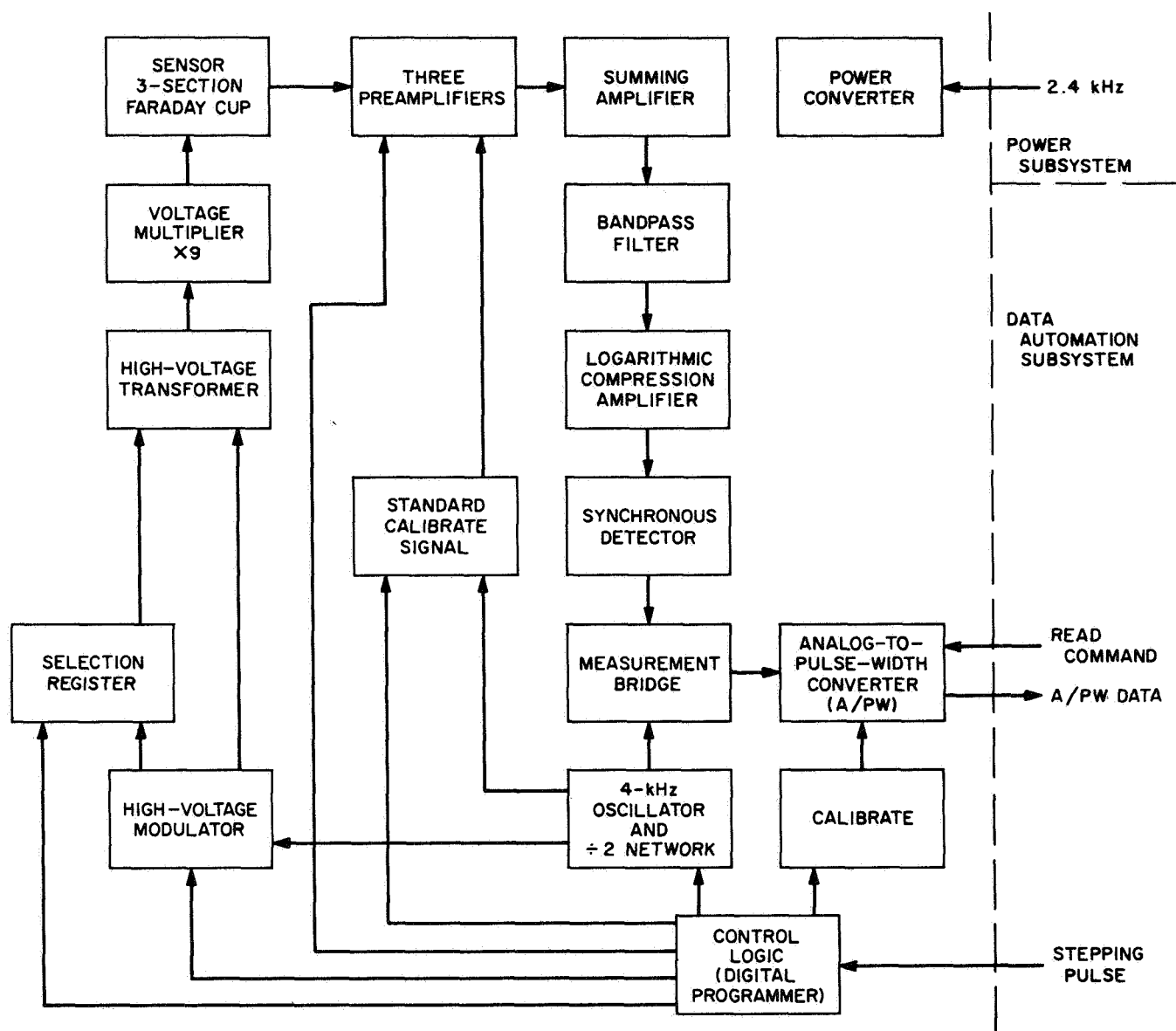


Fig. VIII-4. Solar plasma probe, functional block diagram

variation of  $10^{-5}$  in the output of the filter was compressed to a variation of only 5 V at the compression amplifier output. The synchronous detector acted as a narrow-band filter passing only that ac signal from the compression amplifier which had both the same frequency and phase as the modulator signal, thereby reducing the output due to noise from the compression amplifier. The detector output was a dc signal in the range 0 to +6 V.

The bridge gates acted as combined bilateral switches and as current amplifiers. These gates served to transfer

the output signal level of the measurement chain to a large value capacitor for level storage. The time constant during the *on* period was low so that the output responded to the signal level during the last portion of the period, because the level of the high voltage was not constant until the last portion of the measurement period.

The analog-to-pulse-width (A/PW) converter was really an analog-to-pulse-delay converter. The readout operation was triggered by a command pulse and the readout consisted of another pulse delayed by a time proportional to the input level.

The 4-kHz oscillator and divide-by-2 network were the basic timing source for the entire instrument. An astable multivibrator operating at 4 kHz drove a flip-flop to produce a 2-kHz square wave. The oscillator frequency and stability directly affected the performance of the measurement chain. Adjustment of the oscillator frequency was critical because of the phase sensitivity of the synchronous demodulator combined with the phase shift of the bandpass filter. Temperature stability of the oscillator was somewhat improved by the addition of a sensistor temperature compensation circuit to correct high temperature frequency variations. A capacitor-discharge-type starting circuit was originally eliminated from the oscillator, but was reincorporated when starting problems were encountered in the first unit. Eventually the starting problem was traced to an intermittent timing capacitor and was not associated with lack of starting circuit.

The high-voltage driver circuits counted down the oscillator frequency by a 2:1 factor and provided driving and sync signals to the high-voltage output chopper and to the synchronous detector. The high-voltage circuits were turned off while the sync signal continued to be supplied to the synchronous detector. This allowed the standard signal self-check circuits to monitor gain without interference from signals generated in the cup.

A gating circuit was provided to program control the high-voltage driver output stages. The gates were arranged to allow the high voltage to turn on only during the measurement and high-voltage check steps of the program. These circuits were also used by the high-voltage disable provision in the probe, which allowed an external connection between two pins to disable the high-voltage output.

During the design of the high-voltage circuits, a primary concern was to reduce their power consumption. A potentially more reliable and shielded transformer was developed for this circuit, but had higher consumption of power than with the unshielded transformer; the latter had originally been designed for the instrument flown on an *EOGO* satellite. It was concluded that a transformer designed to duplicate the efficiency of this transformer and yet make use of more reliable construction techniques could not meet the size limitations. Thus, the NES2245 transformer was chosen for the system. During flight unit screening, a high-voltage breakdown was experienced in several units. As a result, the size of this unit was increased slightly to provide

more insulation. In addition, these transformers were encapsulated by moulding in an epoxy resin.

The high-voltage rectifier chain was redesigned to provide 32 voltage steps. Figure VIII-5 illustrates the *EOGO* and the SPP high-voltage rectifiers for comparison. The number of voltage multiplier steps was doubled to provide approximately half the percentage modulation for a given dc level. This required a change in turns ratio in the transformer to provide approximately half the *EOGO* voltage output. The maximum reverse voltage applied to the diodes was reduced from 2 kV in *EOGO* to 1.1 kV and the maximum voltage across the capacitors was reduced from 4 to 2.2 kV. A reduction in the capacitor values and series-limiting resistors provided a faster rise time in the overall output level. However, even with these changes an 80-ms time period was necessary to allow a reasonably constant output level to be reached.

The bleeder resistor was increased in value from 100 to 300 M $\Omega$  to minimize power consumption. In addition, a specially designed high-voltage resistor rated at 15 kV

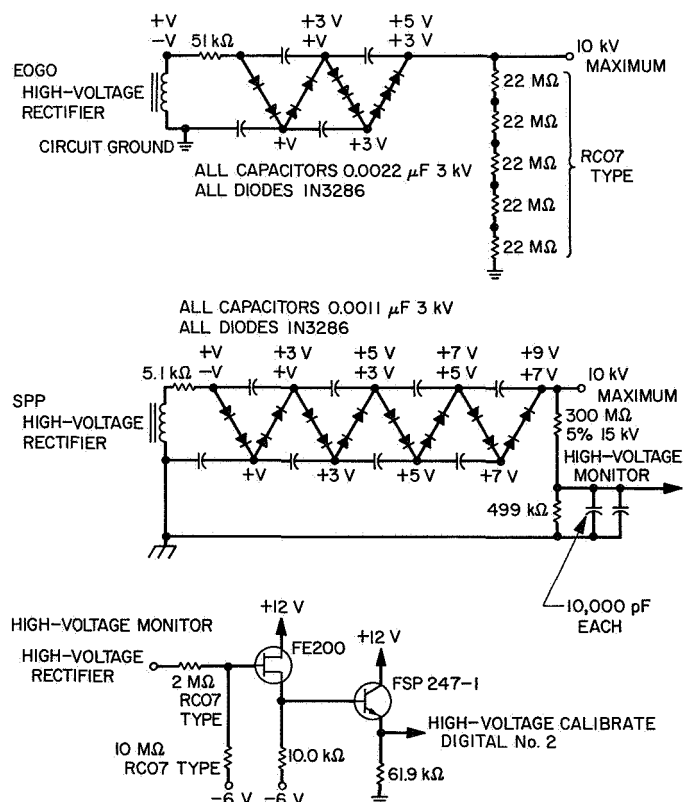


Fig. VIII-5. *EOGO* and SPP high-voltage rectifier chains and high-voltage monitor

was chosen to increase reliability. The bleeder resistor formed part of a voltage-divider network to allow the high-voltage dc level to be monitored by the high-voltage self-check. Provision was made to install a 100 k $\Omega$ , 10 kV-rated resistor in series with the output to limit arc current when an external arc occurred, but no suitable resistor could be obtained for this application.

It was found during preliminary testing that an arc in the high-voltage circuits would cause failure of transistors in unrelated circuits. This problem was aggravated by the fact that the rectifier board had not been conformally coated to provide high-voltage insulation. The cause of these failures was traced to the grounding system originally used. All circuits, including the high-voltage rectifier system, were connected to the chassis ground at only one point, the preamplifier. As a result, a long path existed for the arc current if the high voltage arced to the chassis, thus overstressing other circuits tied to this ground path. The solution to this problem was to ground the high-voltage rectifiers to the chassis within the high-voltage housing.

The selection register and high-voltage regulator were essentially identical to the *EOGO* circuits. The only major change was to provide a circuit to offset the voltage levels by a half step to provide a total of 32 levels. This was done by alternately gating one of two Zener diodes into the circuit to provide two different voltage levels. The resistor values and the Zener diode voltages in this circuit were selected for each unit to provide the desired output voltages for each step. The variation in output with temperature was believed due to the temperature variation of the Zener diodes. A 33- $\Omega$  resistor was put in series with the output of the regulator for the purpose of improving the high-voltage output waveform. Variation of this resistor value primarily affects the level of only the highest voltage steps.

A system of three monostable multivibrators provided the clock triggers and enable gates required in the probe operation. A multivibrator extended the 10- $\mu$ s trigger pulse from the spacecraft to a 2-ms plasma clock pulse. This pulse was needed to enable the gates of the flip-flops in the programmer. Two additional multivibrators provided an 80-ms enable gate delayed by 200 ms from the plasma clock. The delay was required to allow time for the preamplifier gates and regulator voltage levels to settle after being switched at the plasma clock rate. The 80-ms time was a compromise time between that required by the high-voltage circuits to reach full output level and the length of time that the power

storage capacitor for the high voltage could be discharged. It was found important that the diamond gates be derived from a gate with a minimum delay in turnoff time. This was to assure that the diamonds were gated off simultaneously with the high voltage and sync signals.

**2. Digital programmer.** The basic design of the circuit elements in the programmer was essentially the same as in *EOGO*. The time constant of the flip-flop gates was reduced by a factor of 5 to allow use of  $\frac{1}{8}$ -W resistors and to provide more reliable triggering with a short trigger pulse. Resistor values in various gates were changed to meet new circuit requirements. The logic arrangement for the counter trigger circuits was completely revised. It was necessary to revise the programmer to provide additional steps for the standard signal self-check and to eliminate possible hang-up conditions in the logic. A 66-step program was developed to meet these requirements with 15 high-voltage steps. An additional requirement was then made that the program contain steps equal to a multiple of four. The logic was revised to provide a 72-step program with 16 voltage levels. This program provided a total of eight possible self-check steps with six steps being used actively.

The logic for the programmer was designed such that there was no counter step or flip-flop combination which could cause the counter to hang up or from which the programmer would not eventually resume its proper sequence. In this design, the probe functioned during all program cycles and the levels of operation of several circuits were changed. Thus the total program was really 144 steps in length. These changes resulted in an offset in the 16 high-voltage steps to provide a total of 32 different levels and provide 2 different standard signal input levels. The marker output indicated which portion of the program was being used.

**3. Standard signal self-check.** The standard signal circuit was a new design for the SPP. The original circuit was provided to check the gain of the measurement chain for each preamplifier at  $10^{-9}$  A input level. Later the circuit was revised to provide a two-point check for each preamplifier at approximately  $3 \times 10^{-9}$  and  $4 \times 10^{-11}$  A input. The standard signal circuit made use of a small resistor common to all three dc return circuits of the cup input. No crosstalk between preamplifiers resulted from this resistor because the preamplifier feedback circuit held the input voltage close to zero signal level. This resistor was used to apply test signals to the probe from the bench checkout equipment. The transistor circuits of the standard signal input system



provided a cascade of three switching circuits to reduce the signal level during gate cutoff to a level below the minimum signal. During the fourth program step immediately preceding the standard signals, Preamplifier 2 was gated on. The output signal during this period thus indicated the noise level of the system with the cup high voltage and standard signal circuits gated off.

**4. High-voltage self-check.** The high-voltage self-check circuit was first designed to monitor the input dc voltage to the high-voltage driver. The design was later changed to a system which directly monitored the output of the high-voltage rectifier system. The output bleeder resistor, a voltage divider, reduced the average dc level of the high voltage to a workable level. A field-effect source follower and an emitter follower provided near unity gain for this dc signal level; see Fig. VIII-5. This level is gated into the telemetry output during the high-voltage self-check period, providing a telemetry indication of the voltage level of the step checked. The time constant of the circuit was sufficiently short that the output was representative of the voltage level at the end of the 80-ms measurement period. The step which was checked was changed from the highest step to the third from the highest step because of decay in the top step. Two different levels were checked for this step depending on the cycle of the programmer.

**5. Temperature and marker check.** The temperature, marker, and the high-voltage self-check provided dc levels directly to the output of the probe independent of measurement chain circuits. The temperature circuit provided a dc level to the output which is a function of the temperature of the sensor sensing-element located near the center of the Digital 2 board in the 32A3 tray. The function of the marker was to provide two different fixed levels to serve as references and to indicate in which of two program cycles the probe was operating during the previous measurement steps. The temperature, marker, and high-voltage levels were gated to the output storage capacitor by a diamond circuit separate from that of the measurement chain. The output from the measurement chain was not gated on during these periods. The outputs from the self-check circuits were combined by a non-additive type mixer. The gate circuits were arranged to rise to +6 V when off. The bridge was gated on during the last step and the output was at a high level. This high output resulted in a maximum signal output from the A/PW converter. The spacecraft data automation subsystem counter normally overflowed on this high signal and produced a

zero output, which was convenient for data reduction because it was easy to locate.

**6. Power supply.** A large amount of decoupling was required in the design of various circuits to compensate for lack of load regulation in the power supply. In addition, the circuits were susceptible to spikes still present from the 2.4-kHz power input. The use of a power storage circuit in the -30-V supply considerably reduced the peak power consumption of the system, but the design of the high-voltage circuits was not optimized for such operation, and the desired level of the highest voltage step was beyond the present design capability.

## D. Results

The results have been previously reported by Lazarus, Bridge, Davis, and Snyder, Ref. 1.

The proton flux was calculated as follows:

$$\text{Flux (particles/cm}^2 \text{ s)} = \frac{1}{Aq} \sum_{j=1}^N I_j$$

where

$A$  is the effective area of the detector (11.4 cm<sup>2</sup>).

$q$  is the charge of a proton.

$I_j$  is the total current measured in the  $j$ th energy step corrected for the overlap of the windows by assuming that the spectrum is flat.

$N$  is the channel at which the dip between the proton and alpha particle peaks occurs. (In this calculation, the energy steps have been rearranged in order of increasing energy.)

The density was then calculated by dividing each term of the sum given above by a velocity corresponding to the mean value of the voltage for that step. The bulk velocity was then calculated by dividing the flux by the density.

**1. Interplanetary data.** Figures VIII-6 through -8 show 3-h averages of the proton flux, density, and bulk velocity. The points A and B along the time axis of the density graphs mark points of equal solar longitude assuming a solar sidereal rotation period of 25 and 25.5 days, respectively. The time associated with a sequence of measurements is the time (UT) at which the first measurement of the data sequence was received on the earth. The main features confirm those observed by

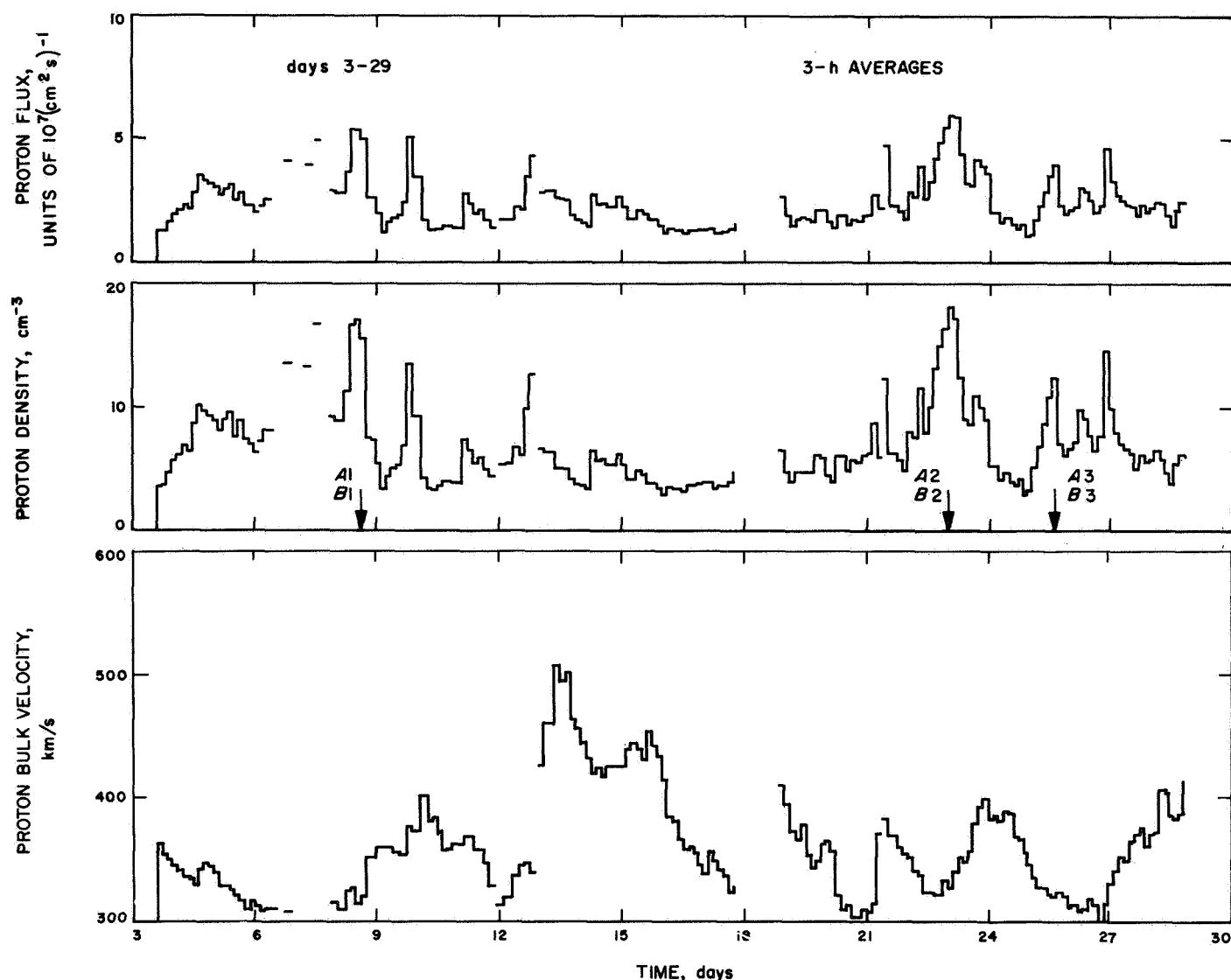


Fig. VIII-6. Days 3-29, 3-h averages

Snyder and Neugebauer on *Mariner II*, Refs. 2-4: (1) An  $\sim 27$ -day general periodicity (as viewed by the spacecraft), though clearly not all features repeat in the density and bulk velocity, and (2) a typical sequence of an increase in density followed by an increase in bulk velocity. If one considers the situation in a frame of reference rotating with the sun, the region of higher density is encountered before the spacecraft penetrates a region of higher velocity. The fact that this sequence of events tends to recur when the spacecraft returns to the same solar longitude suggests that a quasi-steady transition between streams of different velocity has been established.

**2. Results near Mars and near the earth.** The spacecraft traversed the earth's magnetosphere on the dawn

side roughly in the ecliptic plane and at an angle of  $\sim 111$  deg to the sun-earth line. Figures VIII-9a through -9d show spectra taken during the spacecraft passage through the earth's magnetosphere. Inside the magnetopause, typical currents obtained were usually less than  $5 \times 10^{-12}$  A, which appeared to be the noise level at that time. (Outgassing of the sensor was probably still contributing to the noise level.) There were occasional peaks of  $2 \times 10^{-11}$  A; see Fig. VIII-9a. The observed currents fluctuated rapidly and the spectrum broadened to that shown in Fig. VIII-9b, which was associated with the transition region. Figures VIII-9c and -9d show spectra just inside and outside of the shock boundary at a geocentric distance of  $\sim 35$  earth radii. The lower energy peak corresponds to protons and the higher energy peak

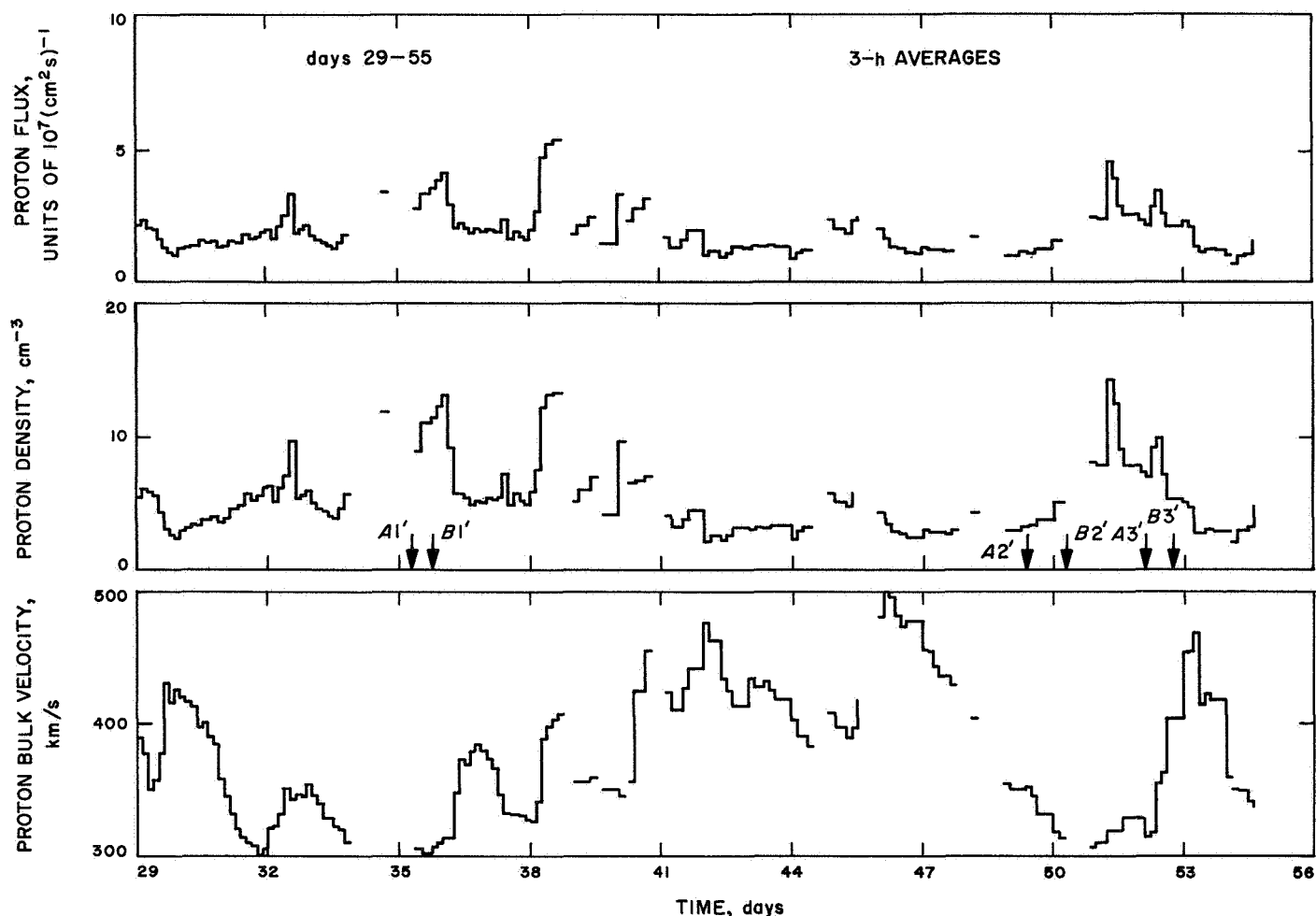


Fig. VIII-7. Days 29-55, 3-h averages

is ascribed to  $\alpha$  particles moving with the same bulk velocity as the protons. Conditions fluctuated rapidly near the shock boundary and Fig. VIII-9c may well be outside the shock.

Figure VIII-10 shows the trajectory of the spacecraft in the vicinity of Mars as viewed in the sun-Mars-spacecraft plane. (The plane rotates about the sun-Mars line during encounter and thus gives rise to the peculiar-looking trajectory.) The magnetopause corresponds to a scaled version of the earth's magnetopause assuming that the magnetic moment of Mars is 1/1000 that of the earth and taking into account the ratio of dynamic pressures observed near Mars and near the earth. Also shown in Fig. VIII-10 are spectra taken at various times during encounter. The failure in the high-voltage circuitry makes detailed interpretation of the spectra uncertain. Nevertheless, it is clear that there is always considerable flux observed.

If it is assumed that the topology of the Martian magnetosphere is similar to that of the earth and that the magnetic dipole moment of Mars is roughly aligned with its spin axis, the same earth-like sequence of *transition region* and *magnetopause* should have been seen as Mars was approached. Since there was no indication of a magnetopause, an upper limit can be placed on the magnetic dipole strength of Mars.

A magnetopause boundary shape was plotted in Fig. VIII-10 as obtained from magnetic field and plasma measurements taken near the earth by experiments on board *IMP-I*, Ref. 5. The data were scaled so that the magnetopause would be just tangential to the *Mariner* trajectory. The average bulk speed and density of the plasma during the *IMP* measurements were 300 km/s and 6 particles/cm<sup>3</sup>. From the first three plasma spectra shown in Fig. VIII-10, an average bulk velocity of 330 km/s and an average density of 0.8 protons/cm<sup>3</sup> was

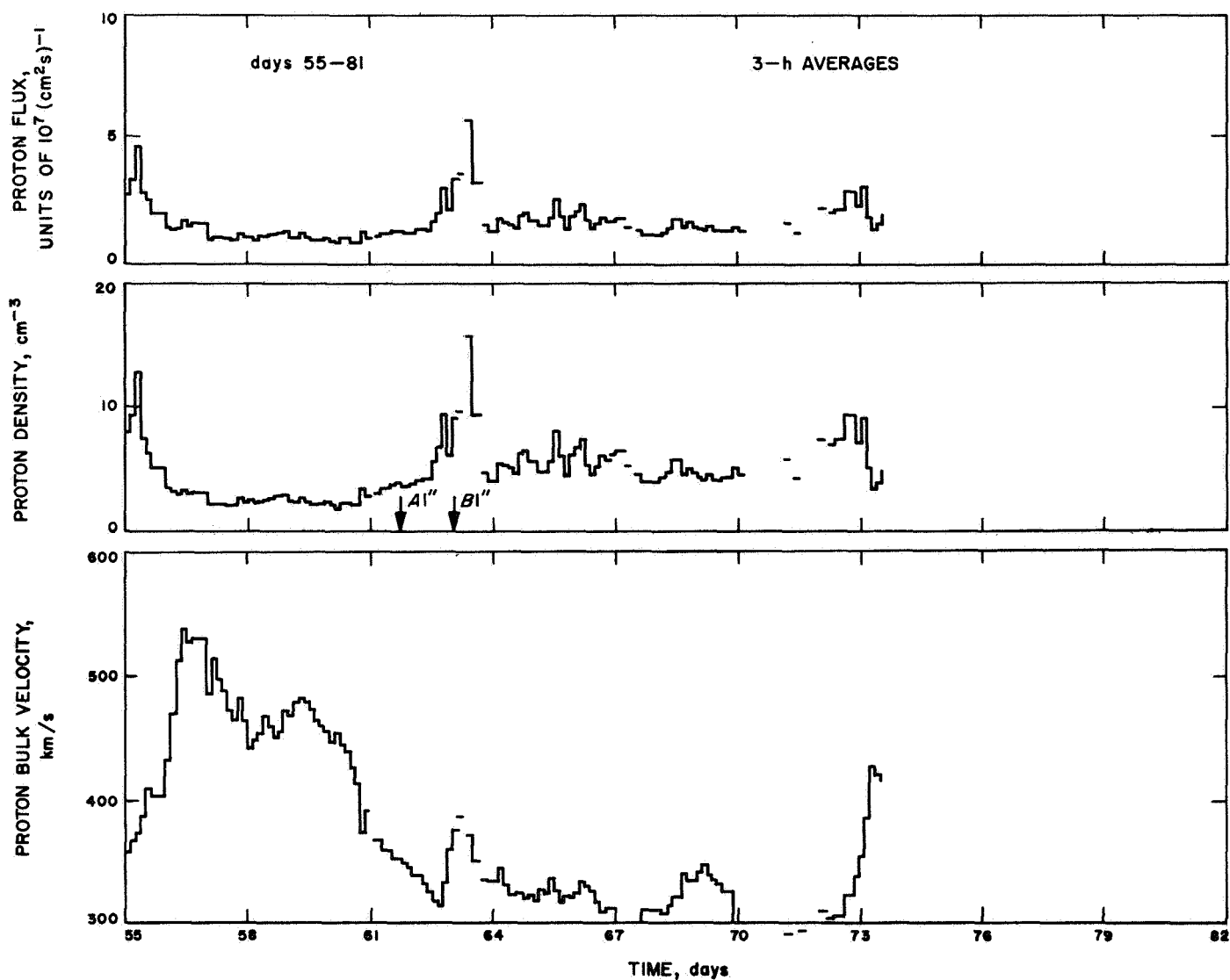


Fig. VIII-8. Days 55-81, 3-h averages

obtained. Thus the dynamic pressure at the time of encounter was about 1/9 the average value observed by IMP-1.

Considering only the relative sizes of the magnetopause, the magnetic moment of Mars must be less than 1/500 that of the earth; in addition, for a fixed magnetopause position, the estimate of the magnetic moment is proportional to the square root of dynamic pressure. In this case, this fact would further reduce the magnetic moment estimate by a factor of almost 3. The distortion of the spectra by the failure mentioned earlier makes an absolute determination of the particle density very difficult, and the actual density may well have been as much as twice the value reported above. Therefore it is felt that

a conservative upper limit on the dipole strength of Mars would be 1/1000 that of the earth.

It would have been possible to make a more definite statement about the magnitude of the Martian dipole strength had a transition region been detected. Examination of the data does not show the broad energy spectrum which is associated with the passage through the earth's transition region. However, due to the high-voltage failure, there was no firm knowledge of the plasma energy spectrum below the peak and hence the possibility cannot be ruled out that in fact a transition region was traversed. Consequently there was only justification in basing the conclusions on the non-detection of a Martian magnetosphere.

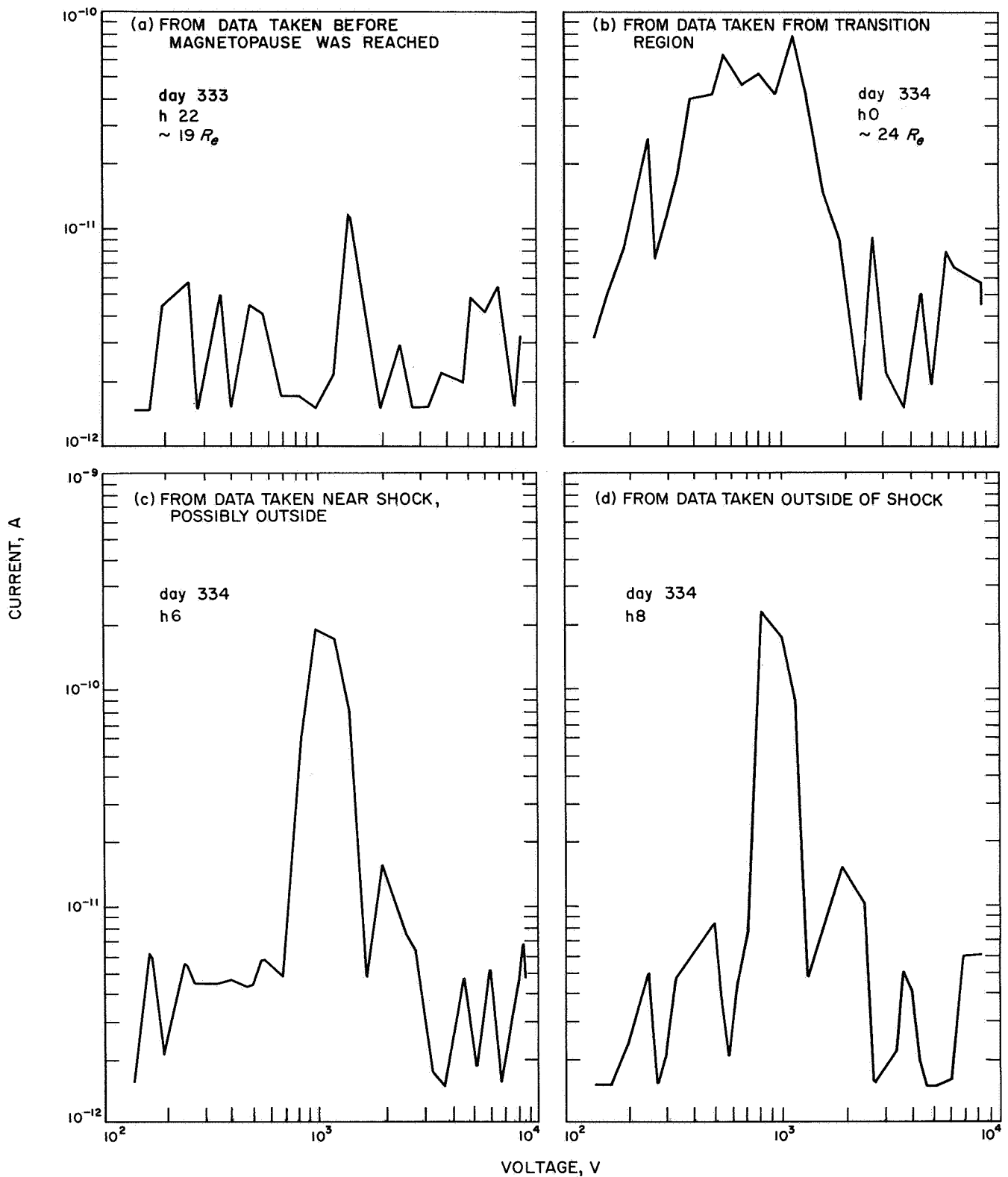
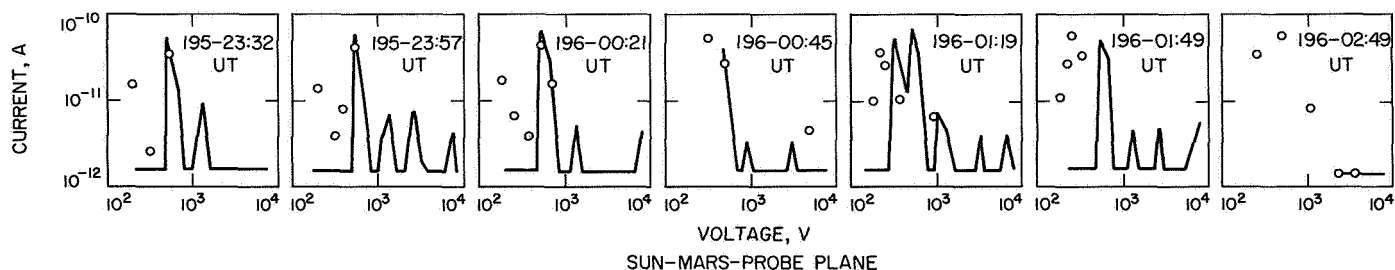


Fig. VIII-9. Spectra, days 333 and 334, current vs voltage



CIRCLED POINTS ARE DATA UNCORRECTED FOR THE EFFECTS OF THE HIGH-VOLTAGE SUPPLY FAILURE

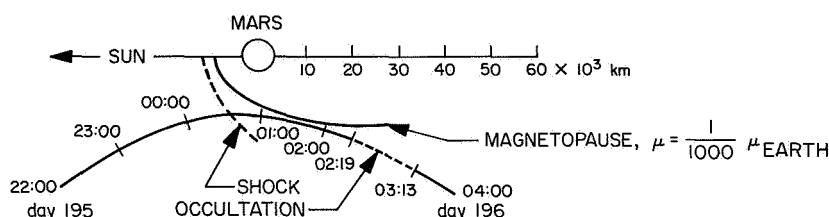


Fig. VIII-10. Individual spectra taken during Mars encounter, and sun-Mars-probe plane

**3. High-voltage supply failure.** On Dec. 6, 1964, a failure in the high-voltage supply occurred. The cause has been diagnosed as an open bleeder resistor in the high-voltage supply. In order to understand fully the analysis procedure for the remaining portion of the data, it is necessary to discuss in some detail the influence that the failure had on the operation of the instrument.

The effect of the high-voltage supply failure may be seen in Fig. VIII-3. After reaching the high points of the voltage sequence, specifically step 8 and the high-voltage calibration, the dc-voltage component did not follow the descending sequence of steps, but decayed in a roughly exponential fashion. This decay time is an inverse function of the temperature and consequently increased as the flight progressed making interpretation of the spectra increasingly uncertain. The modulator did provide the proper energy *windows*, but their dc level was determined by the extent of the decay. When the dc level had finally decayed to a value equal to or less than the dc level of the next step in the sequence, the dc level of that next step was established at its proper value. Thus, for the decay time illustrated in Fig. VIII-3, the upward going steps, after step 1, have their correct values. From the time of failure to Jan. 3, 1965, the steps were sampled at such a high rate that the dc voltage could not decay below an energy corresponding to the bulk velocity of

the plasma. After Jan. 3, 1965, the sampling rate was reduced by one quarter, and useful data was obtained.

The narrow energy spread of the plasma itself allowed a determination of the decay time. In the case shown in Fig. VIII-3, there was a peak in step 4 of the single collector sequence; but there was also a large peak at the time of step 15 of the *summed* sequence. Assuming that the peak of step 4 was genuine, the peak at the time of step 15 must indicate that the dc voltage had decayed to the point where its value would be appropriate for step 4.

On the downward going steps, when single collector measurements were being made, the collector 1 measurement would often be correct, while the data from the other two collectors clearly showed that the dc level was not steady. In order to take account of this effect, the data was corrected in the following manner: (1) for each of steps 4, 5, and 6, the collector currents were added together; (2) by using the data for the step containing the maximum current, the ratio of collector 1 current to that of collectors 2 and 3 was found; (3) these ratios were used to correct the currents observed in the downward going steps, assuming that the collector 1 current was correct; and (4) the current from steps 1, 2, 15, and 16 was discarded. These corrections increased the value of bulk velocity by about 10%.

## References

1. Lazarus, A. J., Bridge, H. S., Davis, J. M., and Snyder, C. W., "Initial Results from the *Mariner IV* Solar Plasma Experiment," *Space Res. VII*, pp. 1296-1305, Noord-Hollandsche Uitgevers-Mij., Amsterdam-C., N. Z. (North Holland Publishing Co., Amsterdam), 1965.
2. Snyder, C. W., and Neugebauer, M. M., "Interplanetary Solar Wind Measurements by *Mariner II*," *Space Res. IV*, pp. 89-113, 1966.
3. Neugebauer, M. M., and Snyder, C. W., "*Mariner II* Observations of the Solar Wind, 1. Average Properties," *J. Geophys. Res.*, Vol. 71, p. 4469, 1966.
4. Neugebauer, M. M., and Snyder, C. W., "*Mariner II* Observations of the Solar Wind, 2. Relation of Plasma Properties to the Magnetic Field," *J. Geophys. Res.*, Vol. 72, p. 1823, 1967.
5. Bridge, H., Egidi, A., Lazarus, A., and Lyon, E., "Preliminary Results of Plasma Measurements on IMP-A," *Space Res. V*, p. 969. Edited by King-Hele. Noord-Hollandsche Uitgevers-Mij., Amsterdam-C., N. Z. (North Holland Publishing Co., Amsterdam), 1965.

## Bibliography

- Anderson, H. R., et al., "Mariner IV Measurements Near Mars: Initial Results," *Science*, Vol. 149, p. 1226, 1965.
- Ness, N. F., and Lyon, E. F., "A Study of the Interplanetary Plasma," *J. Geophys. Res.*, Vol. 70, p. 2989, 1965.
- The Solar Wind*. Edited by R. J. Mackin, Jr., and M. M. Neugebauer. Pergamon Press, 1966.

## IX. Occultation Experiment

### A. Introduction and Purpose

The *Mariner IV* occultation experiment was conducted by a team of investigators from the Jet Propulsion Laboratory, Cornell University, and Stanford University. Dr. Arvydas Kliore, member of JPL's Systems Analysis Section, was principal investigator. The co-investigators were D. L. Cain and G. S. Levy of JPL; V. R. Eshleman and G. Fjeldbo of Stanford; and F. D. Drake of Cornell. Specific contributions concerned with model studies and analysis of results were made by G. Fjeldbo, W. C. Fjeldbo, and V. R. Eshleman of Stanford. Discussions, analyses, and results of the occultation experiment have been well documented by members of the investigating team. These primary sources are listed as references for the material contained in this section. Other references and bibliographies can be obtained by examining these reports and papers.

For many years, astronomers and space scientists have been concerned about the nature of the atmosphere and ionosphere of Mars. Before the *Mariner IV* occultation experiment, knowledge of the atmospheric properties of the Mars environment, such as surface pressure, density, and scale height, was presumptive and poorly defined.

Estimates of the surface pressure, based on spectroscopic observations of weak and strong CO<sub>2</sub> absorption bands, were between 10 and 40 mbars (Refs. 1, 2). Some models of the Martian ionosphere estimated the peak electron density to be between 10<sup>5</sup> and 2 × 10<sup>7</sup> electrons/cm<sup>3</sup> (Ref. 3).

A capsule entering the Martian atmosphere would provide the best opportunity for direct measurement of constituents and local properties. However, since the flight of atmospheric entry capsules was not anticipated before 1969, the desired information would not be available early enough for use in the design of the lander capsules necessary for early biological experiments. As an alternative, in the spring of 1964 Dr. Kliore and his co-investigators proposed the *Mariner IV* occultation experiment (Ref. 4) as a means of deriving significant information by observing the refractive effects of the Martian atmosphere on the spacecraft radio signal. As shown in Fig. IX-1, telemetry signals from a spacecraft flown in a Mars occultation trajectory would traverse the atmosphere and ionosphere of the planet just before and immediately after occultation. Some of the physical properties of the Martian atmosphere could be inferred from the changes caused in the frequency,



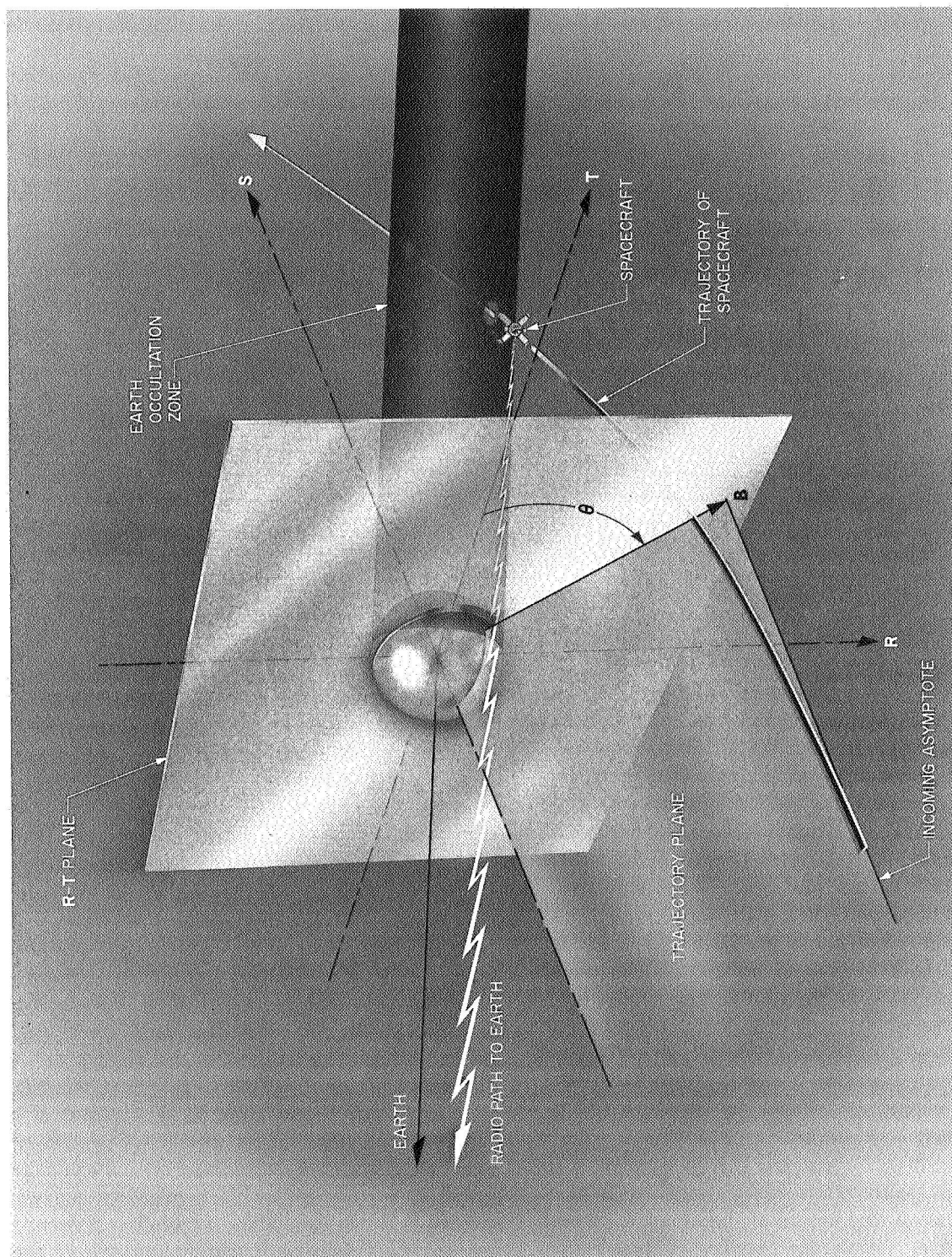


**Fig. IX-1. Geometry of occultation**

phase, and amplitude of the telemetry signals. The precision radio tracking techniques required to perform the experiment were within the capability of the Deep Space Instrumentation Facility operated by NASA and JPL. The only change in mission plans required to conduct the occultation experiment was a slight adjustment of the originally planned encounter trajectory.

As the spacecraft approached the occultation zone, the presence of an ionosphere and atmosphere would cause the velocity of propagation of the radio signal to change from that in free space. The radial gradient in the effective index of refraction between free space and the planetary surface would cause the radio beam to be refracted slightly from a straight-line path. The effect of change in the velocity of propagation of the radio signal and the effect of radio-beam refraction would cause the phase path of the signal at any time to differ from what would be observed in the absence of an atmosphere and ionosphere. If the geometry of the spacecraft trajectory and the spatial characteristics of the index of refraction were known, the phase change could be computed. If the geometry and the amount of phase change were known at any given time, the spatial characteristics of the index of refraction, and therefore of the atmosphere and ionosphere, could be computed, or inferred by model-fitting (Refs. 5, 6). For a successful experiment, the total change in the radio signal's phase or frequency due to all effects, other than penetration of the Martian atmosphere, would have to be accounted for to an accuracy of at least one part in 100 billion (Ref. 7). Among the other effects would be those caused by the motion of the spacecraft, motion of the receiving stations on the rotating earth, transit time of the signal, and the refractivity of the earth's atmosphere.

The purpose of the occultation experiment can be stated in general as measuring, collecting, and analyzing electromagnetic signal data to provide more accurate values of certain characteristics of the Martian atmosphere (Ref. 8), particularly the presence and intensity of the ionosphere, the surface pressure, and the scale height in the lower atmosphere. Scale height ( $H$ ) refers to the height of the atmosphere needed to produce a decrease in pressure by a factor of about 2.72.

## B. Instrumentation

During the occultation experiment, measurements of signal frequency, phase, and amplitude were made by the ground transmitter and receiver systems of the Deep

Space Instrumentation Facility (DSIF). The ground stations, which were modified especially for the experiment as shown in Fig. IX-2 (Ref. 9), used a rubidium standard to drive a frequency synthesizer. During entry into occultation, the synthesizer was modulated, multiplied 96 times in frequency, amplified, and then transmitted to the spacecraft at  $2.1 \times 10^9$  Hz. When the spacecraft receiver locked in with the ground-station signal, the downlink frequency to the DSIF was derived from the spacecraft-receiver voltage-controlled oscillator (VCO), which was phase-locked to the received uplink signal. During exit from occultation, no uplink signal was received by the spacecraft and the downlink frequency was derived from a free-running crystal oscillator in the spacecraft receiver. The RF signal was amplified and transmitted from a high-gain antenna on the spacecraft.

The ground transmitter and receiver systems employed an 85-ft-diam parabolic antenna with a cassegrainian simultaneous-lobing feed. For the receiver front end, a traveling-wave maser, cooled by a closed-cycle helium refrigerator operating at 4.2°K, was used. After amplification by the maser, the signal was split into two separate receiver channels.

The first channel consisted of a phase-locked receiver operated in the standard DSIF receiver configuration. The ground-receiver VCO was kept in phase synchronism with the received signal. Through a series of frequency multiplications, divisions, and additions, the transmitter-exciter frequency was coherently compared to the receiver VCO to obtain the two-way doppler frequency. The receiver automatic gain control (AGC), which is a received-signal, power-level tracking servo, is used to determine received power level. Appropriate AGC voltages were recorded on magnetic tape and the doppler count was digitized. This system yielded frequency information in real time. The first channel was also used as the sum channel of the pointing system for the simultaneous-lobing antenna.

The second receiver channel—a manually tuned, constant-gain, triple-conversion superheterodyne—operated in a non-standard configuration. It amplified and frequency-translated the downlink signal to the audio-frequency region of the spectrum before recording it on magnetic tape. The local-oscillator signals for this receiver were derived from the rubidium frequency standard, which drove a pair of synthesizers. The first local-oscillator frequency was periodically stepped to

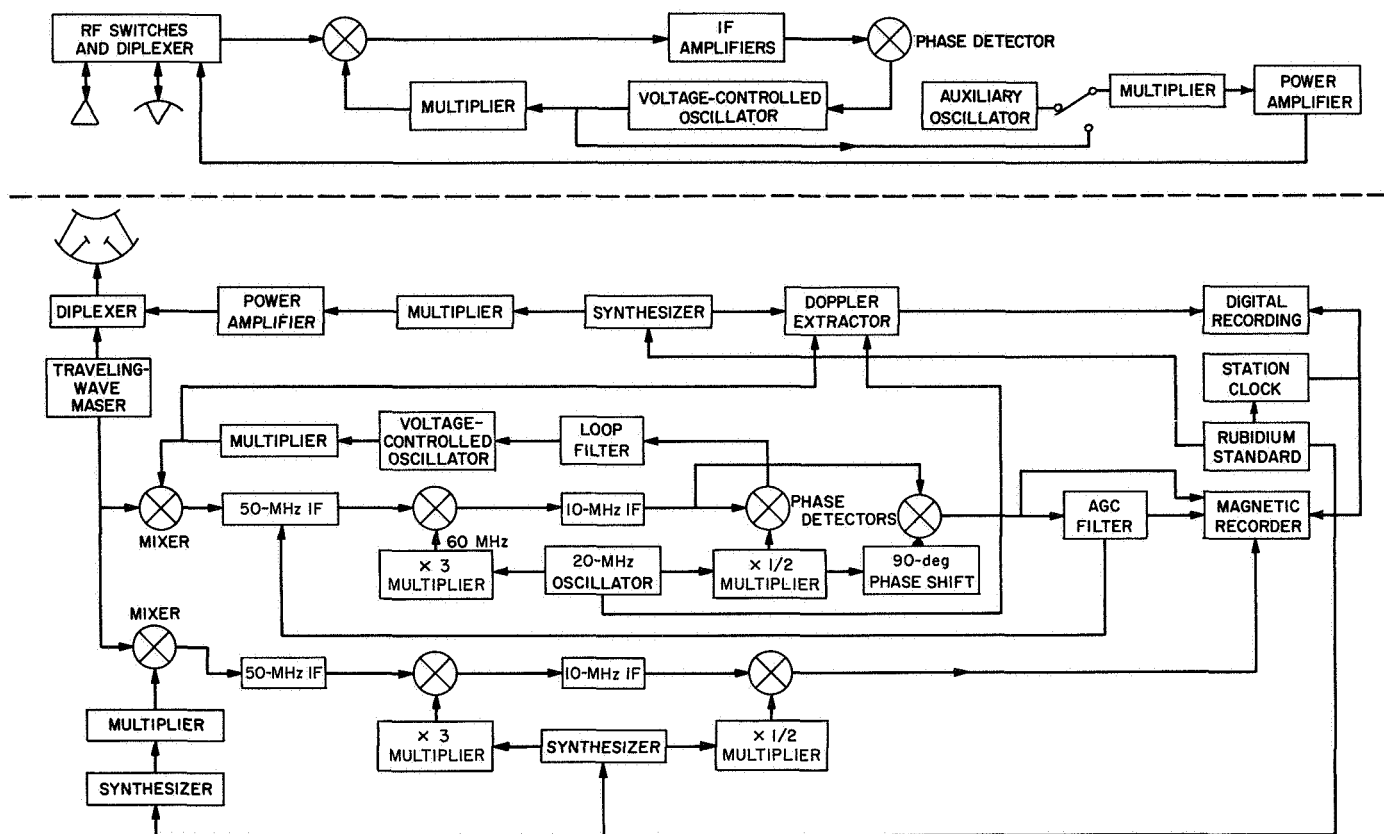


Fig. IX-2. DSIF instrumentation for the occultation experiment

keep the signal in the receiver pass band. The second and third local oscillators were derived from the second synthesizer, operating at 19.996 MHz. The output of the third mixer had a pass band of 1–3 kHz, which was recorded on magnetic tape. Since the local-oscillator frequencies were derived from the rubidium standard, the frequency integrity of the doppler was maintained. After the mission, the analog information on the magnetic tape was digitized for processing. A power spectrum of the audio open-loop signal, made from the digitized tape through an IBM 7094 computer system, is illustrated in Fig. IX-3.

### C. Data Analysis

During the intervals of time preceding and following the occultation of the spacecraft by Mars, two types of data were taken (Ref. 10). These consisted of the received spacecraft signal processed through the two types of receiver systems. The receiver channel operating in the standard configuration yielded a cumulative count of the RF doppler frequency, when the receiver VCO

was in phase synchronism with the received signal. This was referred to as closed-loop operation.

At the two Goldstone Deep Space Stations (Pioneer, DSS 11, and Echo, DSS 12) the doppler frequency was multiplied by a factor of 8 prior to counting in order to reduce quantization errors. At the Tidbinbilla station in Australia (DSS 42) every zero crossing was counted, providing a times-two multiplication of the doppler frequency. The other Australian station (Woomera, DSS 41) took unmultiplied doppler data.

During the time before entry into occultation (observed at about 02:31:11 GMT on July 15, 1965) DSS 11 was transmitting to the spacecraft, as well as receiving the transponded signal along with the other three stations. Since the same frequency standard was used for the transmitter and receiver at DSS 11, it was said to be operating in a “two-way lock” with the spacecraft. The other stations used their own frequency standards for receiver reference, and this type of operation was referred to as “three-way.” All stations maintained lock until extinction of signal, and thus four complete sets of

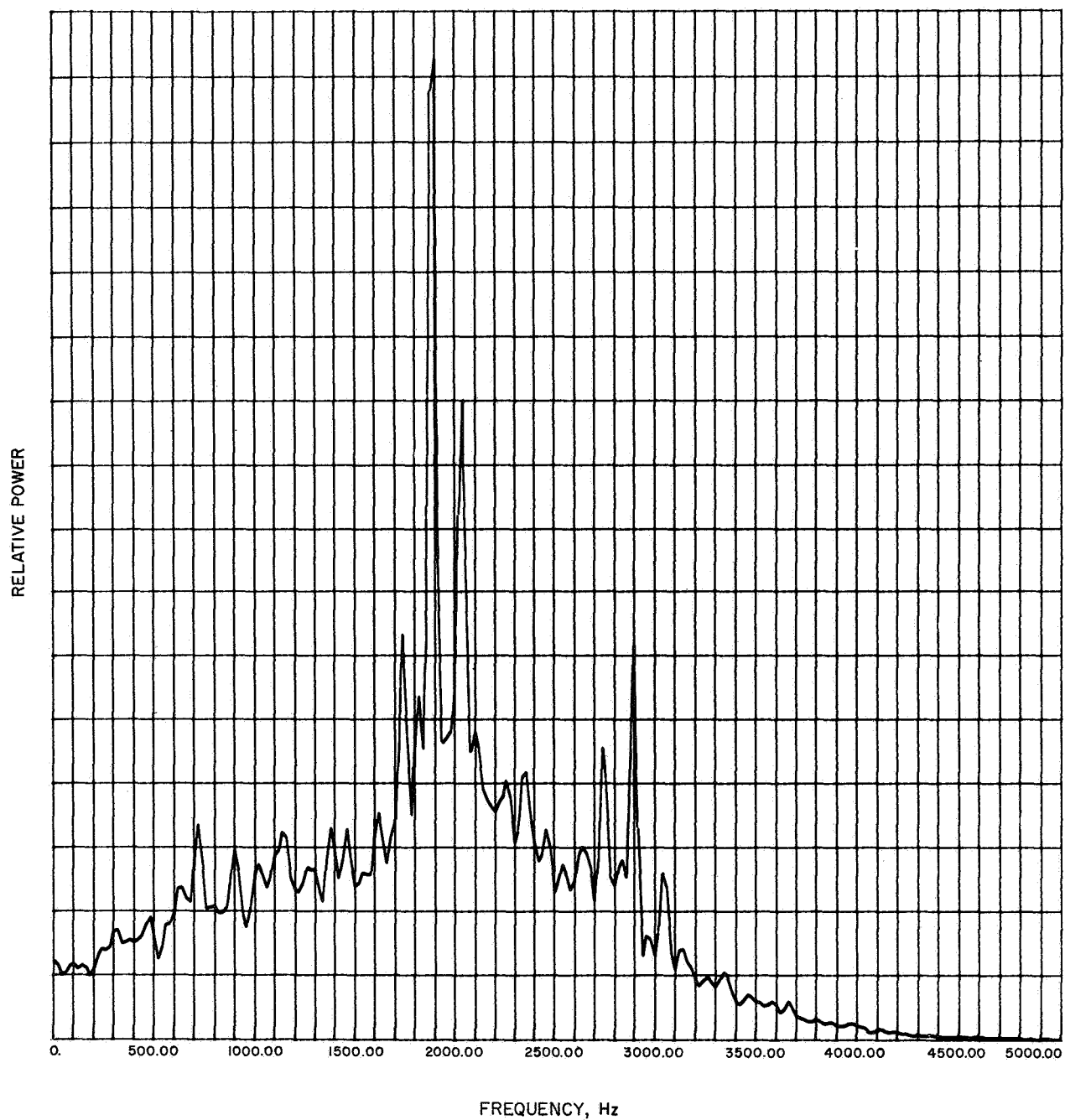


**Fig. IX-3. Power spectrum of signal at the time of switching from one-way to two-way frequency**

closed-loop data were obtained during entry of the radio ray into the Martian ionosphere and atmosphere.

After the end of occultation (observed at 03:25:09 GMT), the closed-loop receivers at the Goldstone stations did not reacquire the signal until several minutes past the exit time, and no useful data were obtained. However, the Tidbinbilla station reacquired at about 03:25:48, and Woomera at 03:25:32, which provided useful data on the ionosphere on the occultation-exit side of Mars.

In addition to these data, the second receiver channels of the Goldstone stations, which had been modified, yielded a frequency-translated analog tape recording of the receiver S-band signal. The signal voltage was FM-recorded, along with suitable auxiliary signals, to maximize the frequency fidelity of the recording. During the occultation-entry phase, the recorders at DSS 11 and 12 were started at about 02:11:00 GMT and continued recording to about 5 min past loss of signal to obtain a noise calibration. The recorders were started again at 03:20:00 and both recorded the entire occultation-exit sequence from the first reappearance of the spacecraft signal at 03:25:09. The signal first appeared at the frequency of the spacecraft auxiliary oscillator, and at about 03:25:16 an abrupt shift of about 1 kc in the received frequency indicated that the spacecraft receiver

had acquired the signal transmitted by the Goldstone Venus station (DSS 13) approximately 7 s after emerging from behind the limb of Mars. From this point in time the spacecraft transmitter was effectively referenced to the Venus station frequency standard, and all receiving stations were operating in the "three-way" mode. The open-loop data are extremely important, because they provide the only information about the nature of the neutral atmosphere on the side of Mars probed at exit from occultation.

The data coverage provided by the various Deep Space Stations is shown graphically in Fig. IX-4.

The elevation angles at Goldstone DSS 11 and 12 were approximately 44 and 35 deg for occultation entry and exit, respectively. The two Australian stations observed the spacecraft at lower elevations. At entry, Tidbinbilla was receiving at about 21 deg elevation, and Woomera at about 15 deg, which is almost at the lower limit. At exit, the elevation angles were 31 and 25 deg for Tidbinbilla and Woomera, respectively.

**1. Audio recorded data.** The digitized audio signal was divided into 1-s increments, and a spectrum analysis of each increment was performed. Then each 1-s interval was filtered by a narrow-band-pass digital filter. After filtering, a least-squares sinusoidal fit was made for each

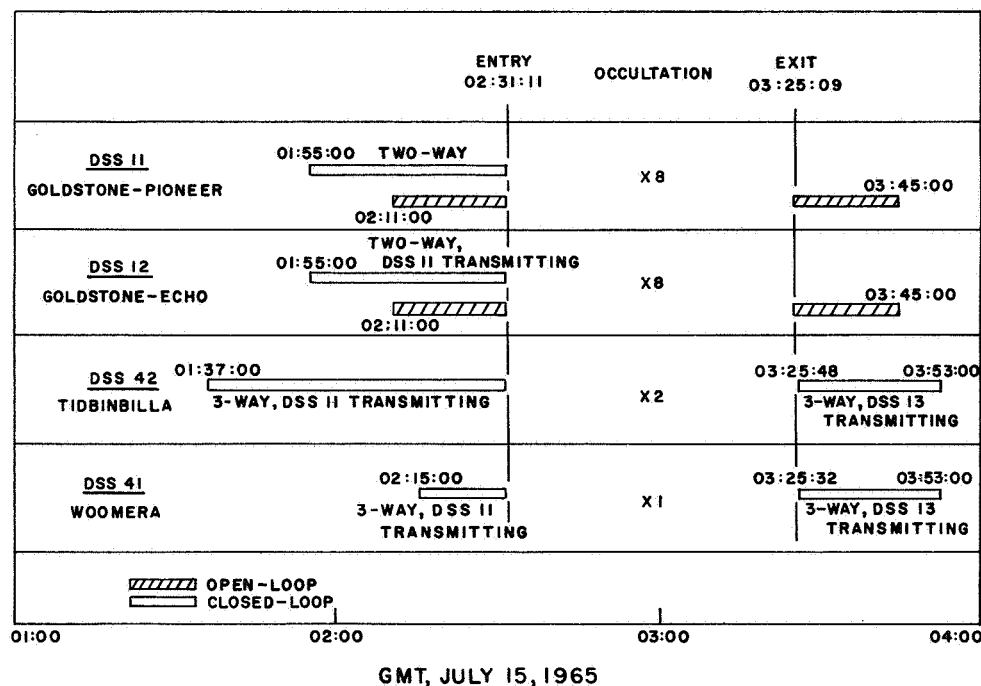


Fig. IX-4. Data obtained during occultation experiment

1-s interval. The analysis of these data has not been completed; however, a portion of the data, from DSS 11 and 12 upon emersion, are shown in Fig. IX-5. Here the doppler shifts due to the station-probe motion have been removed, so that the remainder should represent, to a good approximation, the effects of the Martian atmosphere alone.

The vertical line at 03:25:17 in Fig. IX-5 indicates the switch from the on-board auxiliary oscillator to the coherent lock condition. The bias due to the drift in the auxiliary oscillator has been removed, and the one-way doppler has been doubled. The agreement of the data from the two stations is excellent. It can be seen that the occultation-exit data show no perceptible ionospheric effects. The rate of change of frequency due to the atmosphere is also significantly different from the entry data.

**2. Phase-lock data.** Two methods have been used to calculate the phase-change (cycle count) information obtained from the phase-locked loops. The first method, used by the JPL orbit-determination program (Ref. 11), is to compute the phase change in a given time by term-by-term integration of a truncated Taylor series. This program was used in the manner of a predictor, to give estimates of what the data would have been if no atmosphere existed. The parameters of the atmosphere then were deduced by operating on the "residuals" (data from which all effects, except the planetary atmosphere, were removed).

The objection to this method is that the ray paths on up and down legs near the planet are not clearly represented. To overcome this objection and to provide increased accuracy of computation, a second method was employed. The same general physical-mathematical

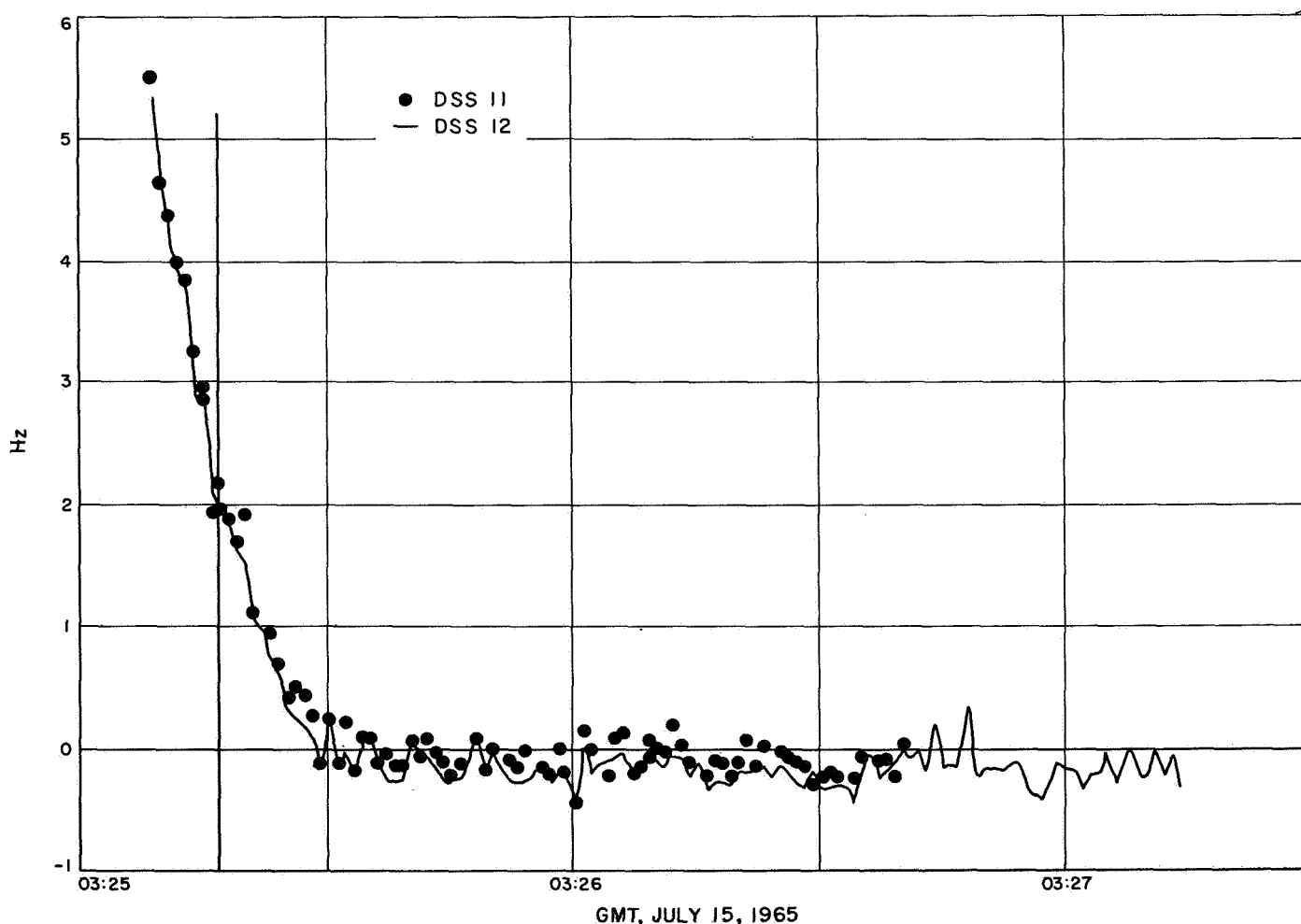


Fig. IX-5. Occultation-exit audio doppler residuals, DSS 11 and 12



model approach as in the orbit-determination program was used.

The phase of the radio wave was computed directly, rather than computing changes in the phase over short periods of time as before. This involved the use of higher precision (less than 1 cm in  $10^{13}$  cm), but the objection of taking derivatives everywhere was removed. (For example, the derivatives of the nutating motion of the earth or of ray-tracing integrals are unnecessary.) The computer program adjusts only the estimates of the planetary atmosphere parameters. The sources of the other data needed, of which all coordinates of position are equator and equinox of 1950.0, are as follows.

*a. Probe Mars-centered coordinates.* Estimates were taken of the spacecraft position and velocity from the orbit-determination program, which excluded all data affected by the planet's atmosphere. These estimates included a refined mass constant for Mars. The most powerful data for determining the orbit came near closest approach to the planet, some 80 min before occultation. This trajectory was computed to only 8 decimal places in the orbit-determination program, but was recomputed with the same initial conditions to 16 places to yield the requisite smoothness. The accuracy of these coordinates was not as important as the ability to reproduce the data during occultation with no short-term periodic errors that might be mistaken for (correlated with) planetary atmospheric effects.

*b. Heliocentric planet positions, earth and Mars.* The JPL double-precision (16 decimal place) ephemeris tapes (Ref. 12) were used, along with the standard look-up and interpolation routine. In addition, the data were smoothed, because the least significant bit of the time argument (Julian date, double precision) induced 30-cm noise into the data computation. A more satisfactory correction to this problem is being pursued.

*c. Geocentric station locations.* Rotations are made to account for precession and nutation.

In computing the transit time of the signal, the speed of light is assumed to be constant (299,792.5 km/s), traveling in a straight line in heliocentric space, whenever no atmospheric effects are present. When near Mars, the path is found by ray tracing, assuming spherical layering about the center of the planet. The times  $t_1$  through  $t_5$ , which define the positions of the earth, Mars, and the spacecraft, are found by a successive-substitutions iterative method.

All of the bending as the ray passes the planet is assumed to occur instantly (at times  $t_2$  and  $t_4$ , up and back) and is computed in Mars-centered coordinates. The retardation time is taken into account in the solution for  $t_1 \cdots t_5$ . The solution method computes a no-atmosphere closest-approach distance (straight lines) first and uses this estimate as the initial condition for ray tracing with the given atmospheric model. The resulting asymptotic distance of the light rays is used to compute two straight-line paths, one from earth going toward the planet, the second going away from the planet to the spacecraft. The resulting angle, purely from geometry, is compared with the refractive ray bending and the error is reduced by Newton's method. The small parallactic displacement of the ray passing through the earth's atmosphere is ignored, but would be consequential for a lunar-distance occultation.

The retardation of the signal as it passes through the earth's atmosphere is primarily a function of the elevation angle. The change in path length for the Goldstone stations during the occultation period was only about 1 cm, because of the high elevation angle (44 deg) and the small change in the angle. However, for the Australian stations, the change was about 12 cm during the same time. To provide information on any unusual turbulent conditions in order to improve corrections to the data, special meteorological measurements were made at Goldstone (Ref. 13). As it was, a nearby storm threatened, which would have produced 1- to 10-cm errors in the apparent path length, but it cleared just hours before the experiment. An attempt will be made to use all available meteorological data to improve the corrections for Tidbinbilla and Woomera.

Once the data have been computed and compared with the observations, a least-squares fitting is made, using finite-difference partials of the adjustable parameters. The adjustable parameters consist of a phase-count bias, station reference frequency, and parameters associated with the atmospheric model.

The current model consists of a spherically layered lower atmosphere with a constant lapse-rate layer and an isothermal (exponential) layer. The adjustable parameters are a reference refractivity defined at an arbitrary height, the specific heat ratio, and the exponential scale height of the isothermal layer. The ionosphere consists of a single Chapman layer, with the adjustable constants being scale height, height of maximum electron density, and maximum electron density. Additional adjustable

parameters may be easily included, up to a maximum of 15, in the current version.

The computer program was written in FORTRAN IV (with the exception of the ephemeris routine) for use on an IBM 7094 computer.

Some results of the application of the program are shown in Fig. IX-6. The data were taken at the Goldstone Pioneer site during entry into occultation, counting at eight times received frequency, and displayed as counts at the received frequency. The residuals shown are small relative to the total atmospheric effects, but obviously show systematic errors that remain. Some systematic error is a result of using an ionospheric model that is not realistic, both in assumptions of form of electron profile and spherical symmetry along the ray. Some of the error is associated with small discrepancies noted between data computed by this pro-

gram and the data produced by the orbit-determination program outside the planetary atmosphere. To reduce the effect of both of these errors on the determination of the lower atmospheric parameters, a bias (1.4 cycles) was added at 02:30:45 GMT after the rays had gone below the ionospheric shell, but before reaching any trace of the lower neutral layer.

## D. Results

Data analysis of the *Mariner IV* occultation experiment has yielded initial results on atmospheric and ionospheric properties that are surprisingly different from anticipated results. The model studies indicate that the occultation results for the lower atmosphere and the ionosphere of Mars exhibit a degree of self-consistency that tends to substantiate the basic correctness of the interpretations. While much more work should be conducted on data analysis and atmospheric model studies,

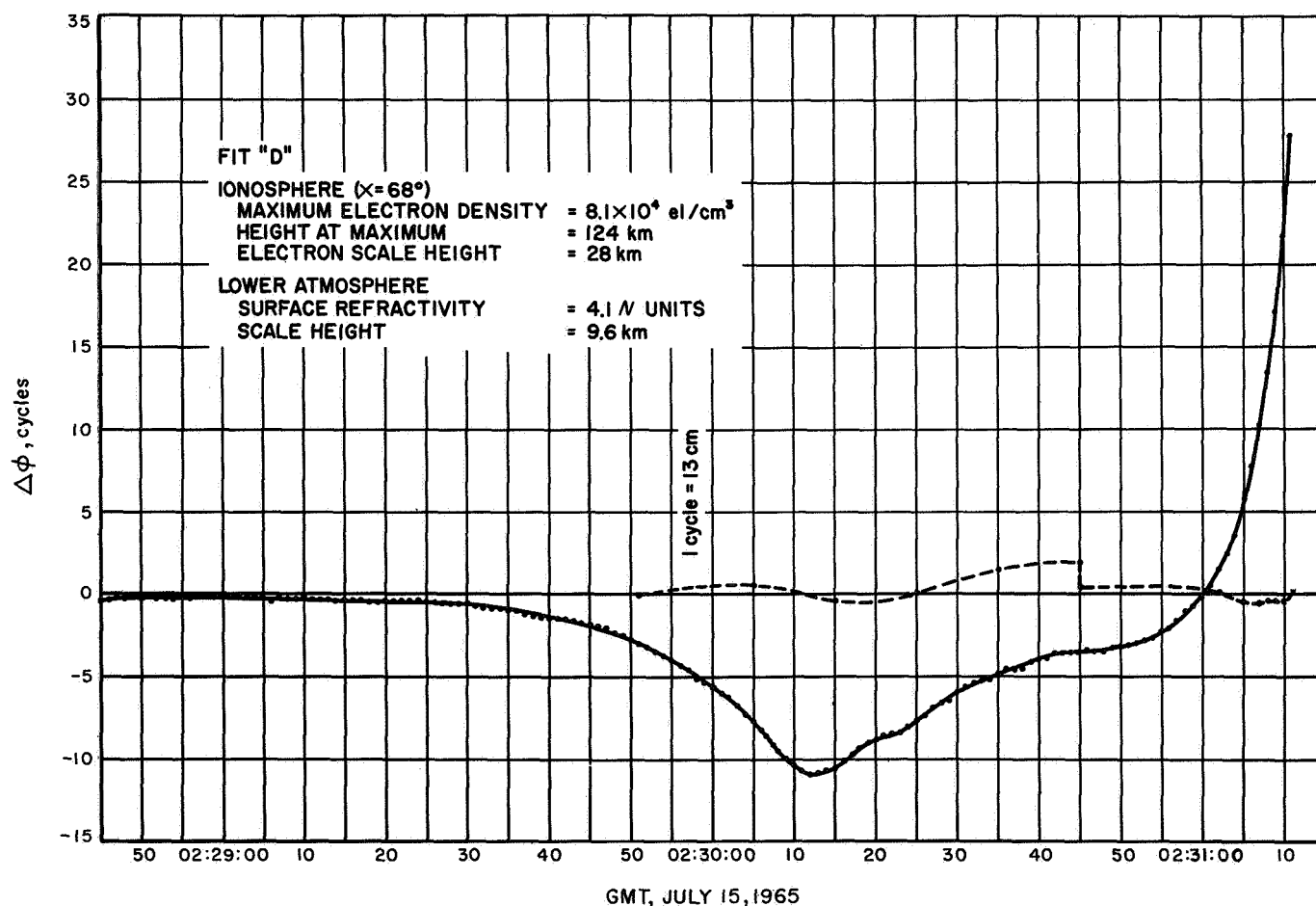


Fig. IX-6. Difference, observed data minus computed data, in cycles



it seems clear that the following salient characteristics of the atmosphere of Mars have been well established (Refs. 7, 14, 15):

- (1) Mars has a tenuous atmosphere. For example, the molecular number density near the surface is only about 0.8% of the earth's, and corresponds to an altitude of about 34 km on earth.
- (2) Carbon dioxide must be the principal atmospheric constituent in order to explain both the occultation and spectroscopic measurements. This suggests that the atmosphere was formed primarily by outgassing of the planet.
- (3) Model studies suggest that the carbon dioxide is dissociated between 70 and 80 km by solar ultra-violet radiation, and the  $\text{CO}_2$ , CO, and O are distributed in the upper atmosphere by diffusion. Thus atomic oxygen is the principal constituent above about 90 km.
- (4) The principal ion in the main daytime ionospheric layer (a Bradbury layer, like the  $\text{F}_2$ -region on earth, where the profile above the peak is controlled by ambipolar diffusion) is  $\text{O}^+$ , and the critical reaction for its loss is probably  $\text{O}^+ + \text{CO}_2 \rightarrow \text{O}_2^+ + \text{CO}$ .
- (5) The atmosphere of Mars is very cold at all altitudes, the temperature being about 180°K near the surface (at the time and place of the occultation immersion measurement) and about 80°K at ionospheric heights. Between these height regions it is even colder, with frozen  $\text{CO}_2$  particles probably being an almost permanent feature of the atmosphere.
- (6) Because of the low temperature, the atmosphere of Mars is confined near the planet (the exosphere begins near 140 km, where the atomic mean free path equals the scale height), and the height profile of atmospheric mass density is several orders of magnitude below that of the earth at all heights, even though gravity is 62% lower on Mars. Thermal escape of the atmosphere is now insignificant, although loss due to action of the solar wind may play an important role in the continuing evolution of the atmosphere.

#### 1. Lower atmosphere.

a. *Immersion measurements.* Doppler and amplitude data were taken during both occultation entry and exit by the Deep Space Stations at Goldstone, California,

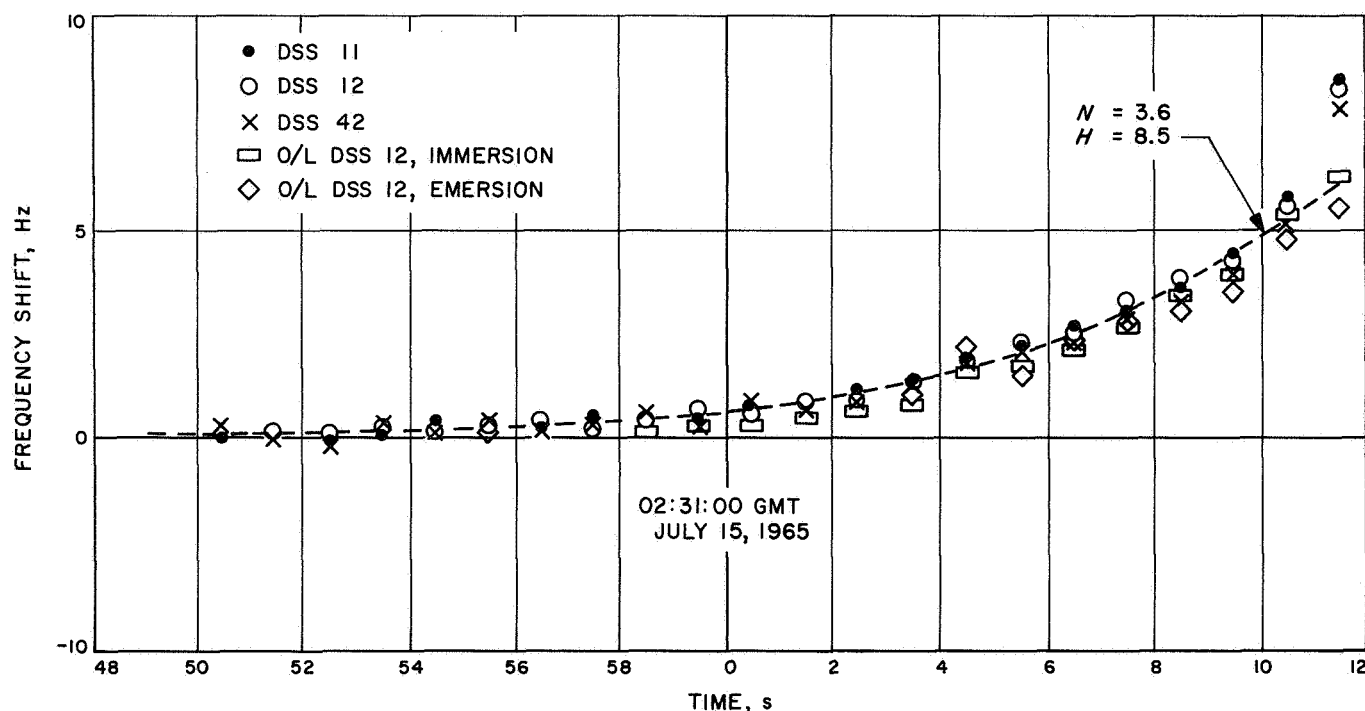


Fig. IX-7. Range-rate doppler residuals from DSS 11, 12, and 42

and Tidbinbilla and Woomera, Australia. The Goldstone stations (DSS 11 and 12) took standard tracking data doppler (closed-loop) as well as open-loop records of the received signal. The Australian stations (DSS 41 and 42) took only doppler data. At entry into occultation, all data were taken while the spacecraft transmitter frequency reference was provided by a frequency standard on the earth. At exit from occultation, a 9-s portion of the data was received while the spacecraft transmitter frequency reference was provided by an on-board crystal oscillator. During this mode, the precision of phase measurements was significantly degraded.

Figure IX-7 shows the range-rate doppler residuals based on data received at DSS 11, 12, and 42 during entry into occultation. The observed phase changes minus the predicted phase changes in 1 s are plotted. The points marked O/L (open-loop) were obtained from the open-loop records by means of spectral-density

analysis. The other points were derived directly from data processed through the JPL orbit-determination program. One may observe that the data from the various sources show a high degree of consistency, except for the doppler points at 02:31:11.5, which are suspect, because the time of loss of signal was estimated to be between 02:31:11.2 and 02:31:11.6 GMT.

The plot in Fig. IX-8 shows the total phase change as a function of time as derived from DSS 11 (Goldstone Pioneer) doppler residuals. The maximum effect of the ionosphere appears at about 02:30:30 GMT and the final upswing, beginning at about 02:30:50, is caused by the neutral atmosphere. Note the extreme smoothness of the data suggested by the low scatter of the data points.

An expanded portion of the phase-change plot is shown in Fig. IX-9. The graph relates only to the neutral atmosphere, since the estimated effects of the ionosphere

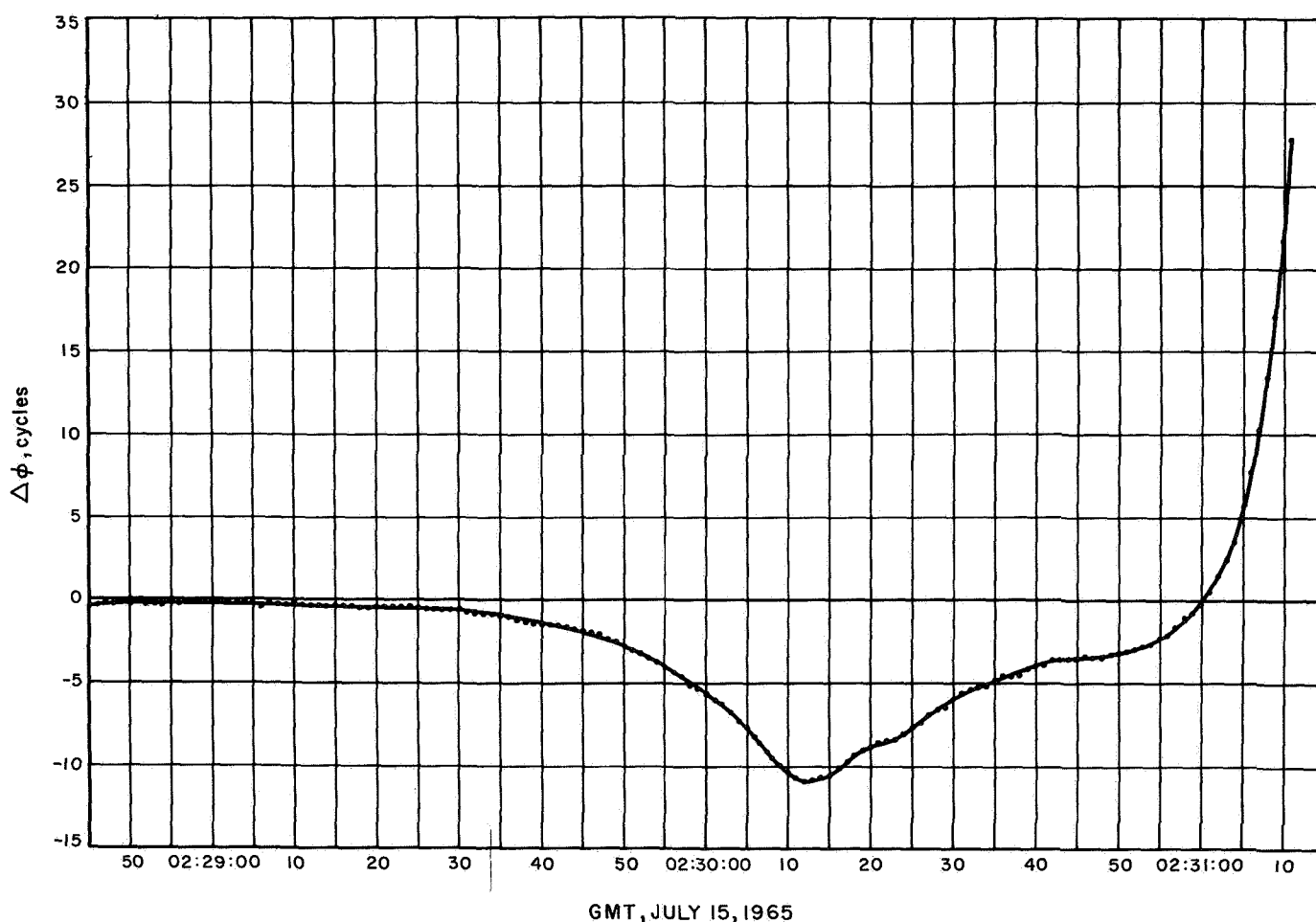


Fig. IX-8. Phase difference (residual sum) — DSS 11 data

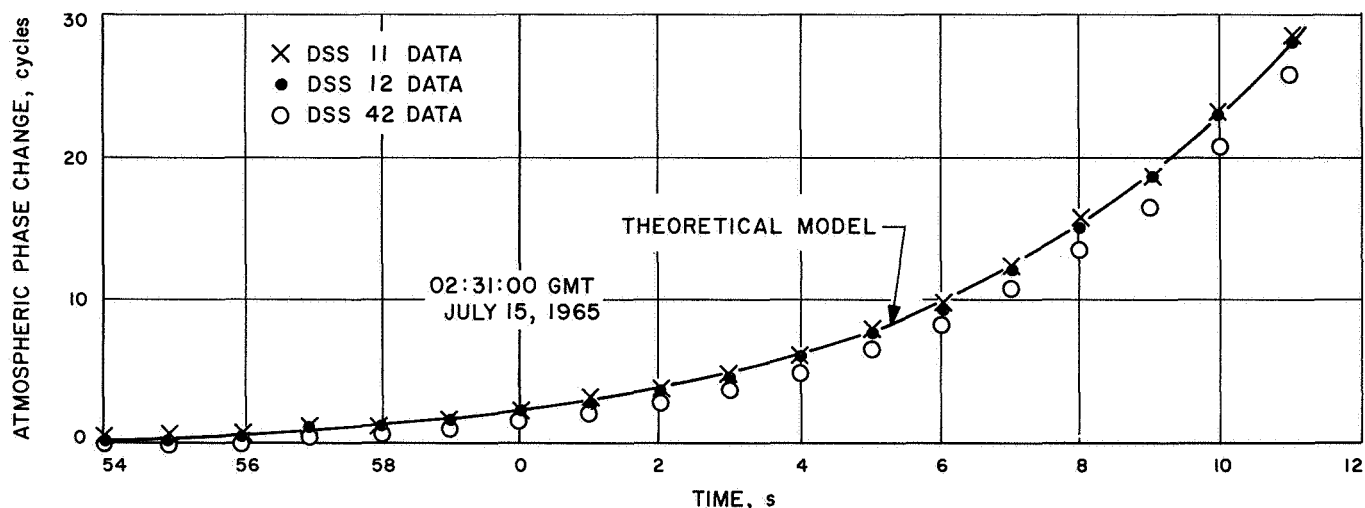


Fig. IX-9. Phase change due only to atmosphere

have been removed. Signal extinction time is assumed as 02:31:11.2 GMT. The solid curve represents the computed phase change for a theoretical exponential model atmosphere having a surface refractivity  $N$  of 3.7  $N$ -units  $[(n - 1) \times 10^6]$ , where  $n$  is the index of refraction and a scale height of 9 km. Even with this relatively crude model, the fit is excellent.

The dotted line in Fig. IX-7 represents the computed doppler residuals for a similar model atmosphere, having a scale height  $H$  of 8.5 km and an  $N = 3.6$ . As in the case of the phase change (Fig. IX-9), the fit of the data appears to be quite good.

Figure IX-10 relates maximum phase change, maximum frequency change (doppler), and refractive gain (at the time of signal extinction, 02:31:11.2) to the surface refractivity and scale height of an exponential density model of an atmosphere. Suggested values of  $5.5 \pm 0.5$  Hz,  $29 \pm 2$  wavelengths, and 1.5 to 2.0 dB lead to the stippled area in the graph.

A cursory study of the Fresnel pattern in the amplitude recordings leads to the belief that signal dropout was due to a diffracting edge, establishing the very important fact that the final ray paths grazed a surface feature on Mars. All references to surface conditions refer to the altitude of this surface feature, the altitude of which relative to the mean surface of Mars is not known. However, the geometry of the experiment would make it likely that it was higher than the mean surface. The mean surface density and pressure would be about 1% greater for each 90 m of height of the occulting fea-

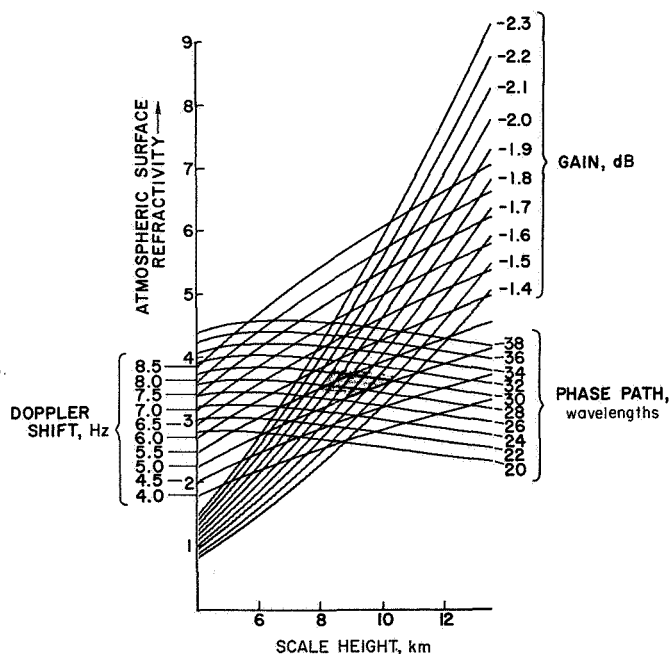
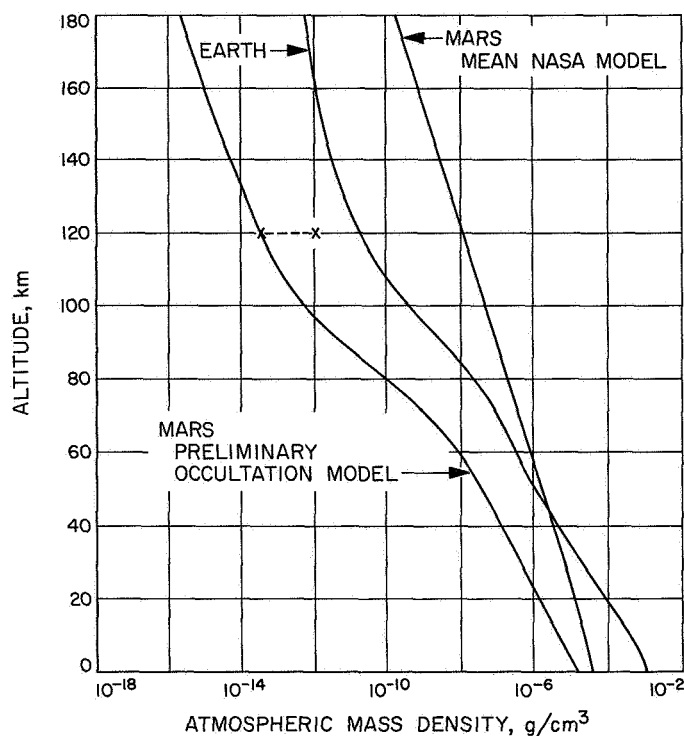


Fig. IX-10. Maximum changes in doppler, phase, and amplitude as functions of surface refractivity and scale height

ture above the mean surface level. So far, analysis has shown no obvious change of scale height with altitude to about 30 km.

Figure IX-11 illustrates how the atmospheric mass density varies with altitude for any of the oxygen models (Bradbury ionosphere) (Ref. 14). The mass density at 120 km altitude would be of the order of  $3 \times 10^{-14}$  g/cm<sup>3</sup>



**Fig. IX-11. Atmospheric mass density vs altitude above Electris at the time of entry into occultation**

for these models. However, the mass density could be a factor of 30 higher at this altitude if the main layer were a Chapman layer. This difference in interpretation results in the uncertainty indicated at 120 km altitude in Fig. IX-11.

Since gravity is about 62% lower on Mars, it was thought that the atmospheric mass density would decrease much more slowly with altitude than on the earth. Thus, nearly independent of the atmospheric pressure assumed near the surface, it was proposed that above 30 to 50 km altitude the density would become greater than the density at the same altitudes in the earth's atmosphere. However, the occultation data analysis reveals quite a different state of affairs. The low temperatures in the upper and lower atmosphere, together with the larger molecular mass, compensate for the lower gravity in controlling the scale height. Hence, the mass-density profile does not cross over the corresponding profile for the earth's atmosphere, but remains several orders of magnitude lower all the way up to the exosphere, which begins at about 140 km (Bradbury layer) or 180 km (Chapman layer).

The question of how the mass density varies with altitude in the Martian atmosphere also has some practical

implications. In determining the lifetime of a satellite in orbit around Mars, it is important to know how the atmospheric density varies with altitude. Most previous models required an orbit altitude up to several thousand kilometers to ensure that a satellite would have a lifetime of at least 50 years, but the occultation measurements show that a few hundred kilometers should be sufficient.

Table IX-1 summarizes the results for the lower atmosphere as obtained from the measurements made during immersion of the spacecraft into occultation (Ref. 7). In the table, case (a) is for 100% CO<sub>2</sub>, while case (b) is for 80 to 100% CO<sub>2</sub> by number density, with the remainder N<sub>2</sub> and Ar in any ratio. While the relative abundances of CO<sub>2</sub>, N<sub>2</sub>, and Ar are assumed, all of the other results shown in the table follow directly from the atmospheric refractivity and scale height measured near the surface of Mars. The main uncertainty in these results is the height of the occulting surface feature above the mean surface. Another suggested source of error is dust suspended in the atmosphere. These two effects would act in opposite directions, but only the altitude effect, amounting to a 1% change in number density per 90 m of height, is thought to be of possible significance.

Ionization near the surface of Mars could also cause errors. However, even during abnormal blackout in the

**Table IX-1. Summary of preliminary results for the lower atmosphere of Mars<sup>a</sup>**

Parameter	Measurement
Surface refractivity	3.6 ± 0.2 N-units
Surface scale height	9 ± 1 km
Surface number density	
(a) all CO <sub>2</sub>	1.9 ± 0.1 × 10 <sup>17</sup> mol/cm <sup>3</sup>
(b) up to 20% N <sub>2</sub> and/or Ar	2.1 ± 0.2 × 10 <sup>17</sup> mol/cm <sup>3</sup>
Surface mass density	
(a) all CO <sub>2</sub>	1.43 ± 0.10 × 10 <sup>-5</sup> g/cm <sup>3</sup>
(b) up to 20% N <sub>2</sub> and/or Ar	1.50 ± 0.15 × 10 <sup>-5</sup> g/cm <sup>3</sup>
Temperature near surface	
(a) all CO <sub>2</sub>	180 ± 20°K
(b) up to 20% N <sub>2</sub> and/or Ar	175 ± 25°K
Surface pressure	
(a) all CO <sub>2</sub>	4.9 ± 0.8 mbar
(b) up to 20% N <sub>2</sub> and/or Ar	5.1 ± 1.1 mbar
<sup>a</sup> Location: Immersion was over Electris at 50°S lat, 177°E lon; local time 1 p.m., winter; solar zenith angle, 67 deg	

earth's polar atmosphere, the electron-number density apparently does not exceed  $10^3 \text{ cm}^{-3}$  at the density level corresponding to the Martian surface conditions. Using  $10^3 \text{ cm}^{-3}$  as an upper limit to the surface electron density at Electris during the measurement would increase the number density given in Table IX-1 by less than 0.3%.

The number-density scale height deduced from the immersion data appears to be constant with altitude at least up to about 30 km. This result seems reasonable also on theoretical grounds, since radiative exchange considerations show that the temperature-lapse rate in a carbon dioxide atmosphere should be relatively low in winter at high latitudes, which corresponds to conditions during immersion.

*b. Emersion measurements.* The emersion measurements over Mare Acidalium in the northern hemisphere

of Mars indicate a surface pressure that is several millibars higher than the immersion results. The difference in surface pressure may be caused by an altitude difference, due either to local surface features or to departures of the mean surface from a gravitational equipotential surface. The temperature and apparent lapse rate were also higher over Mare Acidalium. This is to be expected, since it was summer in the northern hemisphere during the measurement.

In Fig. IX-12, the open-loop residuals obtained during exit from occultation are compared by superposition on the residuals obtained during entry. As mentioned previously, the first 9-s portion of the occultation-exit data consists of one-way residuals, and the balance are two-way. In order to obtain a continuous curve of exit residuals, it was necessary to connect the two portions, which were obtained separately. As a first approximation,

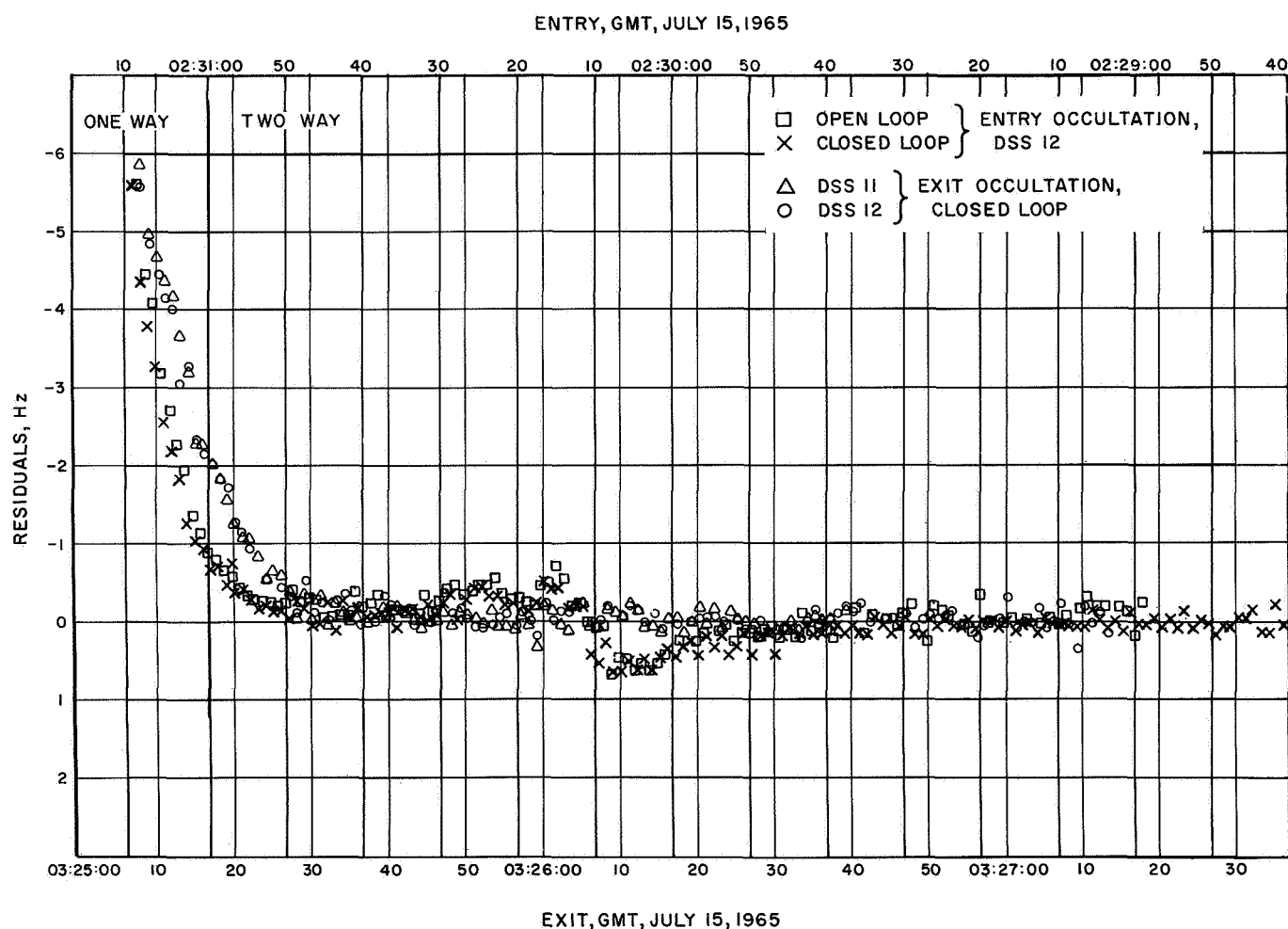


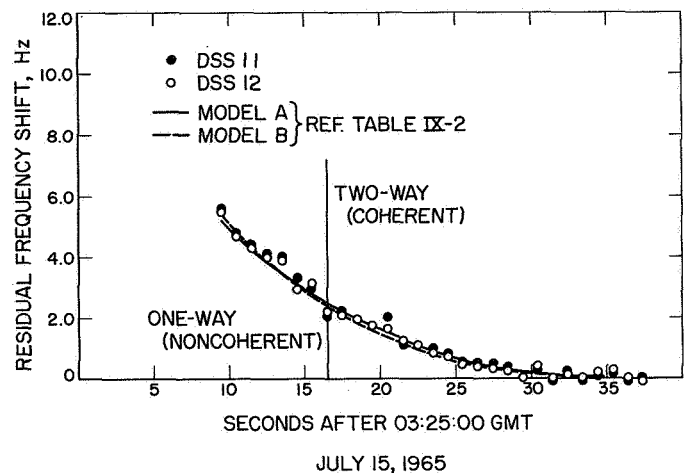
Fig. IX-12. Comparison of occultation-entry and -exit residuals

the magnitude of two-way residuals is twice the magnitude of corresponding one-way residuals; therefore, the one-way portion in Fig. IX-12 was obtained by multiplying all residuals by 2, and was attached to the two-way portion at a point that yielded the smoothest continuous curve. It is understood that this method is approximate, and appropriate allowances are made in subsequent discussion.

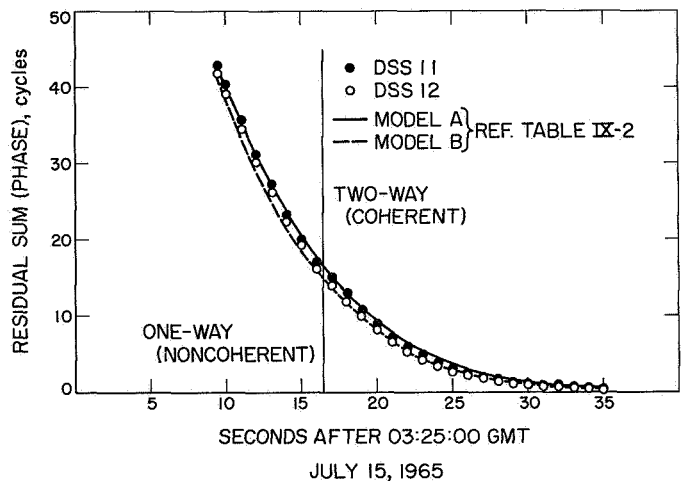
Confusing as it may be, Fig. IX-12 leads to two interesting observations. First, there is no observable effect of the ionosphere on the exit (dark-side) residuals. Secondly, the behavior of the residuals indicating the influence of the neutral atmosphere is markedly different, both in the regions of one-way and two-way operation (separated by the heavy vertical line), suggesting that the lower atmosphere measured over Mare Acidalium has different properties than that over Electris.

Figure IX-13 shows the occultation-exit residuals plotted on an expanded scale, and Fig. IX-14 shows the corresponding residual sums, for both DSS 11 and DSS 12 data. It was found that, in contrast to the occultation-entry data, the exit data did not fit very well with the models having a constant scale height above the surface. Consequently, several models having linear temperature-lapse rates were tried, and the resulting fit for two of them, referred to as models A and B in Table IX-2, are shown superimposed upon the data in Figs. IX-13 and IX-14.

Judging from the figures, model B appears to fit the data better than does model A. However, any conclu-



**Fig. IX-13. Occultation-exit residuals with theoretical models**



**Fig. IX-14. Occultation-exit residual sums with theoretical models**

**Table IX-2. Parameters of theoretical model atmospheres**

Parameter	Model A	Model B
Surface temperature, °K		
100% CO <sub>2</sub>	257	239
80% CO <sub>2</sub> , 20% Ar	252	235
Surface refractivity, N-units	4.175	4.2
Tropospheric lapse rate, °K/km	3.0	2.0
Tropopause altitude, km	21	21
Temperature above tropopause, °K		
100% CO <sub>2</sub>	194	197
80% CO <sub>2</sub> , 20% Ar	189	193
Surface pressure		
100% CO <sub>2</sub>	8.1	7.6
80% CO <sub>2</sub> , 20% Ar	8.7	8.2

sions regarding the temperature-lapse rate and the tropopause altitude must be approached with caution, primarily because of the presence of the segment of one-way data (Fig. IX-12). The 9-s one-way segment is sufficiently near to correspondence with the assumed temperature-lapse region in the atmosphere to arouse the suspicion that a more exact handling of this portion of the data may considerably affect the nature of the indicated tropospheric region above Mare Acidalium.

In order to obtain some indication from the occultation-exit data of the near-surface conditions, it was attempted to obtain the refractivity and scale height near the surface, as well as the probable errors associated with these estimates, on the basis of the maximum frequency shift

(residual) and phase change (residual sum). From Figs. IX-13 and IX-14 these maxima range from about 5.54 to 5.6 Hz for the frequency, and from about 42.0 to 43.2 cycles for the phase.

Based on analysis of 1-s-count tracking data during the flight of the probe, the standard deviation of the random error was found to be about 0.1 Hz for two-way residuals, and about 0.3 Hz for one-way residuals. In addition, since the one-way and two-way segments of data were artificially connected, there may be a systematic misalignment error equal to the standard deviation of the one-way measurements. Using these error figures, the probable range on the measurement of the maximum frequency shift is from about 5.1 to 6.1 Hz.

To obtain the residual sums (phase) (Fig. IX-14), 25 residual points were summed. The first 16 of these were two-way points, with a random error of 0.1 Hz, and the final 9 (in the order of summation) were one-way points, with a random error of 0.3 Hz and a systematic error of 0.3 Hz. Thus, the total probable error is about 3.7 Hz, and the probable range from about 39 to 46 Hz.

Comparing these values with computed maxima in phase and frequency shift for simple exponential atmosphere models, it was observed that the corresponding surface-refractivity values range from 3.9 to 4.5 *N*-units, and the scale height from 11 to 13 km, as shown in the second column of Table IX-3. Assuming the same composition as used in the discussion of the occultation-entry results, the number density, mass density, temperature, and pressure near the surface were computed to correspond to these ranges of refractivity and scale height. These are also listed in Table IX-3.

Although the probable errors in these quantities are quite large, it appears that several cautious conclusions can be drawn. First, the temperature near the surface at the occultation-exit region is higher than that at the entry region. This is not very surprising, even in view of nighttime conditions there, because the seasonal influence on the temperature may be expected to dominate over the diurnal. (It was late summer in the northern hemisphere of Mars at the time of the *Mariner IV* flyby.) More surprising is the higher value of refractivity near the surface indicated by the emersion data. This, coupled with the higher temperature, leads to surface-pressure estimates some 50 to 60% higher than those observed in the entry region. The possible significance of this result will be discussed later; however, it is interesting to note that a pressure difference of the indicated

**Table IX-3. Comparison of atmospheric quantities computed from occultation immersion and emersion data**

Parameter	Immersion	Emersion
Surface refractivity, <i>N</i> -units	3.6 ± 0.2	4.2 ± 0.3
Scale height near surface, km	9 ± 1	12 ± 1
Surface number density, 10 <sup>17</sup> mol/cm <sup>3</sup>		
100% CO <sub>2</sub>	1.9 ± 0.1	2.25 ± 0.15
80% CO <sub>2</sub> , 20% Ar	2.1 ± 0.1	2.45 ± 0.15
Surface mass density, 10 <sup>-5</sup> g/cm <sup>3</sup>		
100% CO <sub>2</sub>	1.43 ± 0.1	1.65 ± 0.15
80% CO <sub>2</sub> , 20% Ar	1.55 ± 0.1	1.85 ± 0.15
Surface temperature, °K		
100% CO <sub>2</sub>	180 ± 20	240 ± 20
80% CO <sub>2</sub> , 20% Ar	175 ± 20	235 ± 20
Surface pressure, mbar		
100% CO <sub>2</sub>	4.9 ± 0.8	7.6 ± 1.3
80% CO <sub>2</sub> , 20% Ar	5.2 ± 0.8	8.2 ± 1.3
Maximum electron density, ionosphere, electrons/cm <sup>3</sup>	9.0 ± 1.0 × 10 <sup>4</sup>	<4 × 10 <sup>5</sup>
Altitude of maximum electron density, km	123 ± 3	—
Electron scale height above maximum, km	22 ± 3	—

magnitude would imply an elevation difference between immersion and emersion regions of about 5.7 km for a scale height of 13 km, and 4.8 km for a scale height of 11 km.

**2. Radius measurement.** An estimate of the trajectory of the probe was obtained by a least-squares fit to two-way doppler data taken from tracking stations at Goldstone, California; Australia; and Johannesburg, South Africa. These tracking data included only data near Mars, from July 10, 1965, to July 17, 1965, including as much data as possible affected by the acceleration of Mars, while excluding data affected by the long-time action of random components of attitude-control forces, solar-radiation forces, etc. In the fitting procedure used to estimate this trajectory, corrections were made not only to the orbit, but also to the mass of Mars and two coordinates of each tracking station. The oblateness of the planet was not estimated; the best available estimate was used.

The areocentric (Mars-centered) coordinates thus obtained were then used to form the basis of estimates of the planet's radius by fitting the atmosphere-affected data to a simple model (Ref. 10). This model was used to estimate the atmosphere on Mars, and the same model was used to estimate the closest-approach distance of the radio beam. Ray-tracing theory only was used. This theory was assumed to be valid up to the point where the signal decreased (during occultation entry) in intensity by a factor of 4, indicating, on the basis of a plane wave obscured by a knife edge, that one-half of the plane wave was cut off. In this definition of time of occultation, only the ray returning to earth is considered, since the earth-probe signal cannot be accurately measured in amplitude as instrumented. The two ray paths, up and back, differ in radial distance from the center of the planet by about 2 km.

The occultation-entry time obtained from a strip-recorder was 02:31:11.2 station time at Goldstone, California. The station clock was a rubidium-vapor-cell atomic oscillator closely synchronized ( $\pm 0.005$  s) with the time broadcasted by radio station WWV in Washington, D.C. Any errors in the occultation-entry time are associated primarily with the difficult problem of measuring the signal that was not far from the threshold of the receiver; even so, no error greater than 0.5 s is thought possible. The spacecraft velocity normal to the surface of Mars was about 2.1 km/s; thus, the effect of this error on the radius estimate is limited to about 1 km.

The time of exit from occultation was computed by different means, since the standard phase-locked loops were not in operation. Instead, the recorded open-loop signal was analyzed and the time of commencement of signal obtained from the recordings (which also recorded station time) was found to be 03:25:09.5 GMT. The error was analyzed to be less than 1.0 s. The corresponding radii computed are given in Table IX-4 (Ref. 16).

The errors shown in Table IX-4 take into account timing errors, atmospheric model errors, and trajectory estimate errors. The trajectory estimate errors are about 1 km, and are computed from the covariance matrix, which is an auxiliary output of the least-squares orbit-fitting process and indicates errors in the orbit if the fitting model is assumed to be perfect.

Results suggest two separate conclusions: first, the atmospheric pressure over the area corresponding to exit from occultation (Mare Acidalium) appears to be higher than that over the entry area (Electris/Mare Chronium); second, computation of the radii of the closest-approach point of the radio beam at the times of occultation entry and exit yielded the result that the radial distances from the mass center of Mars of the surface features that ultimately obscured the beam were not equal on the two sides. More precisely, the surface on the entry side (Electris) appears to be some 5 km higher than it is at the exit side (Mare Acidalium). One may, therefore, be tempted to combine the two and to conclude that these observations are self-consistent, since the change in surface pressures measured at the two locations corresponds closely to the observed difference in radii. However, such a conclusion must be reconsidered. First, the rather large probable errors in both determinations must be taken into account. Second, the atmospheric pressure may be expected to vary with altitude above the mean gravitational equipotential surface, and not with absolute radial distance from the center of mass. Thus, if the dynamical value of flattening of 0.0052 is assumed, the radius of the surface would change by about 2.8 km between the latitudes of 50.5 and 60.0° (assuming hemispheric symmetry), indicating about 2.3 km higher local elevation at the entry region than at the exit region. On the other hand, if the photometric value of 0.0117 given by Dollfus (Ref. 17) is used, the surface radius would change by about 6 km between the two latitudes. Under this assumption, the entire difference in radius would be ascribed to the variation in mean surface, and no local elevation difference would appear to exist.

**Table IX-4. Computations of the radius of Mars**

Event	Time, GMT	Radius <sup>a</sup> , km
Entry into occultation	02:31:11.2	3384 $\pm$ 3
Exit from occultation	03:25:9.5	3379 $\pm$ 4
<sup>a</sup> From the mass center of Mars.		

Obviously, no clear conclusions can be drawn from these results regarding the cause of the observed difference in pressure between the two regions. Most probably it is caused by a difference in equipotential altitude of the two regions; however, the question of whether this difference is local in nature, or is caused by a deviation of the mean surface from the equipotential, cannot be answered on the basis of these results.



**3. Ionosphere and upper atmosphere.** The occultation data analysis helped form a more complete picture of how the Martian atmosphere changes with altitude. This picture includes the temperature profile, number-density profiles, and the controlling physical and chemical processes. The precision with which one can determine the refractive index, and therefore the number density, in the lower neutral atmosphere depends on how well one can separate the refractive effects caused by the ionized and the neutral regions of the Martian atmosphere.

When an electromagnetic wave propagates through an ionized medium, its wavelength is longer than it would be in free space. Data from three tracking stations (DSS 11 and 12 at Goldstone, California, and DSS 42 at Tidbinbilla, Australia) plotted in Fig. IX-15 show how this effect caused a decrease in the two-way phase path as *Mariner IV* moved in behind the Martian ionosphere. As shown in Fig. IX-15, the main ionospheric layer on Mars caused an 11-cycle phase decrease—or an apparent position change of the spacecraft of about 75 cm in the direction of the earth ( $\lambda \approx 13.6$  cm). Starting about 02:30:20 GMT another change of only about 4 cm was observed at each of the tracking stations, and it is believed that this was caused by a minor layer in the lower ionosphere.

From the ionospheric phase-path data one can determine the electron-density profile of the Martian ionosphere. The preliminary electron-density profile, shown in Fig. IX-16, was computed from the data taken as the propagation paths probed through the ionosphere above the bright area, Electris. The solar zenith angle was about 67 deg, and the local time was early afternoon. Electris is in the southern hemisphere of Mars at 50° latitude and it was winter there at the time of the measurement (Refs. 4, 18).

The peak electron density seems to be about  $10^6$  cm<sup>-3</sup> at an altitude of 120 km. The plasma scale height at the top side is about 24 km. Both the small scale height and the low altitude of the main layer indicate that the Martian atmosphere is considerably colder than previously anticipated.

In measurements made during occultation exit, the radio energy probed through the nighttime ionosphere above Mare Acidalius in the northern hemisphere of Mars. The signature of the night-side ionosphere appears to be very weak and the measurements suggest that its electron density was down by at least a factor of 20 from the peak density measured on the day side.

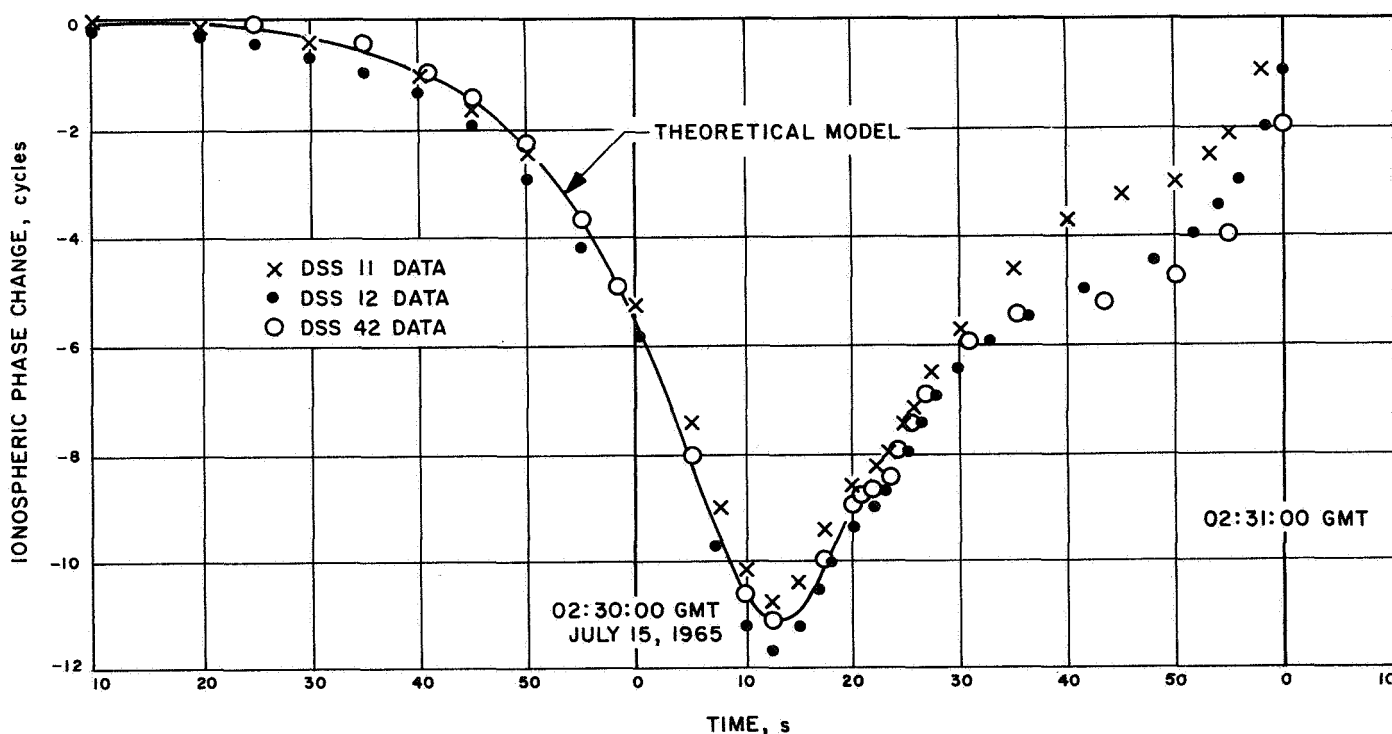
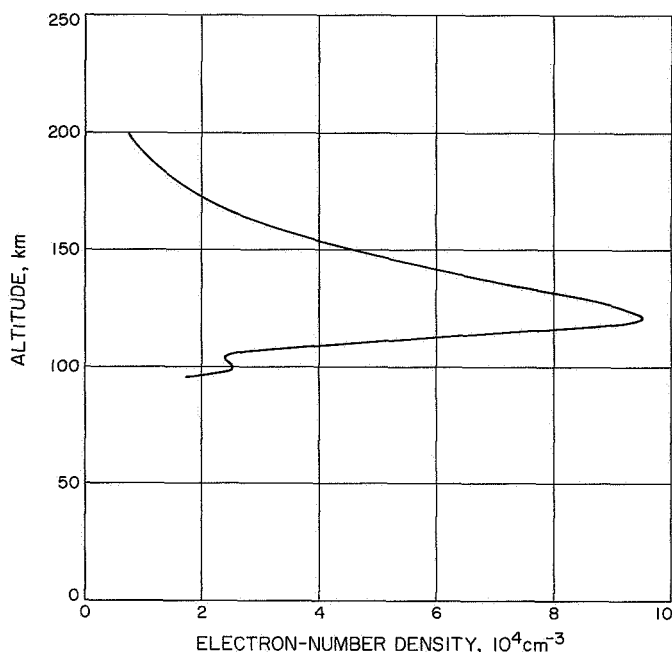


Fig. IX-15. Ionospheric phase change vs time, during occultation entry



**Fig. IX-16. Electron-number density vs altitude above Electris at the time and location corresponding to entry into occultation**

The observational evidence provided by *Mariner IV* has led to three markedly different types of models for the Martian atmosphere. They differ in particular in explaining the characteristics of the main ionization layer observed in the atmosphere of Mars over Electris, near 50°S lat and 177°E lon at 1330 local time in late winter. By analogy with the formation of ionization layers in the earth's upper atmosphere, these three classes of models are denoted as  $F_2$ ,  $F_1$ , and E (Refs. 19, 20).

The  $F_2$ , or Bradbury, models rest on the assumption that the observed ionization peak results from a rapid upward decrease of the ion-recombination loss coefficient, together with downward plasma diffusion. In the  $F_2$  models, the electron-density peak is above the region where most of the electron production and recombination occur. The  $F_1$  and E models are based on the assumption that the observed ionization profile is a Chapman layer, where the peak coincides with the electron production peak caused by solar UV- and X-rays, respectively.

The interpretation of the *Mariner IV* data in terms of  $F_2$  and  $F_1$  models was first suggested by the radio occultation team and later expanded upon by Fjeldbo et al. (Refs. 19, 20). In each case, the  $F_2$  explanation was favored. Number-density and temperature profiles for

these models are shown in Figs. IX-17 and IX-18. While rather particular  $F_2$ ,  $F_1$ , and E models are shown in the figures and discussed, most of the arguments presented here apply to a general comparison of these three classes of models.

Below about 30 km altitude, there is not much latitude in determining the neutral-number-density and temperature profiles from the measured refractivity, since the atmosphere must consist almost entirely of  $\text{CO}_2$ . At ionospheric heights, the interpretation of the radio occultation data appears to be considerably more ambiguous, with proposed neutral number densities differing by factors up to  $10^4$  and suggested upper atmospheric temperatures varying from below 100 to more than 400°K (Refs. 21, 22, 23).

The solid curves of Figs. IX-17 and IX-18 apply to an  $F_2$  model, in which carbon dioxide is dissociated into atomic oxygen and carbon monoxide at about 70 km altitude. Above the dissociation region, O, CO, and  $\text{CO}_2$  are assumed to be in diffusive equilibrium so that the lightest constituent (O) predominates in the upper atmosphere. At the ionization peak (120 km altitude), the atomic oxygen density was determined by equating the photo-ionization rate and the rate of downward plasma diffusion. The  $\text{CO}_2$  density at this altitude was estimated by equating the rates of diffusion and recombination loss of electrons. The limiting recombination loss mechanism at the ionization peak used for this model is  $\text{O}^+ + \text{CO}_2 \rightarrow \text{O}_2^+ + \text{CO}$ , with a rate coefficient of  $10^{-9} \text{ cm}^3/\text{s}$ .

Below the dissociation region, there might be layers of  $\text{O}_2$  and  $\text{O}_3$ . However, the chemical reaction rates are poorly known and the extent of mixing can only be estimated based on analogies with the earth's atmosphere. Thus, the actual  $\text{O}_2$  and  $\text{O}_3$  densities are uncertain.

Above the ionization peak the atmospheric temperature for the  $F_2$  model was determined from the observed plasma scale height, assuming thermal equilibrium between the plasma components and the neutral gas. The preliminary work reported by the team of investigators in the occultation experiment (Ref. 7) indicated a plasma scale height of about 20 to 25 km, whereas subsequent and more complete analysis gives 23 to 29 km. This spread is mainly due to variations in data taken at different tracking stations.

Between approximately 30 and 100 km altitude above Electris, the refractivity was too low to be detected.

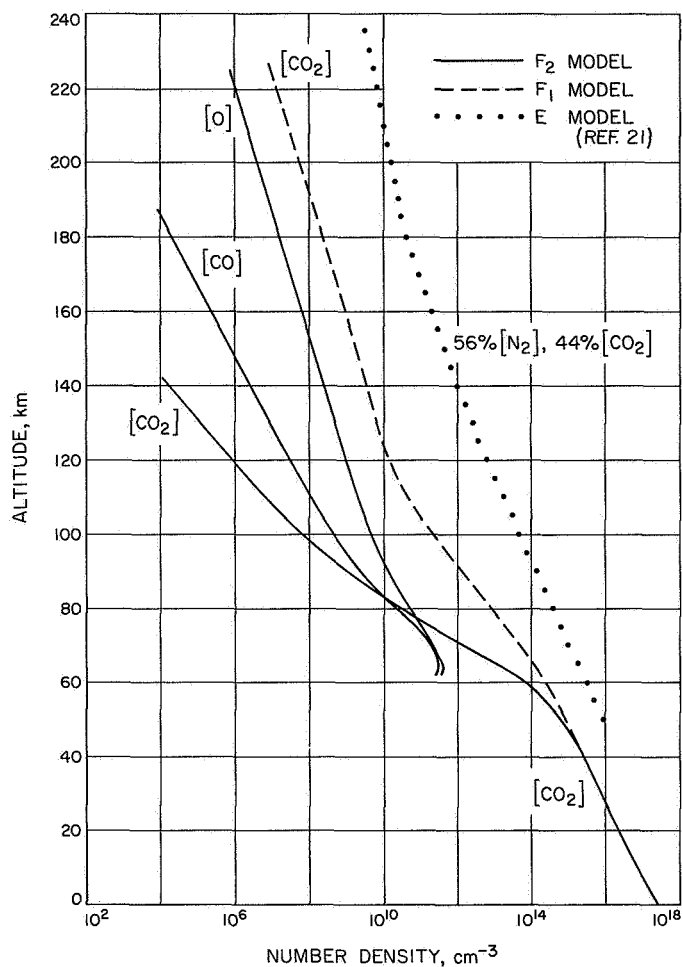


**Fig. IX-17. Number density vs altitude for three different atmospheric models**

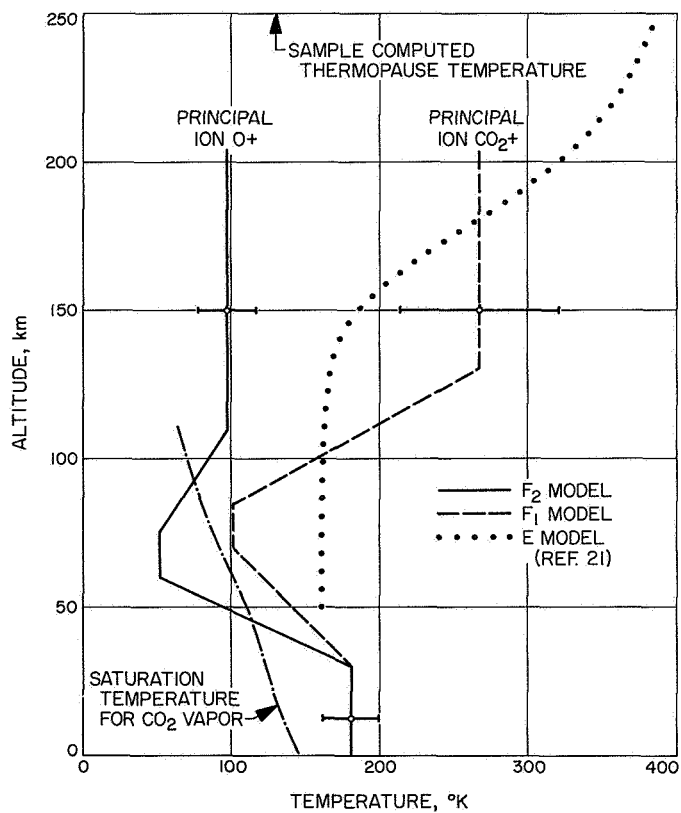


**Fig. IX-18. Temperature vs altitude for three different atmospheric models**

However, one can utilize the temperature and density of  $\text{CO}_2$  above and below to determine the average temperature for this intermediate region. Based on the theoretical heat-balance computations, the mesopause temperature minimum was put at an altitude corresponding to a density level of about  $10^{13} \text{ cm}^{-3}$ .

The  $F_2$ -model temperature profile shown in Fig. IX-18 dips below the saturation temperature for  $\text{CO}_2$  vapor. It is well known that supercooling of  $\text{H}_2\text{O}$  droplets takes place in our own atmosphere, and an analogous situation might conceivably exist on Mars with regard to  $\text{CO}_2$ . The main difference would be this: since the pressure is lower than the triple point,  $\text{CO}_2$  remains in the gas phase rather than in the liquid phase. On the other hand, if the sublimation time were shorter than the diffusion time in this region of the atmosphere, one would anticipate the formation of  $\text{CO}_2$  particles so that the temperature profile might follow approximately the saturation temperature for  $\text{CO}_2$  vapor. This effect might help explain some of the haze and particle layers observed with earth-based telescopes and with the *Mariner IV* television camera. It may also explain why pressure estimates based on optical scattering from the atmosphere of Mars gave a surface pressure approximately one order of magnitude larger than the values obtained from the occultation experiment, and the more recent spectroscopic observations.

The major objection to an E-region hypothesis is the difficulty of making it compatible with the constant plasma scale height observed above the ionization peak. The measured two-way phase-path data can be presented so that they can be compared directly with assumed scale heights for a spherically symmetrical ionosphere. This has been done in Fig. IX-19, where the plasma scale height is very nearly constant from just above the peak, at 120 km, to an altitude of 200 km and perhaps even to 250 km, or over a height range of 3 to 5 plasma scale heights.

If the upper atmosphere of Mars consists primarily of molecular constituents (such as  $\text{CO}_2$ ,  $\text{CO}$ , or  $\text{O}_2$ ), the ionization peak might be produced by solar ultraviolet flux. This third alternative, denoted as the  $F_1$  model, is also indicated in Figs. IX-17 and IX-18, assuming 100%  $\text{CO}_2$ . In this model, the ionization peak occurs at a neutral density of about  $10^{10} \text{ cm}^{-3}$ , where the slant optical depth in the ultraviolet part of the spectrum is unity.

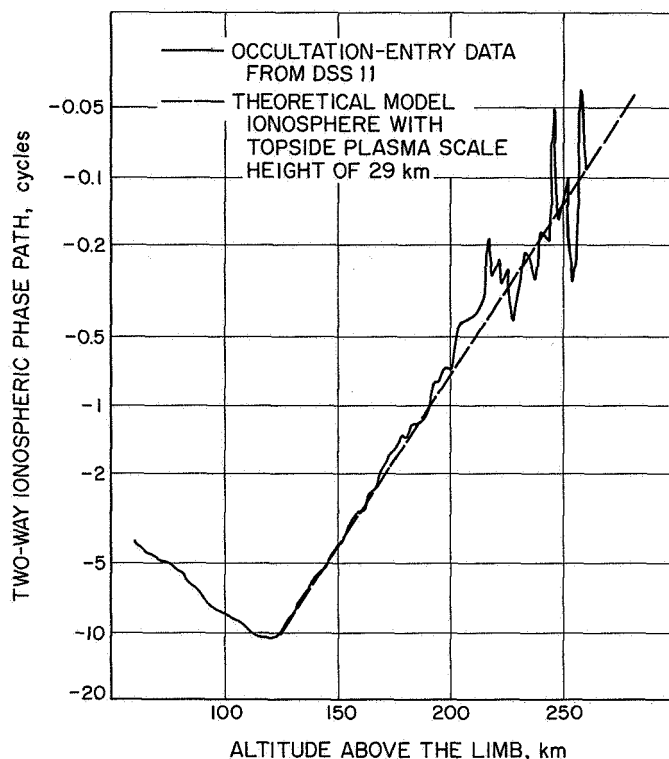


**Fig. IX-19. Two-way ionospheric phase path vs altitude above the limb**

Both the E and  $F_1$  hypotheses require mixing or negligible dissociation of  $\text{CO}_2$  in order to avoid the preponderance of atomic oxygen in the region where the data show a constant plasma scale height. This is one of the reasons the  $F_2$  model is favored. Of the  $F_1$  and E models, the former is more attractive because:

- (1) No appreciable temperature gradients are expected on the topside of the  $F_1$  peak, since most of the solar flux is absorbed at lower altitudes. Thus, the topside plasma scale height would be constant without making any improbable assumptions about the altitude variations of the ion mass and the recombination coefficient.
- (2) In the  $F_1$ -region of the  $F_1$  model, the recombination coefficient would need to be about  $10^{-7} \text{ cm}^3/\text{s}$ , as compared with the  $10^{-5} \text{ cm}^3/\text{s}$  in the  $F_1$ -region of the E model. This lower value is in better agreement with the value expected for dissociative recombination of  $\text{CO}_2^+$ .

## References

1. Kaplan, L. D., Munch, G., and Spinrad, H., "An Analysis of the Spectrum of Mars," *Astrophys. J.*, Vol. 139, No. 1, Jan. 1964.
2. Kuiper, G. P., "Infrared Spectra of Stars and Planets, IV: The Spectrum of Mars, 1-2.5 microns, and the Structure of Its Atmosphere," *Commun. Lunar and Planetary Lab.*, Vol. 2, No. 31, University of Arizona, 1964.
3. Norton, R. B., *A Theoretical Study of the Martian and Cytherean Ionospheres*, NASA TN D-2333. National Aeronautics and Space Administration, Washington, D. C., July 1964.
4. Kliore, A. J., Cain, D. L., Levy, G. S., Eshleman, V. R., Drake, F. D., and Fjeldbo, G., "Mariner IV Occultation Experiment," *Astronaut. Aeronaut.*, Vol. 3, pp. 72-80, July 1965.
5. Kliore, A. J., Cain, D. L., and Hamilton, T. W., *Determination of Some Physical Properties of the Atmosphere of Mars From Changes in the Doppler Signal of a Spacecraft on an Earth-Occultation Trajectory*, Technical Report 32-674. Jet Propulsion Laboratory, Pasadena, Calif., Oct. 15, 1964.
6. Fjeldbo, G., and Eshleman, V. R., "The Bistatic Radar-Occultation Method for Study of Planetary Atmospheres," *J. Geophys. Res.*, Vol. 70, No. 13, July 1, 1965.
7. Kliore, A., Cain, D. L., Levy, G. S., Eshleman, V. R., Fjeldbo, G., and Drake, F. D., "Occultation Experiment: Results of the First Direct Measurement of Mars's Atmosphere and Ionosphere," *Science*, Vol. 149, No. 3689, pp. 1243-1248, Sept. 10, 1965.
8. Sloan, R. K., "The Scientific Experiments of Mariner IV," *Scientific American*, Vol. 214, No. 5, pp. 62-72, May 1966.
9. Levy, G. S., Ootshi, T. Y., and Seidel, G. L., *Ground Instrumentation for Mariner IV Occultation Experiment*, Technical Report 32-984. Jet Propulsion Laboratory, Pasadena, Calif., Sept. 15, 1966.
10. Cain, D. L., Kliore, A. J., and Levy, G. S., "The Mariner IV Occultation Experiment: Summary of Data and Reduction Methods," Paper 66-148, presented at the AIAA Third Aerospace Sciences Meeting, New York, January 24-26, 1966.
11. Hudson, R. H., Nead, M. W., and Warner, M. R., *The Orbit Determination Program of the Jet Propulsion Laboratory*, Technical Memorandum 33-168. Jet Propulsion Laboratory, Pasadena, Calif., Mar. 18, 1964.
12. Peabody, P. R., Scott, J. F., and Orozco, E. G., *User's Description of JPL Ephemeris Tapes*, Technical Report 32-58. Jet Propulsion Laboratory, Pasadena, Calif., Mar. 2, 1964.
13. Smyth, J. B., and Cashman, L. B., *Radio Meteorology at JPL Goldstone Pioneer Station July 14, 1965*, Report SRA-462. Smyth Research Associates, San Diego, Calif., July 1965.

## References (contd)

14. Cain, D. L., Drake, F. D., Eshleman, V. R., Fjeldbo, G., Kliore, A., and Levy, G. S., *Proceedings of the Symposium on Propagation Factors in Space Communications*, Advisory Group for Aeronautical Research & Development, Ionospheric Research Committee, 10th meeting, held in Rome, Italy, Sept. 21-25, 1965.
15. Kliore, A., Cain, D. L., Drake, F. D., Eshleman, V. R., Fjeldbo, G., and Levy, G. S., "Preliminary Results of the Mariner IV Occultation Measurements of the Atmosphere of Mars," in *Proceedings of the Caltech-JPL Lunar and Planetary Conference*, Pasadena, Calif., September 13-18, 1965, pp. 257-266.
16. Kliore, A., Cain, D. L., and Levy, G. S., "Radio Occultation Measurement of the Martian Atmosphere Over Two Regions by the Mariner IV Space Probe," paper presented at the 7th International Space Science Symposium, Committee on Space Research (COSPAR), Vienna, Austria, May 10-19, 1966.
17. Dollfus, A., "Physique planétaire — Mesure des dimensions du globe de la planète Mars," *Comptes Rendus Hebdomadaires des Seances de l'Academie des Sciences*, Vol. 255, pp. 2229-2231, Oct. 29, 1962.
18. Fjeldbo, G., Eshleman, V. R., Cain, D. L., Drake, F. D., Kliore, A. J., and Levy, G. S., "Preliminary Results of the Mariner IV Occultation Measurements of the Upper Atmosphere of Mars," in *Proceedings of the Caltech-JPL Lunar and Planetary Conference*, Pasadena, Calif., Sept. 13-18, 1965, pp. 267-272.
19. Fjeldbo, G., Fjeldbo, W. C., and Eshleman, V. R., "Models for the Atmosphere of Mars Based on the Mariner IV Occultation Experiment," *J. Geophys. Res.*, Vol. 71, pp. 2307-2316, May 1, 1966.
20. Fjeldbo, G., Fjeldbo, W. C., and Eshleman, V. R., "Atmosphere of Mars: Mariner IV Models Compared," *Science*, Vol. 153, pp. 1518-1523, Sept. 23, 1966.
21. Chamberlain, J. W., and McElroy, M. B., "Martian Atmosphere — The Mariner Occultation Experiment," *Science*, Vol. 152, pp. 21-25, Apr. 1, 1966.
22. Johnson, F. S., "Atmosphere of Mars," *Science*, Vol. 150, pp. 1445-1448, Dec. 10, 1965.
23. Gross, S. H., McGovern, W. E., and Rasool, S. I., "Mars — Upper Atmosphere," *Science*, Vol. 15, p. 1216, Mar. 11, 1966.

## Appendix

### Abbreviations

AAC	automatic aperture control	NAS	narrow-angle scan
A/D	analog to digital	NRT	non-real-time
AGC	automatic gain control	OGO	<i>Orbiting Geophysical Observatory</i>
A/PW	analog-to-pulse width	OSE	operations support equipment
AU	astronomical unit	PHA	pulse-height analyzer
B/R	booster regulator	PIV	planet-in-view
CRT	cosmic ray telescope	PN	pseudo-noise
CC&S	central computer and sequencer	POGO	<i>Polar Orbiting Geophysical Observatory</i>
CDD	cosmic dust detector	PSS	planetary scan subsystem
CG	center of gravity	PS&L	power switching and logic
CIT	California Institute of Technology	PTM	proof test model
DAS	data automation subsystem	RT	real time
DN	data number	SAF	Spacecraft Assembly Facility
DSIF	Deep Space Instrumentation Facility	SC	spacecraft
DSN	Deep Space Network	SEP	sun-earth-probe
DSS	Deep Space Station	SFOF	Spacecraft Flight Operations Facility
EOGO	<i>Eccentric Orbiting Geophysical Observatory</i>	SPAC	spacecraft performance analysis and command group
ESP	earth-sun-probe	SPP	Solar Plasma Probe
EPS	earth-probe-sun	SSAC	space science analysis and command group
G-M	Geiger-Mueller	STP	standard temperature and pressure
GMT	Greenwich Mean Time	SUI	State University of Iowa
GSFC	Goddard Space Flight Center	TPS	telemetry processing station
ID	identification data; inside diameter	TRD	trapped radiation detector
IR	infrared	TWT	traveling-wave tube
IMP	<i>Interplanetary Monitoring Probe</i>	UT	Universal Time
MIT	Massachusetts Institute of Technology	VCO	voltage-controlled oscillator
NAMG	narrow-angle Mars gate	WAA	wide-angle acquisition